TRAPPIST observations of sodium jets from Io

Auteur : De Spiegeleire, Amandine
Promoteur(s) : Jehin, Emmanuel; Bonfond, Bertrand
Faculté : Faculté des Sciences
Diplôme : Master en sciences spatiales, à finalité approfondie
Année académique : 2018-2019
URI/URL : http://hdl.handle.net/2268.2/7826

TRAPPIST OBSERVATIONS OF SODIUM JETS FROM IO

By Amandine De Spiegeleire

Under the supervision of Emmanuël Jehin and Bertrand Bonfond

A thesis presented for the degree of Master in Space Sciences

Academic year 2018 – 2019

University of Liège, Faculty of Sciences
Department of Astrophysics, Geophysics and Oceanography

Remerciements

Je remercie premièrement mes deux promoteurs Emmanuël Jehin et Bertrand Bonfond de m'avoir donné l'opportunité de réaliser ce fascinant mémoire et de m'avoir ouvert la porte à ce sujet et à l'étude d'Io. Leurs conseils m'ont été d'une très grande aide. Je remercie également Marin Ferrais pour m'avoir guidé à travers la réduction des données et d'avoir été disponible pour moi. Je remercie toutes les personnes impliquées dans le projet TRAPPIST. Merci à Vincent et à mes sœurs, Astrid et Sarah, pour la relecture de mon manuscrit et pour leurs soutiens tout le long de cette année.

Contents

List of Figures

List of Tables

Chapter 1

Introduction

This chapter has as purpose to introduce TRAPPIST observations of sodium jets from Io.

The solar system is composed of many planets and celestial bodies of the greatest interest, each bringing many questions and new discoveries. The unusual nature of Io, the Galilean satellite closest to Jupiter, makes this celestial object fascinating. As a result of the many observations made over the years, our understanding of Io has drastically changed.

Everything begins with the discovery of Io and the other three big Jovian satellites by Galileo Galilei in 1610. It is the astronomer Simon Marius who suggested the names of the four Galilean satellites: Io, Europa, Ganymede and Callisto. These Galilean satellites attracted the attention of a number of astronomers and mathematicians in the 17^{th} and 18^{th} centuries. The story of Io's exploration grows rapidly as soon as telescopes have become efficient enough to study these planetary bodies beyond their orbits and dynamics. Several space missions have allowed observations of Io. It began in the early 1970s with the launch of Pioneer 10 and 11 probes. These spacecrafts flew by Jupiter in 1973 and 1974, and provided new discoveries about Io's environment. These results provided a better understanding of the nature of Io's interior, surface and atmosphere. One of the discoveries related to the Pioneer mission is that Io has a density much higher than the other Galilean satellites, showing that the latter is depleted in volatile components compared to Europe, Ganymede and Callisto. These probes also revealed that Jupiter had intense charged particles belts embedded in the Jovian magnetic field and the intensity of this radiation proved to be very high at the distance that separates Io from Jupiter. All these new discoveries related to the Pioneer mission have triggered a new craze for the observation of the outer planets. In 1979, the Voyager spacecraft arrived at Jupiter. Images of Io taken by Voyager revealed the surprising and intense volcanic activity of the satellite. The

probe also allowed the detection of SO_2 as a gas representing the first evidence of a neutral atmosphere on Io. In 1995, it is the turn of the Galileo probe to arrive in the Jovian system. Galileo flew several times over Io. The discoveries related to this mission are numerous. Notably, these passages near Io allowed the discovery of a metal core as well as the observation of very intense volcanic eruptions allowing the hypothesis that the Ionian silicate magma would be of mafic and ultramafic composition (rich in magnesium and iron). These flybys also reveal the different geological processes that occur on the volcanoes and mountains of Io, and also, allow to exclude the existence of a magnetic field. In 2000, the Cassini-Huygens probe, mission on the way to Saturn, observes at the same time as the Galileo probe, volcanic plumes on Io. This mission also provides the first proof of aurora in the atmosphere of the Galilean satellite. In 2007, on its way to Pluto, the New Horizons spacecraft flew over Io and photographed its volcanic activity. Juno, a NASA (National Aeronautics and Space Administration) spacecraft orbiting Jupiter launched on 2011, also photographed volcanic plumes on Io. In 2013, Hisaki, a spectroscopic planet observatory satellite from the Japan Aerospace Exploration Agency, was launched in orbit around the Earth in order to study the plasma torus of Io and also the planetary exospheric escape by an extreme ultraviolet (EUV) spectroscopy observation.

By the early 1960s, the first signs of unusual behavior related to Jupiter's satellite, Io, were observed. Since then, following the various space missions as well as the ground-based observation by telescopes, our understanding of this celestial object has been restructured many times. Many questions remain unanswered regarding Io. Therefore, the study of this satellite is very interesting. In this work, we conducted a study of Io in order to observe sodium jets. These jets, which have been reported by several studies (eg. Burger et al., 1999; Schneider et al., 1991; Wilson et al., 2002), would be expelled from Io. For this study, we used the robotic telescope, TRAPPIST-South.

In Chapter 2, we describe Io in order to have the necessary information to understand what the observed jets represent. Volcanism being omnipresent on Io, it plays a very important role and is thus quickly mentioned as well as the different causes producing this activity on the satellite. The volcanic activity of Io allows the presence of a thin atmosphere. This atmosphere is essential since it provides an enormous amount of matter to the Jovian magnetosphere. To finish this chapter, we describe the important interaction between Jupiter and its satellite. These

interactions between the two bodies are the cause of the most surprising phenomena observed in the Jovian system such as volcanoes on Io.

Chapter 3 is devoted to the description of the two robotic telescopes, TRAPPIST-North and TRAPPIST-South. The TRAPPIST project is described as well as the technical details of the telescopes. The location on two observation sites in different hemispheres allows many advantages to the observation such as a large sky coverage and a large amount of observing time.

In Chapter 4, we describe the data acquisition for Io's observation and the reduction of these data. For the preparation of these observations, the first thing to do is to determine the visibility window of Jupiter in order to observe Io. Then, observing plans are sent to the computers controlling TRAPPIST. Once the data is obtained, the raw images are calibrated by different processes described in the sections of this chapter.

The chapter 5 is dedicated to the image processing. The goal of this image processing is to reduce the noise due to the artefacts created by the powerful brightness of Jupiter and improve the signal-to-noise ratio of our images. Different methods are described in this chapter to do so. We develop and explain three methods of image processing with IDL. Then, we describe a method to detect and emphasize the presence or absence of a jet, the rotational gradient method centered on Io. This method is also used as an image processing when centered on Jupiter, also implemented with IDL.

In chapter 6, we first present the results related to the image processing that we carried out by four different methods developed with IDL. We show our results for each night of observations with each of the image processing methods. Then, to quantify which of these four methods works best for our project, we compare and quantify them through the definition of the signal-to-noise ratio. Once this comparison is made and the most optimal method deduced, we perform measurements to quantify the physical observable properties of the sodium jets. We develop the profile of the length of the detected jets and in the case where we observe the widest jet, we measure its width profile over several sections. Finally, we measure the length and the angle with the Jupiter-Io line of the jets we detected.

The chapter 7 is devoted to the conclusion of our study on sodium jet observation with TRAPPIST. We also mention the perspectives related to this study as well as the future work that could result.

Chapter 2

Io

2.1 Introduction

Io is one of the four Galilean satellites of Jupiter. Discovered in 1610 by Galileo Galilei, these satellites have proved that planetary bodies revolve around something other than the Earth and thus confirm the Copernican model of the solar system according to which the Sun is the center of our system. In 1979, the Voyager 1 spacecraft flew over Io and highlighted its active volcanism. Peale et al. (1979) hypothesized that Laplace resonance created a forced eccentricity in Io's orbit. Therefore, Io periodically deforms during its rotation around Jupiter. According to Peale et al. (1979) the dissipation of tidal energy in Jupiter's satellite Io probably melted a large fraction of its mass. The images taken by Voyager 1 confirmed their assumptions. In fact, these images show volcanic plumes up to 300 km high and reveal a brightly colored surface. Several studies on Io volcanism have been conducted using the Galileo, Cassini and New Horizons spacecraft as well as using ground-based telescopes and the Hubble Space Telescope.

Io is the closest Galilean satellite to Jupiter. This satellite is subject to the most intense tidal forces which deform it in a manner determined by the properties of Io. Io's physical properties are shown in Table 2.1 (Lopes, 2014). This Jupiter's satellite is similar in size to the Moon, but its density is higher indicating an interior composition richer in iron. The results of the Galileo mission showed that sulfur dioxide is omnipresent on Io's surface. Io is the most volcanically active planetary body in the solar system. Indeed, the volcanic eruptions present on Io are important and spectacular. Volcanic plumes would feed the atmosphere present on Io since sulfur dioxide is the main constituent (Pearl et al., 1979). The Galileo mission highlighted the existence of aurora caused by collisions between the atmospheric gases of Io and energetic

charged particles trapped in the magnetic field of Jupiter. Indeed, there is a considerable interaction between Io and the Jovian magnetic field. Material consisting of sulfur, sulfur dioxide, sodium, potassium and dust escapes from Io and forms a cloud of neutral particles along its orbital path. A torus, also formed of material escaping from Io, exists along its trajectory maintained by the magnetic field of Jupiter. Several gray areas still surround Io and its interaction with the magnetosphere of Jupiter. Several studies attempt to determine the influence of Io volcanism on the phenomena we observe in the Jovian system (eg., Bonfond et al., 2012; Koga et al., 2018; Yoneda et al., 2013, 2010). Indeed, Bonfond et al. (2012) show the existence of auroral evidence of Io's control over the Jovian magnetosphere. Other study shows also the link between Io's volcanism and the radio emissions of Jupiter (Yoneda et al., 2013).

Table 2.1: Io's physical properties (Lopes, 2014)

Mean radius	1821.6 ± 0.5 km
Bulk density	3528 ± 3 kg m^{-3}
Orbital period	1.769 days
Orbital eccentricity	0.0041
Orbital distance a	421 800 km
Mass	$(8.9320 \pm 0.0013) \times 10^{22}$ kg
Surface gravity	1.80 m s^{-2}
Global average heat flow	> 2.5 W m^{-2}
Radius of core	If pure iron: 656 km If iron and iron sulfide mixture: 947 km
Surface equatorial magnetic field strength	< 50 nT
Typical surface temperature (away from hot spots)	Night: 85 K Day: 140 K
Atmospheric pressure	< 10^{-9} bar (higher at locations of plumes)
Atmospheric composition	Mainly SO_2, SO, S_2, Na

2.2 The interior of Io

At a distance of 421 600 kilometers from Jupiter, Io is the Galilean satellite closest to the gaseous planet. The latter is therefore the object of the Jovian system subjected to the most intense tidal forces. Moreover, the difference in mass between the two bodies generates a very important gravitational attraction by Jupiter on Io. Nevertheless, Europa and Ganymede, two

other Galilean satellites of Jupiter, maintain Io in its orbit by a phenomenon of resonance, the interaction between these three satellites creates the eccentricity observed on the orbit of Io (see Table 2.1). Its period of rotation being synchronous with its period of revolution, Io exposes at all times the same face to Jupiter which generates deformations of the satellite. Indeed, because of its proximity to Jupiter, its synchronous revolution around the giant planet, its orbital eccentricity and the huge difference in mass between the two bodies, Io experienced very strong tidal forces. These tidal forces cause compressions and dilatations of the interior of Io causing heating by internal friction. In fact, as shown in Figure 2.1, Io creates a tidal bulge in Jupiter. This tidal bulge increases the orbital energy of Io at the expense of the rotational energy of the planet. Even if the tidal bulge of Jupiter pulls Io ahead of its orbit, it will rather slow the movement of the satellite. Indeed, the Virial theorem states that when the energy of a body in orbit increases, its kinetic energy decreases while its potential energy increases twice more. Due to the slight eccentricity of Io's orbit, generated by resonance with Ganymede and Europa, the angular velocity of Io will vary (Figure 2.1 b). At the apojove of its orbit (corresponding to its furthest point from Jupiter), the tidal bulge is in the direction of Io's rotation, ahead of the Io-Jupiter line because Io rotates faster than orbiting. Therefore, the rotation of Io is slowed down as its orbital energy increases. At the perijove, the opposite is observed. The gravity of Jupiter increases the rotational energy of Io and its orbital energy decreases. Since the gravitational attraction and the tidal bulge are more important at the perijove than at the apojove of Io's orbit, the influence at the perijove prevails and Io spirals inward toward Jupiter. The energy associated with these compressions, dilatations and shifting is mainly dissipated by friction. The resulting heat of this friction is the cause of the volcanic activity observed on Io (Miller, 2009).

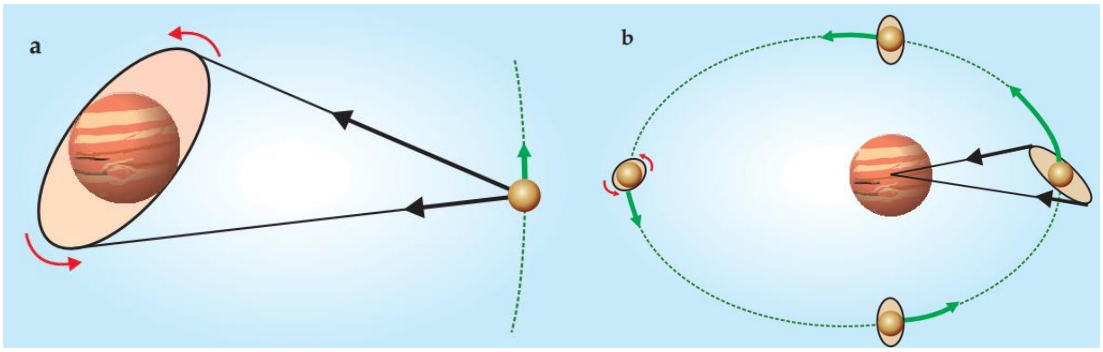

Figure 2.1: Tides in Jupiter and Io. a) A tidal bulge in Jupiter is created by Io's gravity. The red arrows show Jupiter's rotation. The black arrows show the gravitational interaction between Io and the bulge. b) A tidal bulge is created by Jupiter in Io. The green arrows illustrate the instantaneous orbital speed of Io (which varies). The red arrows show the rotation of Io. The orbit eccentricity and the tidal bulges are exaggerated. Source: Miller (2009).

The physical properties of the interior of Io determine its deformation due to these tidal forces. By measuring the deformations of Io, information on its internal structure can be determined. The shape, moment of inertia, density and gravity of Io are comparable to a fluid body differentiated into a metal core and a silicate mantle (Anderson et al., 2001). Indeed, telescopic and spatial data studies combined with geophysical modeling suggest that Io differentiates into a 550-900 km metal core if composed of Fe and FeS or a 350-650 km core if composed only of Fe, in a silicate mantle and in a crust which surely includes an asthenosphere (Lopes, 2014). Kivelson et al. (2002) showed, using the Galileo magnetometer data, that Io did not have a significant intrinsic magnetic field. This could therefore indicate that the core of Io is either completely liquid or completely solid. Since it is suggested that the core of Io is composed of Fe-FeS, it is more likely that the core is completely liquid (Keszthelyi et al., 2004). Indeed, this eutectic composition[1] has a relatively low melting temperature.

The average heat flux at the Io surface can be as high as 2.5 W/m^2 depending on infrared observations (Veeder et al., 1994) and estimations of tidal dissipation. To explain this heat flux at the surface, it has been suggested that heat is mainly transmitted by magma via isolated vents rising from the depth to the surface (O'Reilly and Davies, 1981). This hypothesis allows the existence of a thick lithosphere on Io corresponding to what is observed. Volcanism (see section 2.3) would therefore be an effective means of removing heat from the inside and allowing the maintenance of a thick and rigid lithospheric layer (Monnereau and Dubuffet, 2002). By studying the rotating magnetic field of Jupiter as a sounding signal and using the magnetometer data of the Galileo probe, Khurana et al. (2011) proposes the existence of an electromagnetic induction from a global conducting layer corresponding to a magma ocean of more than 50 km thickness within Io. This hypothesis would explain the data collected by the Galileo mission. However, a more recent study by Blöcker et al. (2018) shows that a magnetic induction signal created by an ocean of partially melted magma is not automatically required to explain the Galileo magnetometer data. They show that the perturbations measured by the probe can be due to the interaction of the plasma with the asymmetric atmosphere in the longitudinal direction of Io.

[1] A eutectic is a mixture of two or more pure substances that melts and solidifies uniformly at a constant temperature. The Fe-FeS mixture is characterized by a eutectic behavior at low pressure (< 10 GPa) with a eutectic melting point at T = 1000˚C (with 31% by mass of sulfur) (Fei et al., 1997).

2.3 Active volcanism on Io

One of the most remarkable features of Io is its active volcanism. Volcanism is an elementary process that has affected all the solid planets as well as most moons of the solar system. Jupiter's satellite, Io, is the most volcanically active object in the solar system, as shown by observations of ground-based telescopes and several spacecraft. Io volcanism has been studied through imaging and spectroscopy. These instruments on board of the Voyager, Galileo, Cassini and New Horizons spacecraft have provided images of erupting plumes as well as the recording of the spatial extent of surface deposits produced by volcanism (eg., Geissler and McMillan, 2008; Porco et al., 2003; Strom et al., 1981; Davies et al., 2018). The images taken by Voyager 1 showed for the first time that the surface of Io was devoid of impact craters which was rather surprising since we find craters on all solid bodies of the solar system. One of the obvious conclusions was that Io's surface was very young and the craters had to be erased. In addition, the infrared interferometer spectrometer on the Voyager 1 spacecraft detected enhanced thermal emission from certain areas of the Io's surface, which constitutes further evidence of active volcanism on the Jupiter's satellite. Ground-based observations have been used to monitor the thermal signatures of Io's active volcanoes (eg., Howell et al., 2001; Rathbun and Spencer, 2010).

The eruptions on Io consist of massive volumes of silicate lava, sulfur and sulfur dioxide. This intense volcanism is constantly changing Io's appearance. While each volcanic center has many exclusive features, the majority can be classified. Although a hotspot may present more than one eruption style over time, Io volcanism is characterized by three types of eruptions based on the appearance of eruptions and the type of lava emitted: flow-dominated volcanism, explosion-dominated volcanism and intra-patera volcanism (Lopes, 2014).

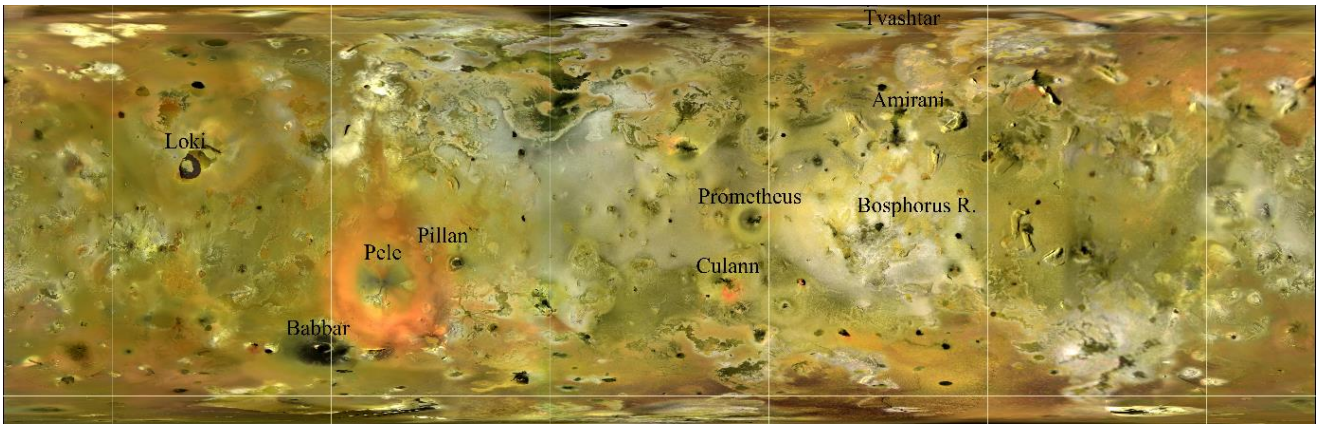

Figure 2.2: Map of some Io's hotspots. The mosaic is in an equal area cylindrical map projection, centered on longitude 180, with grid lines at 30 degree intervals (Adapted from: https://photojournal.jpl.nasa.gov/jpeg/PIA09257.jpg).

2.3.1 Flow-dominated volcanism

Flow-dominated eruptions produce large lava flow fields (Keszthelyi et al., 2001). These lava fields are composed of repeated small breakouts of lava. The hotspots of Prometheus and Amirani (Figure 2.2) are the archetype of this kind of volcanism whose eruptions come from their paterae (volcano-tectonic depressions) or fissures constituting a persistent plume of about 100 km high often including small explosive plumes of over 200 km of height of sulfurous materials vaporized (Kieffer et al., 2000). Flow-dominated eruptions are regular eruptions that can last for several years and have a temperature associated with terrestrial basaltic volcanism (Lopes, 2014). The plumes of this type of eruption would be SO_2 gas formed when the hot lava vaporizes SO_2 snow on the plains. As the flow field advances slowly, the location of the plume source changes. Indeed, the movement of the plume is related to the interaction between the rising hot lava and the snow field underlying the sulfur dioxide (Kieffer et al., 2000). Once the flow stops moving, the plume eventually goes out.

2.3.2 Explosion-dominated volcanism

In contrast to flow-dominated eruptions, explosion-dominated eruptions are characterized by large pyroclastic deposits and intense, short-lived eruptions lasting from several days to several weeks (Keszthelyi et al., 2001). This type of eruption is defined by Pillan, Pele, Surt and Tvashtar volcanoes (Figure 2.2) and come, like the flow-dominated eruptions, from fissures or paterae. The explosion-dominated eruptions produce dark lava flow fields. Both types of

eruptions usually have SO_2-rich plumes of ~100 km high. These plumes form near the flow fronts. Smaller deposits of red material are also observed marking the vent of silicate lavas. Due to the interaction of silicate magma with sulfurous volatile substances, large explosive plumes over 200 km high can occur during this type of eruption, often forming a large red ring of short-chain sulfur around the source regions (see Figure 2.2: at Pele) (Keszthelyi et al., 2001; Turtle et al., 2004). The temperature associated with this type of eruption corresponds to mafic[2] to ultramafic terrestrial volcanism (Lopes, 2014).

2.3.3 Intra-patera volcanism

Intra-patera eruptions are confined to volcano-tectonic depressions called paterae (Lopes et al., 2004). These depressions, ranging in size from 2 to 200 km in diameter, are found everywhere on the Io's surface. Loki, Pele, Emakong and Tupan volcanoes characterize this type of eruption (Figure 2.2). The eruptions associated with this type of volcanism are characterized by the formation or not of a plume in the form of a lava lake. Some of these lava lakes may be subject to a reversal or resurfacing of their upper solid crusts as shown by the observations of Loki's patera undergoing periodic reversals (Rathbun et al., 2002). Most of Io's active volcanoes are paterae (Lopes et al., 2004).

2.4 Io's atmosphere

Discovered for the first time at 7.3 µm by Voyager (Pearl et al., 1979), the tenuous atmosphere of Io is mainly composed of SO_2 and has for minor compounds SO, S_2 and NaCl (Lellouch et al., 2015). This SO_2 comes from active volcanism on the satellite (see section 2.3), sublimation of ubiquitous surface frost warmed by sunlight (Douté et al., 2001), as well as direct degassing of SO_2 by volcanic vents and plumes (Jessup et al., 2004). These different processes regenerated at all times the atmosphere of the moon of Jupiter. According to the data, Io's atmosphere is subject to significant diurnal, longitudinal, latitudinal, seasonal and unpredictable variability

[2]A mafic lava corresponds to a lava whose composition has a high content of magnesium and iron. An ultramafic lava has a highly magnesian composition containing less silica than mafic lavas.

(Lellouch, 2005). This atmosphere is uneven, its density at the location of active plumes is greater. Its average density is about 10^{-9} bars (Lopes, 2014). Despite the continuous supply of material in the atmosphere of Io, its low gravity causes a significant loss estimated at a rate of 1 ton per second (Saur et al., 2003). The material loss processes from Io's atmosphere are mentioned in detail in section 2.5.3.

2.5 The Io – Jupiter interaction

Jupiter, the most massive planet in the solar system, has the strongest magnetic field. The magnetosphere of Jupiter represents a region of space where the motion of the plasma is controlled by the Jovian magnetic field rather than by the solar wind. Galilean satellites are located in the inner regions of this magnetosphere (Figure 2.3). They are subjected to intense radiation bombardment. The very fast rotation of Jupiter (36°/h) (Gledhill, 1967) among others properties, lead to unique phenomena in our solar system: volcanoes on Io and a large input of plasma from Io filling the magnetosphere of Jupiter. Indeed, Jupiter's strong magnetic field, fast rotation and Io volcanism are elements that make the electrodynamic interaction of Io unique in our solar system. In many cases, the configuration of Jupiter's magnetic field near Io's orbit is assumed to be a dipole slightly offset from the center of Jupiter and tilted by 10.31° with respect to the rotation axis towards a System III magnetic longitude (λ_{III}) of 196.61° (Connerney et al., 2018).

The effect of Io on the Jovian magnetosphere is very important. The magnetosphere of Jupiter is affected by Io. Indeed, the contribution of plasma from Io causes the magnetosphere to inflate, the latter having twice the size it should have.

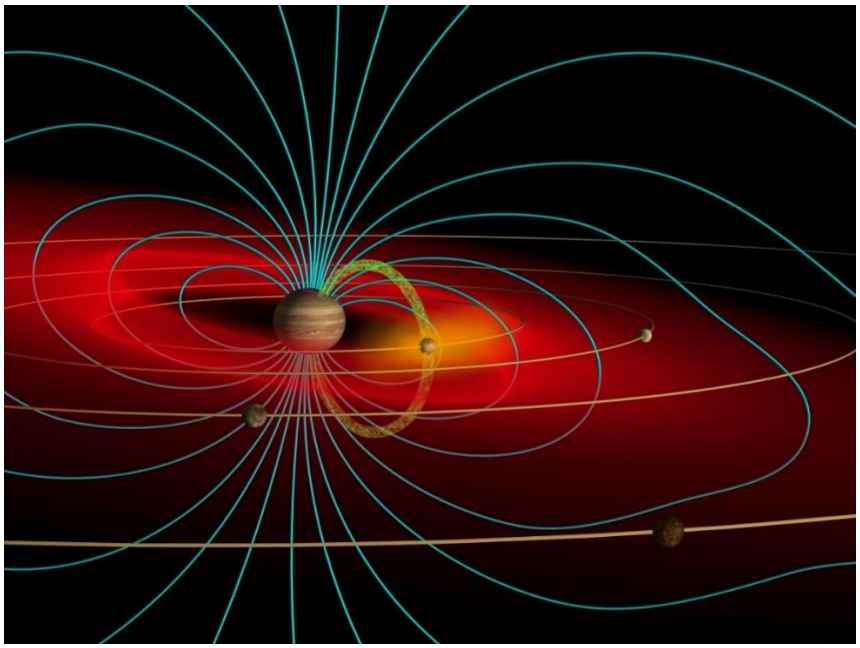

Figure 2.3: The Jupiter magnetic field (blue lines), the Io torus (in red), and the flux tube created at Io (in green). The locations of the orbits of the other Galilean satellites, Europa, Ganymede, and Callisto (in brown). (Credit: John Spencer)

Jupiter's innermost Galilean satellite, Io, is the main source of mass in the Jovian magnetosphere. Io is the most volcanically active body in our solar system (see section 2.3). This volcanism creates, with the sublimation of surface frosts, a tenuous and uneven atmosphere on Io (see section 2.4). The atmosphere of Io loses matter in the Jovian magnetosphere by different processes (Figure 2.8). This matter torn from Io arrives partly ionized and partly neutral. Neutral particles follow Io's orbit around Jupiter and form the neutral clouds (see section 2.5.2). These particles are at 5.91 Jovian radii (R_J = 69 911 km) from the center of the planet (Thomas et al., 2004). They are then ionized by electron impact and charge exchange at time scales of the order of a few hours (Brown, 1983) to constitute the plasma torus (see section 2.5.3).

2.5.1 The magnetosphere of Jupiter

In this section, we briefly describe the magnetosphere of Jupiter and its magnetic field in order to get an overview of the environment and physics in which Io is located. This also allows us to introduce the Io plasma torus which will be detailed in section 2.5.3.

The magnetosphere of Jupiter (Figure 2.4) consists of a cavity created in the solar wind by the magnetic field of the gaseous planet. The magnetosphere of the giant planet is strongly dominated by its rotation (rotation period of ~ 10 hours). It represents the most powerful magnetic field and the largest planetary magnetosphere of the solar system. Indeed, it extends beyond the orbits of the Galilean satellites, more than 7 million kilometers towards the Sun and reaches almost the orbit of Saturn in the opposite direction.

At 5.9 R_J, Io's orbit is embedded in the internal magnetosphere of Jupiter. The inner magnetosphere of Jupiter is dominated by its internal field up to the distance of the orbit of Io. At this distance, the magnetic field is approximately dipolar with a strength of 2000 nT (Bagenal et al., 2004). As mentioned before, Io loses 1 ton s^{-1} of atmospheric materials (Saur et al., 2003) which, once the half ionized, are trapped in the magnetic field of Jupiter, the other half are neutral particles. The coupling of these ions to the planet causes the co-rotation of the magnetospheric plasma with the latter. The plasma is confined to the equator by significant centrifugal forces and will form a torus around Jupiter. This plasma torus is located just outside Io's orbit and rotates with the same angular velocity, as well as in the same direction as Jupiter. It will, in turn, load the magnetosphere of Jupiter with plasma and it will spread out, and form the current sheet. The interaction between Io and Jupiter is very important. Indeed, unlike the Earth whose magnetosphere is essentially shaped by solar winds, the magnetosphere of Jupiter is also shaped by the plasma originated from Io and, as mentioned above, by its own rotation (Bagenal et al., 2004).

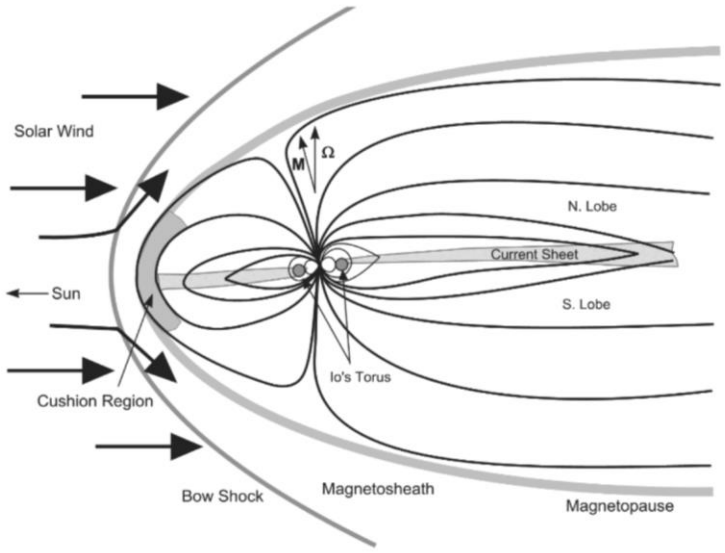

Figure 2.4: Schematic view of the magnetosphere of Jupiter. The dipole moment of Jupiter is tilted by 9.6° relative to the rotation axis Ω (Source: Bagenal et al., 2004).

The magnetosphere of the gaseous planet traps and accelerates the particles in it, creating intense radiation belts. The plasma torus of Io, in co-rotation with Jupiter, drastically modifies the dynamics of the Jovian magnetosphere. By different processes, the plasma slowly escapes from Jupiter's orbit. The iogenic plasma is transported radially by a fluxtube interchange process. A magnetic fluxtube represents a region of the space where the magnetic field is stronger than the surrounding space in which the field is perpendicular to the normal vector (see Figure 2.3, the fluxtube between Io and Jupiter is shown in green). Indeed, it is thought that the transport of the dense plasma from the torus (located at ~ 6 R_J) to the outer part of the Jovian magnetosphere (~ 50 R_J) would be through a fluxtube interchange process (Bagenal et al., 2004). An instability is created between the dense Jovian plasma and the much less dense plasma of the outer magnetosphere leading to an interchange between the outer and inner portions of the magnetosphere fluxtube filled with plasma. During this process, the magnetic fluxtubes containing relatively dense plasma move outwards while the relatively empty fluxtubes move inwards. This radial transport process lasts between 20 to 80 days, equivalent to 50 to 400 rotations of Jupiter. It is thought that the radial motion of the plasma is the slowest near Io's orbit and accelerates away from it. Indeed, the plasma moving away from the planet, the speed of the currents flowing in the torus increases gradually to maintain the co-rotation. Finally, the plasma torus of Io extends as an equatorial plasma sheet from the gaseous planet into the entire magnetosphere (Bagenal et al., 2004). In the outer magnetosphere (~ 40 R_J), as the plasma rotates in the tail, it can be ejected out of the magnetotail as the field lines stretch and reconnect. The plasma is ejected according to the Vasyliunas cycle which consists of a plasma transport mechanism in and out of the magnetotail (Vasyliunas, 1983). This cycle corresponds to the ejection of the plasma of internal magnetospheric origin by the magnetotail.

2.5.2 The neutral clouds

Volcanic eruptions populate the surface of Io and allow the presence of an atmosphere composed of several gases. This atmosphere on Io plays a very important role on the magnetosphere of Jupiter. Volcanic outgassing fills Io’s atmosphere at the time scale of several hours to several days despite the low gravity of the satellite that allows its material to escape through different processes (see section 2.5.4) and form the neutral clouds. The material escaping from Io is composed of volatile volcanic elements such as SO_2, S_2, NaCl, KCl and other compounds. The material escapes from Io’s atmosphere with little or no direct ejection

from the surface. Indeed, despite the silicate volcanism present on Jupiter's satellite, no refractory elements such as Si, Fe, Mg or Al have been detected in the neutral clouds or the plasma torus (Na et al., 1998). The direct ejection of material by volcanoes is considered negligible. Since the vent velocities go up to 1 km s^{-1}, they are too small compared to the Io's escape velocity of 2.6 km s^{-1}. The speed and direction characteristics of the ejection processes of material escaping from Io are the causes of the features observed around this moon. Indeed, neutral clouds that extend over several R_J, far from Io, are formed by atoms that have undergone the sputtering process (see section 2.5.4). Celestial mechanics, in our case, dominated by Jupiter gravity, and loss processes due to interactions with the plasma torus (see section 2.5.4), control the morphology of the neutral clouds.

One of the minor components of Io's atmosphere is sodium (Na). Sodium is a very important component, not for its small quantity in the atmosphere but for its detection power at visible wavelengths (Chamberlain and Hunten, 1987). Indeed, sodium is easily observable and is an excellent tracer of the most abundant elements, unobservable in the visible. Trapped in Jupiter's magnetic field, energetic ions bombard Io's atmosphere and surface. This ion bombardment projects some sodium atoms off Io. In the vicinity of Io and the plasma torus, the neutralization of the atomic and molecular ions generates a release of neutral sodium at a velocity high enough to escape from the Jovian magnetosphere. This results in the formation of a large "nebula", in which the sodium, sprayed at a slower velocity, forms an elongated cloud orbiting with Io around Jupiter. This elongated cloud represents the "banana cloud" (see Figure 2.5 d).

Figure 2.5 illustrates two images from ground-based telescope and one from the Galileo mission of the sodium clouds around Jupiter and near Io. Just after their exit from Io's atmosphere, sodium atoms are visible (Figure 2.5 c) and further, around Jupiter, we observe energy-distinct cloud components (Figure 2.5 b). The sodium nebula is visible at the largest spatial scale (Figure 2.5 a). At the same spatial scale as Figure 2.5 b, Figure 2.5 d shows a diagram of the principal components of the cloud. The sodium clouds generated by Io provide a window to examine a complex chain of processes that seem to dominate the magnetosphere of Jupiter in a way that is not observed anywhere else in the solar system.

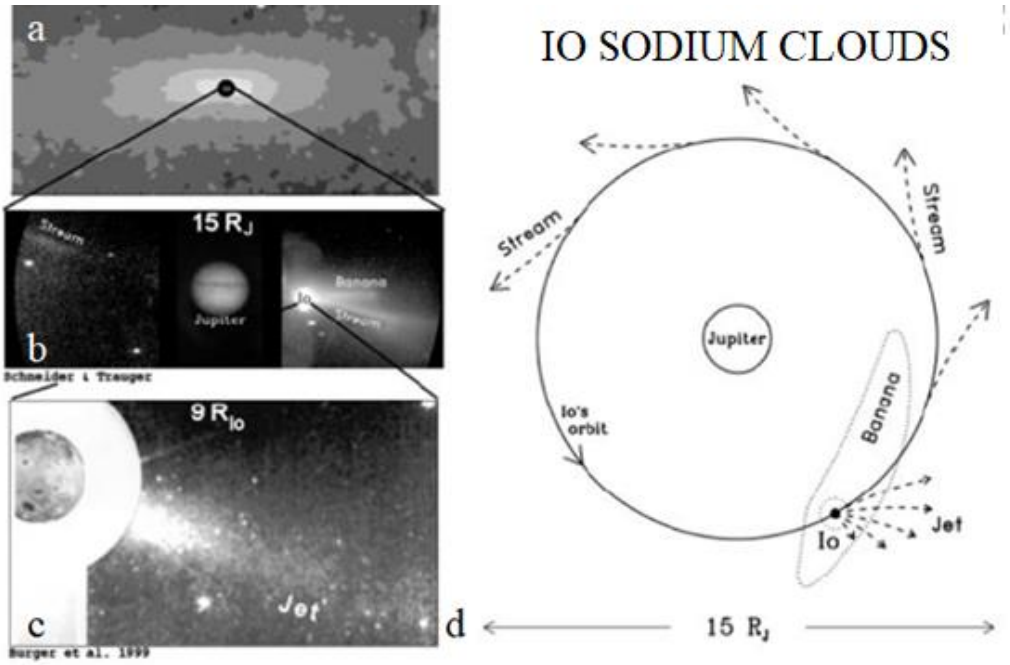

Figure 2.5: Images of the neutral sodium clouds on three different scales (left). A schematic of the sources of these sodium structures (right). (Thomas et al., 2004)

2.5.2.1 The sodium jets

Many studies have reported the observations of jets of sodium in several sets of data (Burger et al., 1999; Wilson et al., 2002; Wilson and Schneider, 1999).

The electric fields due to the magnetospheric interaction of Jupiter with Io forms, by extracting particles from Io's ionosphere, a jet of sodium (Figure 2.5 d). This jet can last during prolonged intermittent periods, its extend is in a direction away from Jupiter and it represents a narrow cloud. The sodium jets appear to point approximately perpendicular to the local unperturbed magnetic field of Jupiter at Io (Wilson and Schneider, 1999). Depending on the magnetic longitude of Io, the direction of these jets oscillates over a period of several hours (Pilcher et al., 1984). This indicates that fresh pickup ions, either Na^+ ions or unidentified molecular ions (NaX^+), are neutralized.

According to previous observations, it has been determined that the directivity of the sodium jet is exclusively anti-jovian. Thus, it is thought that the ions are forced out of the top of the

anti-jovian atmosphere of lo where a recombination or a charge exchange (see section 2.5.4) can produce the jet's fast neutrals (Thomas et al., 2004).

Moreover, the jets are produced solely from the trailing of Io which corresponds to the anti-Jovian quarter of Io. There, the sputtering process contributes the least to the particle feed of the clouds allowing the formation of jets. Thus, changes in atmospheric abundances in this region could alter the strength of the jet's source (Wilson et al., 2002).

2.5.2.2 The sodium streams

Leading Io into its orbit, the "stream" of sodium is a long, narrow cloud that undulates above and below the centrifugal equator of Io (Figure 2.5 d). The centrifugal equator represents an approximately planar surface where the centrifugal forces confine the plasma near the equator. This stream undulates with the same period as the sodium jet. Resulting from neutralization of fresh pickup ion, the stream is linked to the jet. Nevertheless what dissociates them is that the ions forming the jets recombine in a few minutes, or even less, near Io whereas the ions forming the stream recombine in the plasma torus after a few hours leaving Io (Thomas et al., 2004). The stream would be formed by NaX^+ ions, molecular ions escaped from the ionosphere of Io, to explain the well-defined observed structure of the streams (Schneider et al., 1991). Thomas et al. (2004) explain in the study of neutral clouds of Io and the plasma torus that the jets could be produced by the same NaX^+ molecular ions as the streams. This would mean that the jets represent, in fact, higher dissociative recombination rates in the part of the stream closest to Io, which corresponds to a region where the plasma densities are greater.

The X^+ particle of the NaX^+ ion has not yet been identified since it has never been detected by ground-based and spatial observations. Several studies suggest possible candidates. Identified as one of the neutral cloud components (Trafton, 1975), potassium (K) has been proposed as a possible candidate. Indeed, K has been detected by spectroscopy in a jet or stream near Io (Thomas, 1996). The ions of sulfur (S) and oxygen (O) are very likely eventualities given their large amounts in Io's atmosphere (Johnson, 1994). Lellouch et al. (2015) detected chlorine (Cl) in the atmosphere of Io, NaCl ions are therefore also proposed as candidates since, in addition, chlorine was found at concentrations similar to sodium in the plasma torus of Io (Küppers and Schneider, 2000). However, studies have shown that given the relatively low ionization

potential of Na and K (Kumar, 1985; Summers and Strobel, 1996), it is possible that the jet, if it is produced by escaping atomic ions, is composed of atomic particles of K and Na (Thomas et al., 2004).

2.5.3 The plasma torus of Io

The plasma torus of Io is a plasma ring of sulfur and oxygen ions (S^+, S^{++}, O^+, O^{++}, ...) which end up populating the entire magnetosphere of Jupiter (Figure 2.6). The main plasma source of Io's plasma torus is the loss of atoms by ionization from the neutral clouds. This process makes the plasma of the torus a self-maintained plasma. The total mass loss rate of Io, which feeds the torus, is estimated at about one ton per second (Saur et al., 2004). The newly introduced plasma is subjected to electrodynamic forces that accelerate it to the local velocity of the plasma already present. Upstream from Io, the plasma corotates almost completely with Jupiter, meaning at the same angular velocity as Jupiter. This plasma torus is located near Io's orbit. Io orbits around Jupiter with a velocity of 17 km s^{-1}. Io plasma torus has a velocity of about 74 km s^{-1} due to Jupiter's 10 hours rotation period. As Io is immersed in this torus of plasma, the torus plasma passes beyond Io at a relative velocity of 57 km s^{-1} (Saur et al., 2004).

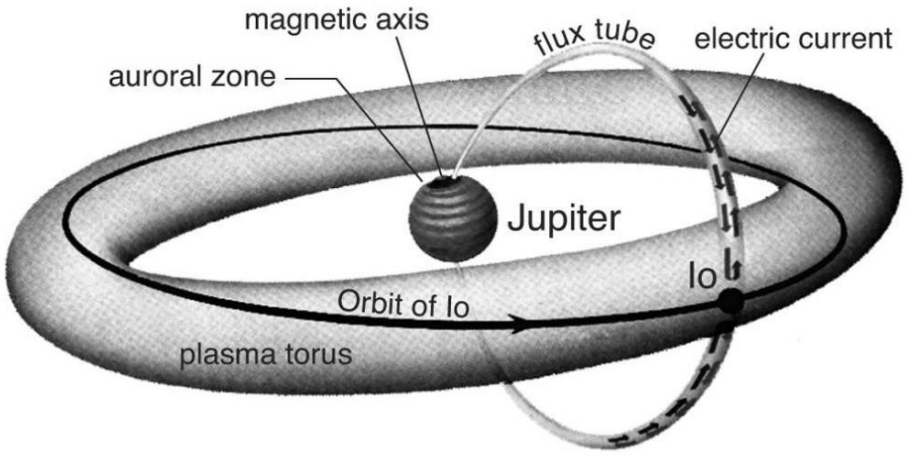

Figure 2.6: Sketch of the Io plasma torus and the general geometrical setup (Source: Saur et al., 2004)

Schneider and Trauger (1995) has documented the complex morphology of the torus through optical imaging. Nevertheless, much of this structure remains inexplicable. The plasma is

radially distributed leading to a spatial distribution of plasma that is not uniform in density nor temperature. Tsuchiya et al. (2019) have statistically studied the azimuthal variations in the plasma temperature and density using Japan Aerospace Exploration Agency's (JAXA) Hisaki satellite data. This study aims to determine the possible influence of the increase of the neutral particles of Io on the azimuthal variations of density and temperature of the plasma. Moreover, Hikida et al. (2018) studied the spectral structure in the ultraviolet (UV) region of the torus because the radiative cooling in the UV wavelength range is very significant in the energy balance of the plasma torus.

The process of plasma distribution in the torus is still poorly understood. However, thanks to the temperature of the ions composing the torus, we can classify different regions. Indeed, the propagation of the ions around the centrifugal equator reflects the thermal motions of the ion in the parallel direction, characterized by $T_{//}$. The centrifugal equator represents an approximately planar surface around which the plasma is distributed because the centrifugal forces confine the torus plasma near the equator (Hill and Michel, 1976).
We distinguish three distinct $T_{//}$ regions (Figure 2.7):

- At 5,4 R_J, the cold torus;
- At 5.7 R_J the "ribbon";
- Outside, the warm torus.

Figure 2.7 illustrates the plasma torus as well as the neutral clouds of Io. The most important part of the torus is the ribbon. The structure of the torus at 5.0 R_J is still unknown. It is strongly thought that density drops very quickly to almost zero (Bagenal, 1997).

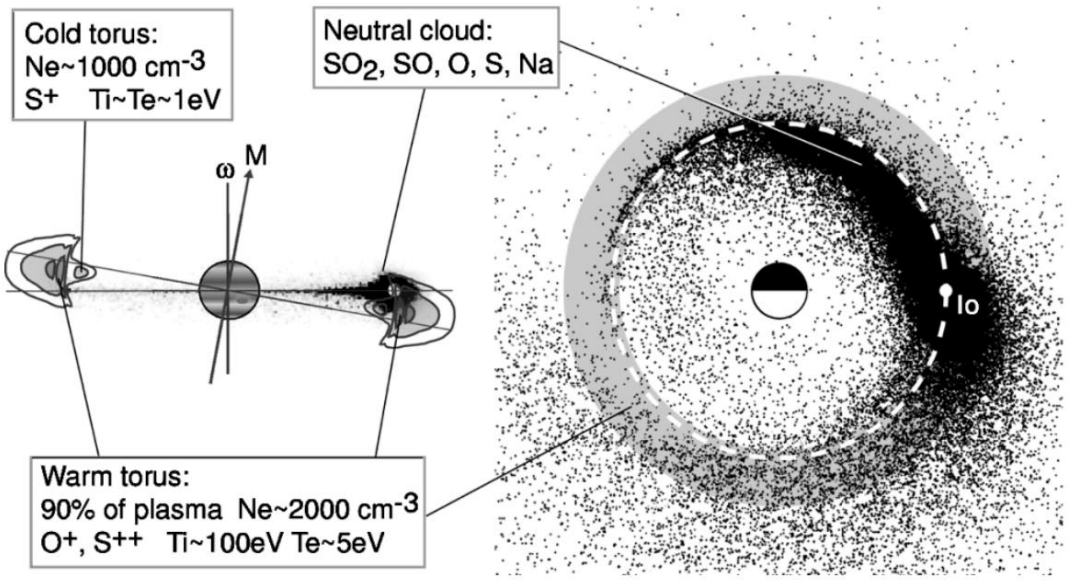

Figure 2.7: Schematic view of the plasma torus and neutral clouds of Io. View from central meridian longitude of 290° where Jupiter's magnetic axis M is titled 9.6° from the rotation axis Ω and the plasma torus is centered on the centrifugal equator (left). Top view from Jupiter where the shapes of the clouds of neutral particles varies between species (right). Source: (Thomas et al., 2004)

The ribbon extends over a few tenth of R_J, and is on average slightly in the orbit of Io. This ribbon represents a high and narrow ring whose occurrence varies with time. Its vertical extent is about 0.5 R_J (Schneider et al., 1997). Ground-based observations of the torus show that, in general, the radial luminosity of the latter is dominated by the ribbon (Brown, 1983). The various observations over the years (Schneider et al., 1997; Schneider and Trauger, 1995) have allowed the hypothesis that the ribbon would be formed by an essentially continuous input at Io, which is combined with the tilted dipole, a dawn-dusk electric field produced by a downtail plasma flow, and a diffusion coefficient dependent upon radial distance (Herbert, 1996; Smyth and Marconi, 1998). Herbert (1996) modeled the geometry of the ribbon.

The cold torus is the region of the plasma torus where significant amounts of S^+ closer to Jupiter than the ribbon were observed by ground-based observations and spectroscopy. These observations show that S^+ emissions in the cold torus can sometimes dominate the ribbon emissions. It is assumed, however, that this dominance is due to a strong variation of the ribbon instead of a significant variability of the cold torus. By the cold temperatures observed, it is thought that the plasma of the cold torus has irradiated the majority of its energy, leading to its concentration at the centrifugal equator (Thomas et al., 2004).

2.5.4 The interaction between the plasma torus and the atmosphere of Io

The interaction between Io and Jupiter is very complex. This complexity is due to the involvement of physics at all levels. In fact, molecular, atomic, ionospheric, atmospheric and plasma physics play a role in the interaction region. Figure 2.8 illustrates the different processes related to the electromagnetic interaction of Io's atmosphere with the plasma torus. As described in section 2.5.3, the plasma torus is frozen without collision in the magnetic field of Jupiter and rotates with almost the same period (~ 10h). Since the orbital motion of Io is much slower (~ 42h), Io is constantly swept by the plasma torus as well as by the Jupiter field lines with a relative velocity of 57 km s^{-1}. As a result of this interaction between the satellite and the plasma torus, electron impact ionization and charge exchange processes, followed by a pickup in the atmosphere of Io, are induced (Figure 2.8).

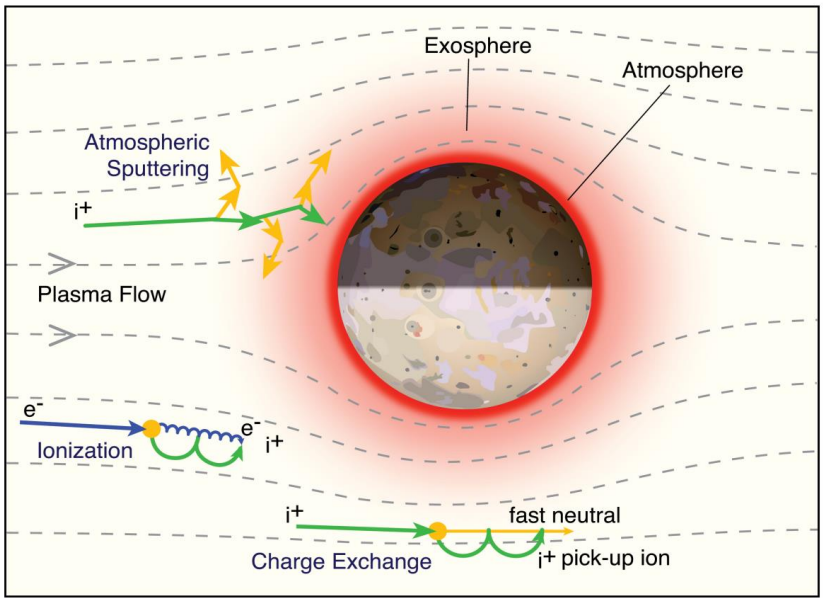

Figure 2.8: Illustration of the processes related to the electromagnetic interaction of Io's atmosphere with the plasma torus (Source: Bagenal et al., 2004)

These different processes are the reasons why materials from Io's atmosphere is escaping. Torus ions that first collide with neutral atoms in the atmosphere, collide with other atoms through the process known as sputtering. Several atoms or molecules of the atmosphere can be ejected into the exosphere of Io and possibly completely escape from it when a torus ion transfers enough momentum. This process is the main means of bringing materials to the neutral clouds

and subsequently to the plasma torus. The process of ionization by electronic impact consists in an electron of the torus ionizing an atmospheric atom which is then accelerated to the speed of the plasma and ends up leaving Io. The charge exchange process occurs between the torus ions and the atmospheric neutrals which results in a fresh ion at high speed. Another process that allows the material of the atmosphere to escape is the process of elastic collisions between ions and atoms. Electron impact dissociation breaks down molecules into their constituent atoms.

A frictional drag on the plasma flow near Io is exerted by the ionization, ion/neutral collision and charge exchange processes whereas the line of field above and below Io maintains its movement to the velocity of co-rotation. In response to the local plasma deceleration, a perturbation of the magnetic field propagating as Alfvén waves along the field lines to the South and North ionospheres of Jupiter is created (see Figure 2.3) (Hinton et al., 2019). A stationary structure downstream of Io is created by the combination of these two velocities and corresponds to the location of the propagating magnetic perturbation created at Io. Upstream of Io, the flow is slowed and then reaccelerated by momentum transfer from the plasma torus above and below Io until quasi full co-rotation a few R_{Io} downstream of Io (Hinson et al., 1998). As a result, after a few rebounds between Io and Jupiter, the plasma returns to complete co-rotation (Delamere et al., 2003).

One of the important energetic contribution to the plasma torus is through the pickup process. This process involves the creation of a new ion by charge exchange or ionization of a neutral from Io's atmosphere. This pickup process takes place in the atmosphere of Io as well as in neutral clouds. The atmosphere of Io would contribute to ~ 20 - 60% of the plasma contribution to the torus as well as ~ 15 - 30% of the energy input, the remainder surely coming from the neutral clouds (Bagenal, 1997). Initially at rest in the atmosphere, the new ions undergo a drift ($\vec{E} \times \vec{B}$, where $\vec{E}$ is the electric field of co-rotation at Io and $\vec{B}$ is the magnetic field) and are captured in the flux, causing a gyroscopic movement of the velocity of the local flux. This process therefore constitutes a net energy input to the Io plasma torus. Then, this energy is used by Jupiter's rotation where collisions transfer the energy of the ions to the electrons. At each rotation, a new plasma is created and represents approximately 2% of the total plasma in the torus of Io. Finally, the plasma slowly diffuses radially and thus fills the Jovian magnetosphere with heavy ions.

Chapter 3

The TRAPPIST telescopes

3.1 Introduction

TRAPPIST (TRansiting Planets and PlanetsSimals Small Telescopes; Jehin et al., 2011) is a project led by the OrCA Group (Origins in Cosmology and Astrophysics) of the Department of Astrophysics, Geophysics and Oceanography of the University of Liege. The TRAPPIST project is dedicated to the detection and characterization of exoplanets, planets outside our solar system and the study of comets and other small bodies in our solar system. This project consists of two 60 cm robotic telescopes. TRAPPIST-South was installed in April 2010 at the ESO observatory in La Silla (Chile) and TRAPPIST-North at the observatory of Oukaïmeden (Morocco) in October 2016. These two telescopes provide high quality photometric data on transits of exoplanets. They also make possible to regularly monitor the gaseous emissions of bright comets.

The first objective of the TRAPPIST program is firstly the photometric observation of new transiting exoplanets. This program consists first of all in follow-up observations of exoplanets that are candidates for transit surveys. The second goal of this program is the characterization of the physical and orbital parameters of known transiting planets. The third and main goal is photometric monitoring of close ultra-cool dwarfs. The second objective of the TRAPPIST program is the study of the chemical composition of bright comets as well as the evolution of their activity during their orbit. To examine the composition of their gas (OH, NH, CN, C_2, ...) and their rate of dust production, these comets are observed with narrow-band cometary filters (Jehin et al., 2014).

The advantages and possibilities of TRAPPIST telescopes are numerous. Indeed, both observatories are controlled via a VPN (virtual private network) connection between La Silla, Oukaïmeden and the University of Liège which allows the control of the telescopes and each subsystem by the researchers of the STAR Institute anywhere in the world with an internet connection. The observation plans are text files which are transmitted each night to the computer inside the dome controlling the telescope. This computer controls every aspect of the observatory robotic operations such as the calibration images acquisition, the telescope pointing and tracking, the astrometry and the focusing and the management of the filter wheel and the dome. Moreover, these telescopes provide the large amount of observing time requested for the research projects. In addition, another advantage of having two telescopes in two different hemispheres allows a large sky coverage.

3.2 TRAPPIST-North

Figure 3.1: TRAPPIST-North telescope at the Oukaïmeden Observatory (Photo credit: Mari-Liis Aru)

The Oukaïmeden Observatory (Fig. 3.1) is managed by Cadi Ayyad University. It is located 50 km South of Marrakech (Morocco) in the High Atlas Mountains at an altitude of 2750 m. This observatory has good observing conditions with about 250 clear nights per year. The characteristics of TRAPPIST-North (TN) is shown in Table 3.1. The telescope is a 60 cm f/8 Ritchey-Chretien built by the German Astelco company and is composed of aluminium and carbon fiber. The CCD camera is a back-illuminated deep depletion CCD e2V chip of 2048x2048 pixels and has a field of view of 20'x20'. This CCD camera can be cooled down to -100°C below ambient temperature. The pixel size is of 13.5 μm and the pixel scale is of 0.60 arcsec/pixel. Three possible read-out modes exist: 1 MHz, 3 MHz and 5 MHz. These modes

correspond respectively to read-out noises of 7 / 12 / 32 electrons and read-out times of 5 / 3 / 1.8 seconds.

Table 3.1: Characteristics of TRAPPIST-North[3]		
Site	Oukaïmeden Observatory (Z53)	
Latitude	31º 12' 22 (N) / 31,2061° (N)	
Longitude	7º 51' 29 (W) / 7,8664° (W)	
Altitude	2751 m	
Δ LAT - Δ LON – Baseline	60.4607° - 62.873° - 8618 km	
Telescope	Model	Astelco RC Lightweight Telescope
	Type	Ritchey-Chretien
	Material	Aluminium and Carbon fiber
	System focal ratio	F/8
	Diameter	60 cm
	Weight	75 kg
Mount	Model	Astelco NTM-500
	Type	German equatorial
	Motors	Direct drive systems
	Drive accuracy	No periodic error
	Speed	Up to 50°/s
	Pointing accuracy	5''
	Differential positioning accuracy	< 1" RMS
	Tracking accuracy without autoguider	1"/4 min
Camera model	Andor IKONL BEX2 DD	
CCD type	Back Illuminated CCD, Deep Depletion with fringe suppression, Extended range dual AR coating	
Array size	2048x2048 pixels	
Pixel size	13.5 μm	

[3] Source: https://www.trappist.uliege.be/cms/c_3313479/en/trappist-eq-TRAPPIST-North

Pixel scale	0.60 arcsec/pixel
Field of view	20'x20'
Full well	100 000 e
Gain	1.1 e/ADU
Peak QE	90 %
Read-out modes	1 / 3 / 5 MHz
Read-out noises	7 / 12 / 32 e
Read-out time	5 / 3 / 1.8 s
Dark current	0.15 e/s (at – 65°C)
Cooling below ambient	-100.0 $\pm$ 0.1°C
Filter Wheel model	Double Apogee AI-FW50-10S
Filters (wheel 1)	B, V, Rc, Ic, Sloan z, Exo (cut blue), NaI, SII
Filters (wheel 2)	OH, NH, CN, C_3, Hα, BC, C_2, GC, RC

3.3 TRAPPIST-South

Figure 3.2: TRAPPIST-South telescope at the La Silla Observatory (Photo credit: E. Jehin)

The ESO La Silla Observatory (Fig. 3.2) is located in the Atacama Desert in Chile at an altitude of 2315 m. This observatory, with a good atmospheric stability, has the best observing conditions in the world with about 300 clear nights per year. The characteristics of TRAPPIST-South (TS) are shown in Table 3.2. The telescope is a 60 cm f/8 Ritchey-Chretien built by the German Astelco company and is composed of aluminium and carbon fiber. The FLI ProLine PL3041-BB CCD camera is a back-illuminated Fairchild chip of 2048x2048 pixels and has a field of view of 22'x22'. This CCD camera can be cooled down to -55°C below ambient temperature. The pixel size is of 15 μm and the pixel scale is of 0.64 arcsec/pixel. Three possible read-out modes exist: 1x1 MHz, 1x2 MHz and 2x2 MHz. These modes correspond respectively to read-out noises of 9.5 / 14 / 14 electrons and read-out times of 6 / 4 / 2 seconds.

Table 3.2: Characteristics of TRAPPIST-South[4]		
Site	La Silla Observatory (I40)	
Latitude	29º 15' 16.588 (S) / 29,2546 (S)	
Longitude	70º 44' 21.818 (W) / 70,7394 (W)	
Altitude	2315 m	
Δ LAT - Δ LON – Baseline	60.4607° - 62.873° - 8618 km	
Telescope	Model	Astelco RC Lightweight Telescope
	Type	Ritchey-Chretien
	Material	Aluminium and Carbon fiber
	System focal ratio	F/8
	Diameter	60 cm
	Weight	75 kg
Mount	Model	Astelco NTM-500
	Type	German equatorial
	Motors	Direct drive systems
	Drive accuracy	No periodic error
	Speed	Up to 50°/s
	Pointing accuracy	5''
	Differential positioning accuracy	< 1" RMS

[4] Source: https://www.trappist.uliege.be/cms/c_3313473/en/trappist-eq-trappist-South

	Tracking accuracy without autoguider	1”/4 min
Camera model	FLI ProLine PL3041-BB	
CCD type	Back Illuminated CCD	
Array size	2048x2048 pixels	
Pixel size	15 μm	
Pixel scale	0.64 arcsec/pixel	
Field of view	22’x22’	
Full well	100 000 e	
Gain	1.1 e/ADU	
Peak QE	96 %	
Read-out modes	1x1 / 1x2 / 2x2 MHz	
Read-out noises	9.5 / 14 / 14 e	
Read-out time	6 / 4 / 2 s	
Dark current	0.1 e/s	
Cooling below ambient	-55.0 $\pm$ 0.1°C	
Filter Wheel model	Double Apogee AI-FW50-10S	
Filters (wheel 1)	B, V, Rc, Ic, Sloan z, I+z’, Exo (cut blue), NaI, H_2O^+	
Filters (wheel 2)	OH, NH, CN, C_3, CO^+, BC, C_2, GC, RC	

Chapter 4

Observations and data reduction

Observation plays an important role in astronomy. Indeed, the goal of astronomical research is to determine the structure of the Universe through its various components and finally, to make an interpretation compatible with the current physics.

4.1 Data acquisition

The target of this work is Io, the satellite of Jupiter. Thus, we acquired data of this celestial body during several nights in 2014 and 2015. The goal of these observations is to observe sodium jets ejected from Io's atmosphere. The primary purpose of these observations was to test TRAPPIST-South and its ability to observe Jupiter and its Galilean satellites. For this reason, different observation strategies were put in place in 2014 (different exposure times, Jupiter centered or Io, ...) to determine which are the best conditions. For the preparation of these observations, we had to determine the visibility window of Jupiter because, to observe Io, we principally centered Jupiter. Jupiter is not visible all night long and all year long. To determine the visibility window, we can use the method ViSiON (Visibility Service for Observing Nights) available on the webservice Miriade of the "Institut de Mécanique Céleste et de Calcul des Ephémérides" (IMCCE). ViSiON gives the length of the visibility windows according to observation criteria and offers plots of Jupiter altitude and airmass during the night of observation (Fig. 4.1). The observation can be limited by several geometric conditions. In

order to observe at best Io, we must take into account its position with respect to Jupiter. Io is the best visible when observed at maximum elongation compared to Jupiter. The maximum elongation of Io corresponds to 2’ 18”. This observation criterion therefore limits the observation time interval and thus the visibility window.

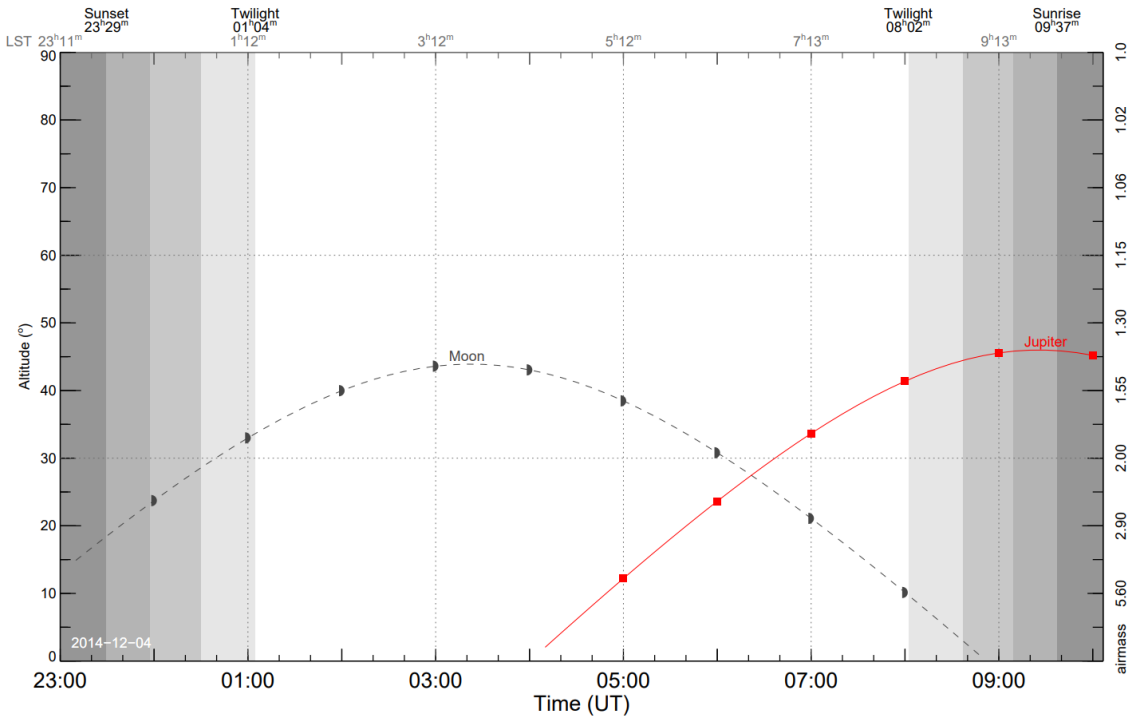

Figure 4.1: Example of visibility plot of Jupiter on December 4, 2014 produced by ViSiON at VO-IMCCE – B. Carry (OCA) & J. Berthier (IMCCE)

In order to start the observations, we have to send an observation plan to the computers that control the telescopes. These observation plans (Fig 4.2) are text files containing important information for the observation (coordinates, observation times, etc.).

```
1 ; ==Io==
2 #waituntil 1, 07:00
3 #autofocus
4 #count 5000
5 #binning 2
6 #filter NaI
7 #INTERVAL 15
8 #trackon
9 Io 09 39 50.37788 14 46 3.2292
10 #trackoff
11 #quitat 09:00
12 ;
```

Figure 4.2: Example of an observation plan.

In order to observe the sodium jets, we used the NaI filter. In fact, the observations with TRAPPIST can be made with different filters (see Table 3.2 and 3.3). TRAPPIST has a double Apogee filter wheel which gives access to 7 broad-bands filters (Johnson-Cousins B, V, Rc, Ic, Sloan z and exoplanet filters I+z' and Exo) and 11 narrow-band cometary filters designed by NASA (OH, NH, CN, CO^+, C_3, BC, C_2, GC, RC, NaI and H_2O^+). The transmission curve of the NaI filter that we used for our observations is illustrated in Fig 4.3. The center wavelength of the NaI filter is 589 ± 0.5 nm and the full width at half maximum (FWHM) is 3.0 ± 0.6 nm.

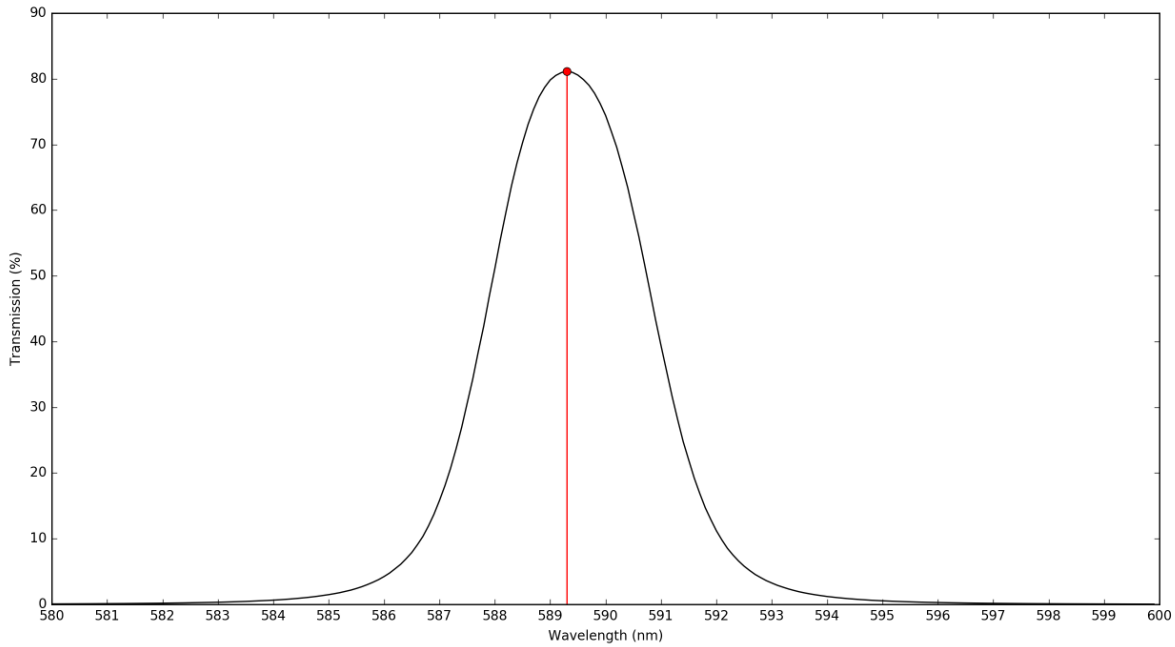

Figure 4.3: Transmission curve of the NaI filter used for Io's observations. The red dot shows the center wavelength of the NaI filter.

The Table 4.1 shows some of Io's observations information. The timeline of our observations is illustrated in Fig. 4.4. We observed 15 events listed in Table 4.1 with a total of 363 image acquisitions.

Table 4.1: Io's observation information					
Date	Telescope	Filter	Binning	Duration (min)	Number of images
1. 2014/12/04	TS	NaI	1	1.3	3
2. 2014/12/06	TS	NaI	2	68	98
3. 2014/12/08	TS	NaI	2	29	23
4. 2014/12/12	TS	NaI	2	43	34
5. 2014/12/19	TS	NaI	2	13	10
6. 2015/01/11	TS	NaI	2	20	15
7. 2015/01/13	TS	NaI	2	87	37
8. 2015/01/20	TS	NaI	2	16	14
9. 2015/01/23	TS	NaI	2	22	14
10. 2015/01/28	TS	NaI	2	22	19
11. 2015/02/01	TS	NaI	2	34	28
12. 2015/02/12	TS	NaI	2	18	15
13. 2015/03/29	TS	NaI	2	18	16
14. 2015/03/30	TS	NaI	2	33	26
15. 2015/03/31	TS	NaI	2	14	11
			Total	438	363

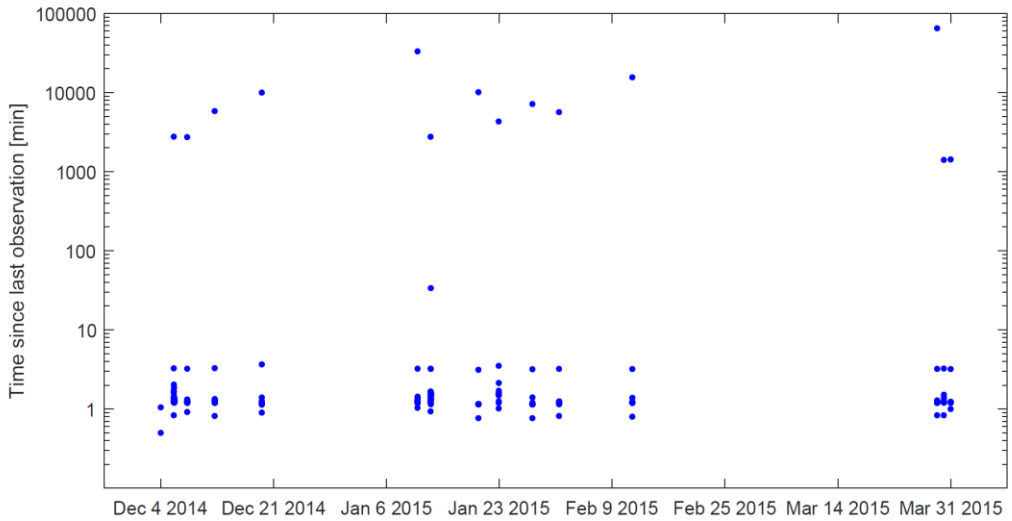

Figure 4.4: Timeline over the events listed in Table 4.1. The blue dots represent an image acquisition and the vertical axis shows how much time passed since the last acquisition.

During the observations, the telescope follows the movement of Jupiter or Io, depending on the observation strategy. Depending on the exposure time chosen, the image profiles on the observed CCD images can be supersaturated, and this is what we observe at Jupiter as well as Io and the other Galilean satellites present on the images (Fig 4.5). The full-well capacity represents the maximum charge capacity of each CCD pixel. If the number of electrons created exceeds this capacity, these electrons flow into the adjacent vertical pixels since the structures in the CCD (channel stops) make possible to avoid horizontal leaks. This vertical discharge is called blooming. The upper limit of the number of electrons detected per pixel is represented by the full well depth. Figure 4.5 represents an image taken during the observation night of December 4, 2014 with a 300-second exposure time and in binning 1x1. This figure also shows the effects of blooming on Jupiter when the number of electrons in a pixel exceeds the full-well depth. A flat-top profile is observed because the central pixels have values that exceed 65535 ADU (Analog-to-Digital Units) and thus, the ADC (Analog-to-Digital Converter) of the CCD is not capable to represent these.

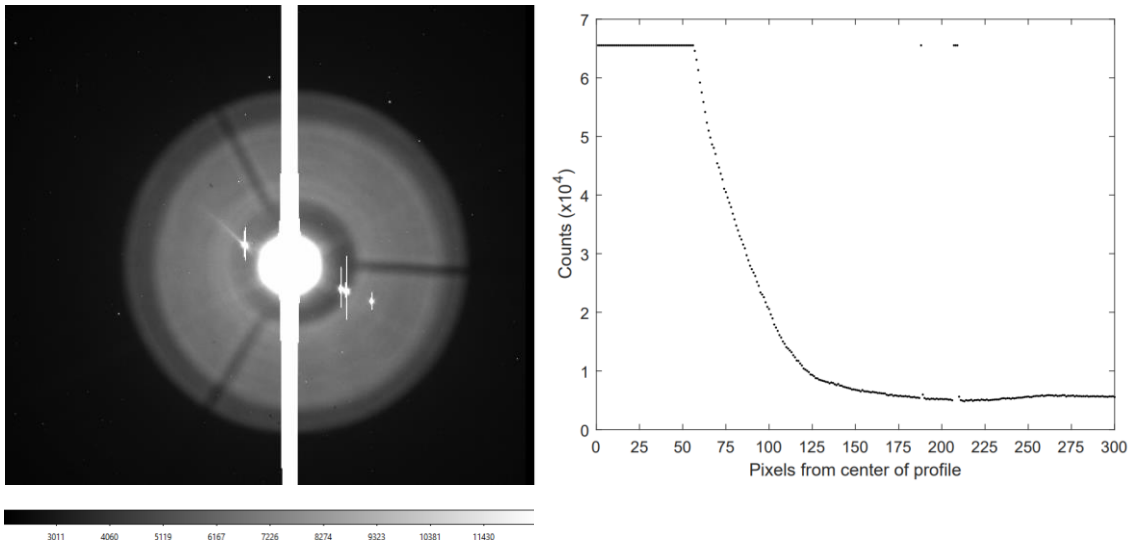

Figure 4.5: Raw image of Jupiter, Io and the other Galilean satellites from December 4, 2014 with the CCD blooming effect on Jupiter, Io, Europa, Ganymede and Callisto (Right). The profile from saturated Jupiter (left).

The figure 4.6 illustrates the positions of Jupiter and its Galilean satellites seen on the Fig. 4.5.

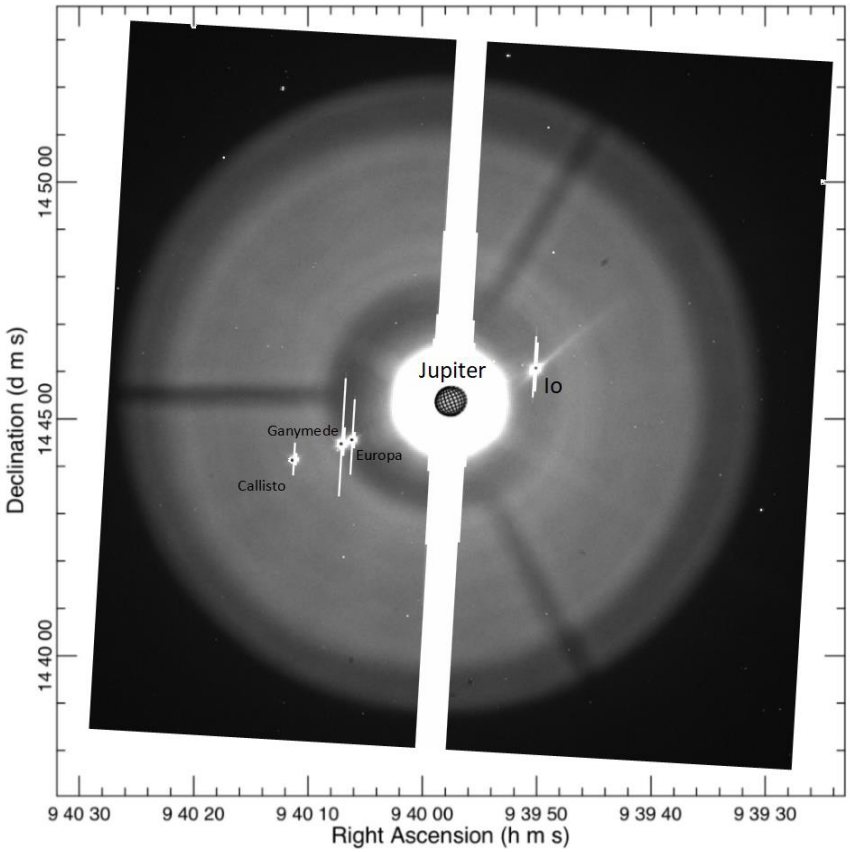

Figure 4.6: Superposition of the image seen in Fig. 4.5 with the position of Jupiter, Io, Callisto, Ganymede and Europa seen at scale, generated by the Jupiter Viewer[5] Tool, PDS Rings Node.

The optics of the telescope produces two types of artifacts on the images. The secondary mirror of the telescope is supported by arms. This mount, called the spider, creates a diffraction pattern that appears as a symmetrical cross around bright celestial objects, thus adding a first artifact to the image (Fig. 4.7). More specifically, the spider acts as an obstacle to the path of light and interference is produced due to the wave nature of light. The second type of artifact related to telescope optics is also created by the telescope spider. A ghost image is created because of reflections between the filter and the detector's planes inside the camera. This ghost image is slightly offset from the bright celestial object, in our case Jupiter, proportionally to the off-axis angle of the image. The Figure 4.8 illustrate the different artefacts on our image from December 6, 2014 which are found on all observation images.

[5] https://pds-rings.seti.org/tools/viewer2_jup.html

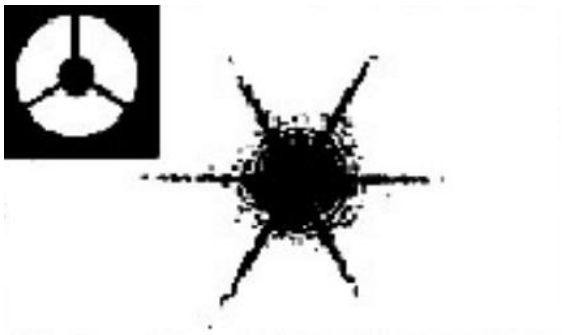

Figure 4.7: Diffraction pattern due to the secondary mirror spiders of the telescope on the image quality. Source: Harvey and Ftaclas (1995).

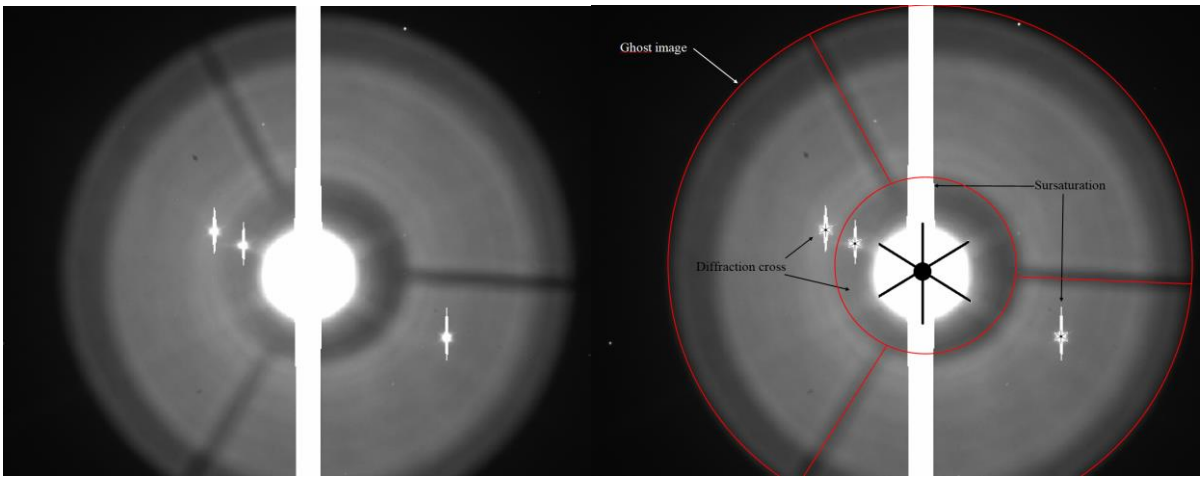

Figure 4.8: Calibrated image of December 6, 2014 (Right). The same image with the superposition of the artefact's explanation due to the telescope optics (Left). In red, the contour of the ghost image.

In summary, there are two types of problems to deal with our images. The first is a problem common to astronomical observation which consists in reducing the raw data. The following sections are devoted to this problem. The second is related to the very powerful brightness of Jupiter which is the consequence of the artifacts on our images. This problem is therefore very specific to our project. Chapter 5 is devoted to image processing related to these artifacts.

4.2 Image calibration

Image calibration, also called reduction, makes possible to correct systematic errors and defects affecting the sensor of the camera and the optical system. Indeed, no electronic imaging device is perfect, raw images cannot be directly used. It is important to emphasize that proper calibration is essential to produce good quality images by eliminating those defects. In fact, the flux recorded during the observation is affected by so-called electronic and thermal noises for each of the sensors as well as for each of the pixels in the same sensor. Each sensor has a different polarization level, a dark current and a sensitivity to light. Hence, these effects have a significant impact when images are taken during the night, the flux is much lower than for images taken with daylight. The intensity in each pixel of the image is affected in a particular way by each of these effects. The reduction solves a large part of the problems caused by these defects. Image calibration results in an undisputable improvement in the signal-to-noise ratio, thus resulting in greater sensitivity.

For our study, in order to perform the calibration of our images, we have worked with previously written scripts using IRAF (Image Reduction and Analysis Facility) tasks. The IRAF tasks allow you to do several operations on astronomical images. Given that we have a large number of images, on several nights, it is very interesting to automate the calibration process with the IRAF tasks. The scripts use the digital file FITS (Flexible Image Transport System) which contain the metadata that describe the images through a header where you can find all the information of the night of observation (type of image, date and time of observation, exposure time, target coordinates, etc.).

The calibration works in three stages, the bias and the dark subtraction, and the flat-field division:

$$\frac{(Image - Dark\ frame - Bias\ frame)}{Flat\ frame} = Calibrated\ image$$

The figure 4.9 shows an example of the result after the image calibration.

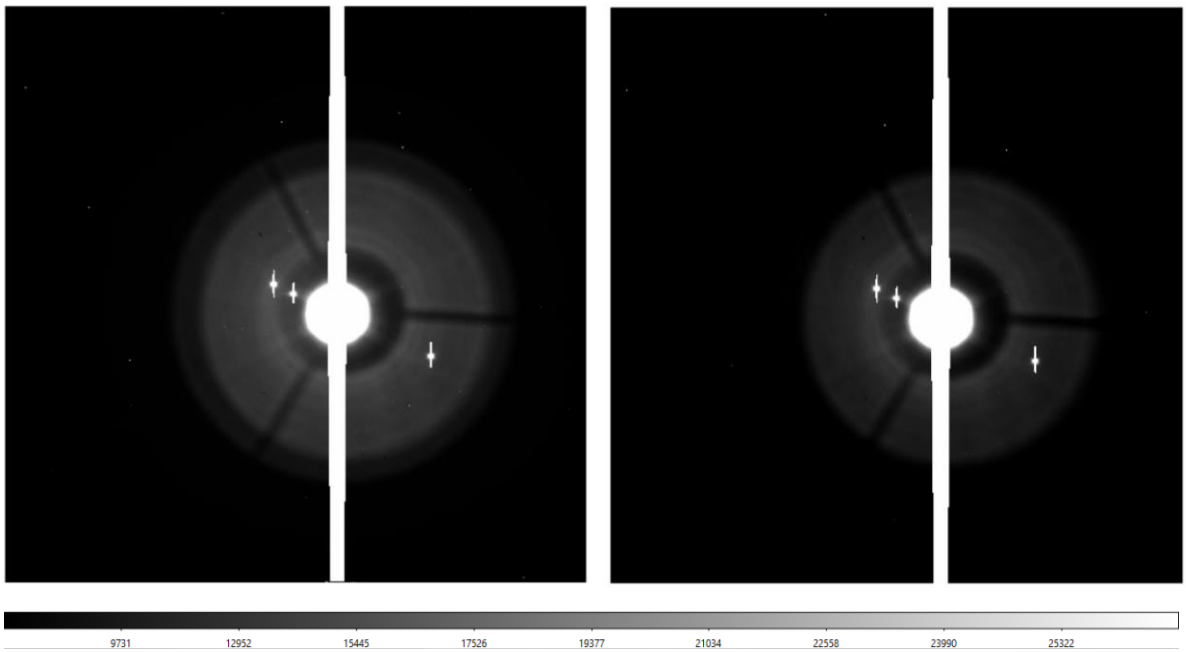

Figure 4.9: Comparison of one image before and after the calibration process.

4.2.1 Bias subtraction

The first step of data reduction is the subtraction of the "bias". An offset occurs when a pixel is read by the CCD camera, this offset is called the bias. This bias is introduced into the CCD chip to ensure that the camera works well in a linear regime. A bias frame consists of a zero-length exposure with the shutter closed. It is therefore easy to obtain bias frames due to this zero-length exposure. These frames were taken for each night of observation at a given binning. Binning is a method that combines a group of pixels into a single pixel. For example, in binning 2x2, the most used for our images, an array of 4 pixels is transformed into a single larger pixel thus reducing the total number of pixels. Each pixel composing the image has a different value. However, for a small amount of noise, the value of one pixel is coherent from one image to another, which makes it possible to subtract the bias that is coherent from one image to another. We find a small amount of read out noise in the bias frame that is produced inside the electronics reading the pixels. We can easily reduce this read out noise by combining several bias frames. This combination of bias frames is called a "master bias" and is produced by averaging the frames via the IRAF *zerocombine* task (Fig. 4.10). Indeed, the IRAF *zerocombine* task averages a set of pixel-by-pixel bias frames in order to obtain a mean bias frame and subtract that frame from each image. The calibration of the bias frames is done by subtracting the master bias from

the bright images as well as from the dark and flat-field frames. Indeed, if the bias is not corrected, the calibration of the flat-field will not work properly.

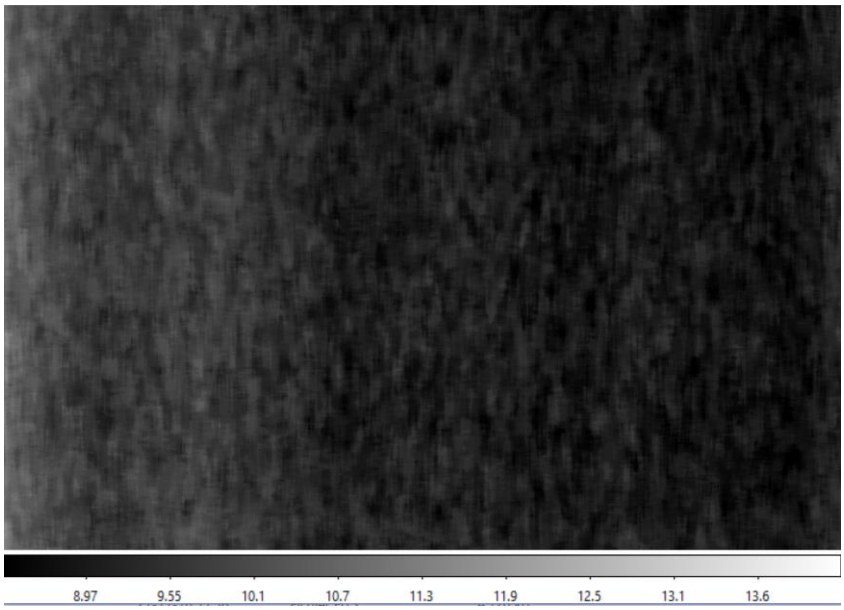

Figure 4.10: Master bias in binning 2x2 created with the IRAF task zerocombine.

4.2.2 Dark subtraction

A certain amount of dark current is produced by each camera sensor. This current accumulates linearly in pixels during an exposure and is produced by heat. In order to minimize this thermal noise effect, the CCD camera are cooled, in the case of TRAPPIST at about -70°C. Unfortunately, the noise associated to this dark current cannot be completely removed. Indeed, the problem of the dark current is its accumulation in each pixel at a different rate. “Hot pixels” are those that have accumulated thermally excited electrons faster, and the others are called "cold pixels". This effect related to the hot and cold pixels is reduced thanks to the subtraction of the dark frame.

A dark frame corresponds to an exposure taken under the same settings as exposure to the light, except that no light hits the chip. The images of the dark frames are thus taken with the same exposure time and the shutter closed to record the dark current. Knowing that at any temperature, each pixel is coherent in its dark current, the dark frame can then be subtracted from the light frame in order to remove the fixed pattern of the image. It is important to note, however, that the actual accumulation of dark current is random despite the dark current rate

being constant. This random accumulation produces noise that we discussed above. Indeed, if the dark current is doubled, the random noise produced increases by the square root of 2, meaning that the hot pixels produce much more noise. Thus, by subtracting the dark frame, the problem of hot spots will be improved because it eliminates the gross pixel-to-pixel variations of the dark current, but while also leaving the noise associated to the image. Being random and unpredictable, this noise cannot be deleted on calibrated images. However, by averaging a set of dark frames, as for the bias master, we can improve the subtraction. By combining dark frames in a “master dark” (Fig 4.11), it is possible to attenuate the noise. By quadrupling the number of frames on average, it is possible to halve the contribution of the noise.

It should also be emphasized that even if the shutter is closed, preventing the light from reaching the camera's sensors, cosmic rays can pass through. These cosmic rays will produce smaller spots of brighter pixels on the image, thus biasing the value of the average when dark frames are averaged to create the dark master. We use a sigma-clip that consists of an average of values that are only close enough to the median to eliminate those cosmic rays hits.

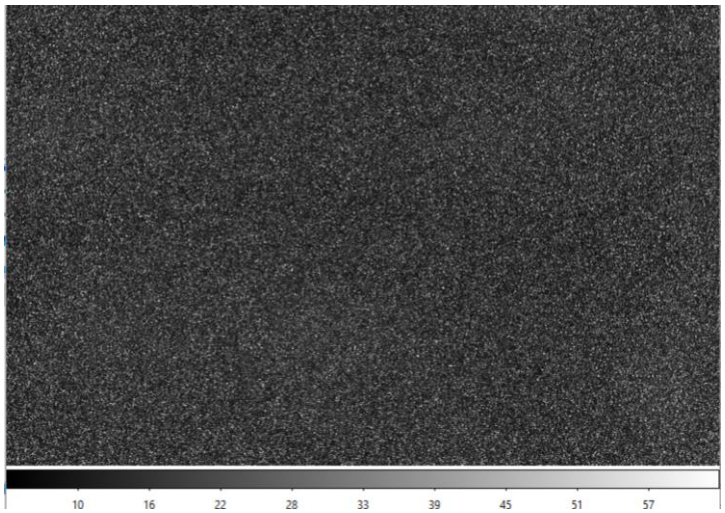

Figure 4.11: Master dark frame in binning 2x2 created with the IRAF task darkcombine.

4.2.3 Flat division

Each pixel of the CCD camera has a slightly different light sensitivity, which adds another noise component to the image. To correct this sensitivity variation, a flat field calibration is performed to obtain good quality images. This calibration is essential for accurate photometric

measurements. There are different sources of flat field variations in addition to pixel-to-pixel variation. On some images, it is possible to see shadows resembling donuts. These donuts result from the presence of dust on the optical surface of the sensor or the camera window. In the optical system, the vignetting effect can also reduce the light flux at the corners of the sensor and thus darken the image. In order to better correct these effects, several uniform field images are usually taken by observing the bright blue sky at dusk or twilight. During this period, the field shows a uniform illumination, hence the name “flat-field” and finally, we find on the images only the variations in sensitivity to light.

All pixel-by-pixel sensitivity variations are printed in the image, whose most sensitive pixels are brighter. By taking these images, bright stars can still appear on them. The pointing of the telescope is shifted between each exposure, in order to remove these bright stars by combining flat-field images with a median pile as these stars will be at different positions on the successive images. Once the flat-field frames are created, the field is renormalized by dividing each of the pixels into the average value of the array. In this way, the different exposures of the sky and luminosity are compensated. Indeed, when the image of the flat-field is multiplied to a raw image, the variations of sensitivities have disappeared. To combine the flat-field frames, we used Sigma cutting to reduce noise as well as eliminate aberrant pixels such as those due to cosmic rays and bright stars. It should be emphasized that flat-field frames are dependent on the filter used. In our observations, the NaI filter was used. Figure 4.12 shows the master flat-field frame of the NaI filter.

Figure 4.12: Master flat-field frame with the NaI filter.

Chapter 5

Image processing

In this chapter, we describe different methods of image processing. These methods were used on the reduced Io images listed on the Table 4.1. The ultimate goal of these methods is to reduce the noise in the image as well as to reduce the effects created by the telescope to obtain the cleanest images to measure the physical properties of the sodium jets. The biggest issue on our images is the background related to the reflective artifacts as mentioned in Chapter 4.

5.1 Introduction

Image processing represents all the techniques for modifying an image in order to improve it and to extract information from it. Image processing is used in many fields such as astronomy, physics, chemistry, remote sensing, medical industry, etc. To process an image, a set of techniques and algorithms are used to analyze, improve, optimize the characteristics of an image. Image processing techniques involve processing an image either as a signal or as a matrix. The image consists of pixels, representing the smallest element of a two-dimensional image that can be controlled programmatically. An image is characterized by its pixel count (the flux) and its resolution (the smallest details visible).

The noise is found in all astronomical measurements, limiting the accuracy of any measurements made from observational data. In general, photons are emitted randomly by astronomical sources and thus, found randomly spaced when they reach the telescope. Therefore, this random grouping of photons introduces noise into the flux measurements and is called “shot noise”. This shot noise corresponds to the irreducible minimum noise level of an astronomical observation.

5.2 Signal-to-noise ratio

The Poisson distribution provides the probability of detecting k photons in a fixed interval of time where the number of photons received in this fixed time interval has an average value N and whose photons are randomly spaced. The probability therefore becomes:

$$P(k) = \frac{N^k e^{-N}}{N!}$$

In astronomy, in most cases, we encounter large N. In these cases, the Poisson distribution tends to a Gaussian distribution with a mean of N and a standard deviation of $\sigma = \sqrt{N}$.

$$P(k) = \frac{1}{\sqrt{2\pi\sigma^2}} e^{-(k-N)^2/2\sigma^2}$$

From this Gaussian distribution, we can deduce that the true mean photon rate of the observed object has a probable mean of N and an uncertainty of $\sqrt{N}$, in the case where we detect N photons per second.

The signal-to-noise ratio (SNR) of an astronomical source is an important quantity because it makes possible to compare the level of the desired signal with respect to the unwanted noise level of an image and thus, measures how well an object is observed. The bigger the ratio, the better the measurement. The SNR, in imaging, consists in the ratio of the mean value of the signal and the standard deviation of the noise. The mean value of the signal represents the useful

image information and the standard deviation of the noise represents the random information of the image. The SNR expression is given by

$$SNR = \frac{Mean\ signal\ value}{Standard\ deviation} = \frac{S}{N}$$

There are different sources of noise for CCD observations:

- The time-independent read-out noise whose amplitude is R (electrons per pixel)
- The shot-noise from the detected photoelectrons from the source whose amplitude is $\sqrt{S_0}$ where S_0 represents the number of photoelectrons detected from the object (photons per second).
- The shot-noise from the thermally excited electrons consisting of the dark current whose amplitude is $\sqrt{S_D}$ where S_D represents the number of electrons detected from the dark current (electron per second per pixel).
- The shot-noise from the detected photoelectrons from the sky background whose amplitude is $\sqrt{S_S}$ where S_S represents the number of photoelectrons detected from the sky background (photon per second per pixel).

These different sources of noise are always present even after data reduction. S_0, S_D and S_S increase with the exposure time. Thus, the longer the exposure time is, the more noise is attributed to the image. Fortunately, the signal increases faster than the noise.

The total number of electrons detected from the source is:

$$S_0 Qt$$

where Q is the quantum efficiency of the CCD representing the fraction of incident photons which produce photoelectrons and t is the exposure time (s).

The total number of electrons detected from the dark current is:

$$S_D t n_p$$

where n_p is the number of pixels where the object is observed.

The total number of electrons detected from the sky background is:

$$S_S Q t n_p$$

The total number of electrons detected from the read-out noise is:

$$R\, n_p$$

Thus, the CCD SNR equation is given by:

$$SNR = \frac{S_0 Qt}{\sqrt{S_0 Qt + S_S Q t n_p + S_D t n_p + R^2 n_p}}$$

One method to increase the signal-to-noise ratio is to increase the exposure time of the observation. However, the CCD arrays can then saturate since the number of electrons captured is limited. There is therefore a compromise to be found between increasing the signal-to-noise ratio and the saturation of the image in terms of exposure time.

For the different nights of observations, three exposure times were chosen: 30, 60 and 180 seconds, in order to test the capabilities of the TRAPPIST-South telescope to observe Jupiter. The only exception is for the first night, December 4, 2014, the exposures of which are 5, 30 and 300 seconds long. The Figure 5.1, 5.2 and 5.3 illustrate the saturation profile of Jupiter for three different exposure times. Comparing these three saturation profiles, we can notice that the flat-top profile is more and more significant since the longer the exposure time, the more the image is saturated. Thus, for each night, the majority of the images is taken with an exposure time of 60 seconds.

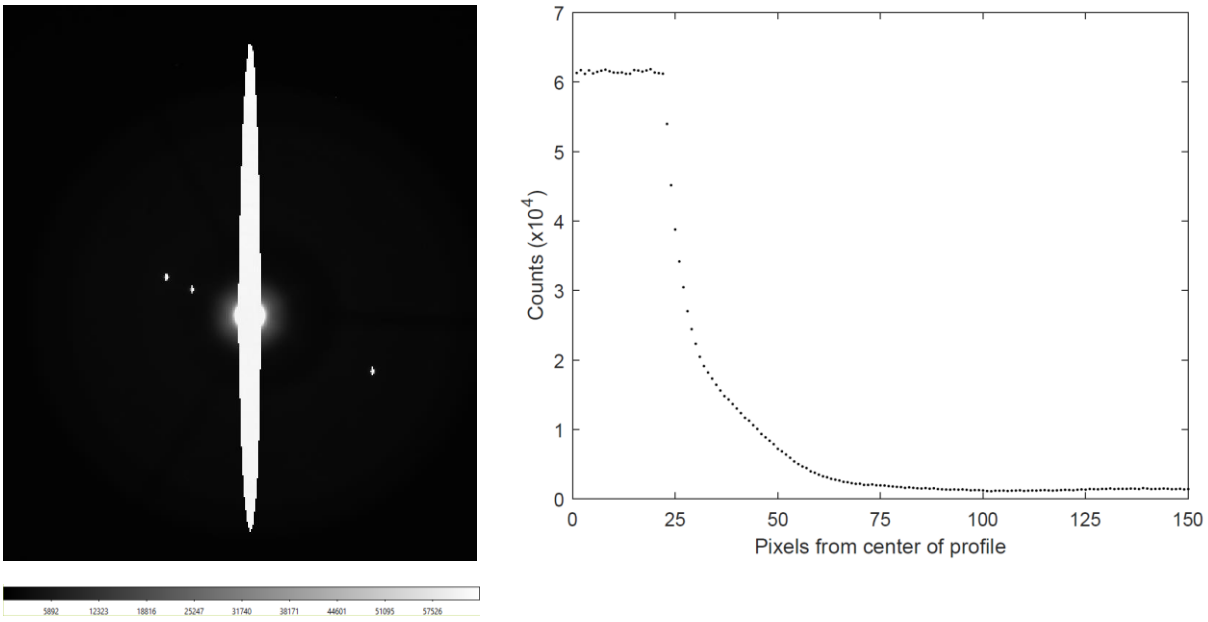

Figure 5.1: The calibrated image from December 6, 2014 with a 30 seconds time exposure (Left). The profile of saturation of Jupiter measured from the center of Jupiter to the end of the vertical saturated part (Right).

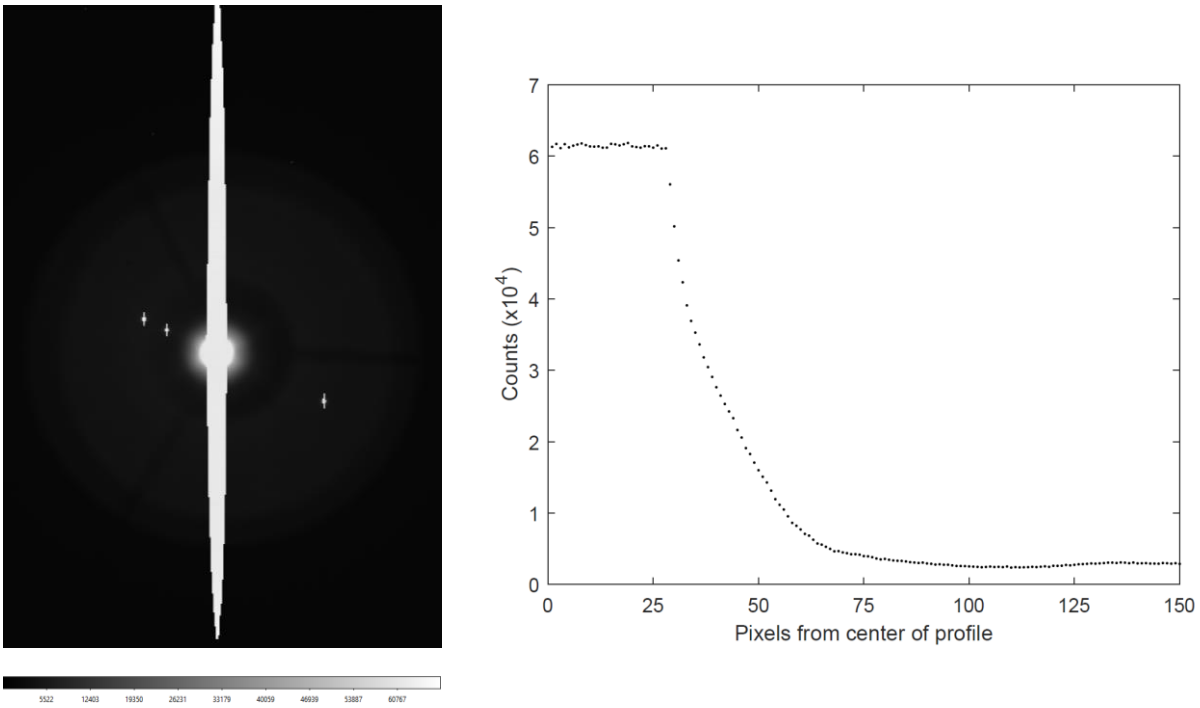

Figure 5.2: The calibrated image from December 6, 2014 with a 60 seconds time exposure (Left). The profile of saturation of Jupiter measured from the center of Jupiter to the end of the vertical saturated part (Right).

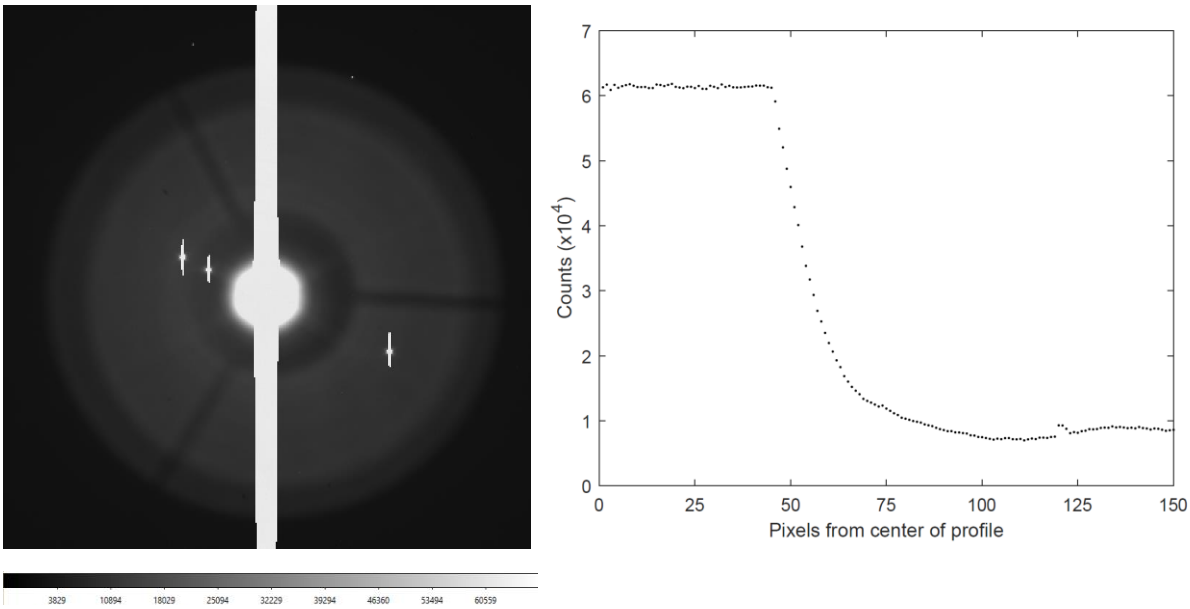

Figure 5.3: The calibrated image from December 6, 2014 with a 180 seconds time exposure (Left). The profile of saturation of Jupiter measured from the center of Jupiter to the end of the vertical saturated part (Right).

5.3 Images processing with IDL

The Interactive Data Language (IDL) is a high-level programming language containing an extensive library of image processing and analysis routines. Our images processed with IDL are grayscale images and consist of two-dimensional arrays. This type of image represents the intensities of the pixels, whose range goes from less intense (black) to more intense (white). When an image is displayed with IDL, the pixel values are adjusted to be between 0 and 255 (Fig. 5.4). Figure 5.4 illustrates the observation night of December 6, 2014 which is used as sample for the explanation of our image processing methods. In order to know where Io is located, the Figure 5.5 shows the position of Jupiter and its Galilean satellites on the image for this night.

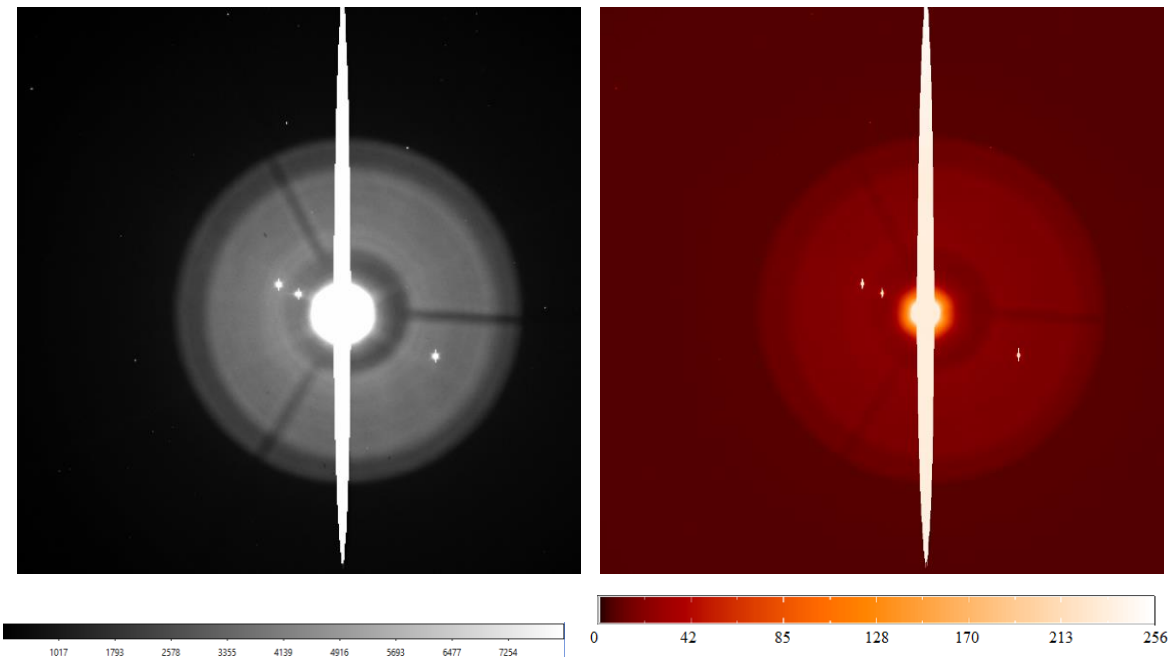

Figure 5.4: The calibrated image from December 6, 2014 (Left). The same image opened with IDL with a red color table (Right).

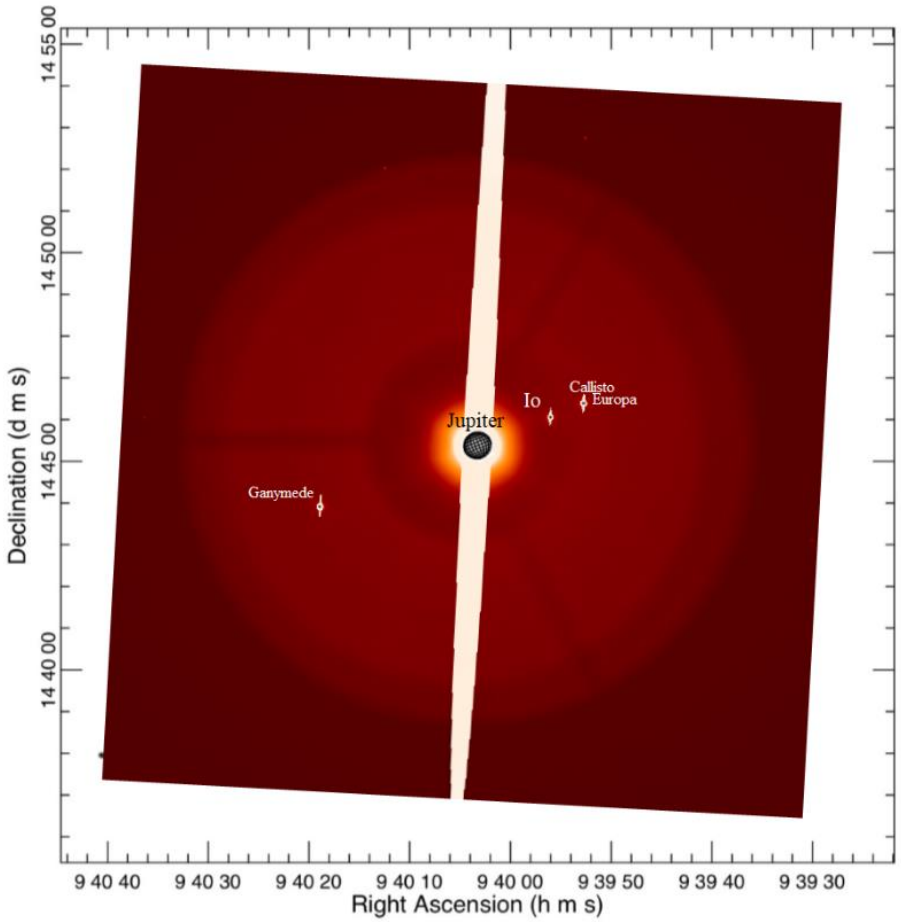

Figure 5.5: Superposition of the image seen in Fig. 5.4 with the position of Jupiter, Io, Callisto, Ganymede and Europa seen at scale, generated by the Jupiter ViewerTool, PDS Rings Node.

For each method, we use similar steps. The first step of our methods is to search the center of Jupiter on our images so we can apply a mask to isolate Jupiter and hide the area contaminated by the planet. Figure 5.6 illustrates the application of this mask on Jupiter. A mask represents a binary image constructed from relational operators (eg. <, >, =, etc.) which allows us to define a relation between our image and the value of the pixel that we want to mask to form the mask. In order to create a mask on Jupiter, we have used logical operations that allow to apply threshold levels in order to clip the pixel values of our image and to locate these pixels. These masks allow us to isolate particular characteristics of our image. The mask is subsequently multiplied by the original image to neglect specific areas.

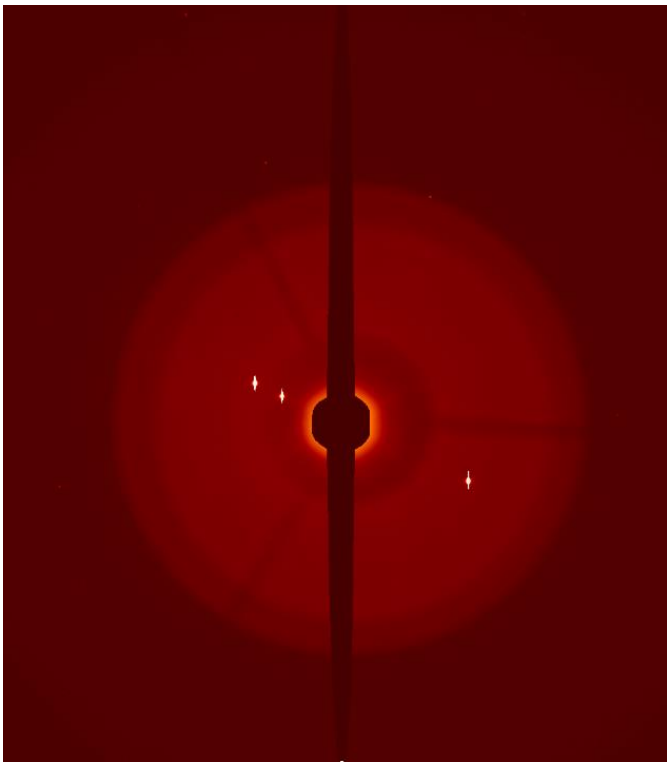

Figure 5.6: The calibrated image from December 6, 2014 with a mask on Jupiter and its contamination.

It is possible to do the same for the Galilean satellites present on the images. Figure 5.7 shows the application of all the masks on the image.

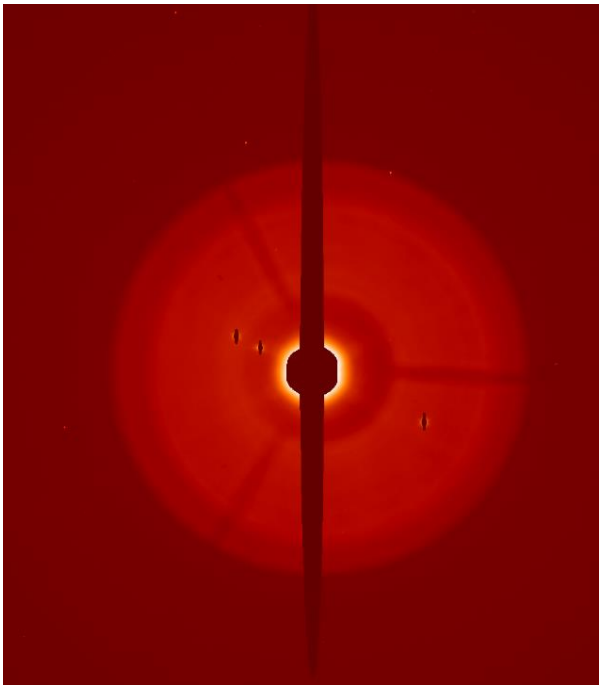

Figure 5.7: The calibrated image from December 6, 2014 with a mask on Jupiter and its satellites.

5.3.1 Unsharp masking method

Unsharp masking is a technique that allows to accentuate images. The term "unsharp" in the method represents the use of a unsharp negative image to create a mask of the original image. Then, a non-blur mask is associated with the original image. This combination produces a less blurry image than the original. This method amplifies the high frequency components of the signal by canceling the low frequency information by a procedure of subtracting a smoothed image from the image of the original image. To create the smoothed image, we use a median filter. As a non-linear method, the median filter makes possible to suppress the noise of the image and thus to improve the signal to noise ratio. This method consists in passing through the signal of the image pixel by pixel, replacing each pixel by the median of the neighboring pixels. The advantage of this filter is that it does not affect the intensity of the gray levels of the contours and intensity variations. It can, however, create a slight shift in the position of a few pixels. This filter is very useful for removing the so-called "salt and pepper" noise from the image while not attenuating the contours and characteristics of the image. The final result of this unsharp masking method is shown in Figure 5.8. The final result illustrates the subtraction from the image with masks on Jupiter and its Galilean satellites of the median of the original image.

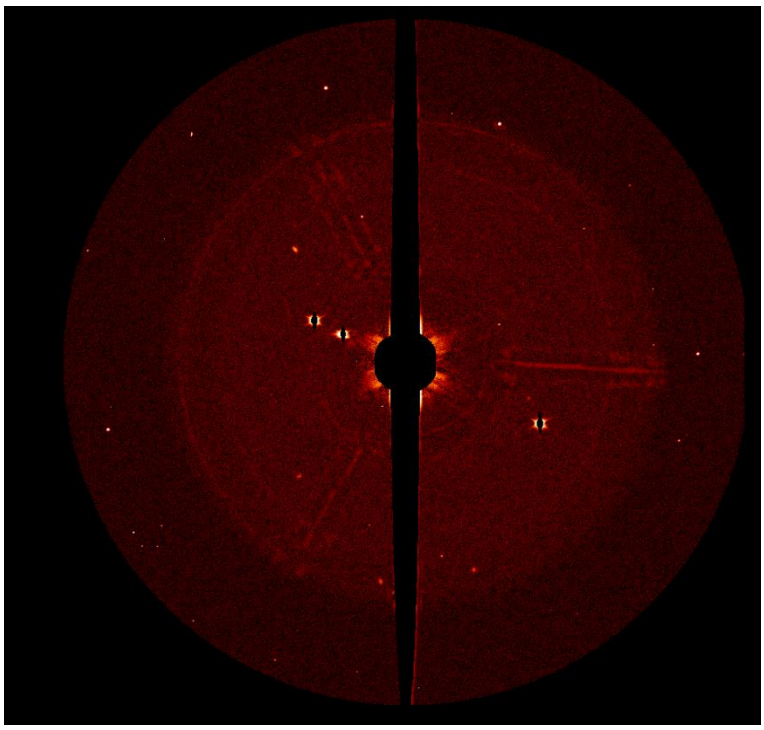

Figure 5.8: Final result of the unsharp masking method for our image from December 6, 2014.

5.3.2 Background subtraction method

The background contaminated by the artifacts created by the high brightness of Jupiter has a central symmetry around Jupiter. This method consists in using this central symmetry of the background in order to be able to subtract it from the original image. Unlike the previous method, this method allows us to manually cut the satellites and their diffraction pattern more precisely as well as to cut the area where the jet would be if it is present. For this method, we perform the same first step as the previous one. We are looking for the center of Jupiter and we apply a mask. Once the satellites and the possible jet are cut, we build a profile consisting of scans taking part of the image that surrounds the center of Jupiter, without taking into account the contaminated Jupiter center. More precisely, angularly averaged radial profiles are created around Jupiter. The Figure 5.9 illustrates this profile where we can see the "holes" created by the cutting of the satellites, the possible jet and the mask related to the saturation of Jupiter. The Y axis of the profile (Fig. 5.9) corresponds to the distance to the center of Jupiter (in pixels) and the X axis represents the length of the profile (in pixels).

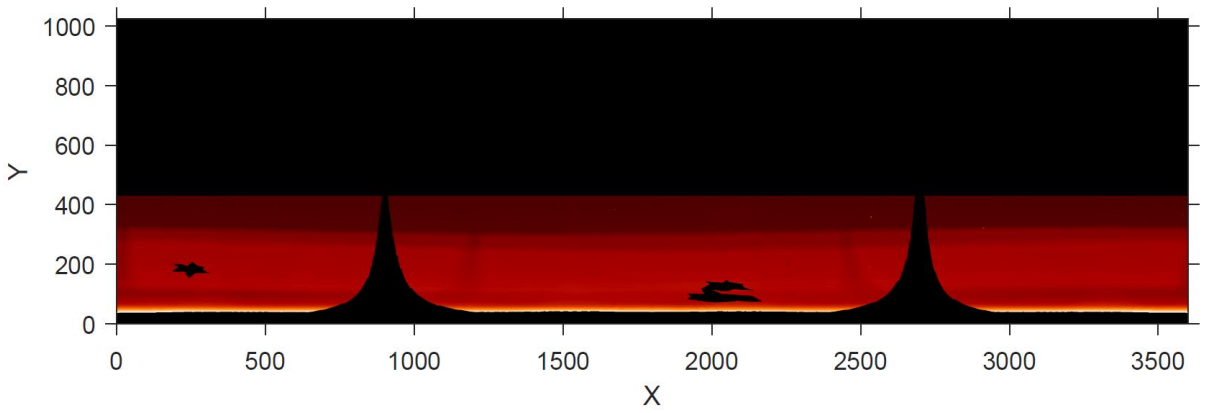

Figure 5.9: Profile with the "holes" of the saturated part of Jupiter and its satellites.

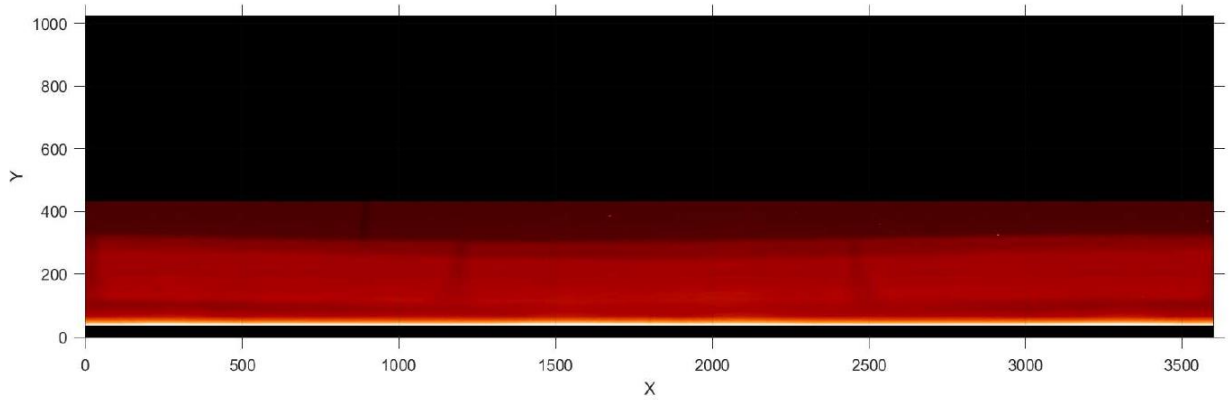

Figure 5.10: The second profile in which the "holes" are interpolated.

Once this profile is created, we interpolate the "holes" that are present, filling them with pixels that are close to the holes and allowing us to obtain a second profile illustrating the background without Jupiter and satellites-related contaminations (Figure 5.10). Subsequently, we reconstruct the image around the center of Jupiter which represents the image of the background of our image. The Figure 5.11 represents the reconstituted background image.

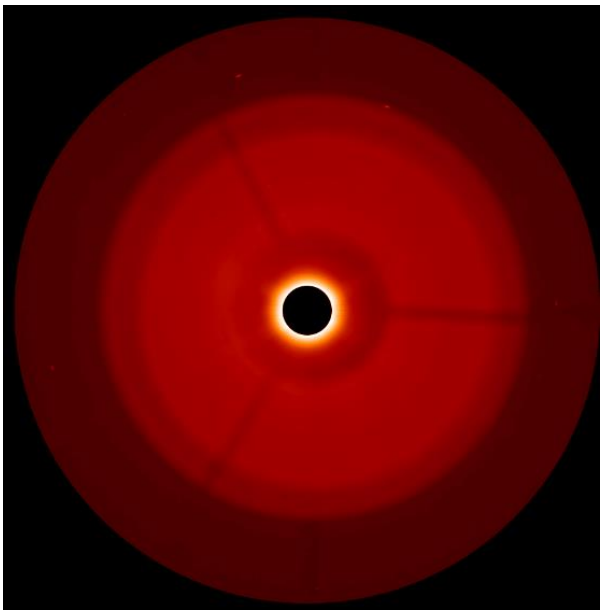

Figure 5.11: The reconstituted background image from our image of December 6, 2014.

The final result of this method is illustrated in the Figure 5.12. In order to obtain this result, we performed a median filter on the original image with masks on Jupiter as well as its satellites

from which we first subtracted the image of the reconstituted background. Indeed, in order to eliminate the pepper and salt noise of our images, we also apply a median filter for this method. This median filter is used on all methods in order to be able to compare their efficiency in a "fair" way. The most important advantage of this method is the fact that we have manually selected and cut the area where the possible jet would be, allowing to keep all its characteristics if present.

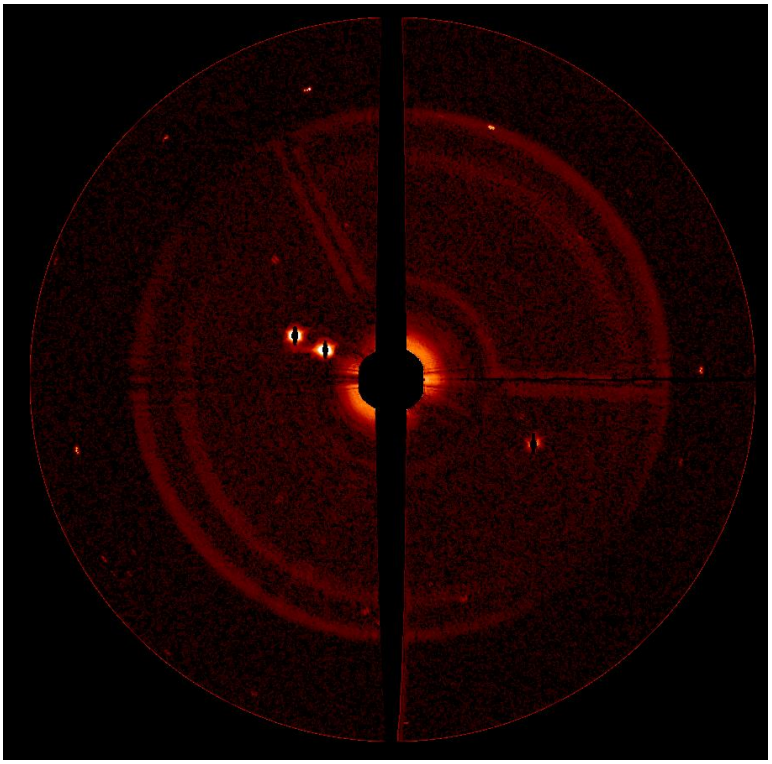

Figure 5.12: Final result of the background subtraction method for our image from December 6, 2014.

5.3.3 Stacking and unsharp masking method

One way to reduce noise for astronomical images is to stack images. For this method, we stack several images of the same night. To stack multiple images, we do an average in order to preserve the digital values composing the image like a single image. By stacking and averaging our images, the signal of our image will increase faster than the noise and thus also increase the signal-to-noise ratio. In order to avoid stacking images where the Galilean satellites would be slightly shifted, for each night, we have stacked a limited number of images, seven for each night. The Figure 5.13 illustrates the stack and average of several images from December 6, 2014. Once the stacking is done, as for the previous method, we locate the center of Jupiter and

we make a mask on the saturation of the gaseous planet as well as on its various satellites present on the image. Finally, we perform the unsharp masking method where the original image is the image stack. The final result of this method shown in Figure 5.14, is the subtraction of the image with the masks and the median of the stack of images.

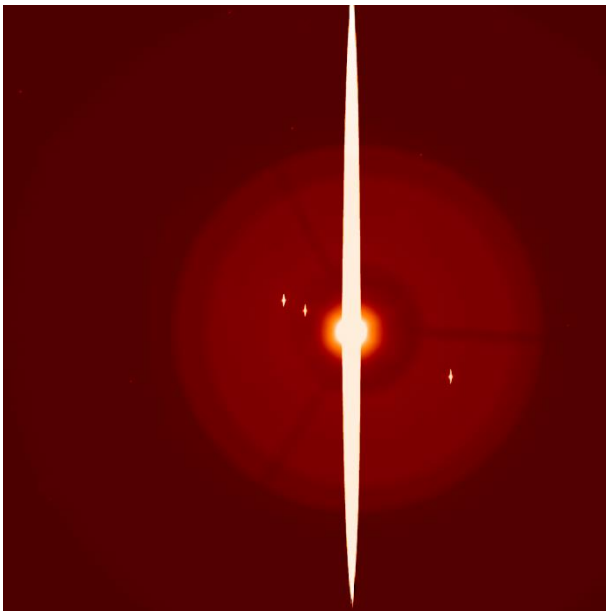

Figure 5.13: The stack of 7 images from December 6, 2014.

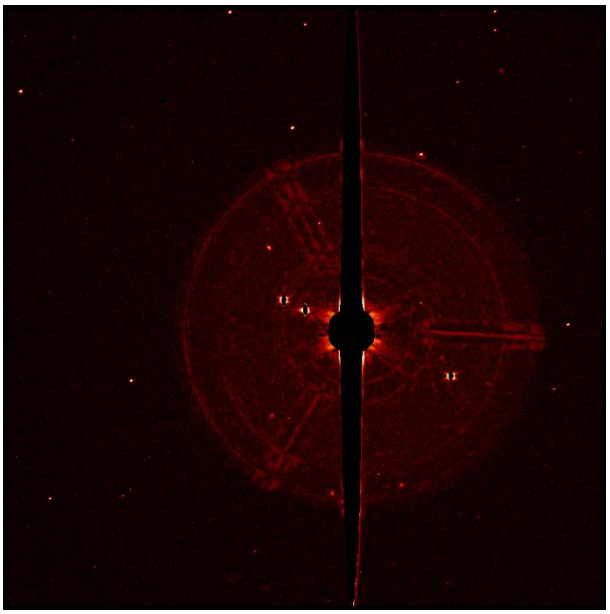

Figure 5.14: The final result for the stacking and unsharp masking method for December 6, 2014.

5.4 Rotational gradient method

The rotational gradient method, introduced by Larson and Sekanina (1985), allows the observation of low contrast details of bright objects that are arranged radially around a point in the image. This method makes it possible to highlight the jets that we observe near Io. By emphasizing azimuthal intensity gradients, the rotational gradient method allows you to observe the jet, if present. The method consists in creating two images with a radial shift (dr in pixels) and a rotation shift (dα in degrees) with respect to a point (x, y), of the same amplitude and opposite signs. In polar coordinates (r, α) with respect to the point (x, y), the rotational gradient method can be seen as:

$$A'(\alpha, r, d\alpha, dr) = 2 . A(\alpha, r) - A(\alpha - d\alpha, r - dr) - A(\alpha + d\alpha, r - dr)$$

where A is the original image, A' is the resulting image, dα is the parameter of the rotation shift and dr is the parameter of the radial shift.

The gradient makes it possible to suppress the object with a symmetry of revolution with respect to (x, y) and produces an image whose average intensity is zero. Finally, the offset is adjusted to have an image with positive thresholds. The values of the radial shift are between 0 and 2. Those of the rotation shift are between 2° and 20°.

However, it must be emphasized that this method is subjective. Indeed, a too important value of the dα can make appear, in certain cases, false details or restore these details with a bad morphology. On the other hand, low-contrast structures may not be noticed if the angle of rotation is too small. Therefore, it is necessary to experiment with different values to best reveal what we want to observe. To perform this method in the best possible way, it is very important to know precisely the position of the center of the object studied.

5.4.1 Rotational gradient method centered on Jupiter

With the intention of processing our images in order to reduce pollution and Jupiter-related artifacts, we perform the Jupiter-centered rotational gradient method. To be able to compare all

the methods used (see section 6.3), we perform this method with IDL. Figure 5.15 shows examples of results obtained by this method with different angles of rotation to determine which is the most suitable for our case of study.

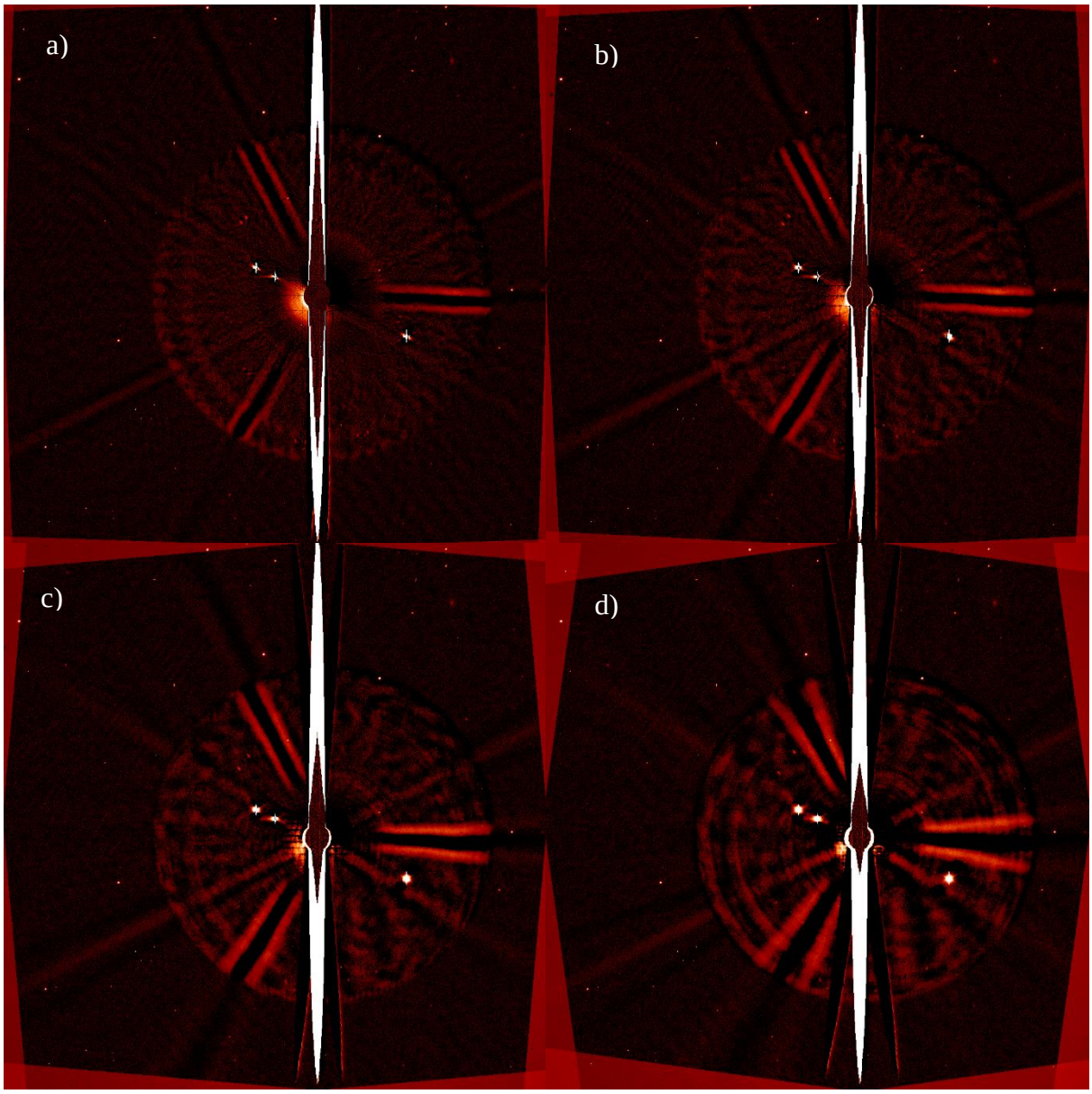

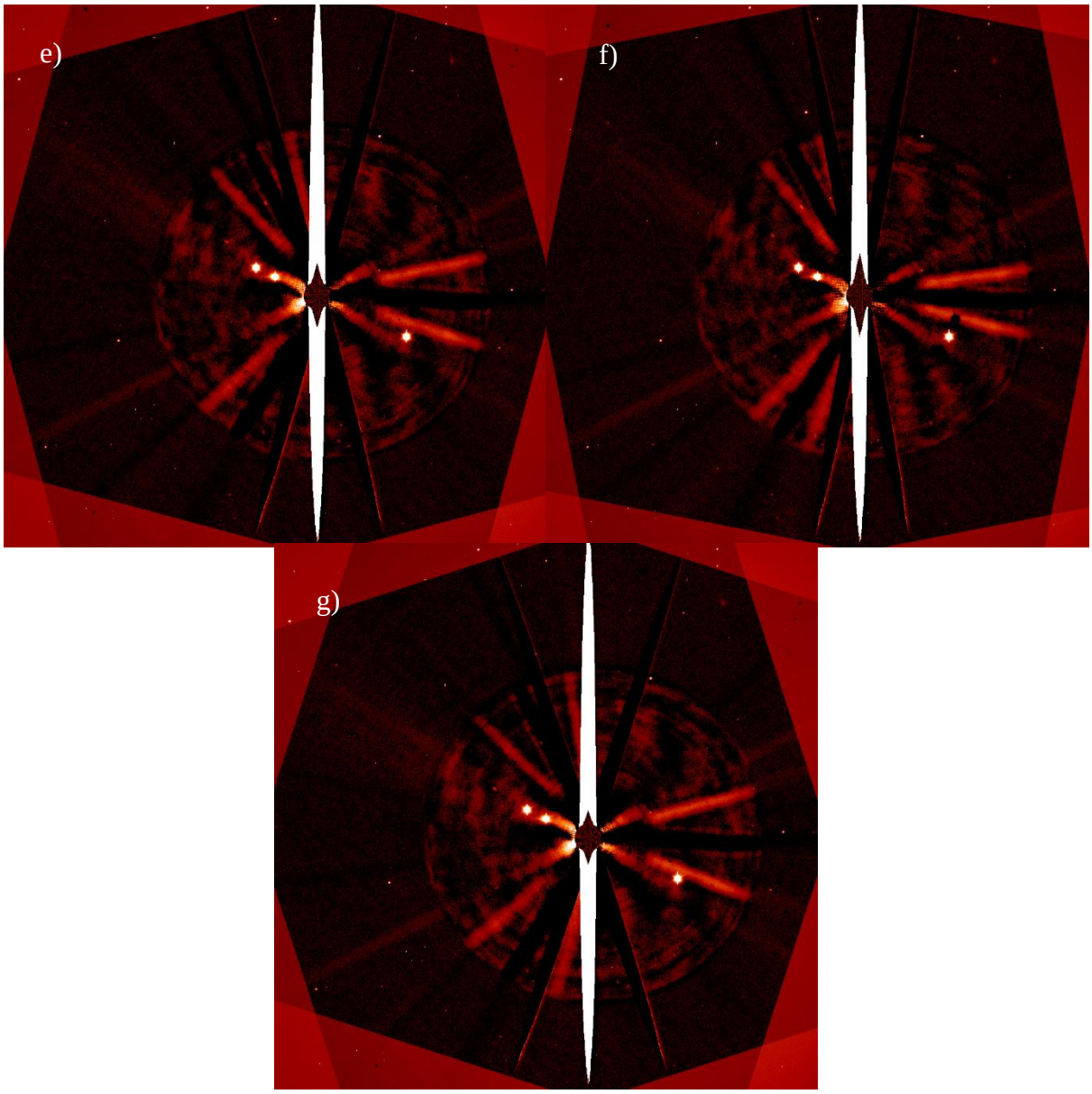

Figure 5.15: Examples of the rotational gradient method centered on Jupiter done with IDL on a calibrated image from December 6, 2014 with different rotation angles. a) dα=2, b) dα=3, c) dα=5, d) dα= 8, e) dα= 11, f) dα= 15, g) dα= 18. The original image is shown on the Figure 5.4.

5.4.2 Rotational gradient method centered on Io

Performing the rotational gradient method centered on Io allows us to emphasize or not the presence of a jet. Indeed, this method allows to accentuate the details of low contrast of an image. This method can thus be used to affirm or not the detection of a jet on our images. Figure 5.16 shows examples of the rotational gradient method applied on Io with different rotation angles of the image seen in Figure 4.5. Figure 5.17 illustrates examples of the method with a

calibrated image from December 6, 2014. We performed this method on all observations with the Cyanogen Imaging MaxIm DL[6] software.

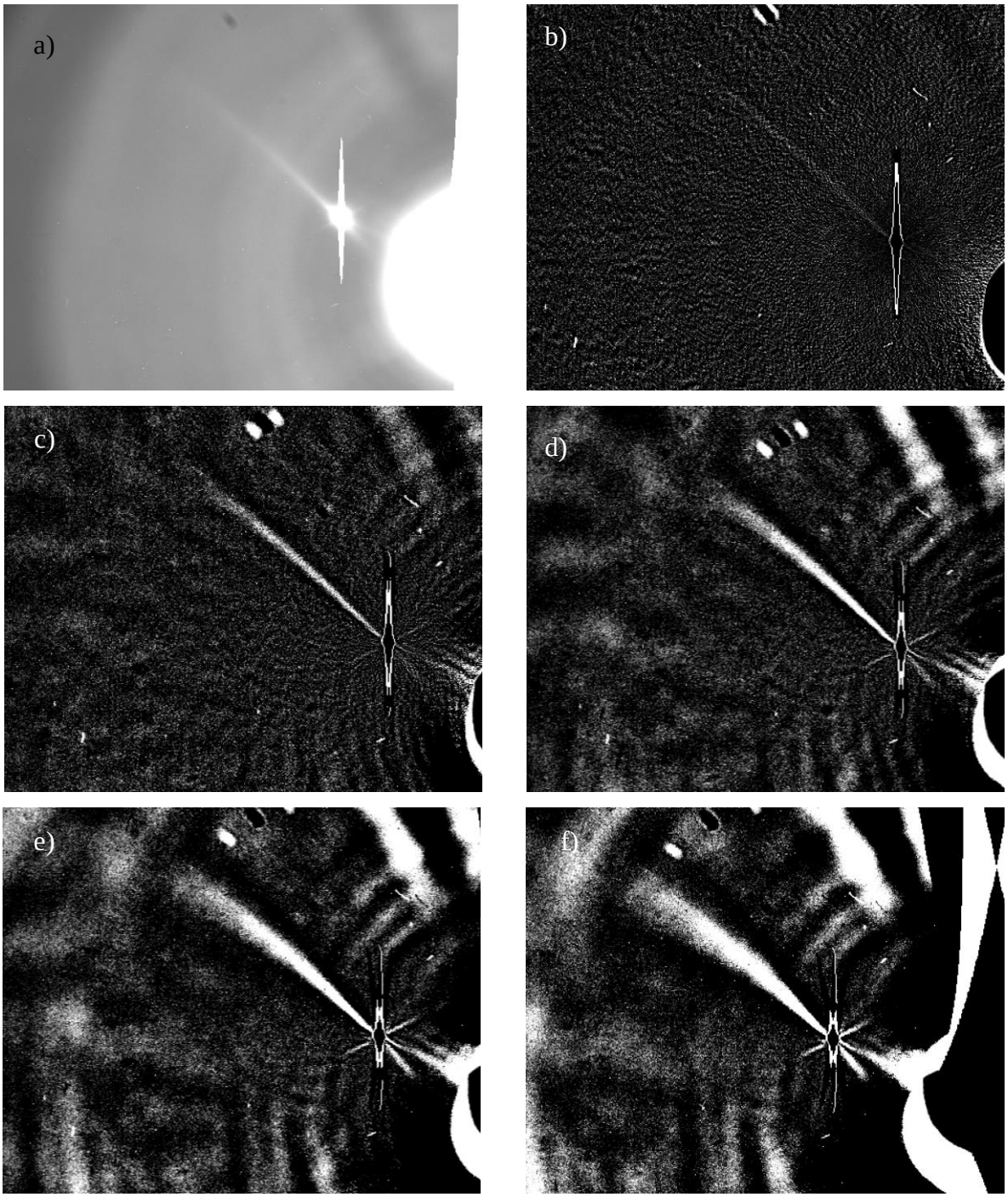

[6] http://www.diffractionlimited.com/help/maximdl/Rotational_Gradient.htm

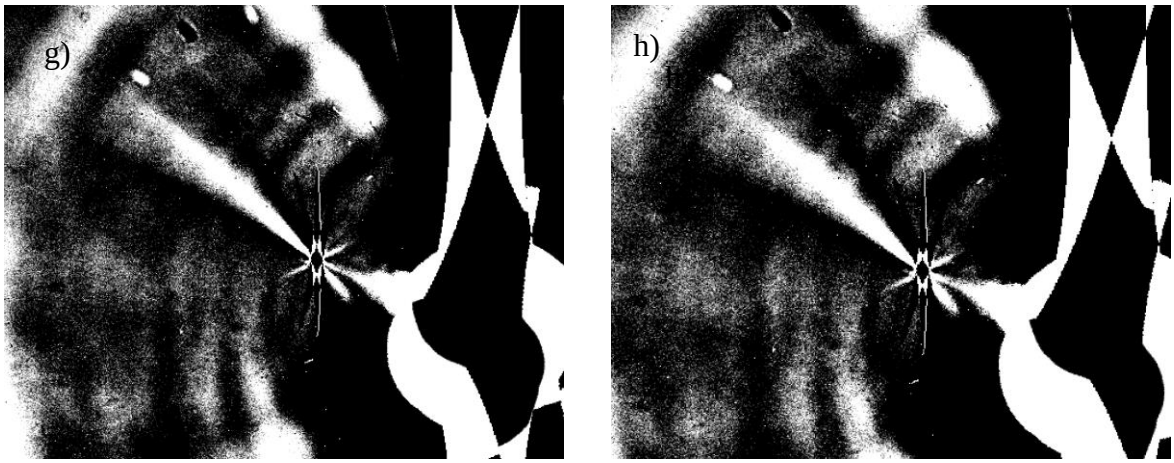

Figure 5.16: Examples of the rotational gradient method done on Io in the raw image illustrated in Fig. 4.6 with different rotation angles. a) original image, b) dα=1, c) dα=3, d) dα= 5, e) dα= 8, f) dα= 11, g) dα= 15, h) dα= 18.

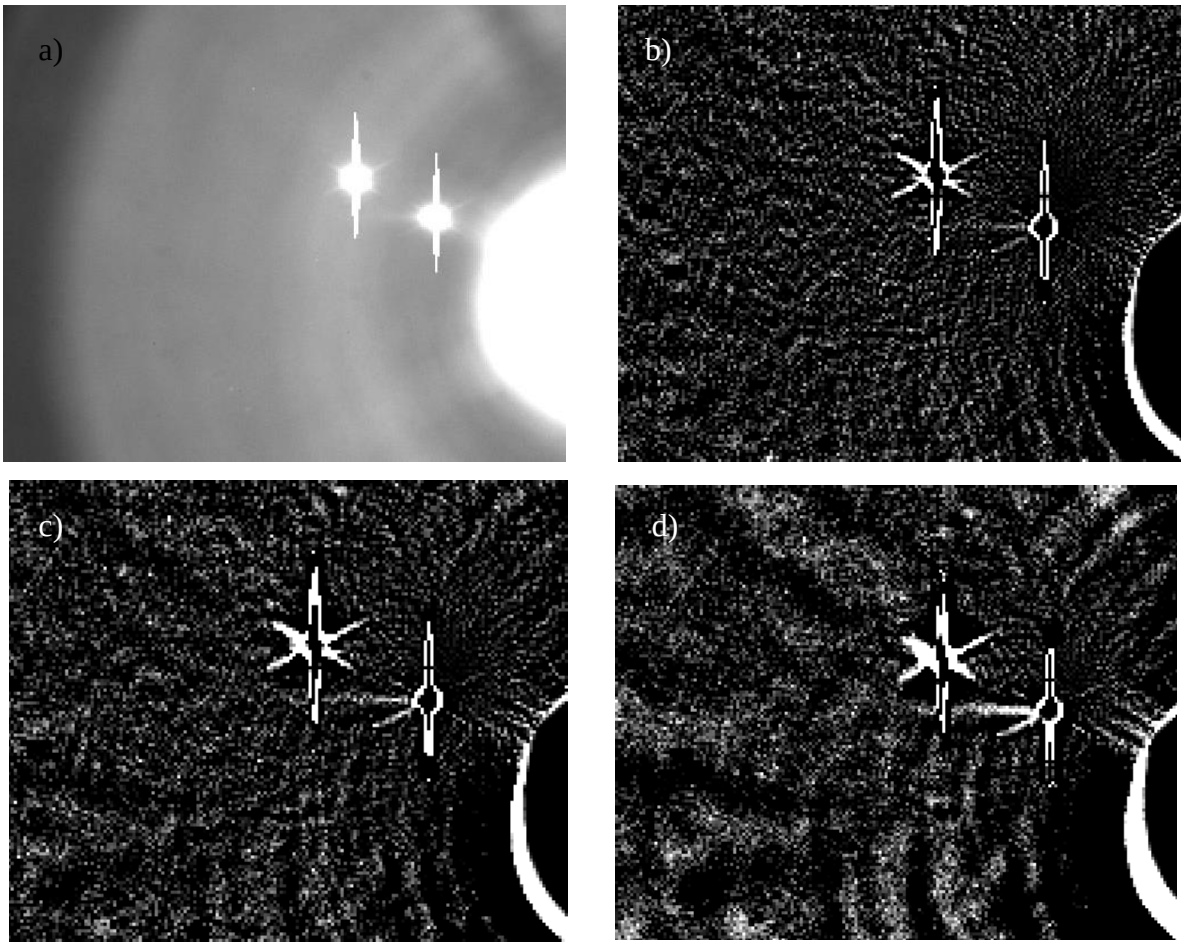

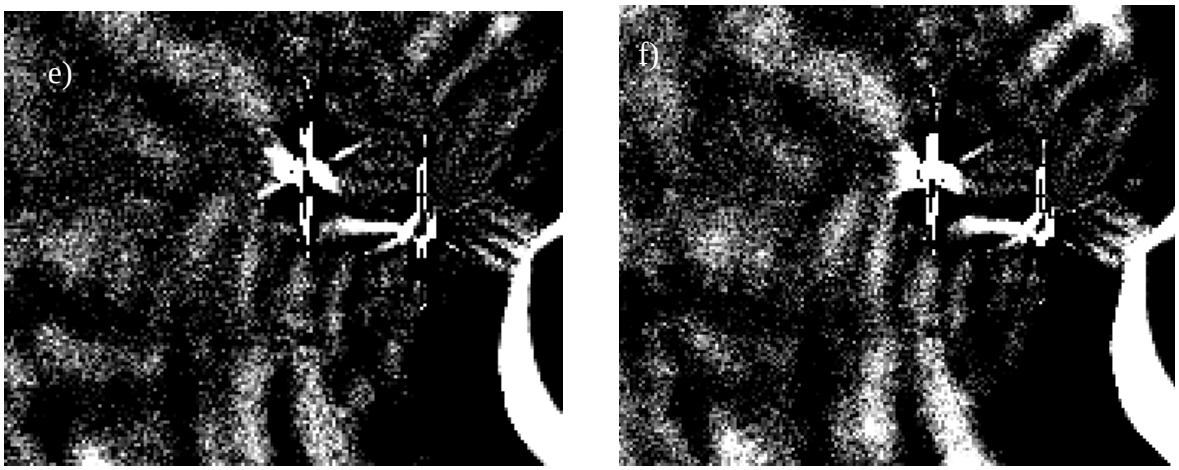

Figure 5.17: Examples of the rotational gradient method done on Io in the calibrated image from December 6, 2014 with different rotation angles. a) original image, b) dα=2, c) dα=3, d) dα= 5, e) dα= 8, f) dα= 11. Io is on the right of the image.

Chapter 6

Results

We present in this chapter the results of our observations and our image processing methods. The first section is dedicated to the results obtained with IDL. Then we present the results obtained with the rotational gradient method that allows us to emphasize the presence of a jet. The last section is devoted to the interpretation of these results and the characterization of the observed jets.

6.1 Images processing with IDL

For each night of observations, we first determined the position of Io on the images with the Jupiter Viewer Tool, PDS Rings Node. Then we executed the code presented in Appendix 1 which allowed us to obtain the different results presented in the next section. For each night, we show four image processing results for the three methods, when possible.

6.1.1 December 4, 2014

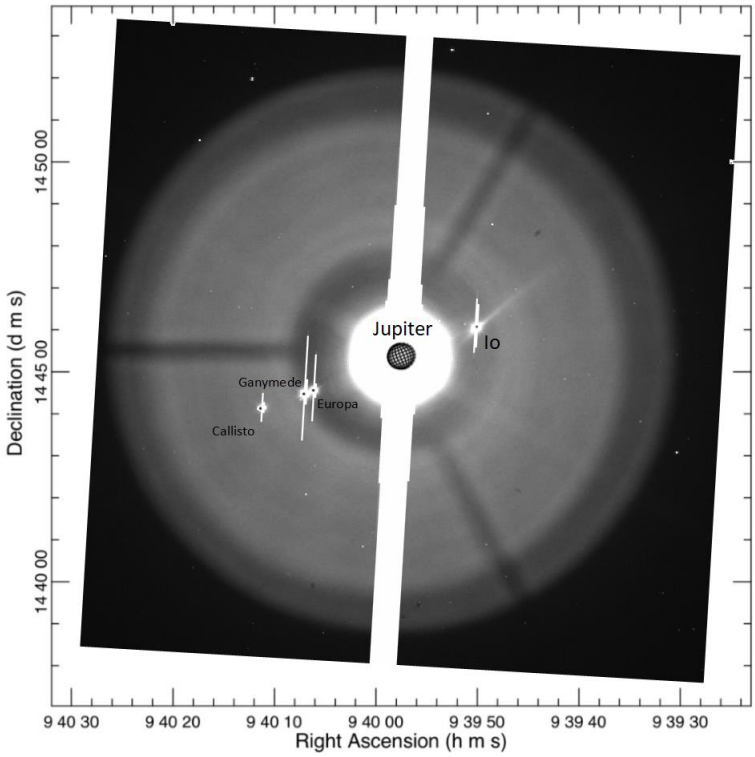

Figure 6.1: Superposition of the image from December 4, 2014 with the position of Jupiter, Io, Callisto, Ganymede and Europa seen at scale, generated by the Jupiter ViewerTool, PDS Rings Node.

For the first observation night, we observed Io with the NaI filter and acquired 3 images in binning 1 of the Jovian system. Figure 6.1 illustrates the position of each Jovian celestial body on the images of December 4, 2014. Figure 6.2 shows the image processing results performed on the reduced images using the unsharp masking method. Figure 6.3 shows the image processing results using the background subtraction method. Unfortunately, the stacking and unsharp masking method is not possible for that night because we did not acquire enough images with the same exposure time. On these two figures (Fig. 6.2 and Fig. 6.3), we can notice the presence of an extraordinary jet and for each of them, we zoomed in on Io.

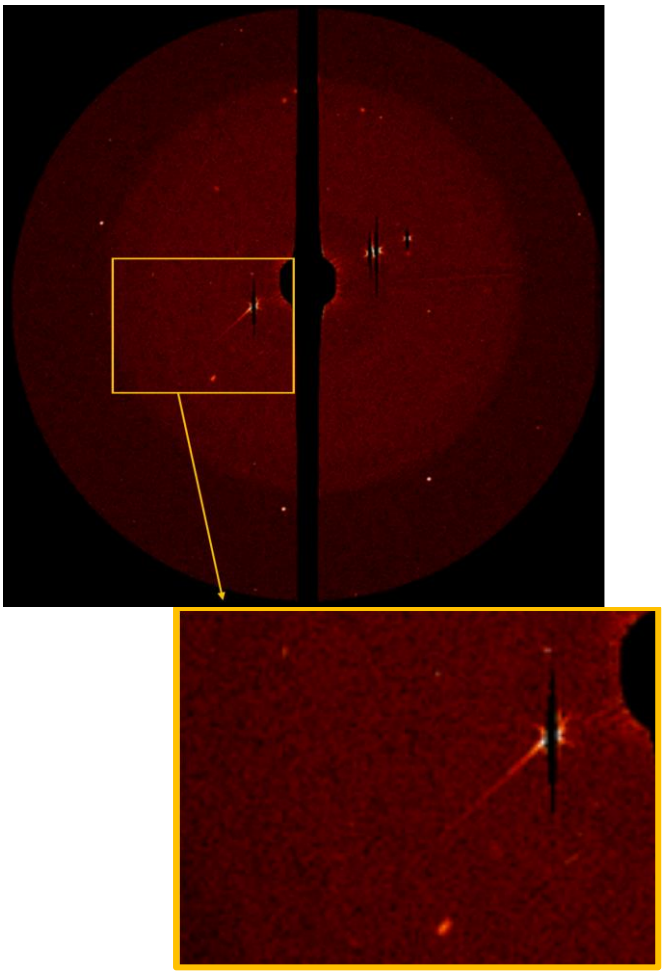

Figure 6.2: Results for an image from December 4, 2014 using the unsharp masking method.

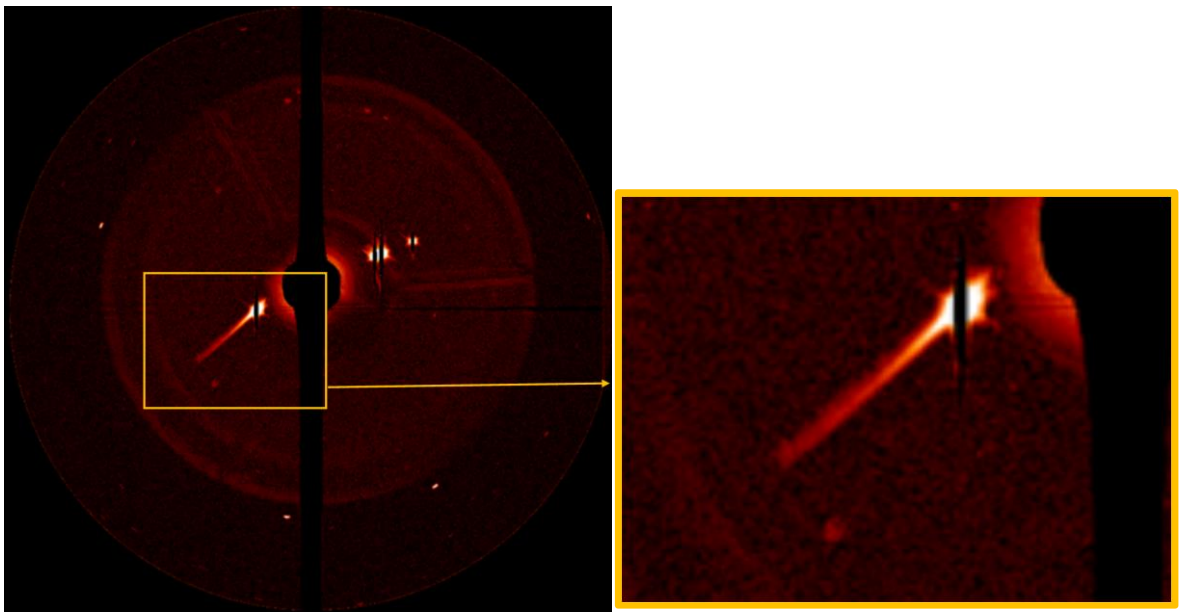

Figure 6.3: Results for an image from December 4, 2014 using the background subtraction method.

6.1.2 December 6, 2014

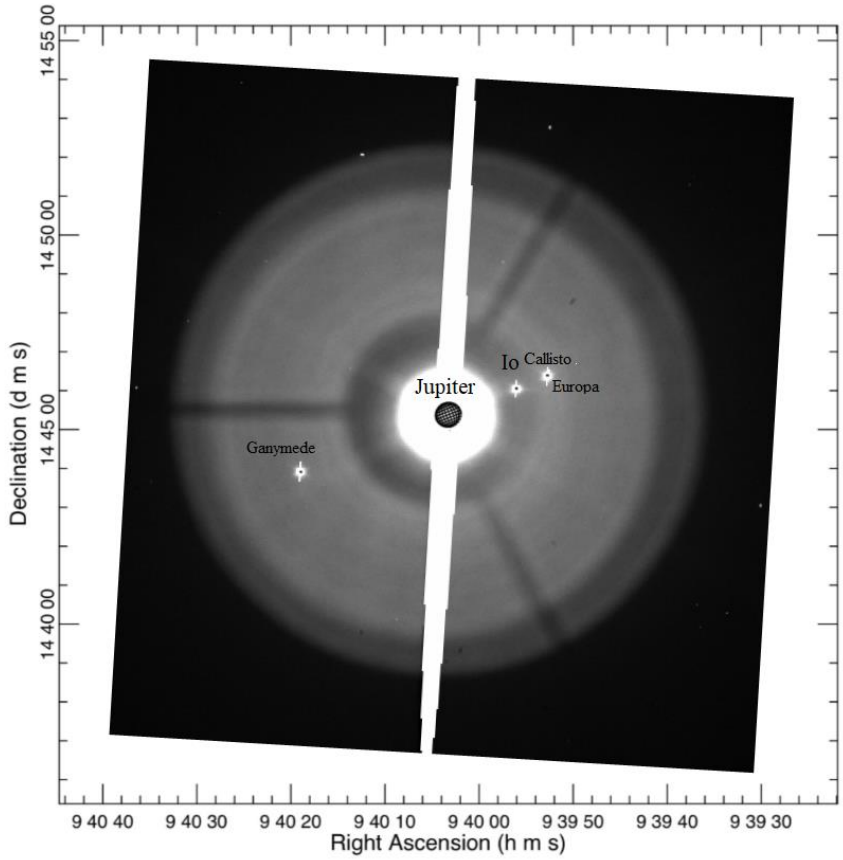

Figure 6.4: Superposition of the image from December 6, 2014 with the position of Jupiter, Io, Callisto, Ganymede and Europa seen at scale, generated by the Jupiter ViewerTool, PDS Rings Node.

For the second observation night, we observed Io with the NaI filter and acquired 98 images in binning 2 of the Jovian system. Figure 6.4 shows the position of each Jovian celestial body on the obtained images. Figure 6.5 illustrates the image processing results performed on the reduced images of December 6, 2014 using the unsharp masking method. Figure 6.6 shows the image processing results performed on the same images using the background subtraction method. Figure 6.7 illustrates the images processing results for that night using the stacking and unsharp masking method. On these three figures (Fig. 6.5, Fig. 6.6 and Fig. 6.7), we can notice the presence of a jet. For each figure, we zoomed in on Io.

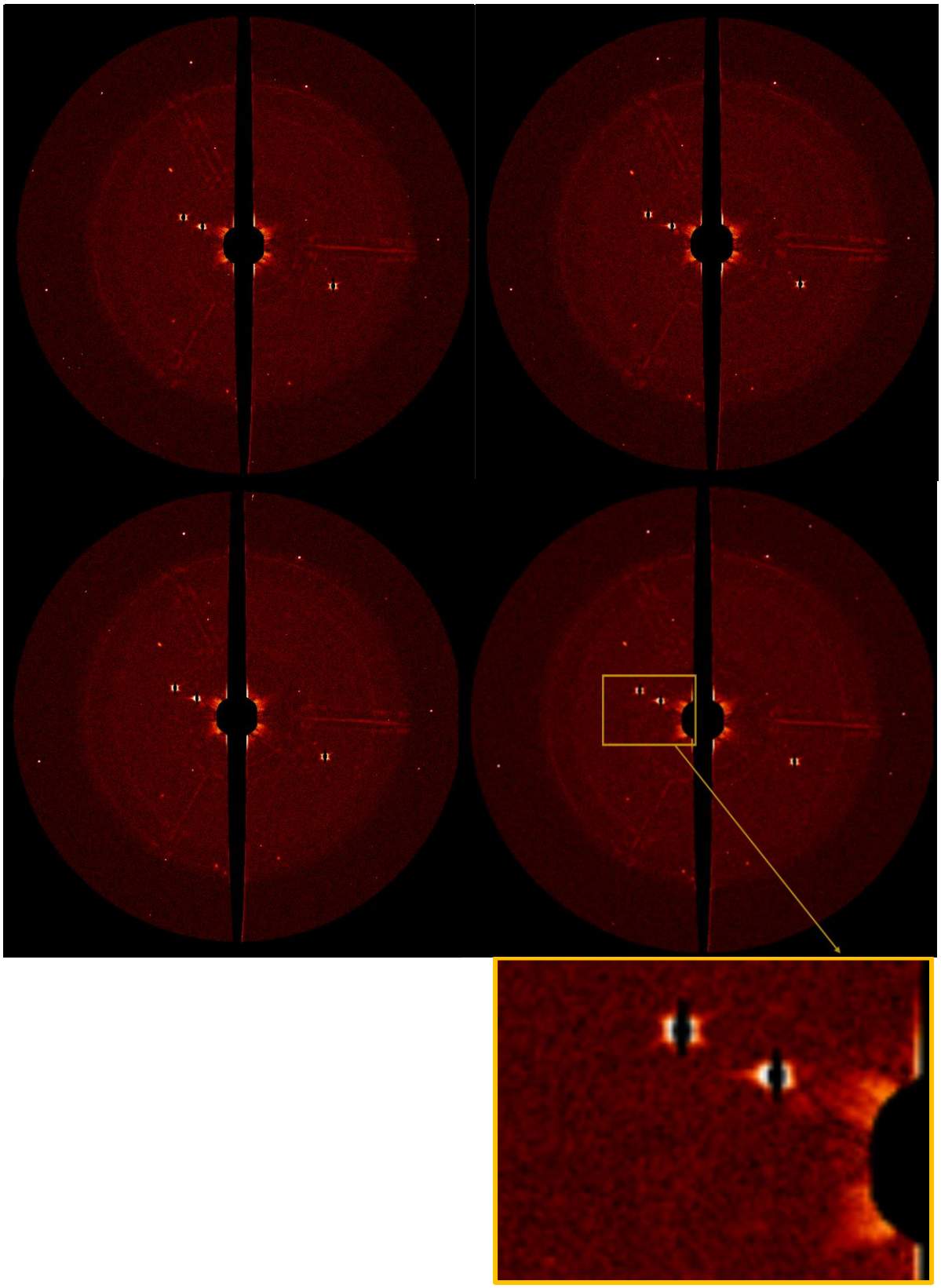

Figure 6.5: Results for four images from December 6, 2014 using the unsharp masking method.

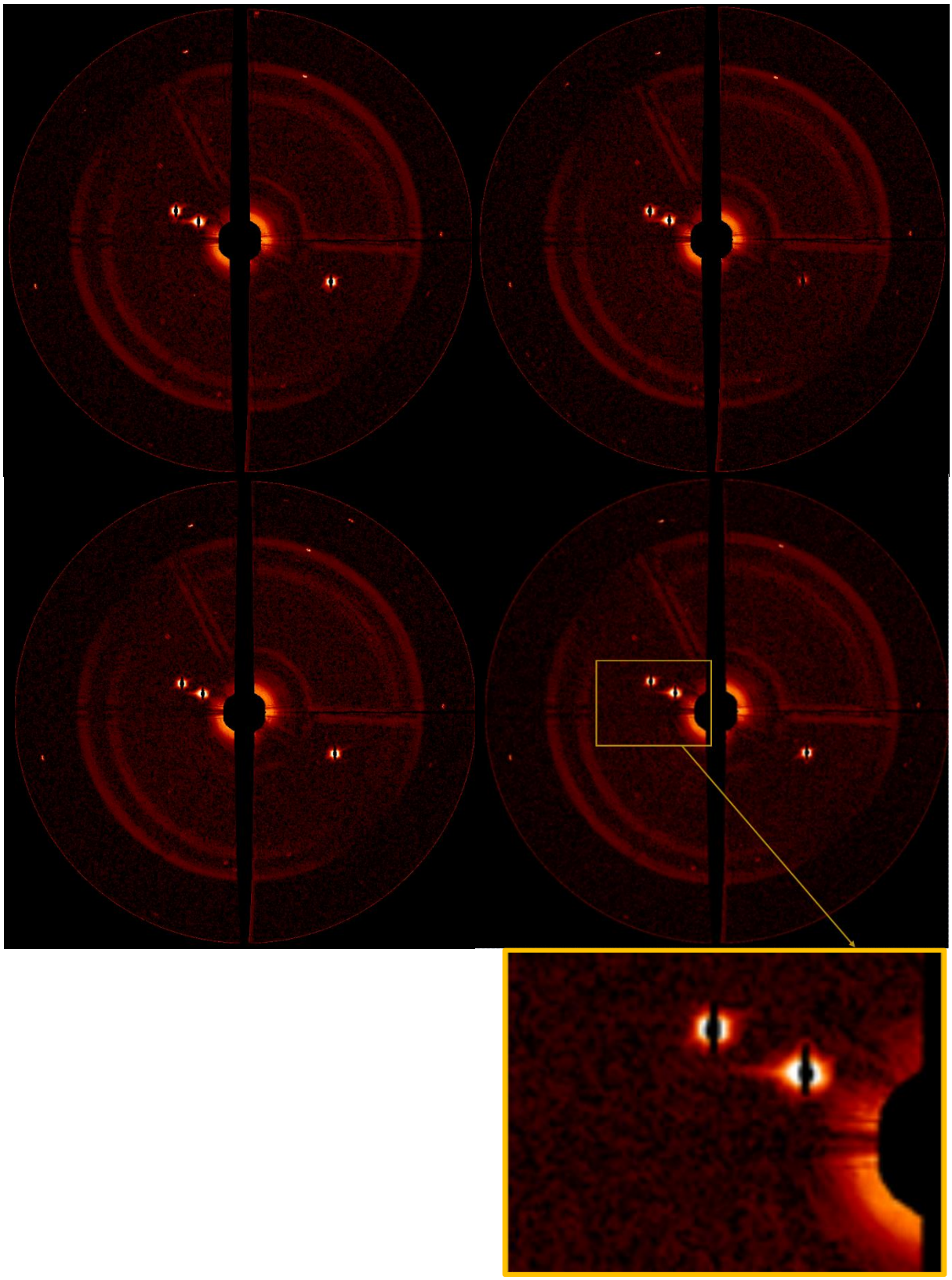

Figure 6.6: Results for four images from December 6, 2014 using the background subtraction method.

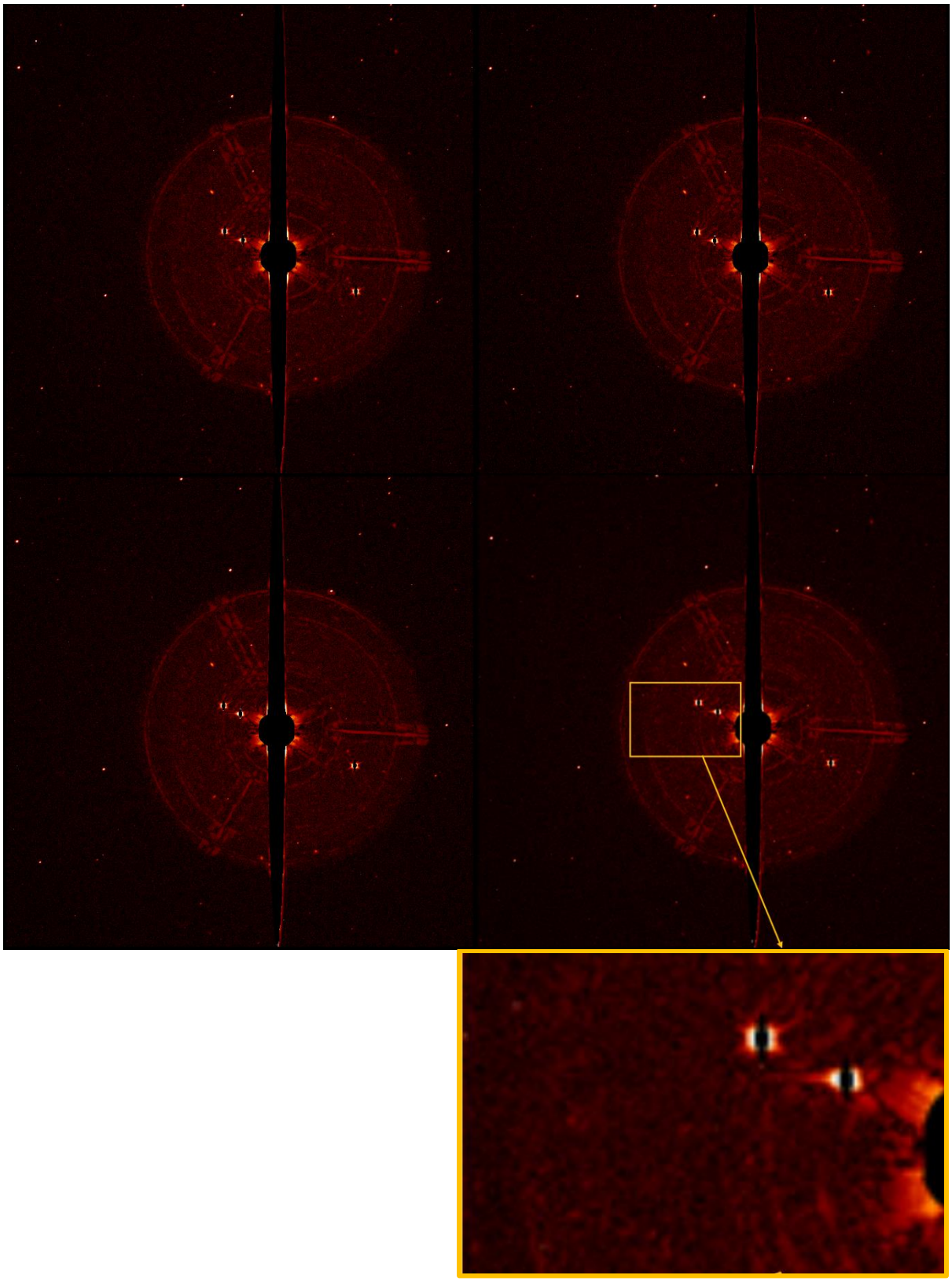

Figure 6.7: Results for images from December 6, 2014 using the stacking and unsharp masking method.

6.1.3 December 8, 2014

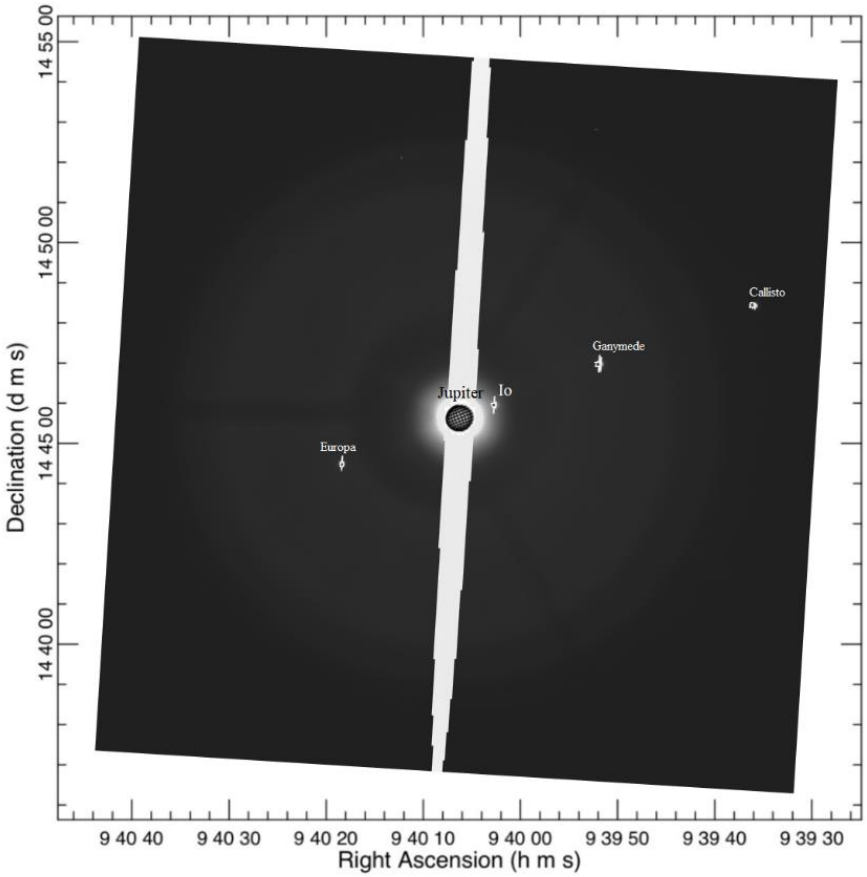

Figure 6.8: Superposition of the image from December 8, 2014 with the position of Jupiter, Io, Callisto, Ganymede and Europa seen at scale, generated by the Jupiter ViewerTool, PDS Rings Node.

For the third observation night, we observed Io with the NaI filter and acquired 23 images in binning 2 of the Jovian system. Figure 6.8 illustrates the position of each Jovian celestial body on a reduced image. Figure 6.9 shows the image processing results performed on a reduced image of December 8, 2014 using the unsharp masking method. Figure 6.10 shows the image processing result performed on the same image using the background subtraction method. Figure 6.11 illustrates the image processing results for the image from this observation night using the stacking and unsharp masking method. The problem for this night is that Io is too close to Jupiter and is therefore in the contamination part of Jupiter and masked by the mask. The detection of a jet, if present, is thus complicated.

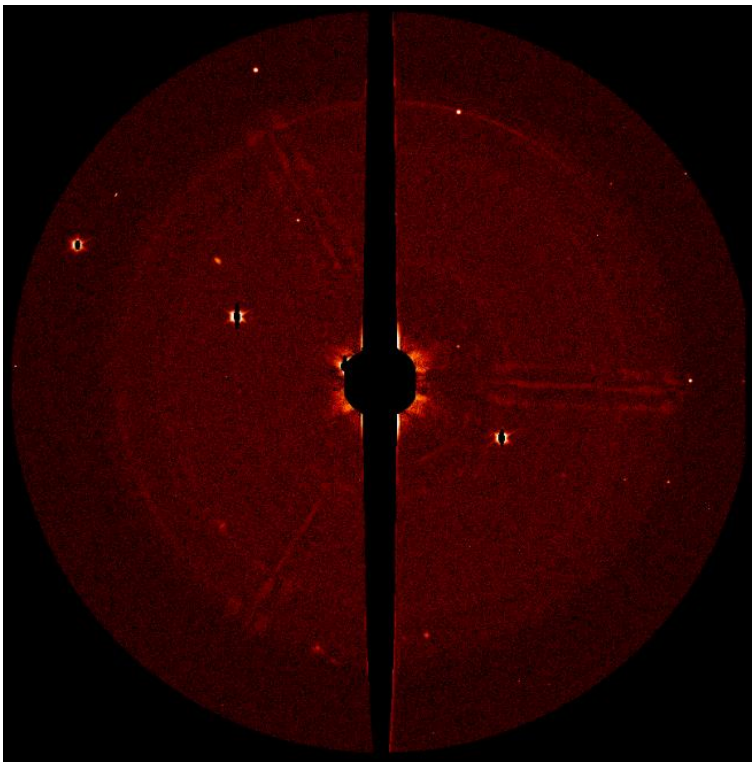

Figure 6.9: Result for one image from December 8, 2014 using the unsharp masking method.

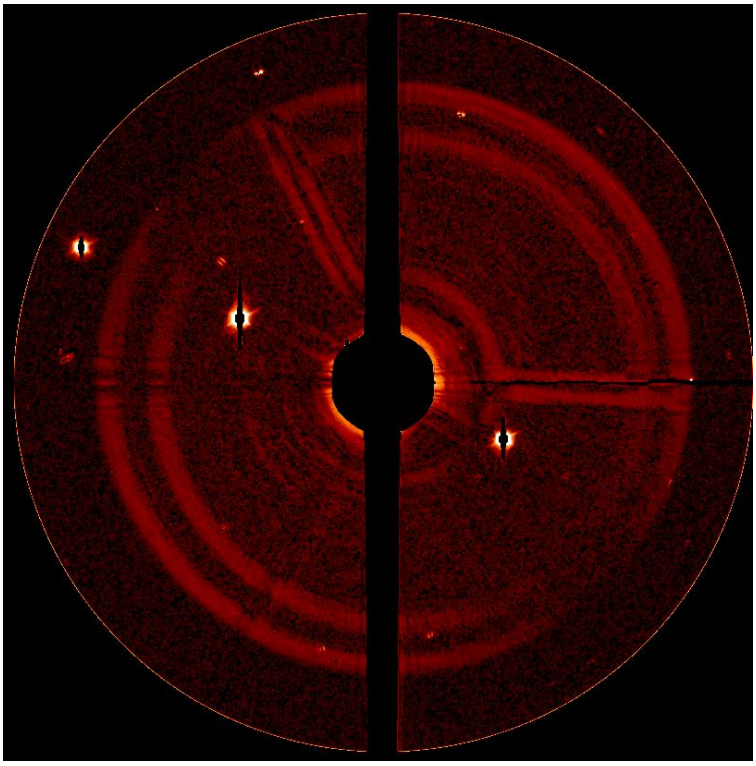

Figure 6.10: Results for four images from December 8, 2014 using the background subtraction method.

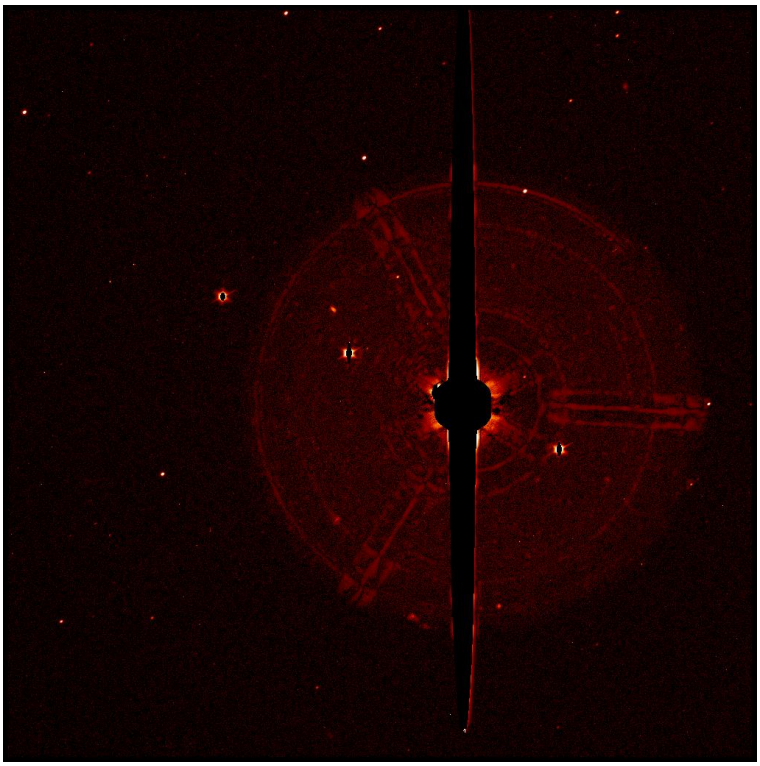

Figure 6.11: Results for images from December 8, 2014 using the stacking and unsharp masking method.

6.1.4 December 12, 2014

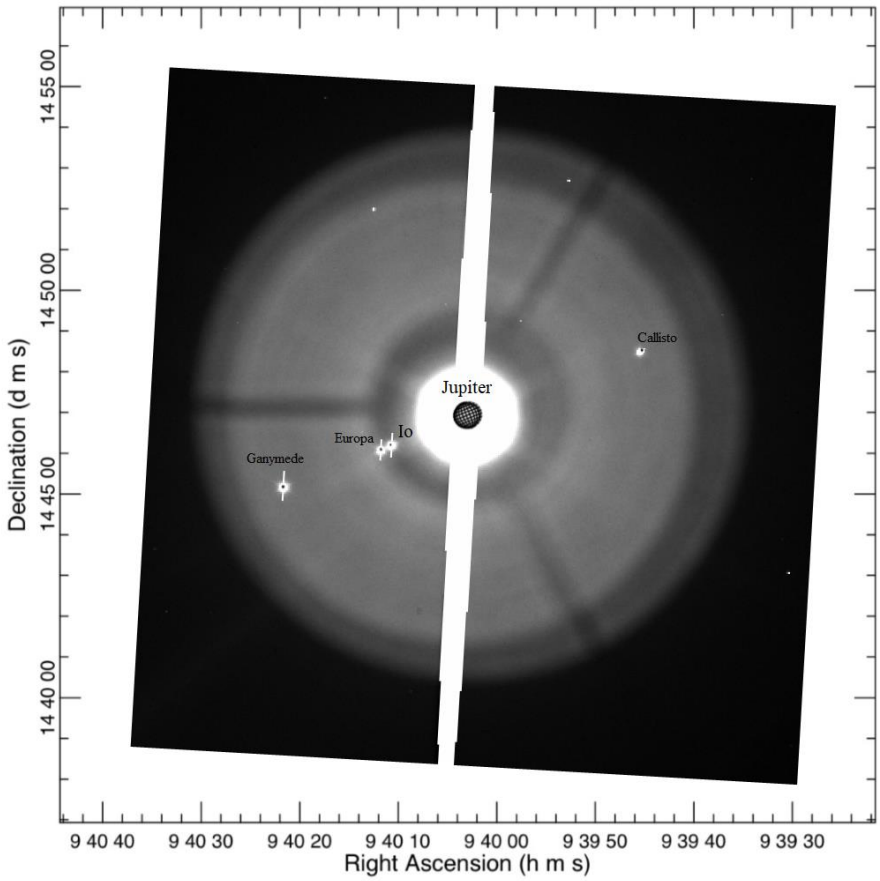

Figure 6.12: Superposition of the image from December 12, 2014 with the position of Jupiter, Io, Callisto, Ganymede and Europa seen at scale, generated by the Jupiter ViewerTool, PDS Rings Node.

For the fourth observation night, we observed Io with the NaI filter and acquired 34 images in binning 2 of the Jovian system. Figure 6.12 illustrates the position of each Jovian celestial body on the images. Figure 6.13 shows the image processing results performed on the reduced images of December 12, 2014 using the unsharp masking method. Figure 6.14 shows the image processing results performed on the same images using the background subtraction method. Figure 6.15 illustrates the images processing results for the night of observation using the stacking and unsharp masking method. For each figure, we zoomed on Io. Unfortunately, for this night, Io is too close to Europa. The detection of a jet, if present, is thus compromised.

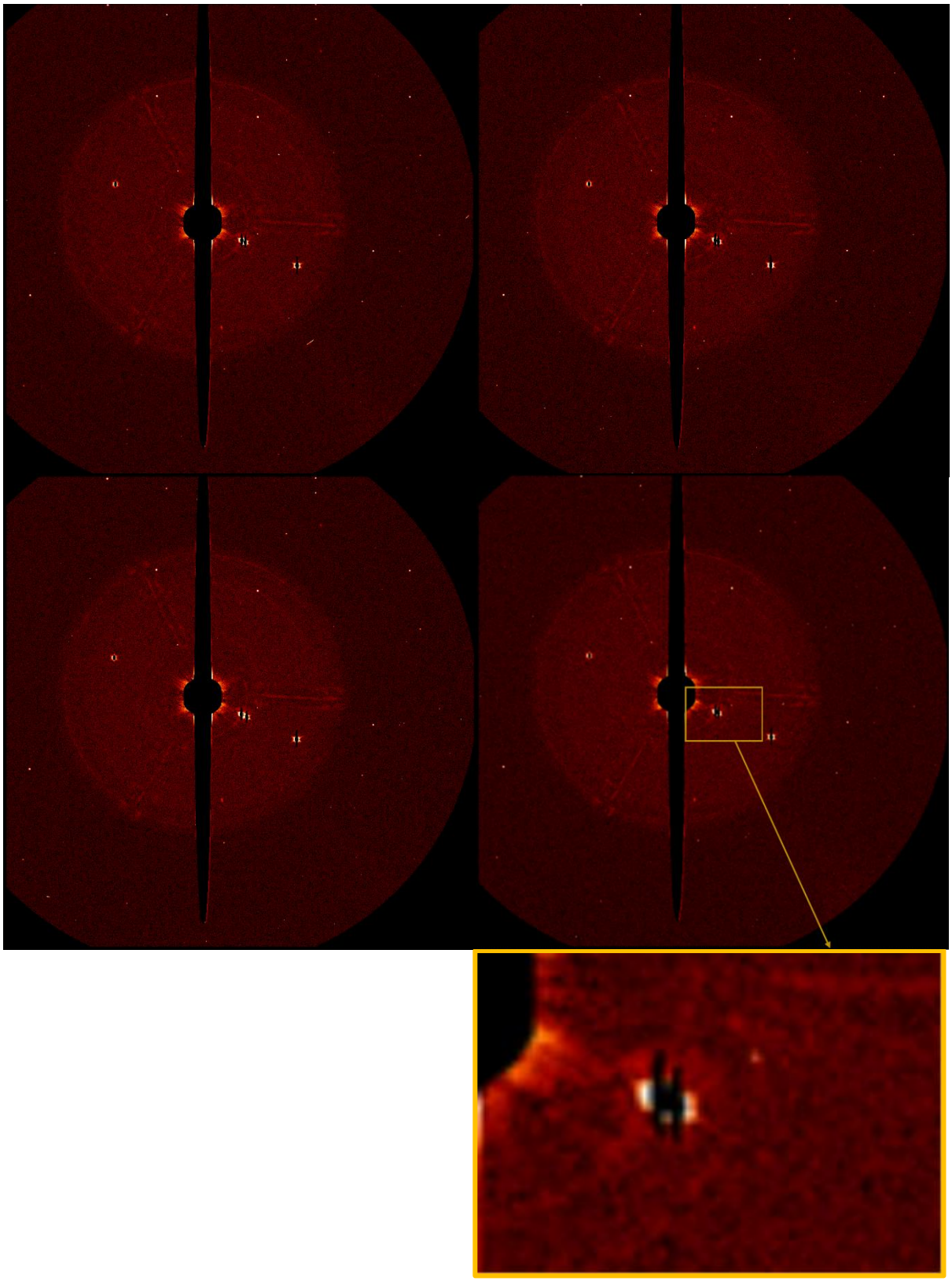

Figure 6.13: Results for four images from December 12, 2014 using the unsharp masking method.

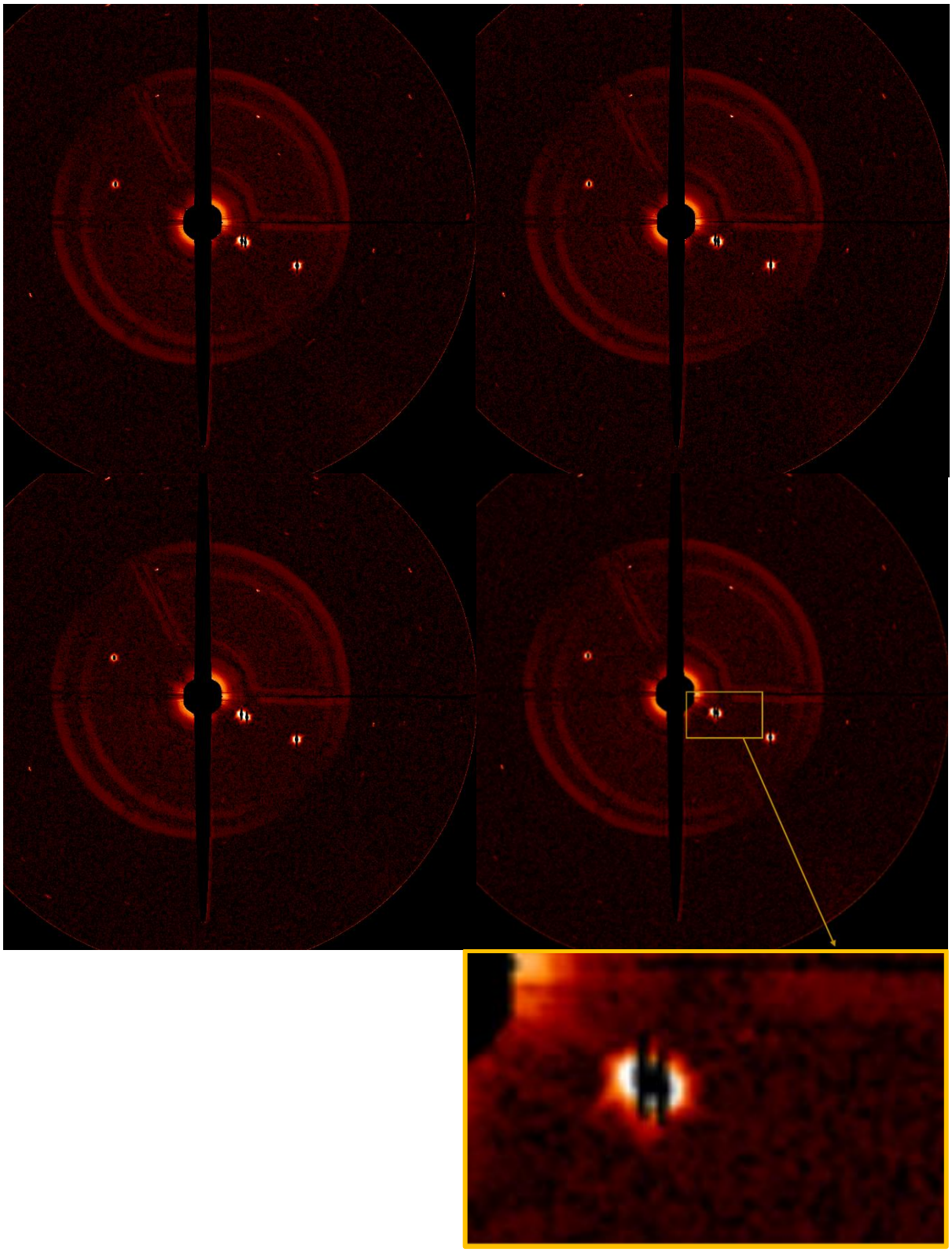

Figure 6.14: Results for four images from December 12, 2014 using the background subtraction method.

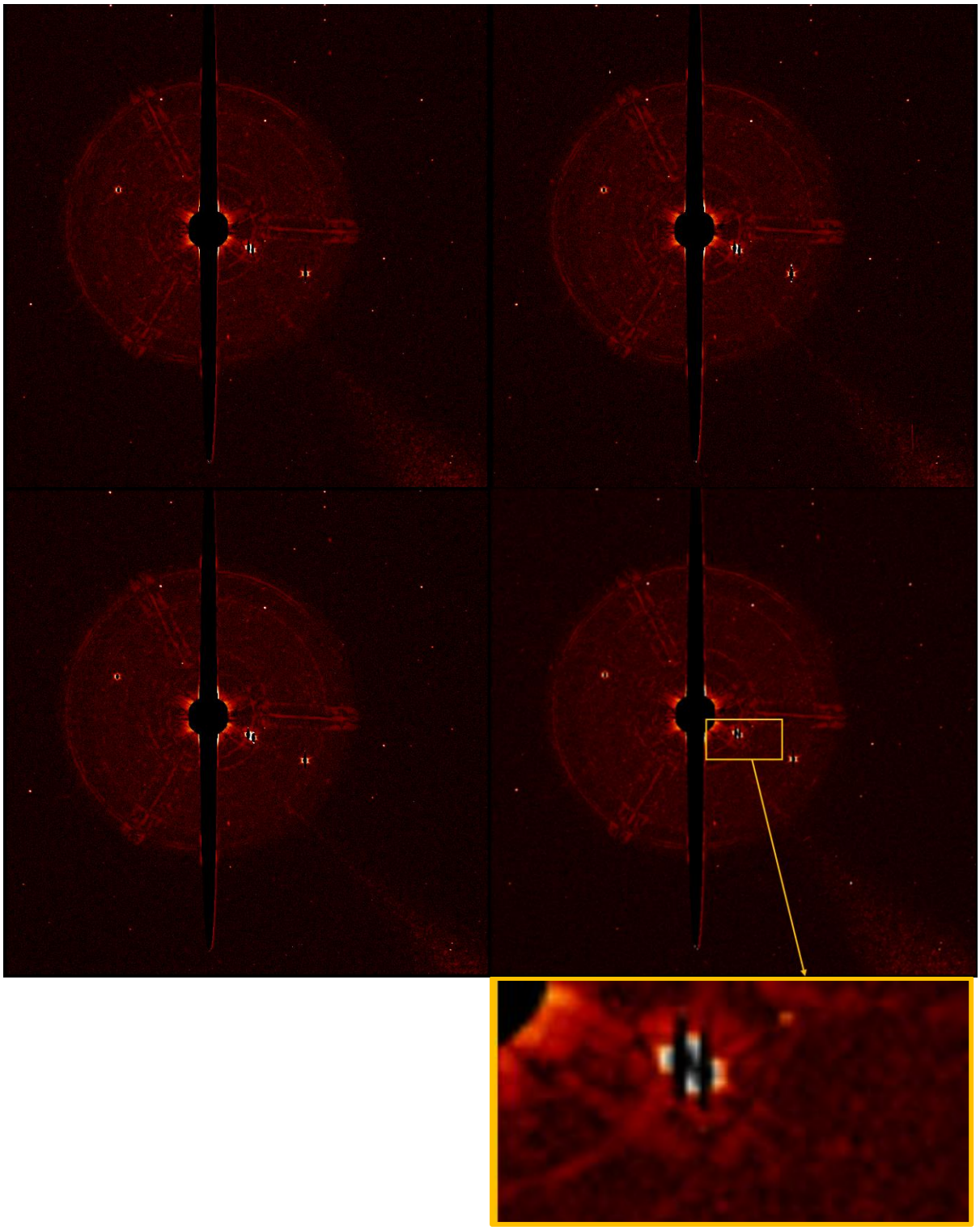

Figure 6.15: Results for images from December 12, 2014 using the stacking and unsharp masking method.

6.1.5 December 19, 2014

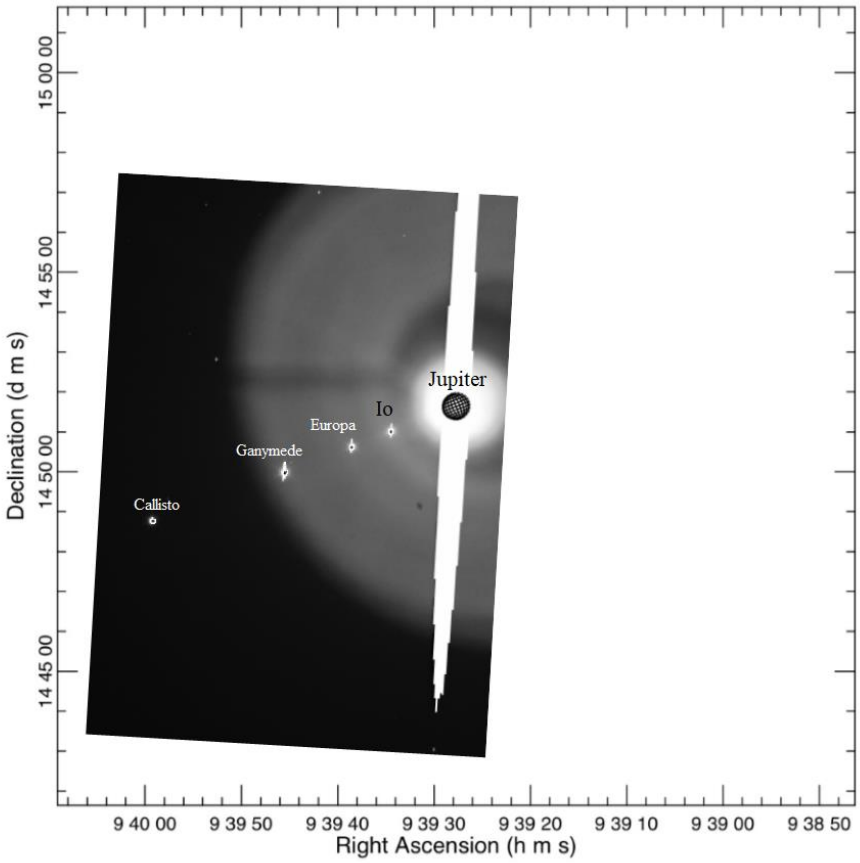

Figure 6.16: Superposition of the image from December 19, 2014 with the position of Jupiter, Io, Callisto, Ganymede and Europa seen at scale, generated by the Jupiter ViewerTool, PDS Rings Node.

For the fifth observation night, we observed Io with the NaI filter and acquired 10 images in binning 2 of the Jovian system. Figure 6.16 illustrates the position of each Jovian celestial body on the obtained images. For this night of observation, we did not center Jupiter in an attempt to minimize the contamination of the giant planet. Figure 6.17 shows the image processing results performed on the reduced images of December 19, 2014 using the unsharp masking method. Figure 6.18 shows the image processing results performed on the same images using the background subtraction method. Figure 6.19 illustrates the images processing results using the stacking and unsharp masking method. For each figure, we zoomed in on Io. We do not detect any jet for that night.

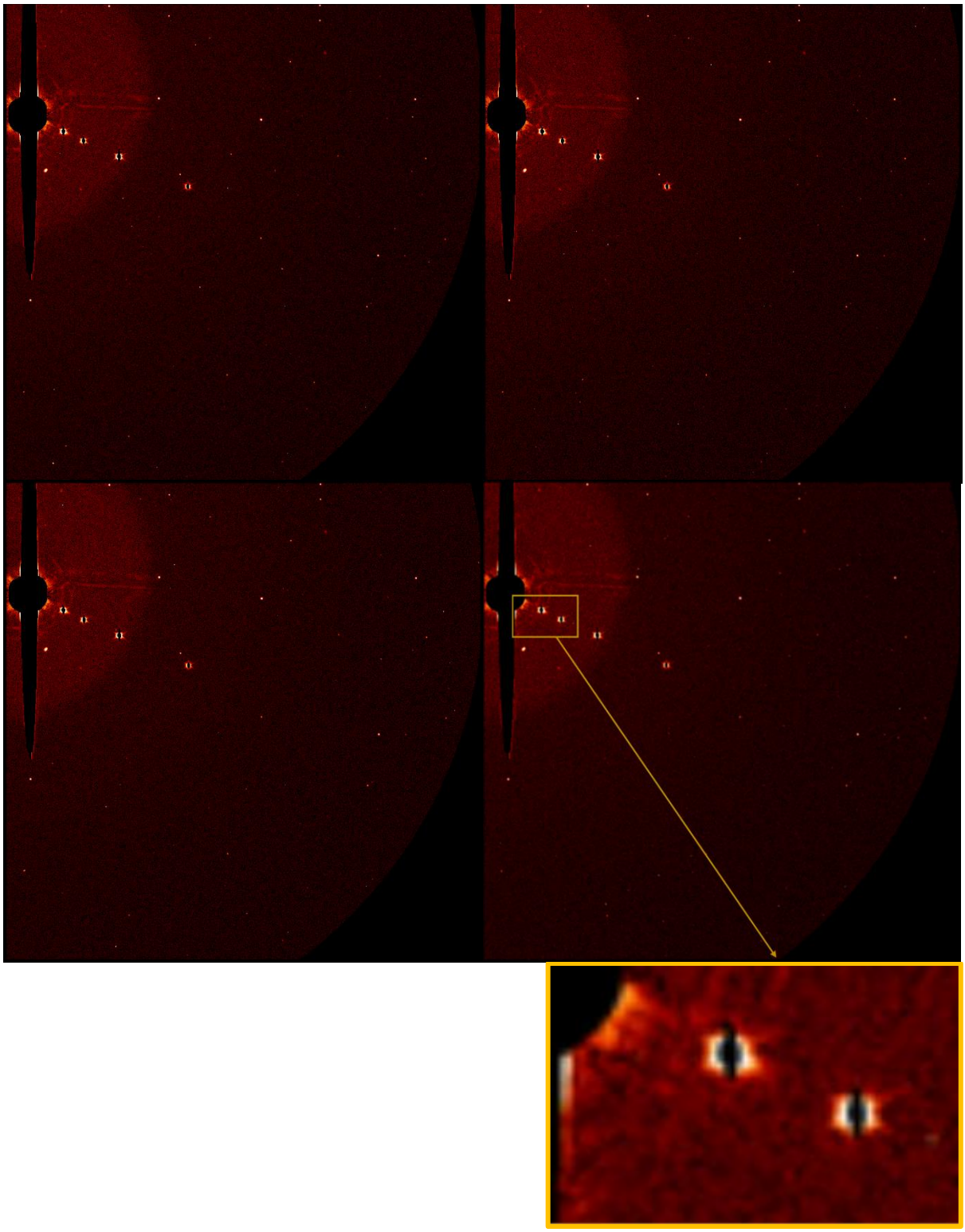

Figure 6.17: Results for four images from December 19, 2014 using the unsharp masking method.

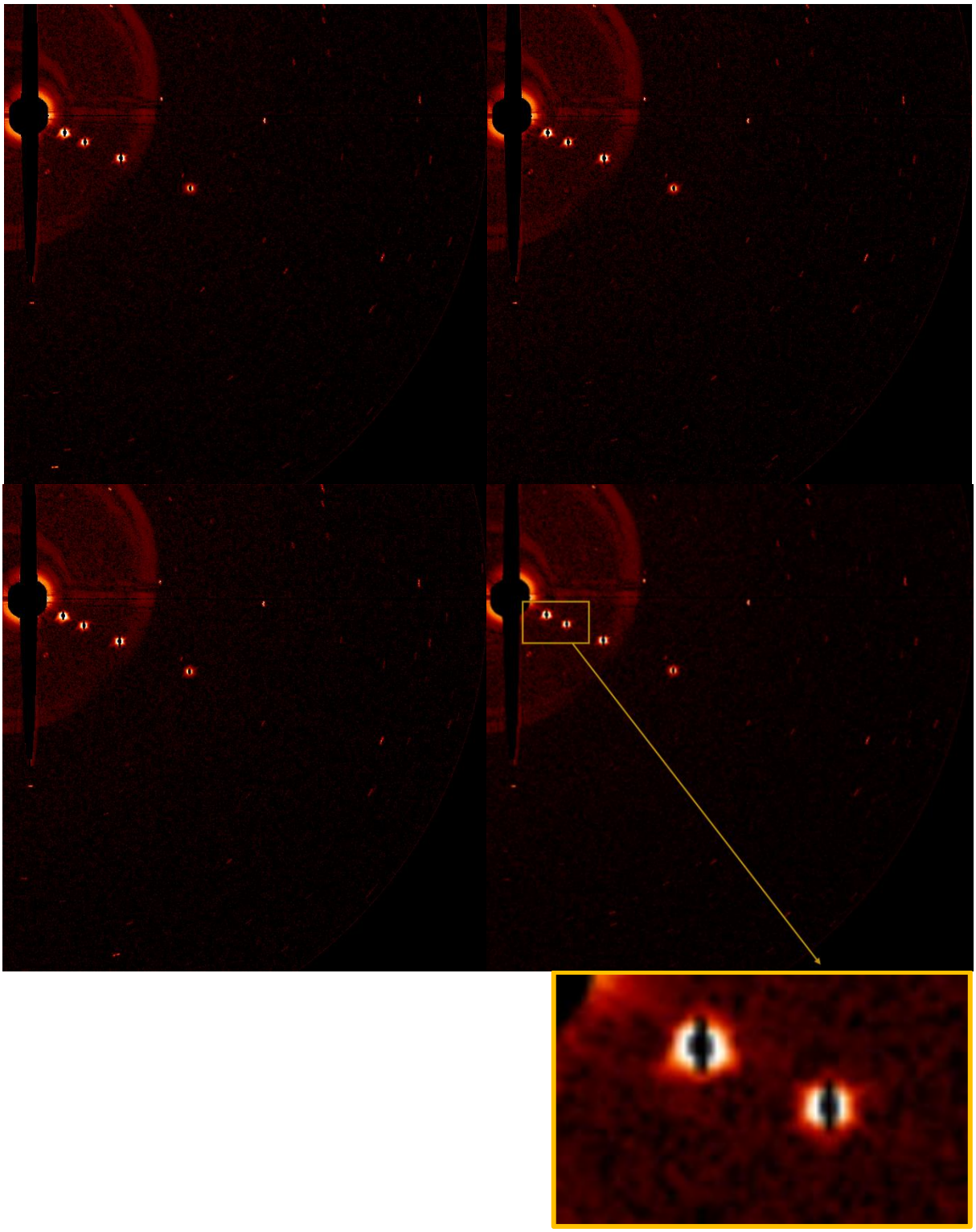

Figure 6.18: Results for four images from December 19, 2014 using the background subtraction method.

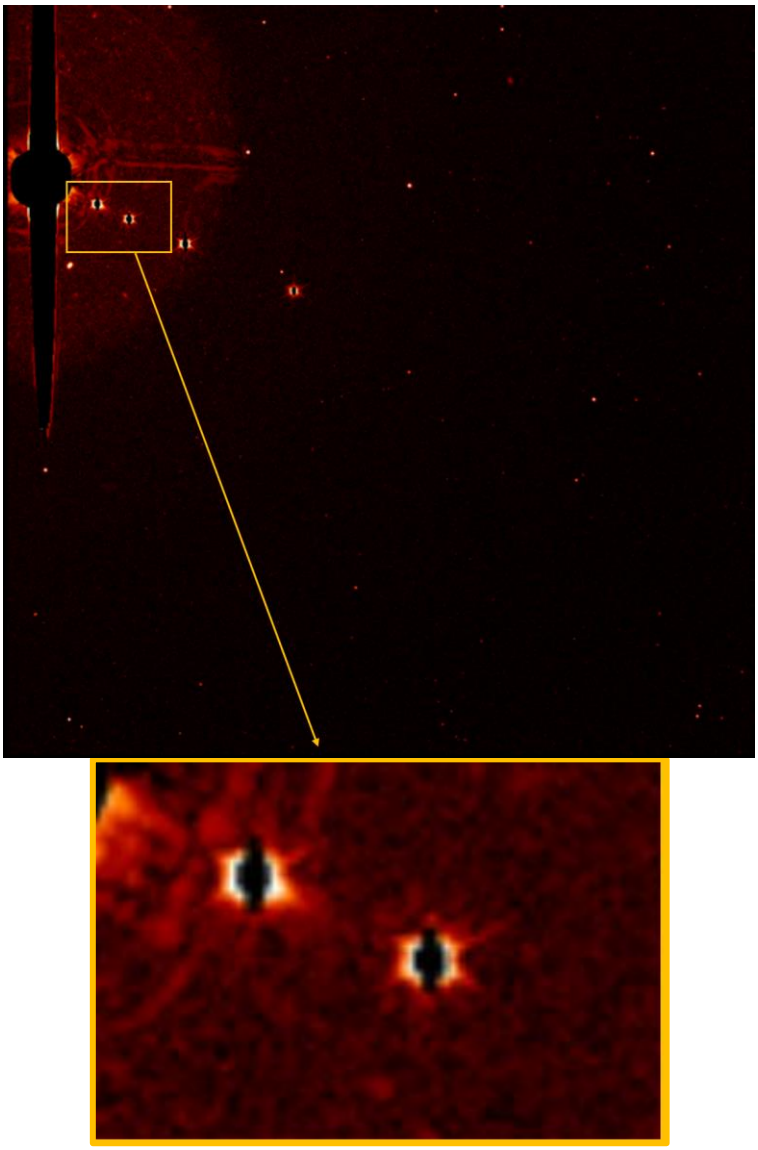

Figure 6.19: Results for images from December 19, 2014 using the stacking and unsharp masking method.

6.1.6 January 11, 2015

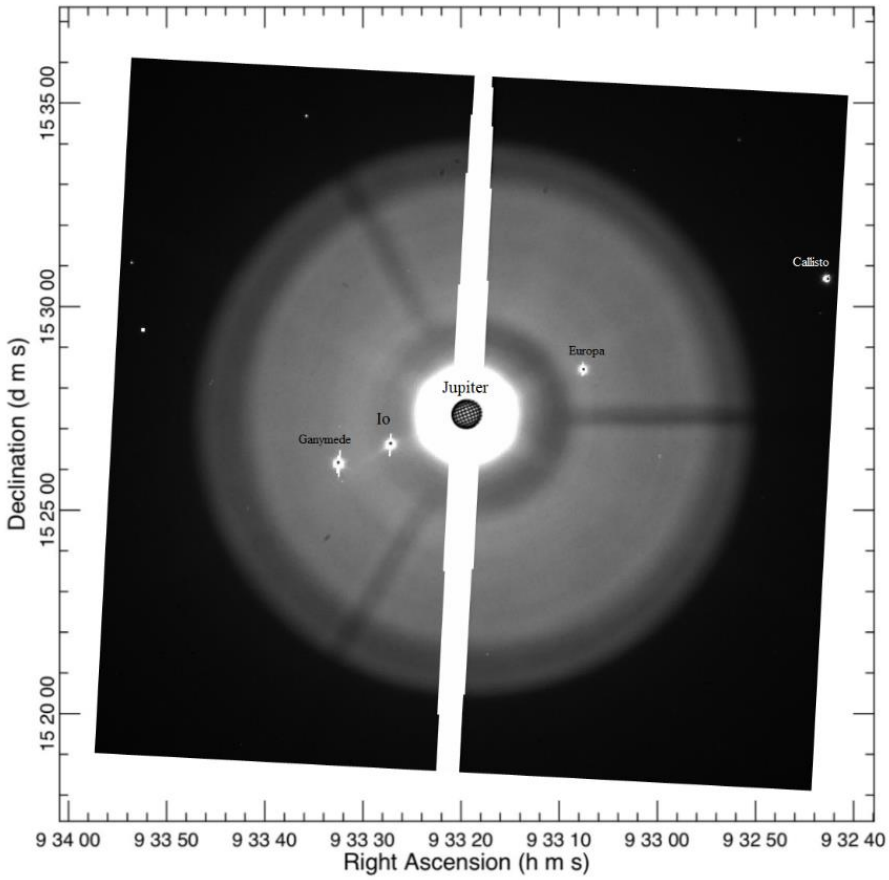

Figure 6.20: Superposition of the image from January 11, 2015 with the position of Jupiter, Io, Callisto, Ganymede and Europa seen at scale, generated by the Jupiter ViewerTool, PDS Rings Node.

For the sixth observation night, we observed Io with the NaI filter and acquired 15 images in binning 2 of the Jovian system. Figure 6.20 illustrates the position of each Jovian celestial body on a calibrated image. Figure 6.21 shows the image processing results performed on the reduced images of January 11, 2015 using the unsharp masking method. Figure 6.22 shows the image processing results performed on the same images using the background subtraction method. Figure 6.23 illustrates the images processing results using the stacking and unsharp masking method. On these three figures (Fig. 6.21, Fig. 6.22 and Fig. 6.23), we can notice the presence of a jet and for each figure, we zoomed in on Io.

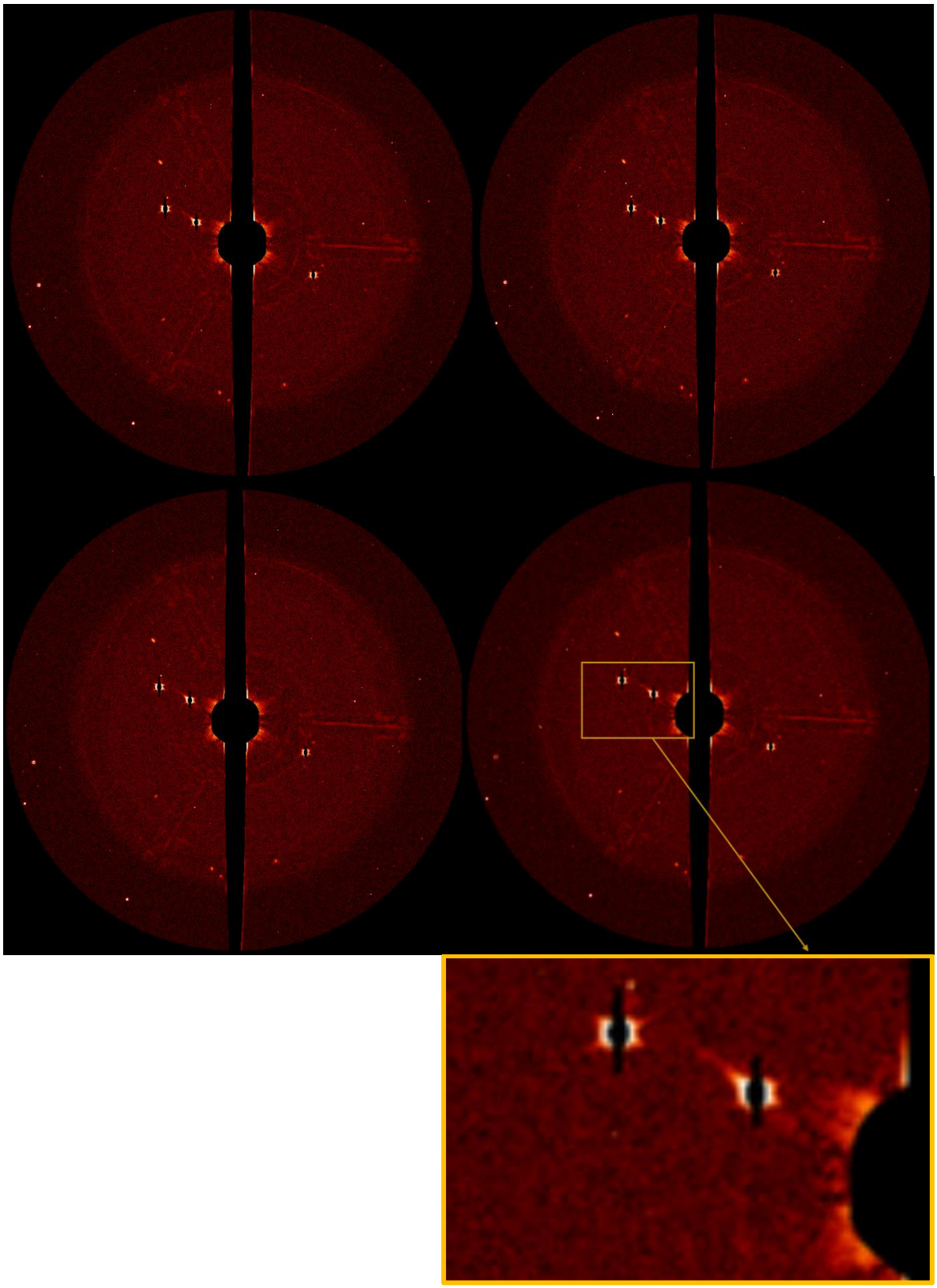

Figure 6.21: Results for four images from January 11, 2015 using the unsharp masking method.

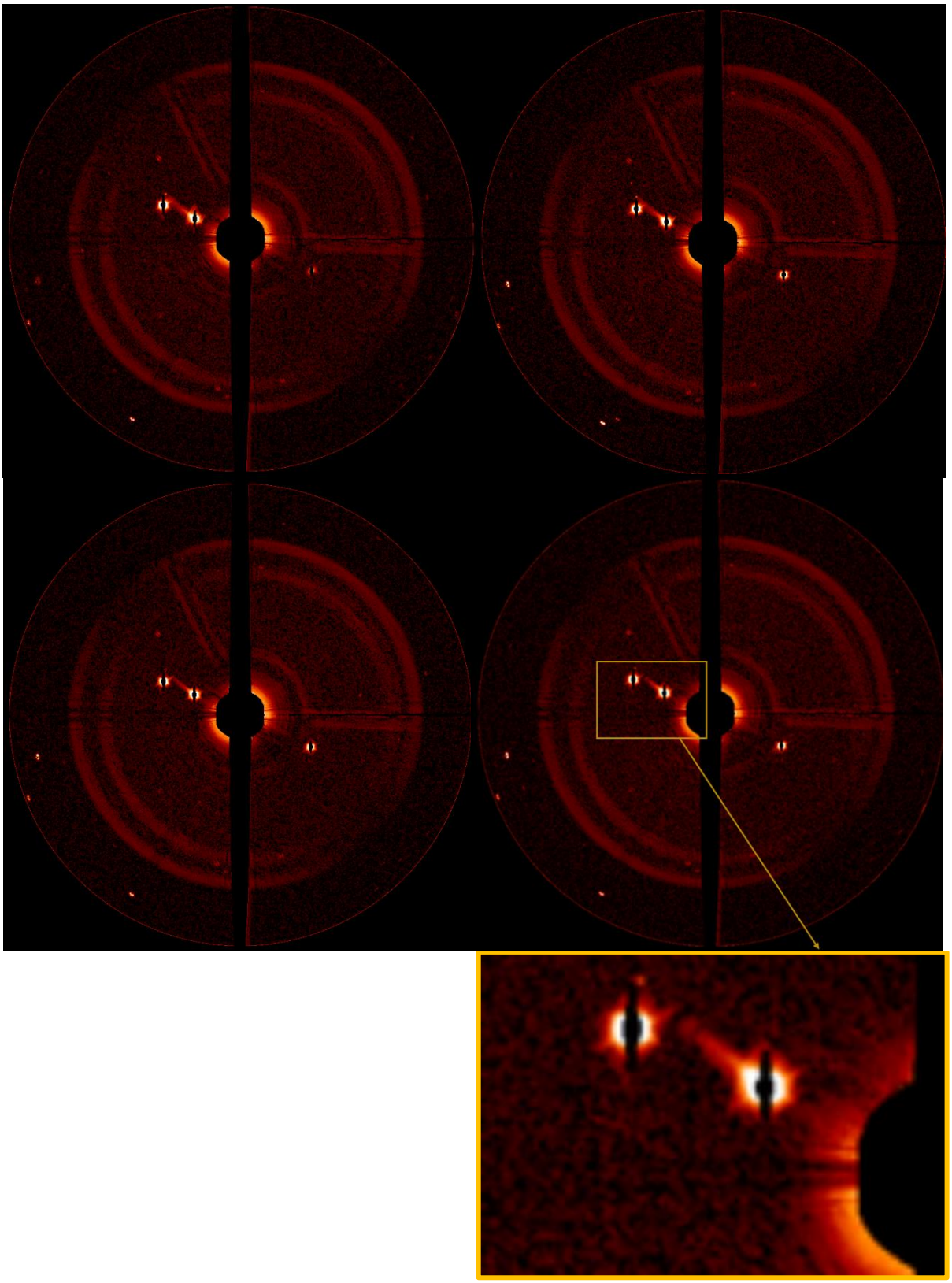

Figure 6.22: Results for four images from January 11, 2015 using the background subtraction method.

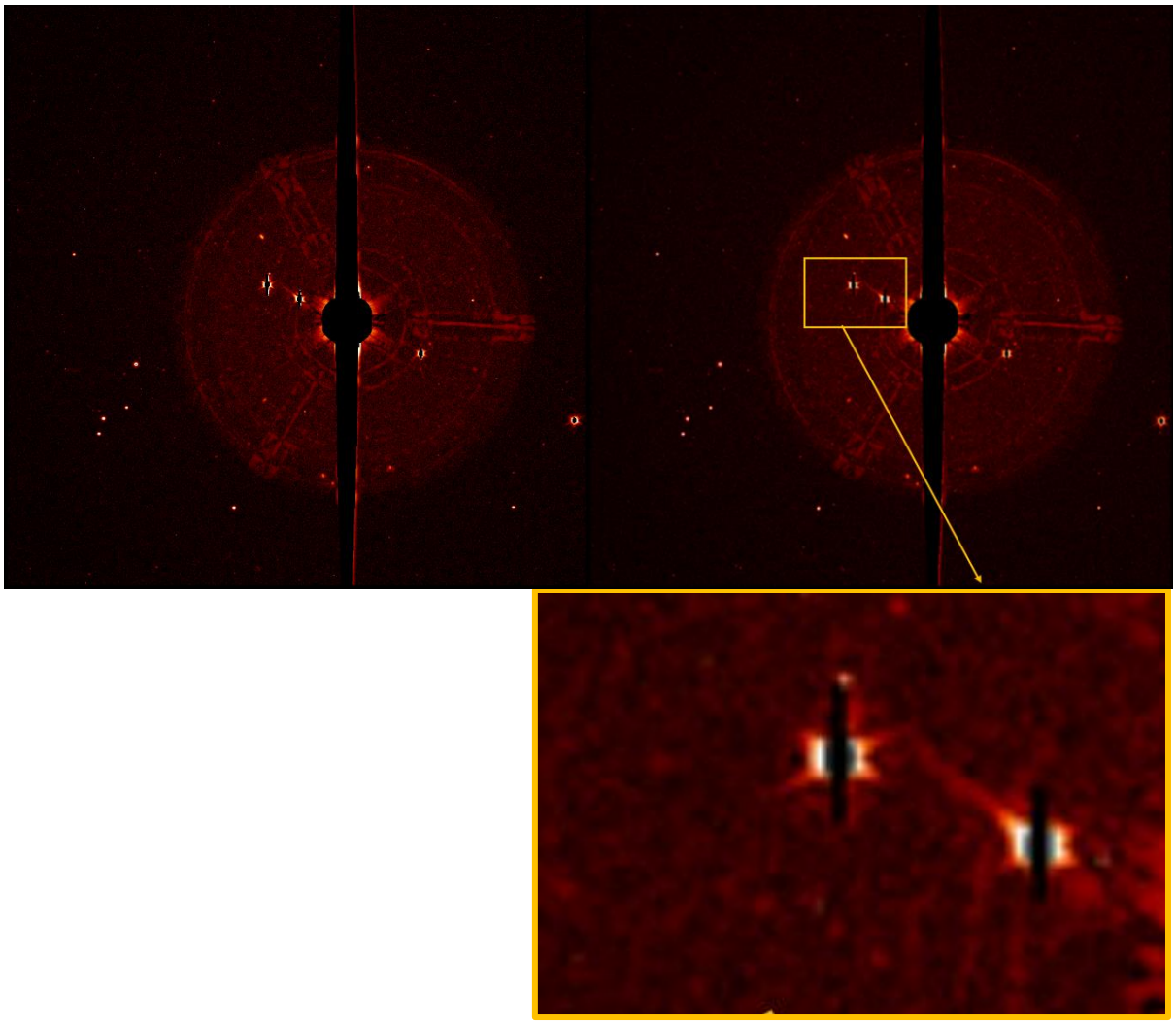

Figure 6.23: Results for images from January 11, 2015 using the stacking and unsharp masking method.

6.1.7 January 13, 2015

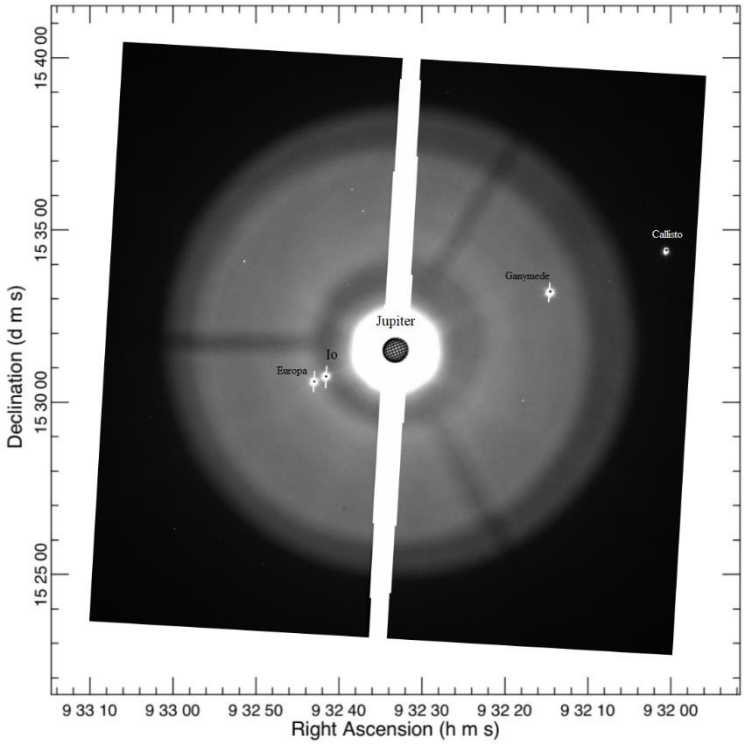

Figure 6.24: Superposition of the image from January 13, 2015 with the position of Jupiter, Io, Callisto, Ganymede and Europa seen at scale, generated by the Jupiter ViewerTool, PDS Rings Node.

For the seventh observation night, we observed Io with the NaI filter and acquired 37 images in binning 2 of the Jovian system. Figure 6.24 illustrates the position of each Jovian celestial body on the obtained images. Figure 6.25 shows the image processing results performed on the reduced images of January 13, 2015 using the unsharp masking method. Figure 6.26 shows the image processing results performed on the same reduced images using the background subtraction method. Figure 6.27 illustrates the images processing results using the stacking and unsharp masking method. Unfortunately for that night, Io is too close to Europa to notice or not the presence of a jet. For each figure, we zoomed in on Io.

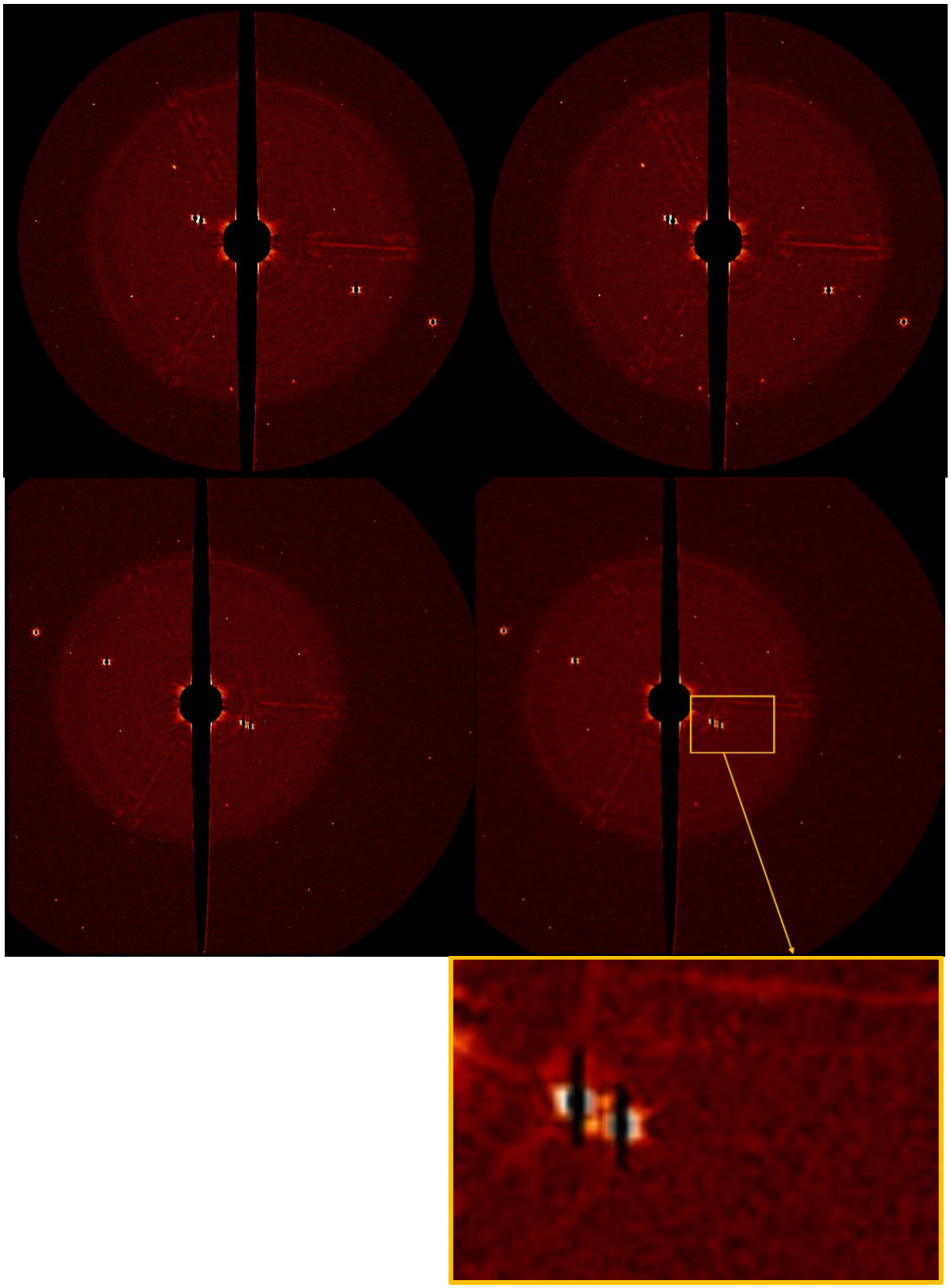

Figure 6.25: Results for four images from January 13, 2015 using the unsharp masking method.

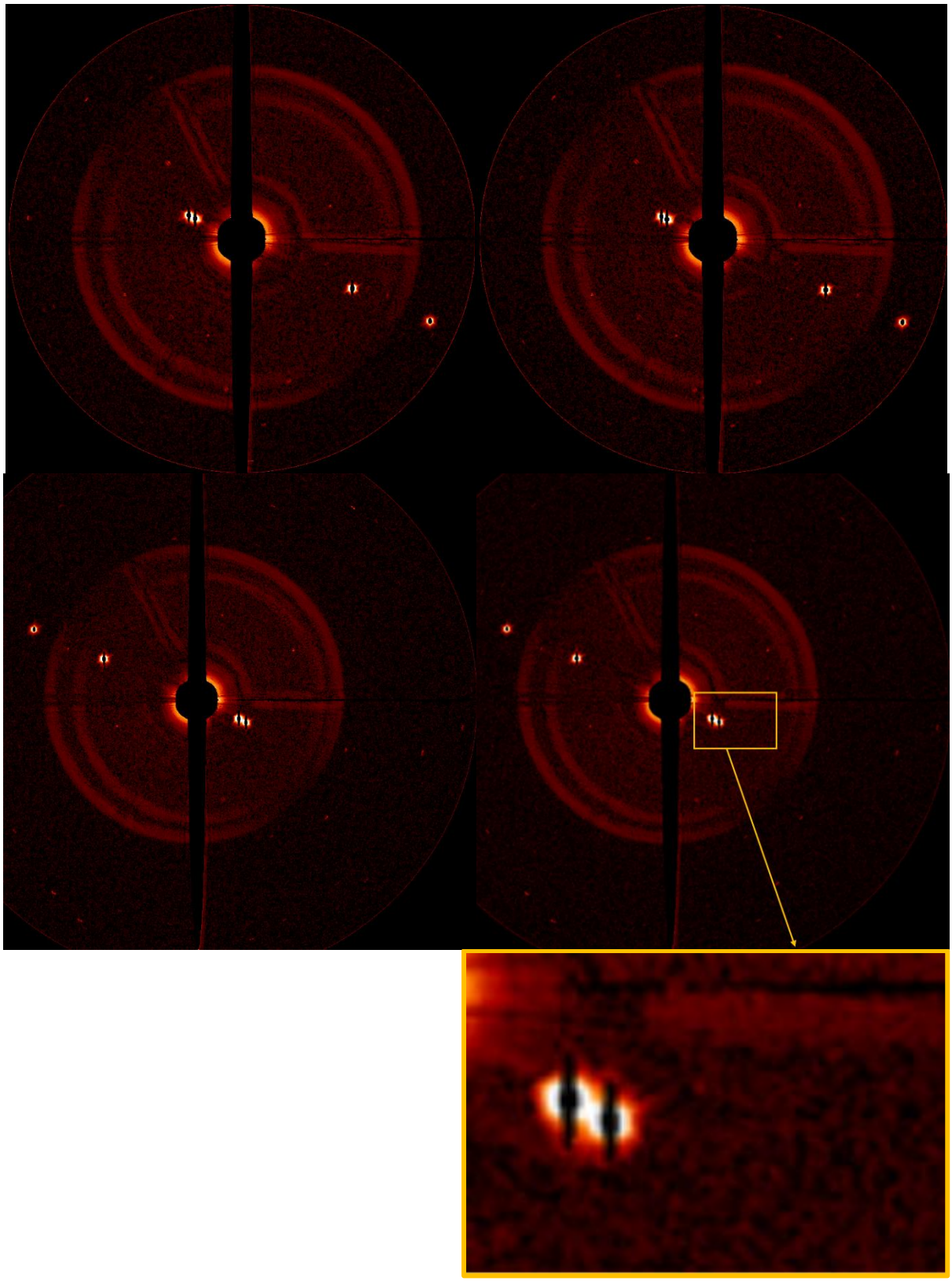

Figure 6.26: Results for four images from January 13, 2015 using the background subtraction method.

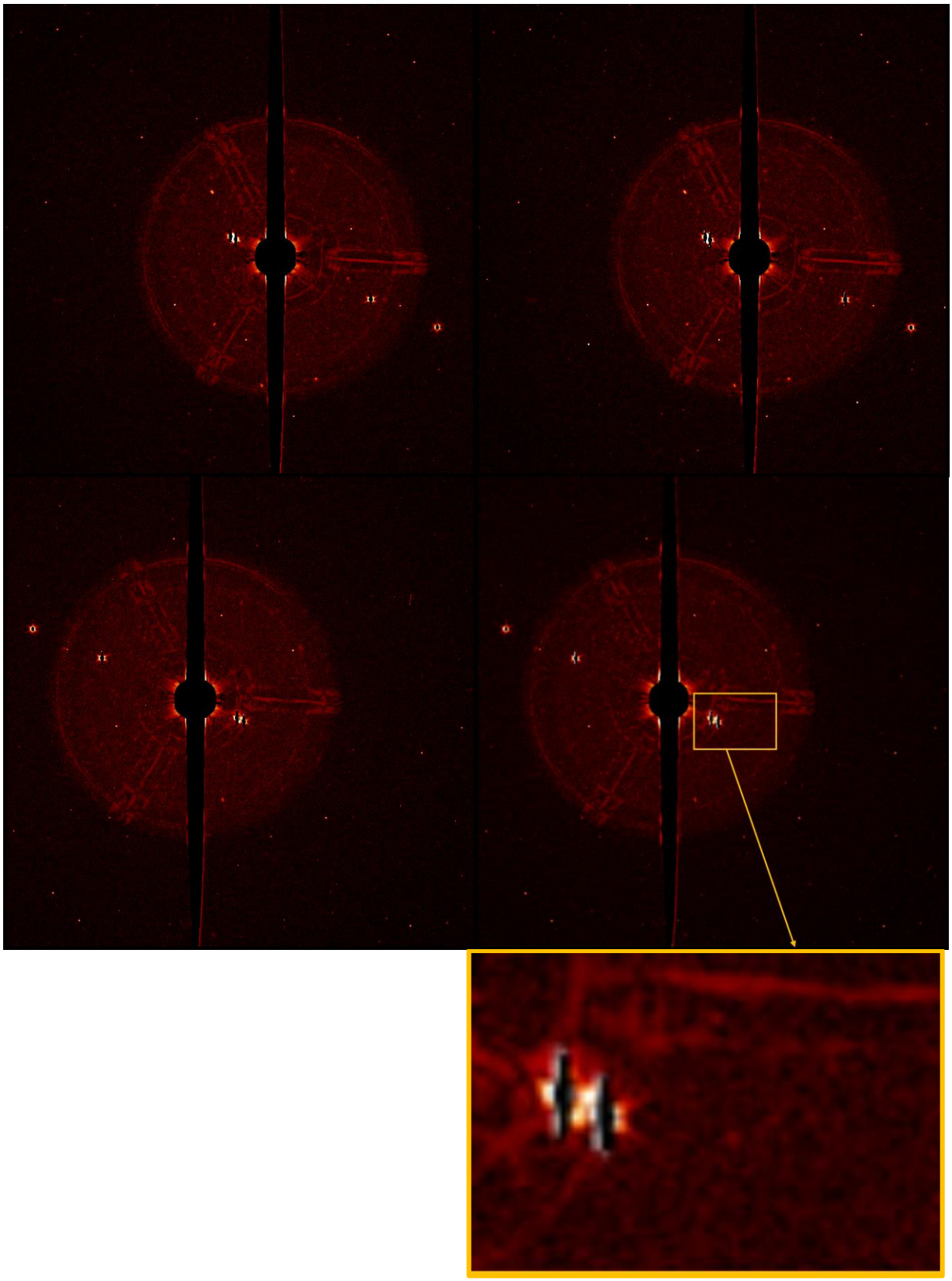

Figure 6.27: Results for images from January 13, 2015 using the stacking and unsharp masking method.

6.1.8 January 20, 2015

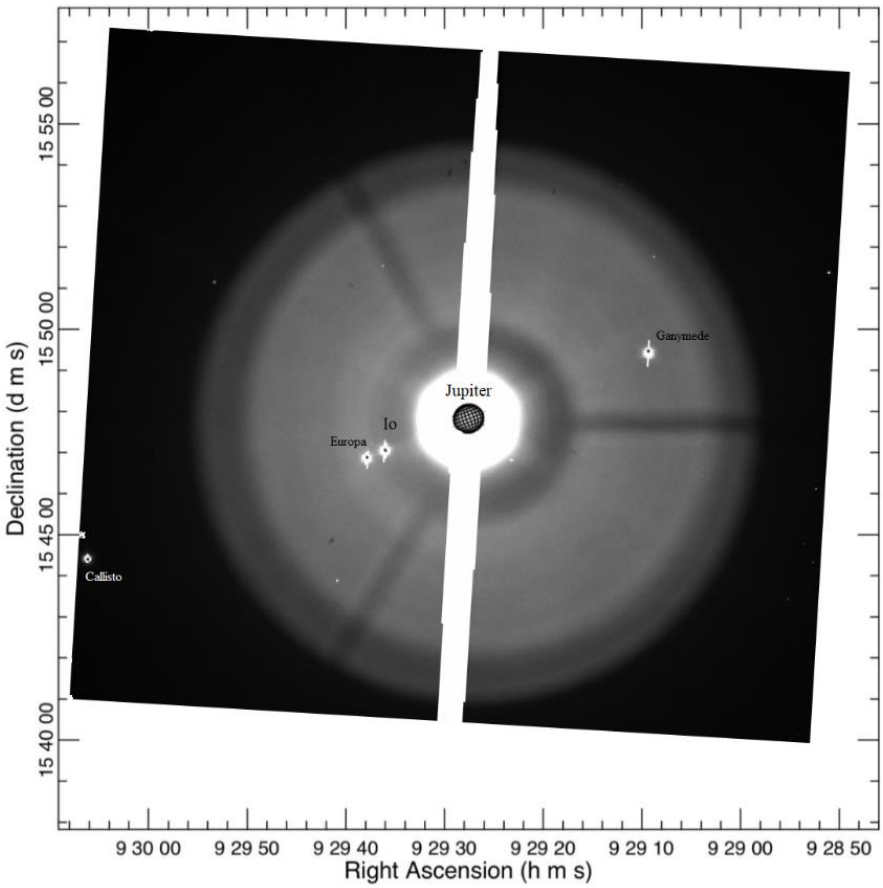

Figure 6.28: Superposition of the image from January 20, 2015 with the position of Jupiter, Io, Callisto, Ganymede and Europa seen at scale, generated by the Jupiter ViewerTool, PDS Rings Node.

For the eighth observation night, we observed Io with the NaI filter and acquired 14 images in binning 2 of the Jovian system. Figure 6.28 illustrates the position of each Jovian celestial body on the images. Figure 6.29 shows the image processing results performed on the reduced images of January 20, 2015 using the unsharp masking method. Figure 6.30 shows the image processing results performed on the same reduced images using the background subtraction method. Figure 6.31 illustrates the images processing results using the stacking and unsharp masking method. Unfortunately for that night, Io is too close to Europa to notice or not the presence of a jet.

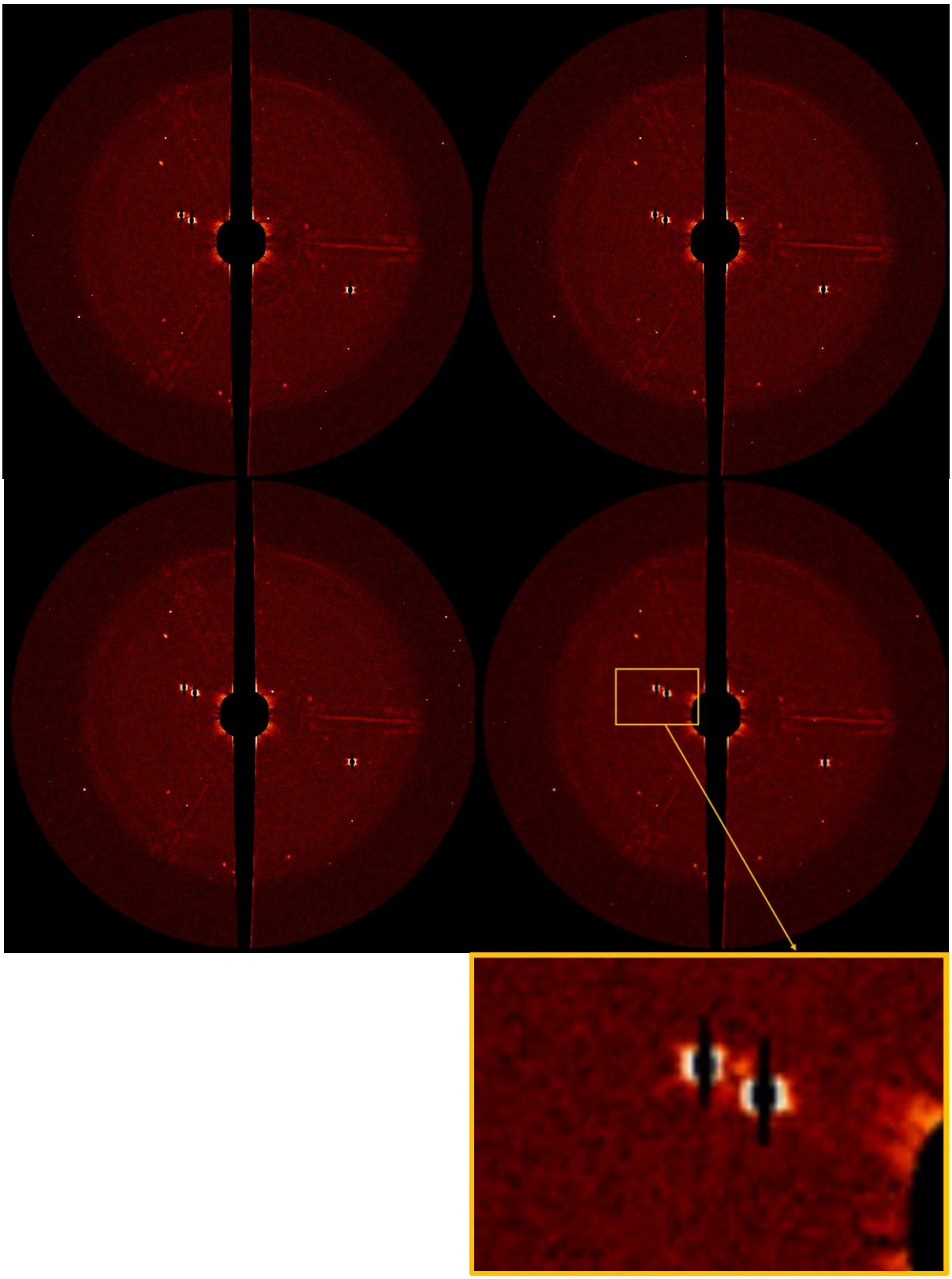

Figure 6.29: Results for four images from January 20, 2015 using the unsharp masking method.

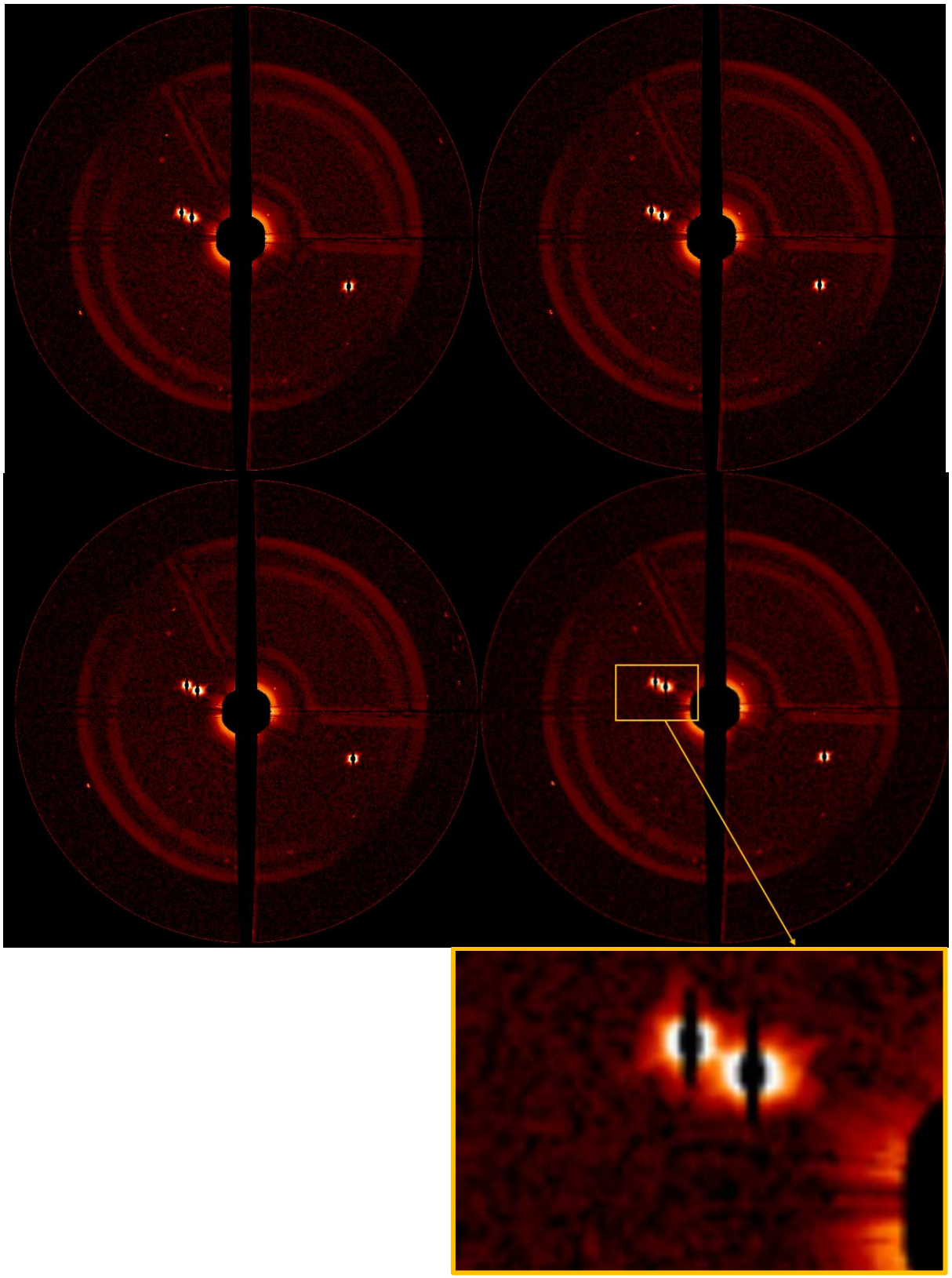

Figure 6.30: Results for four images from January 20, 2015 using the background subtraction method.

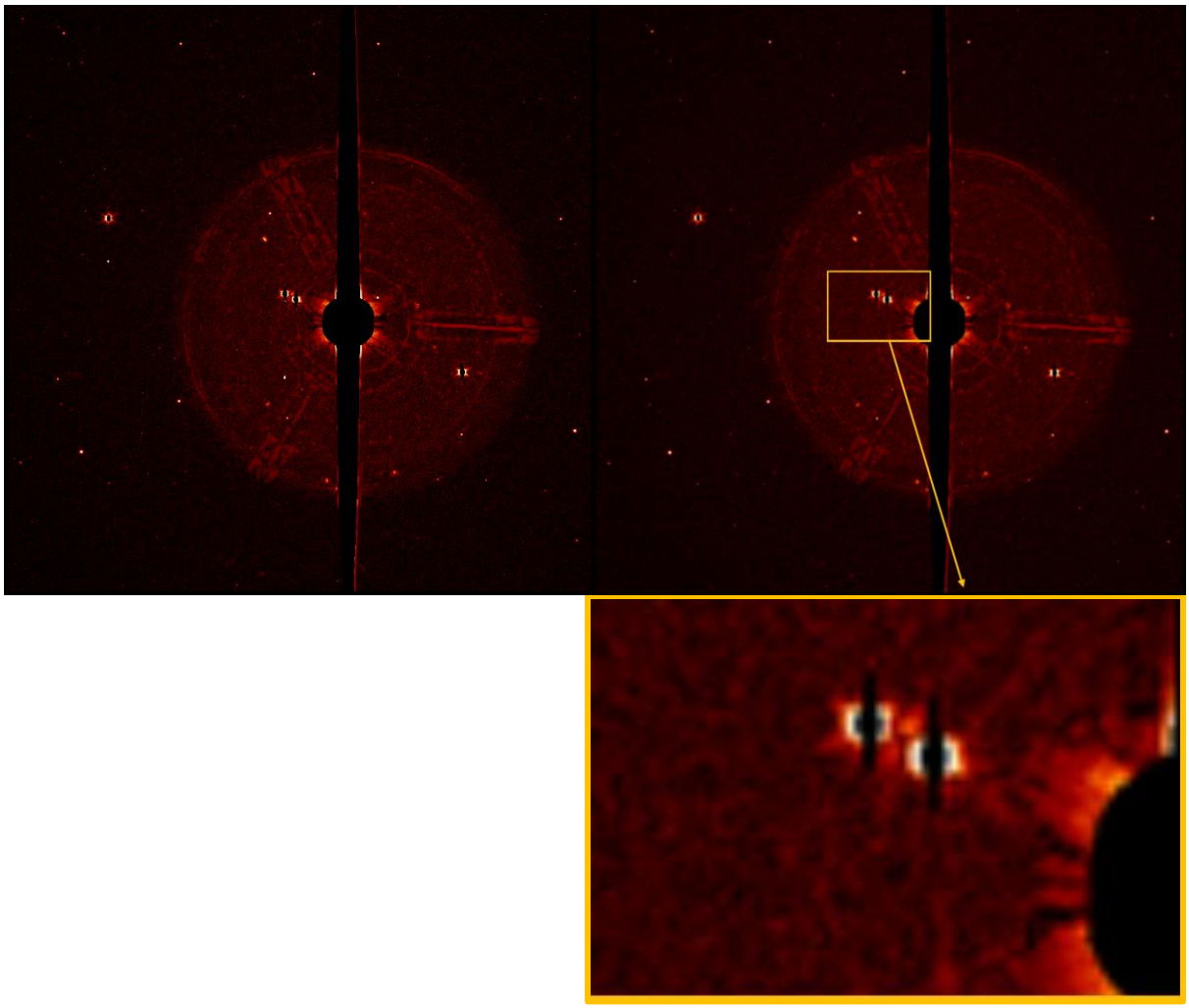

Figure 6.31: Results for images from January 20, 2015 using the stacking and unsharp masking method.

6.1.9 January 23, 2015

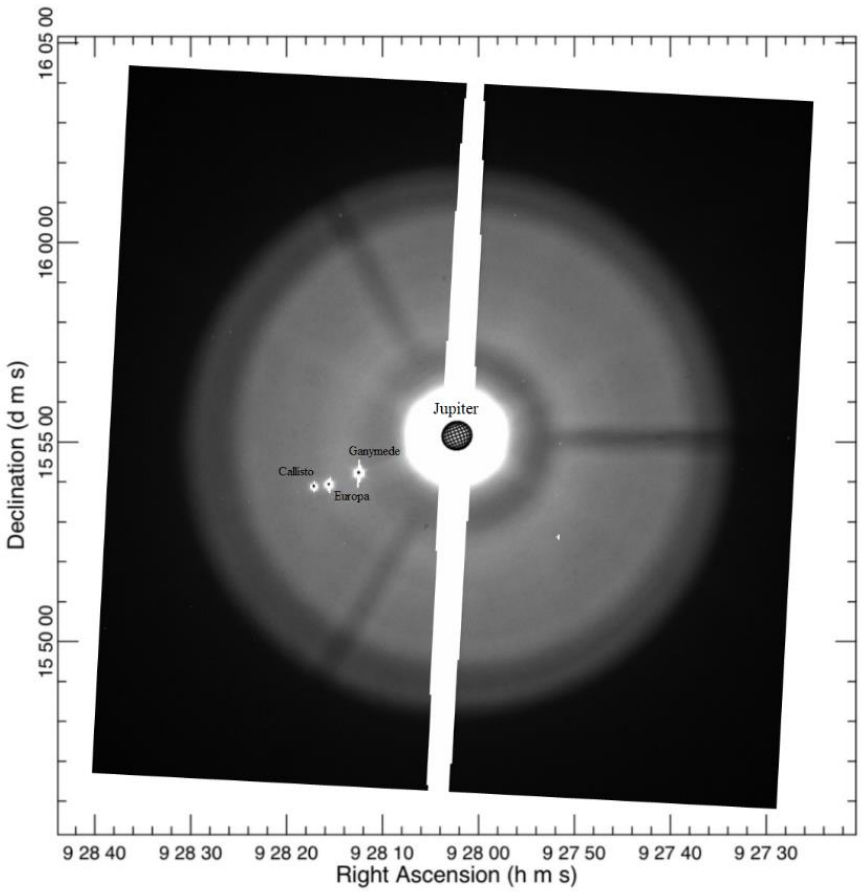

Figure 6.32: Superposition of the image from January 23, 2015 with the position of Jupiter, Callisto, Ganymede and Europa seen at scale, generated by the Jupiter ViewerTool, PDS Rings Node.

For the ninth observation night, we observed Jupiter with the NaI filter and acquired 14 images in binning 2 of the Jovian system. Figure 6.32 illustrates the position of each Jovian celestial body on the images. Unfortunately, Io is not present on the images of the night of January 23, 2015 since the satellite of Jupiter is behind the planet.

6.1.10 January 28, 2015

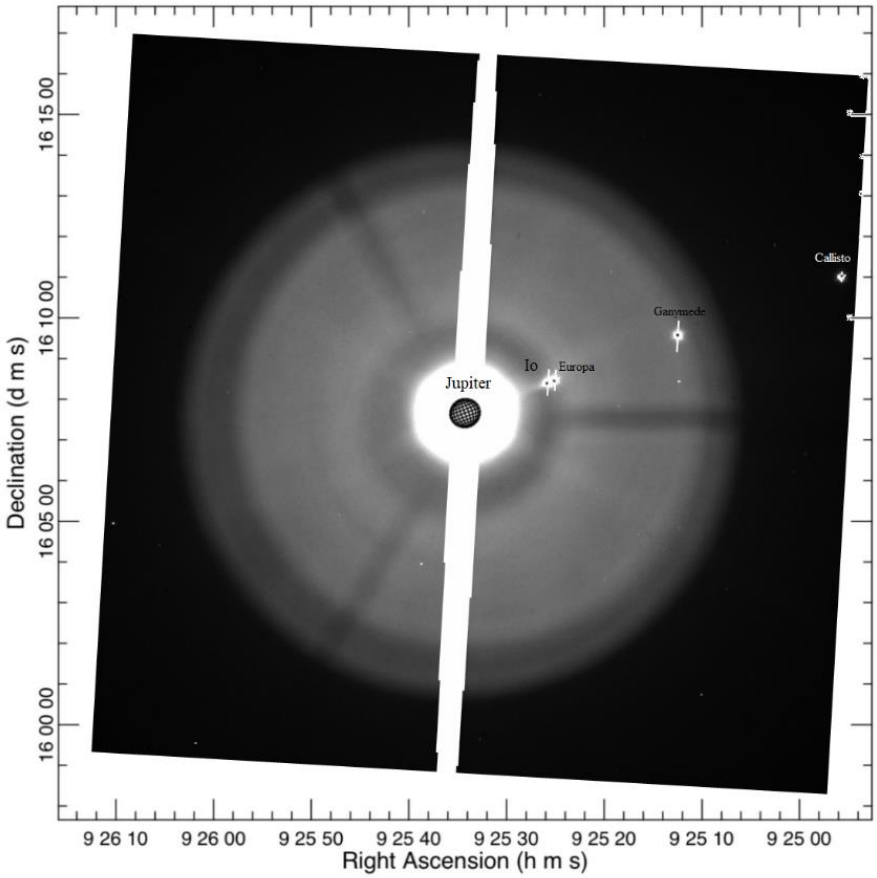

Figure 6.33: Superposition of the image from January 28, 2015 with the position of Jupiter, Io, Callisto, Ganymede and Europa seen at scale, generated by the Jupiter ViewerTool, PDS Rings Node.

For the tenth observation night, we observed Io with the NaI filter and acquired 19 images in binning 2 of the Jovian system. Figure 6.33 illustrates the position of each Jovian celestial body on the images. Figure 6.34 shows the image processing results performed on the reduced images of January 28, 2015 using the unsharp masking method. Figure 6.35 shows the image processing results performed on the same reduced images of January 28, 2015 using the background subtraction method. Figure 6.36 illustrates the images processing results using the stacking and unsharp masking method. For each figure, we zoomed in on Io. Unfortunately for that night, Io is of close of Europa to notice or not the presence of a jet. Although, we observe a possible jet “towards” Jupiter.

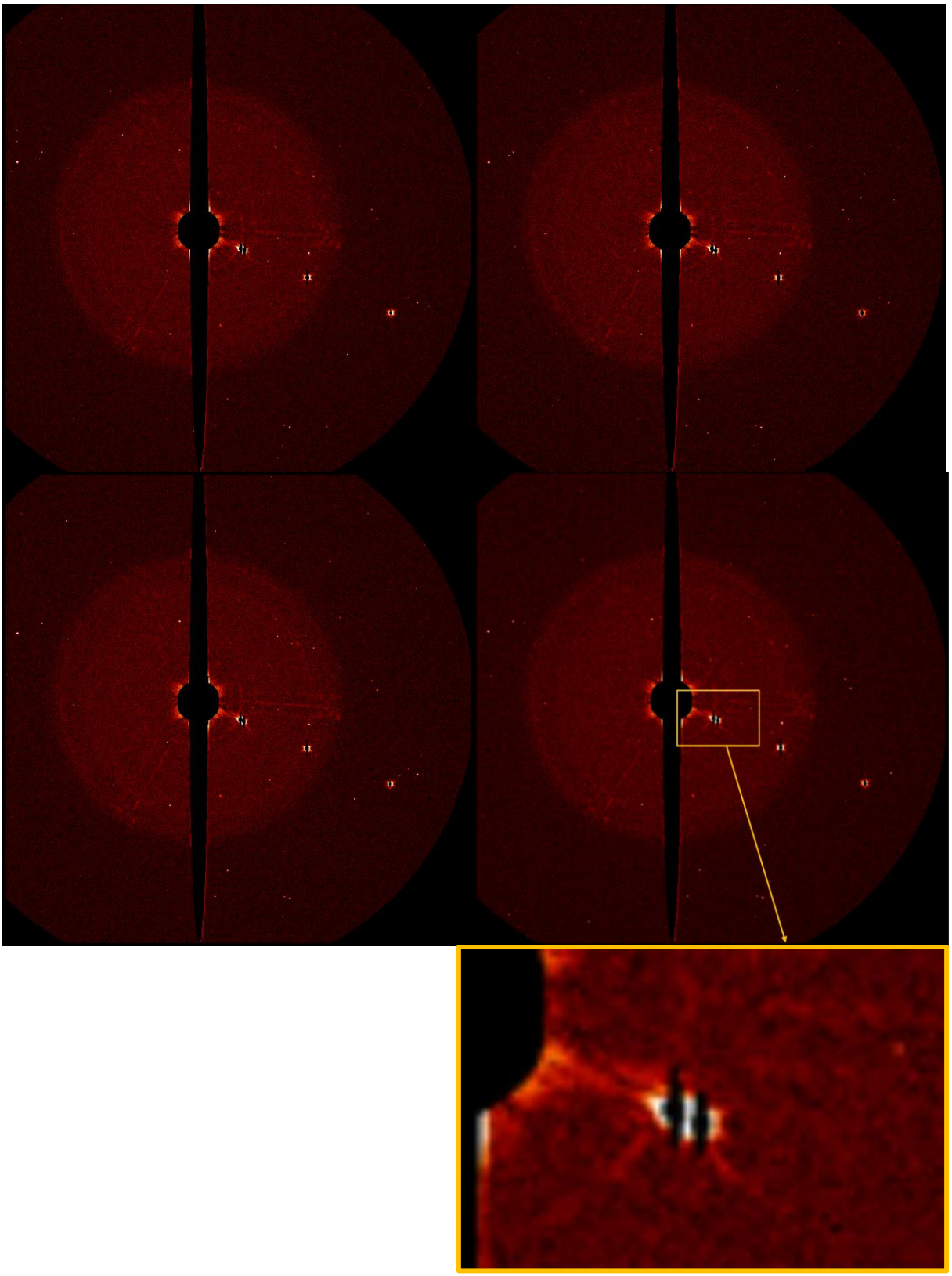

Figure 6.34: Results for four images from January 28, 2015 using the unsharp masking method.

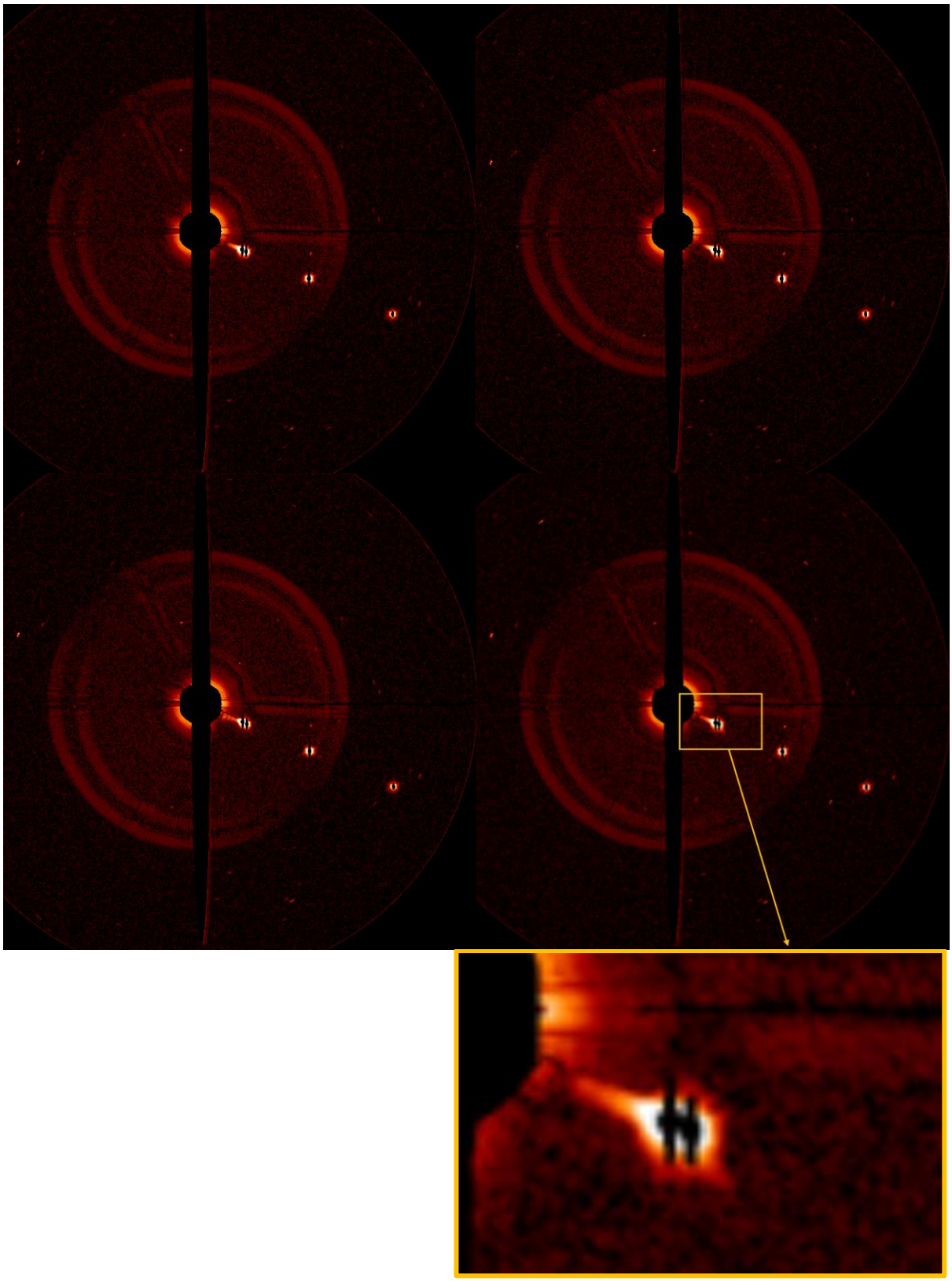

Figure 6.35: Results for four images from January 28, 2015 using the background subtraction method.

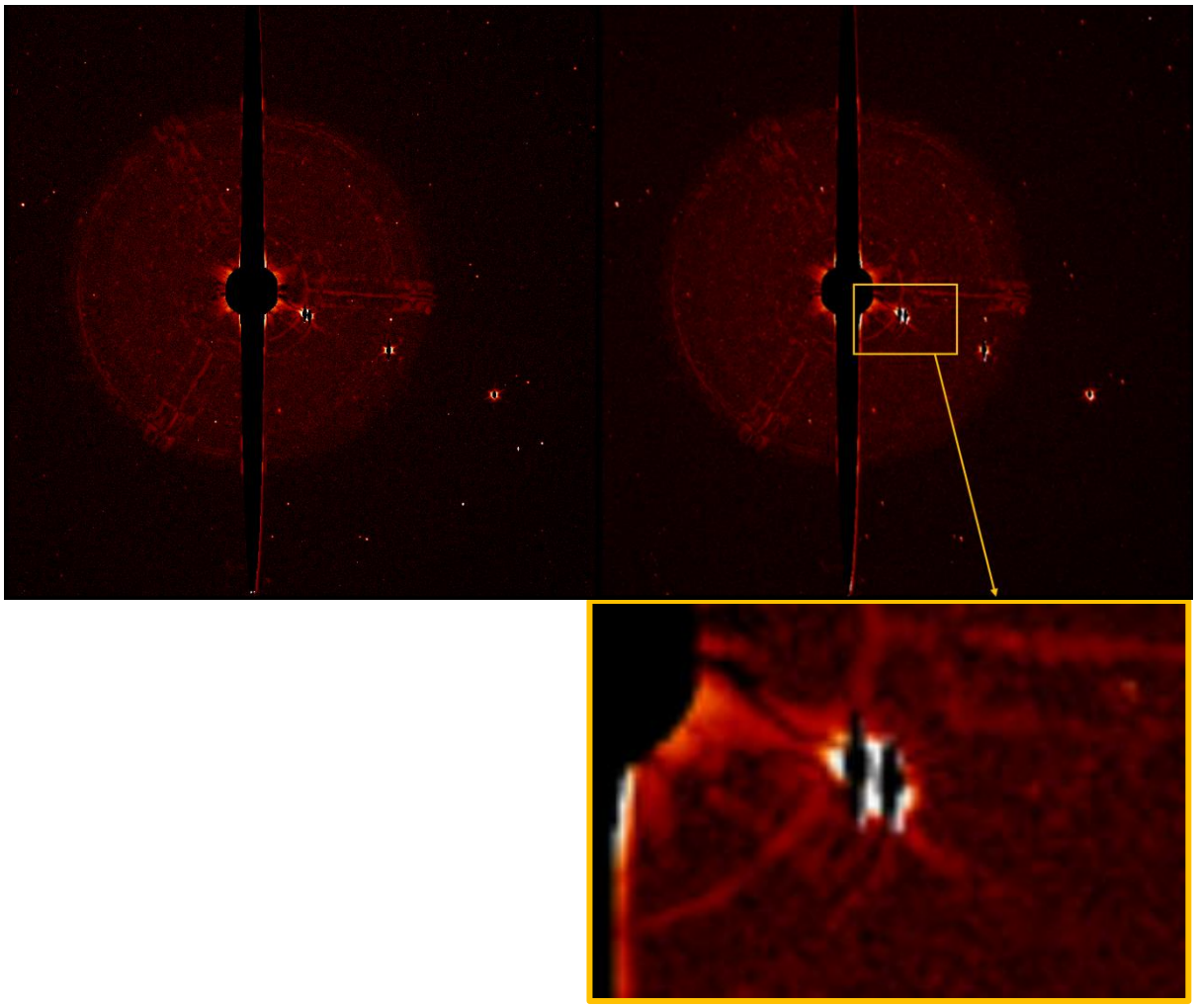

Figure 6.36: Results for images from January 28, 2015 using the stacking and unsharp masking method.

6.1.11 February 1, 2015

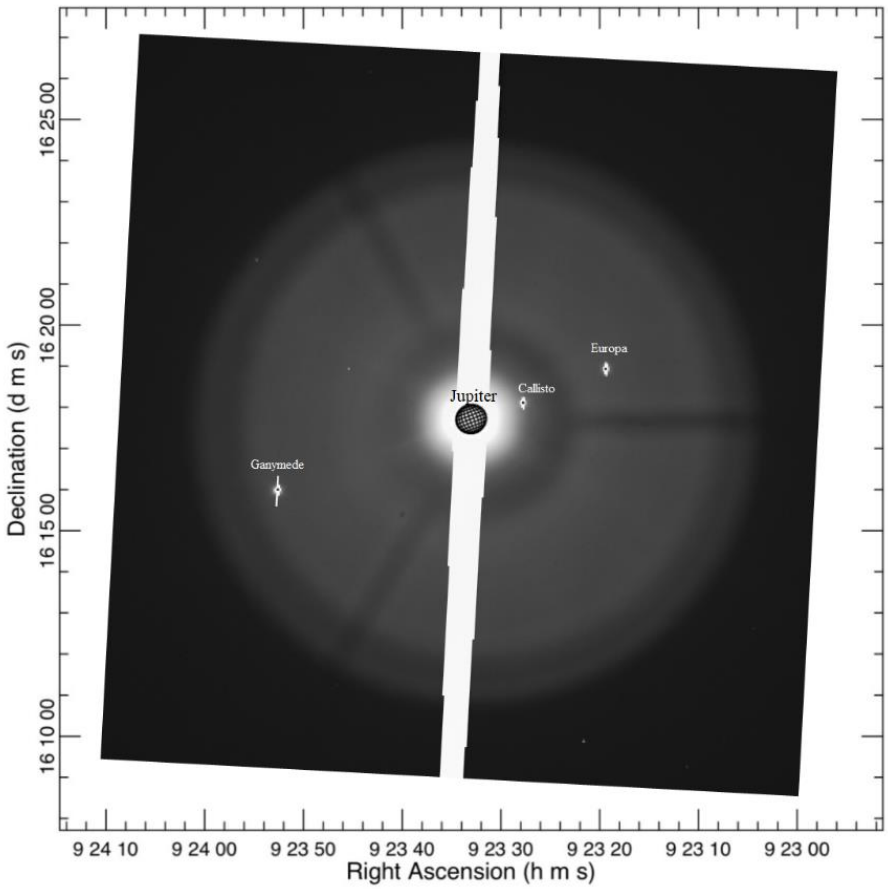

Figure 6.37: Superposition of the image from February 01, 2015 with the position of Jupiter, Callisto, Ganymede and Europa seen at scale, generated by the Jupiter ViewerTool, PDS Rings Node

For the eleventh observation night, we observed Jupiter with the NaI filter and acquired 28 images in binning 2 of the Jovian system. Figure 6.37 illustrates the position of each Jovian celestial body on the images. Unfortunately, Io is not present on the images of the night of February 1, 2015 since the satellite of Jupiter is behind the planet.

6.1.12 February 12, 2015

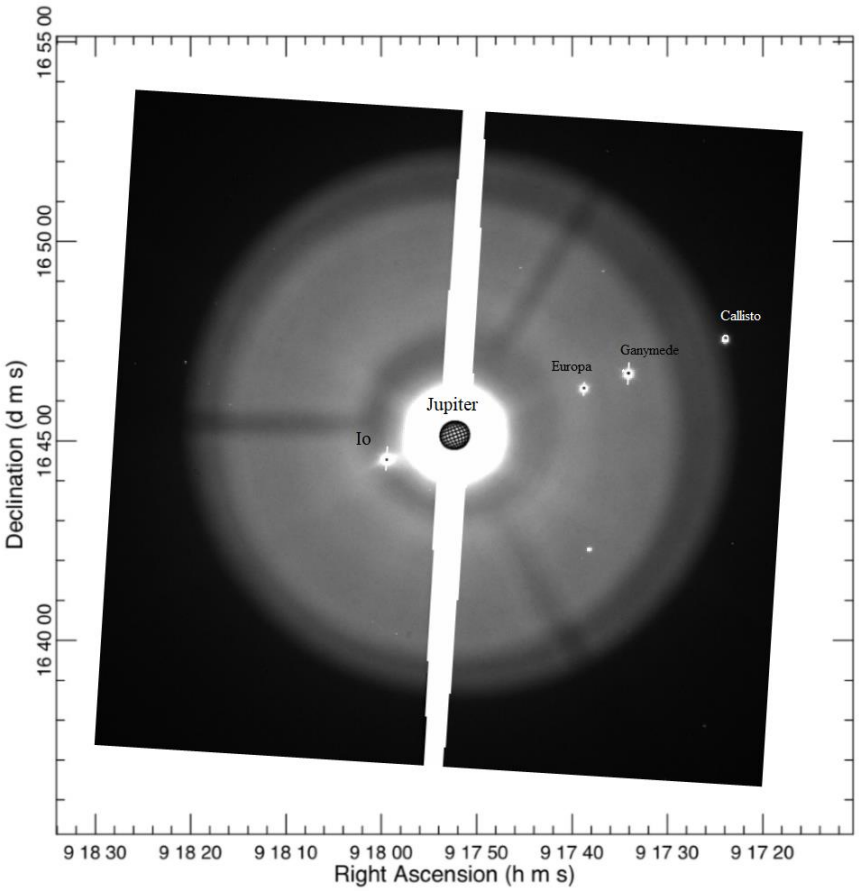

Figure 6.38: Superposition of the image from February 12, 2015 with the position of Jupiter, Io, Callisto, Ganymede and Europa seen at scale, generated by the Jupiter ViewerTool, PDS Rings Node.

For the twelfth observation night, we observed Io with the NaI filter and acquired 15 images in binning 2 of the Jovian system. Figure 6.38 illustrates the position of each Jovian celestial body on the images. Figure 6.39 shows the image processing results performed on the reduced images of February 12, 2015 using the unsharp masking method. Figure 6.40 shows the image processing results performed on the same reduced images of February 12, 2015 using the background subtraction method. Figure 6.41 illustrates the images processing results for the same night using the stacking and unsharp masking method. On these three figures (Fig. 6.39, Fig. 6.40 and Fig. 6.41), we can notice the presence of a jet and for each figure, we zoomed in on Io.

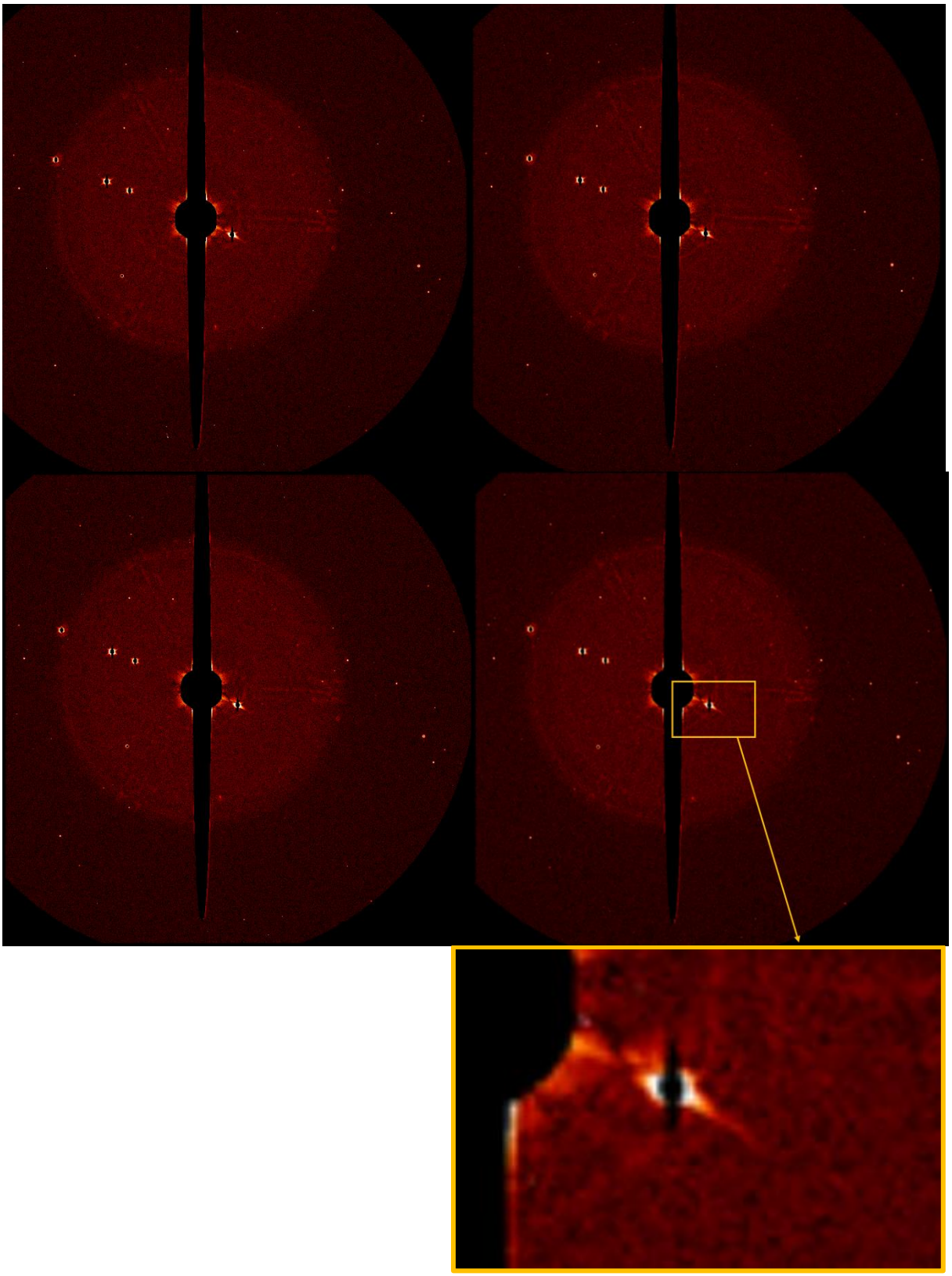

Figure 6.39: Results for four images from February 12, 2015 using the unsharp masking method.

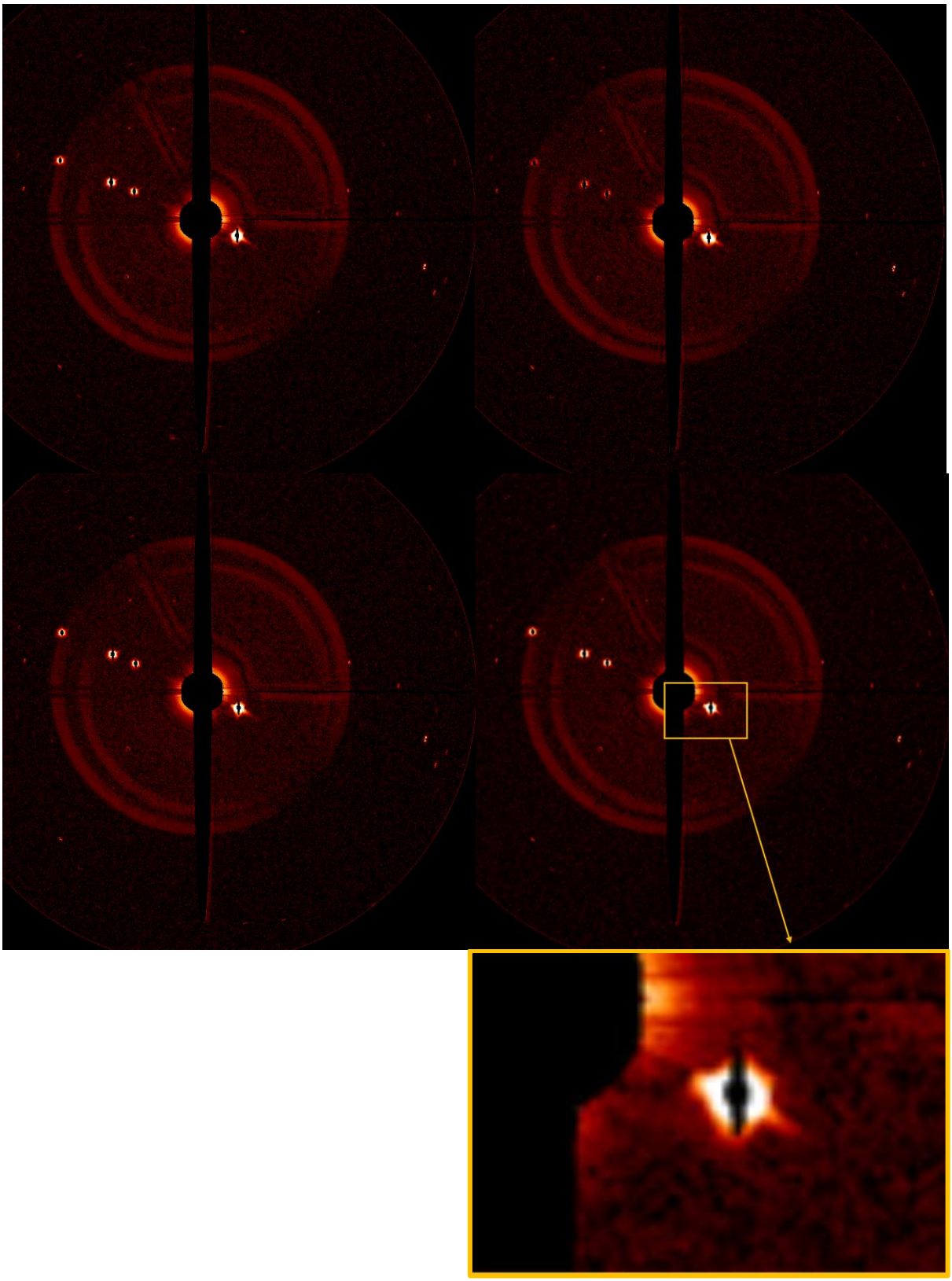

Figure 6.40: Results for four images from February 12, 2015 using the background subtraction method.

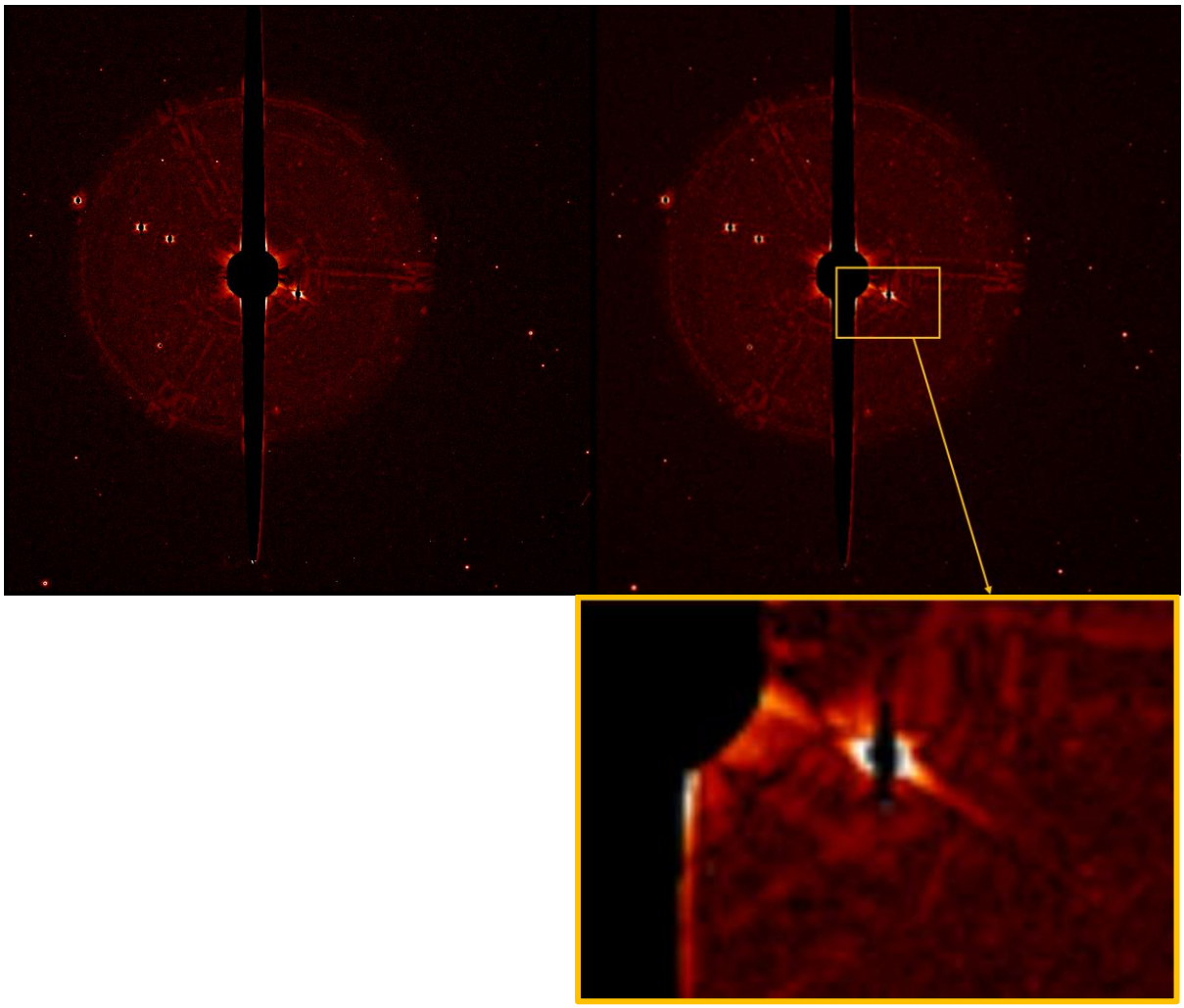

Figure 6.41: Results for images from February 12, 2015 using the stacking and unsharp masking method.

6.1.13 March 29, 2015

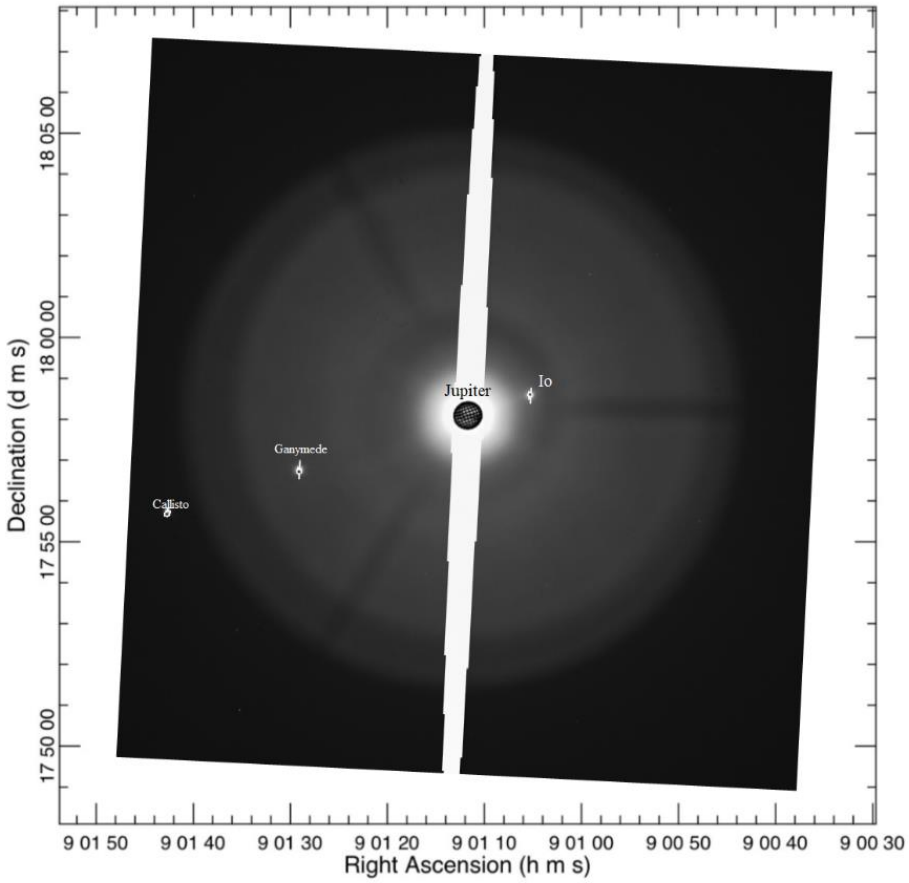

Figure 6.42: Superposition of the image from March 29, 2015 with the position of Jupiter, Io, Callisto and Ganymede seen at scale, generated by the Jupiter ViewerTool, PDS Rings Node.

For the thirteenth observation night, we observed Io with the NaI filter and acquired 16 images in binning 2 of the Jovian system. Figure 6.42 illustrates the position of each Jovian celestial body on the images. Figure 6.43 shows the image processing results performed on the reduced images of March 29, 2015 using the unsharp masking method. Figure 6.44 shows the image processing results performed on the same images using the background subtraction method. Figure 6.45 illustrates the images processing results for the night using the stacking and unsharp masking method. For each figure, we zoomed in on Io. We do not detect any jet for that observation night.

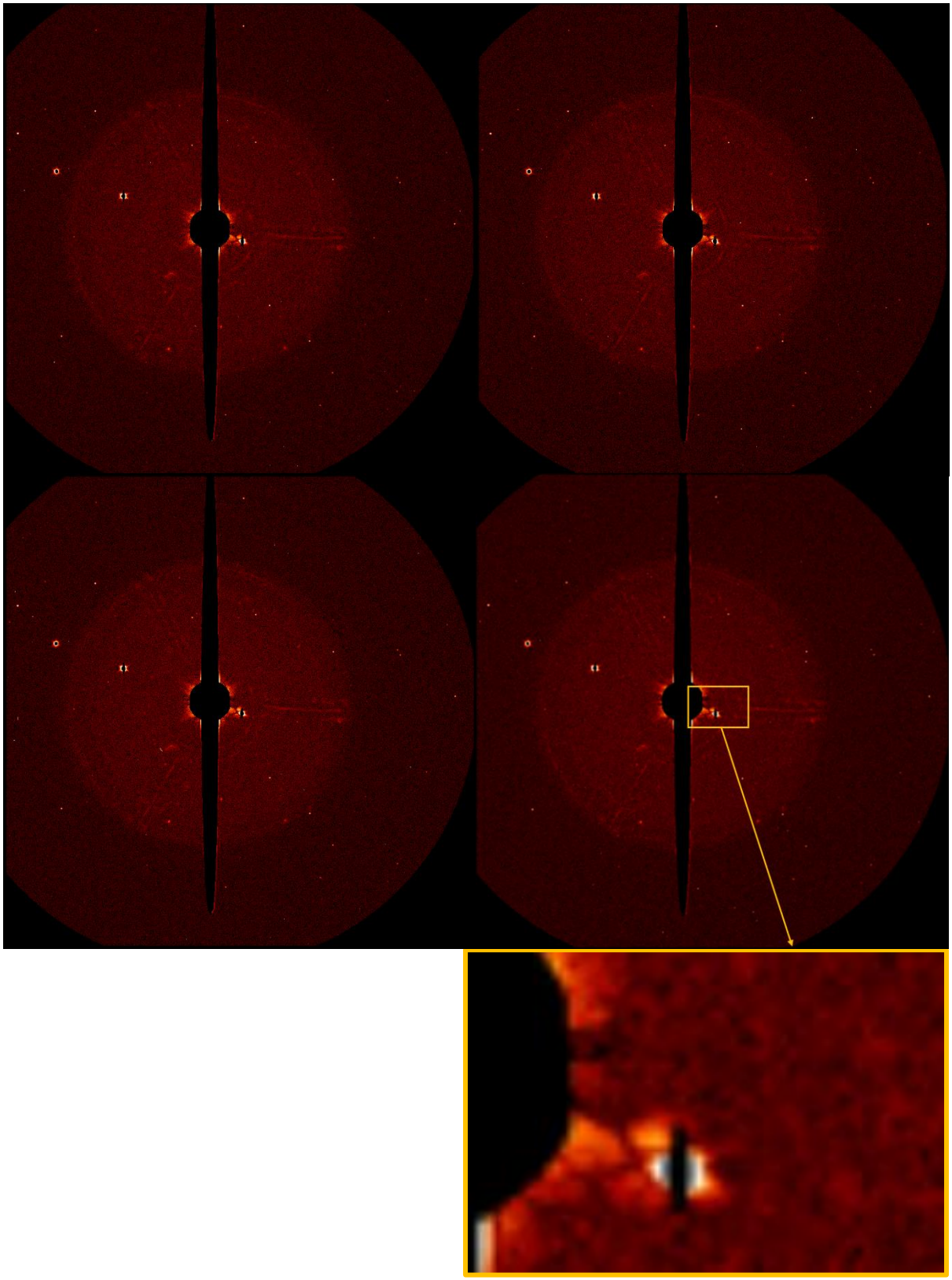

Figure 6.43: Results for four images from March 29, 2015 using the unsharp masking method.

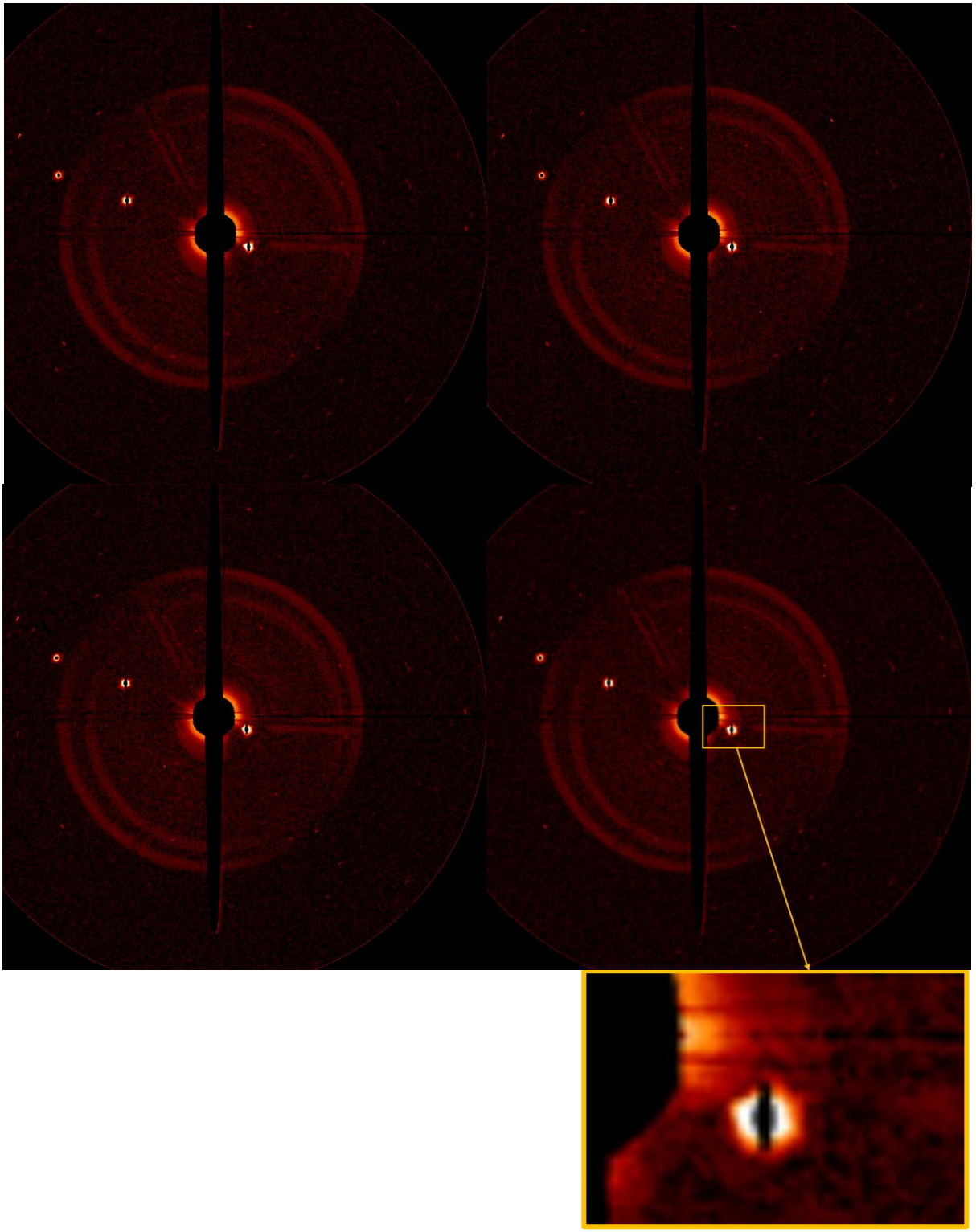

Figure 6.44: Results for four images from March 29, 2015 using the background subtraction method.

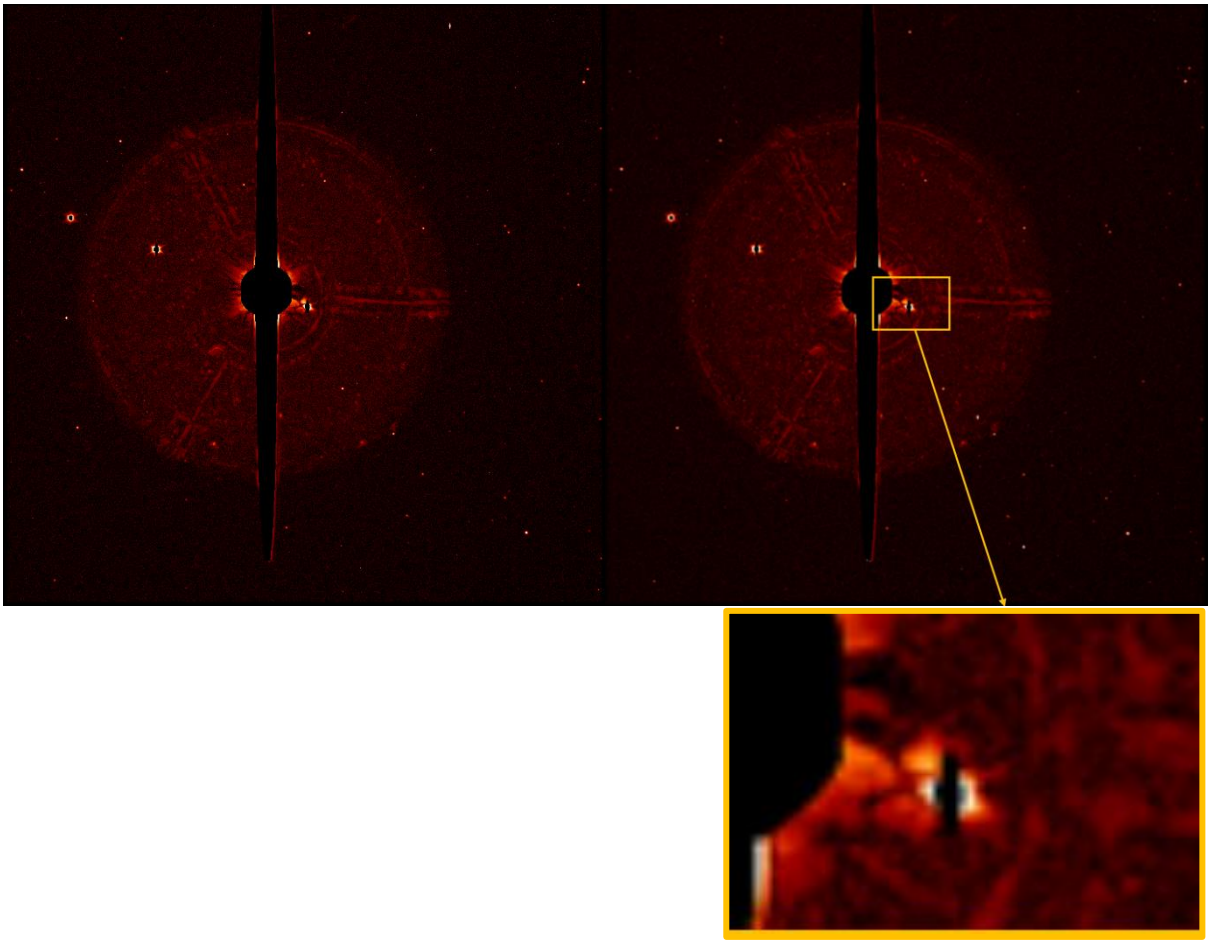

Figure 6.45: Results for images from March 29, 2015 using the stacking and unsharp masking method.

6.1.14 March 30, 2015

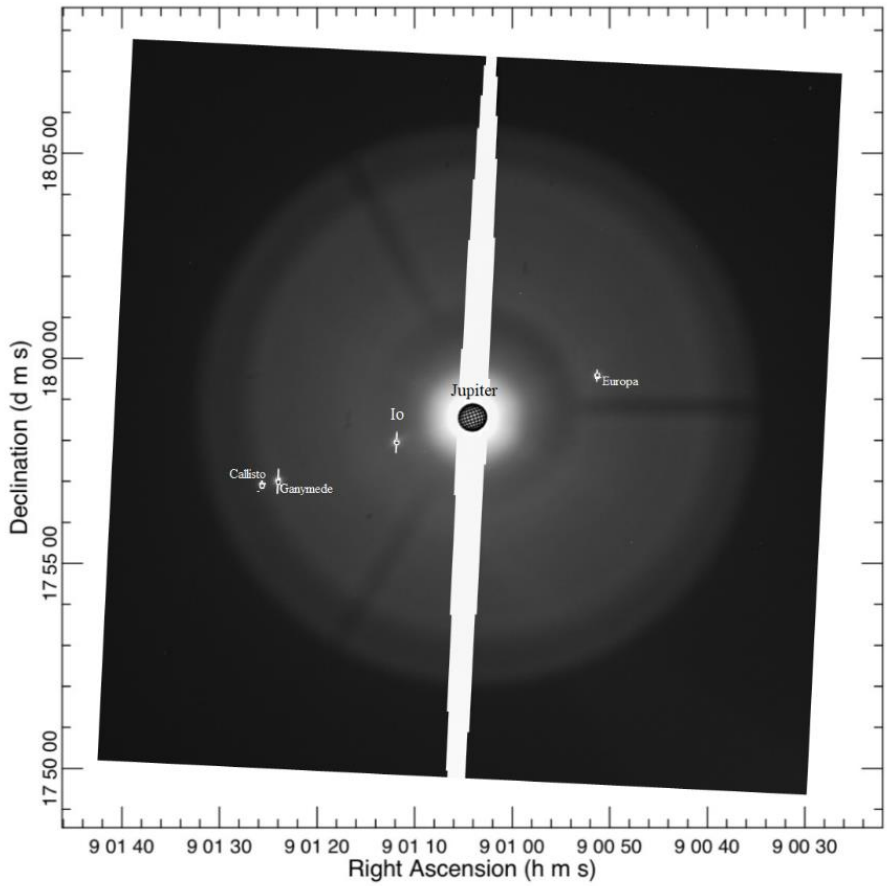

Figure 6.46: Superposition of the image from March 30, 2015 with the position of Jupiter, Io, Callisto, Ganymede and Europa seen at scale, generated by the Jupiter ViewerTool, PDS Rings Node.

For the fourteenth observation night, we observed Io with the NaI filter and acquired 26 images in binning 2 of the Jovian system. Figure 6.46 illustrates the position of each Jovian celestial body on the images. Figure 6.47 shows the image processing results performed on the reduced images of March 30, 2015 using the unsharp masking method. Figure 6.48 shows the image processing results performed on the same reduced images using the background subtraction method. Figure 6.49 illustrates the images processing results using the stacking and unsharp masking method. For each figure, we zoomed in on Io. We do not detect any jet for that night.

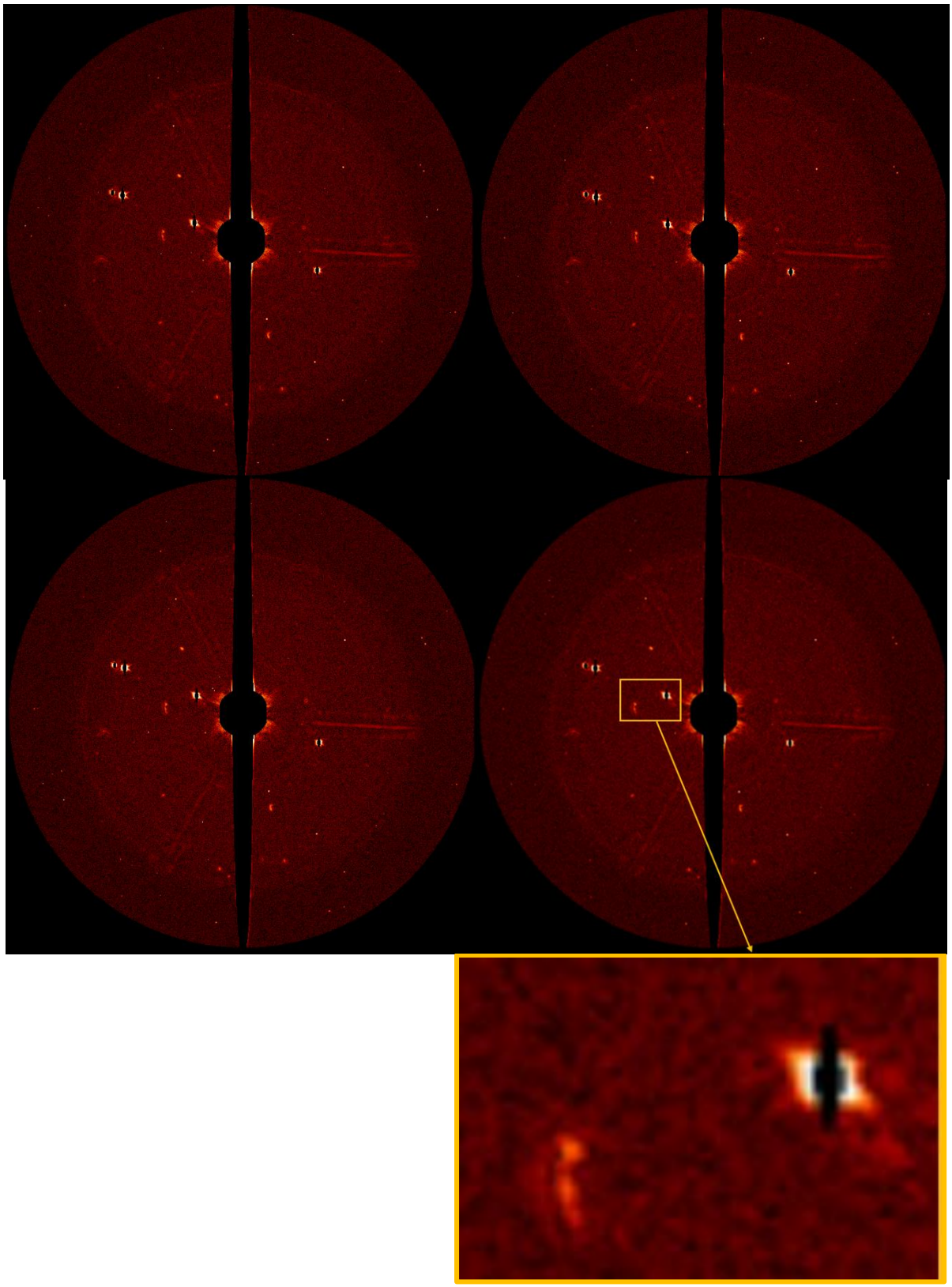

Figure 6.47: Results for four images from March 30, 2015 using the unsharp masking method.

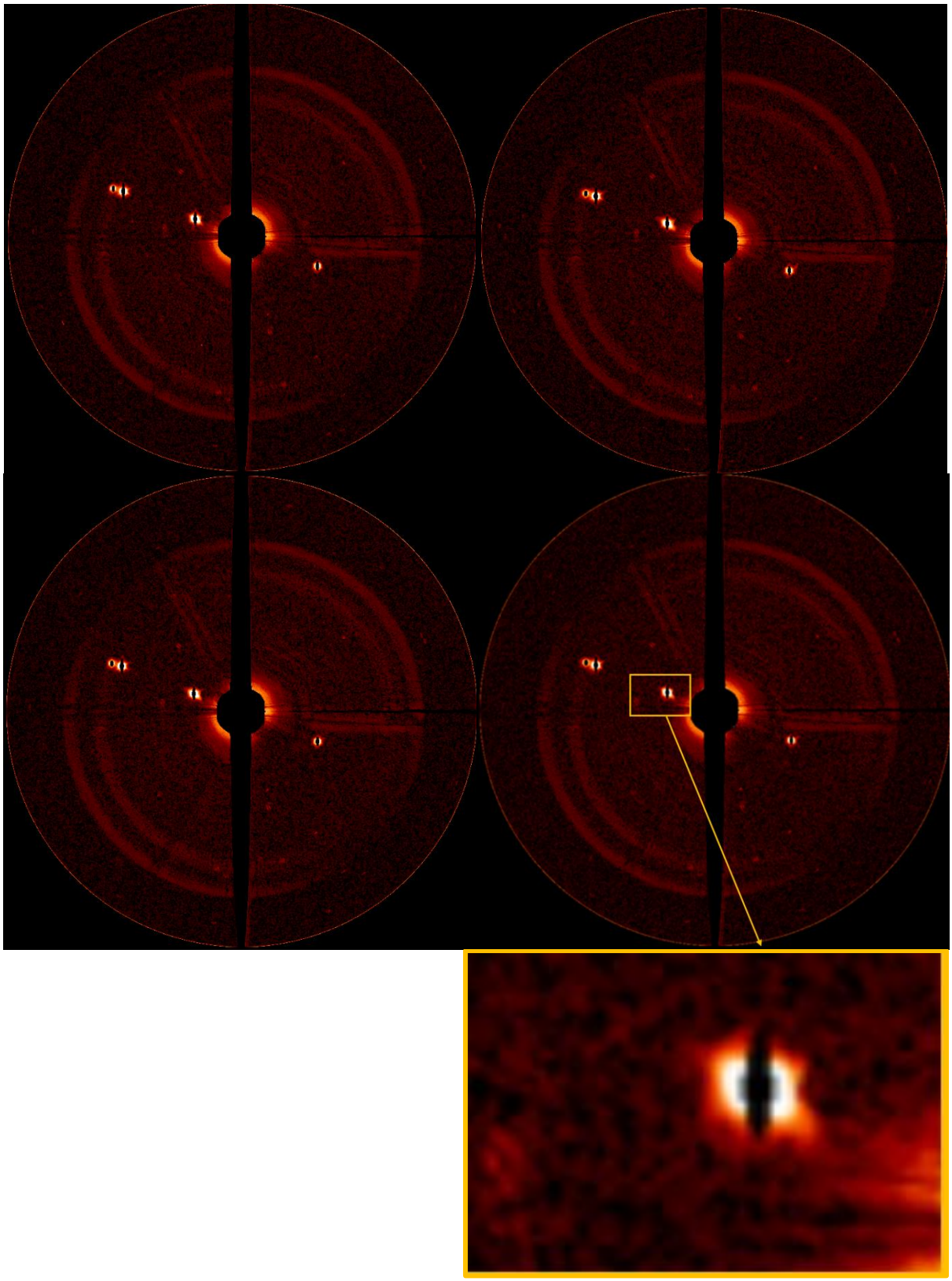

Figure 6.48: Results for four images from March 30, 2015 using the background subtraction method.

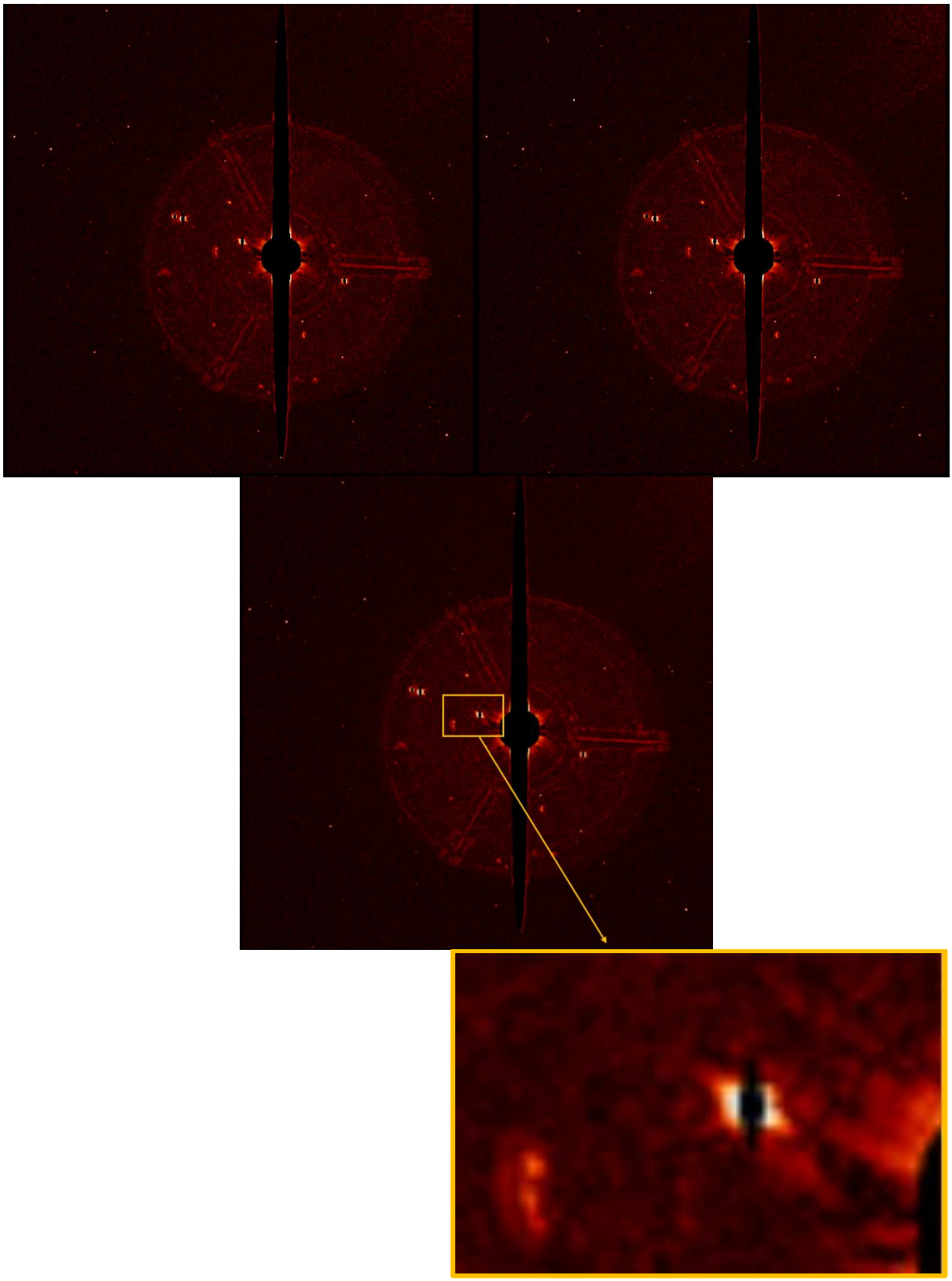

Figure 6.49: Results for images from March 30, 2015 using the stacking and unsharp masking method.

6.1.15 March 31, 2015

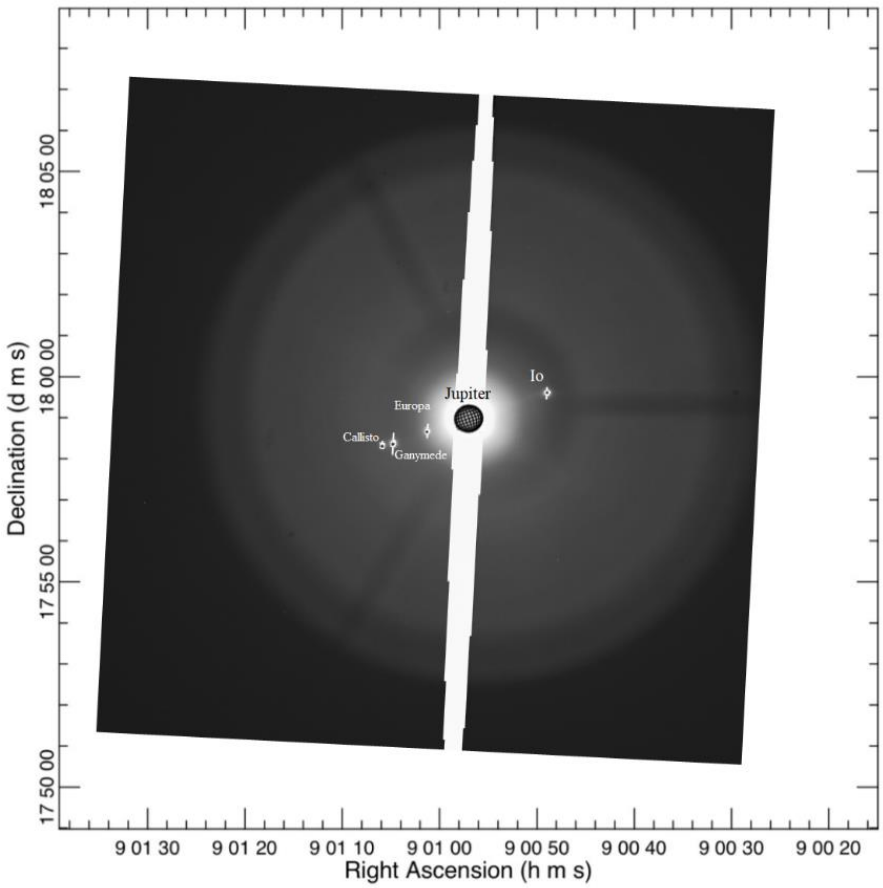

Figure 6.50: Superposition of the image from March 31, 2015 with the position of Jupiter, Io, Callisto, Ganymede and Europa seen at scale, generated by the Jupiter ViewerTool, PDS Rings Node.

For the fifteenth observation night, we observed Io with the NaI filter and acquired 11 images in binning 2 of the Jovian system. Figure 6.50 illustrates the position of each Jovian celestial body on the images. Figure 6.51 shows the image processing results performed on the reduced images of March 31, 2015 using the unsharp masking method. Figure 6.52 shows the image processing results performed on the same images using the background subtraction method. Figure 6.53 illustrates the images processing results using the stacking and unsharp masking method. On these three figures (Fig. 6.51, Fig. 6.52 and Fig. 6.53), we can notice the presence of a jet. For each figure, we zoomed in on Io.

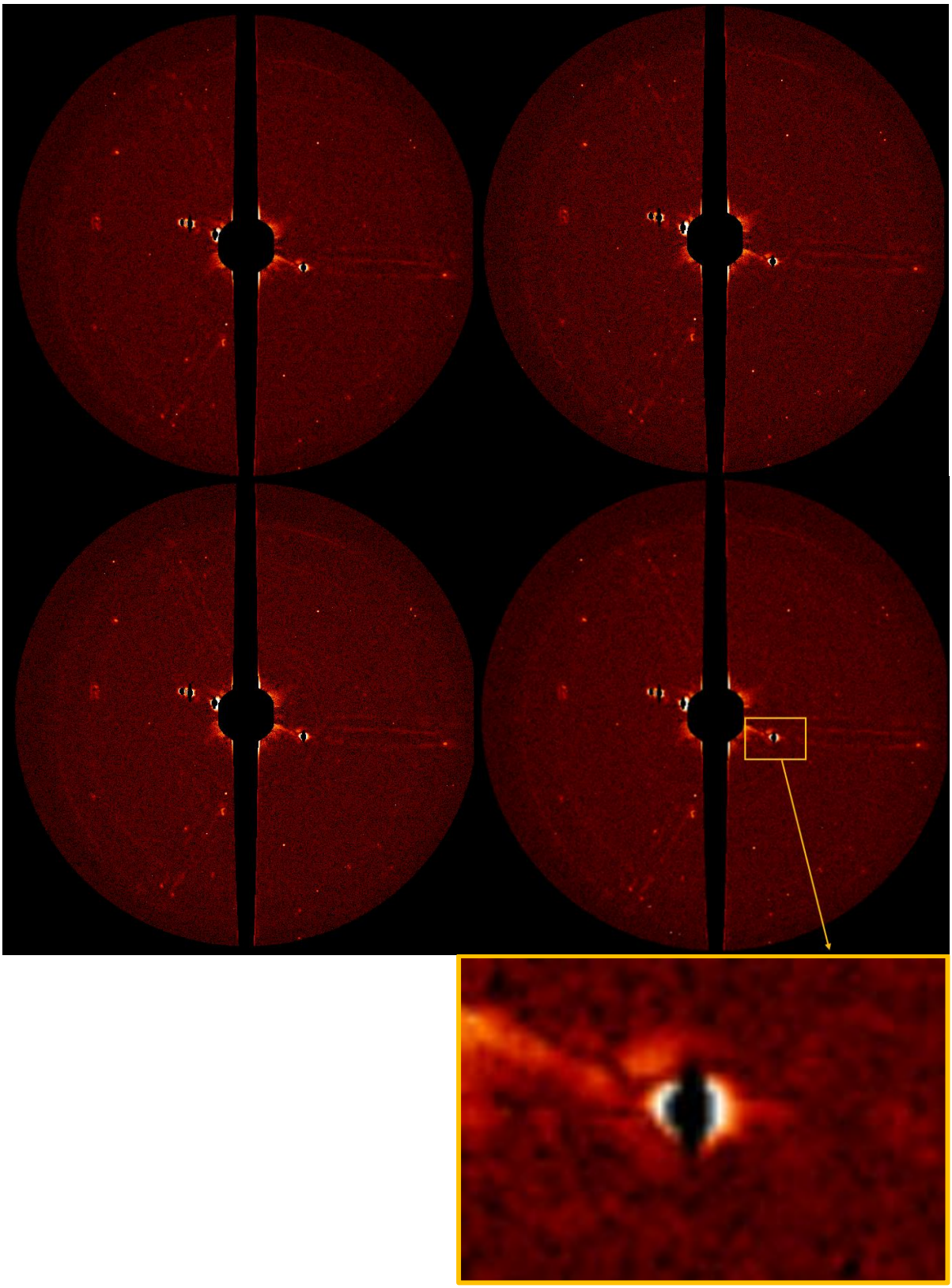

Figure 6.51: Results for four images from March 31, 2015 using the unsharp masking method.

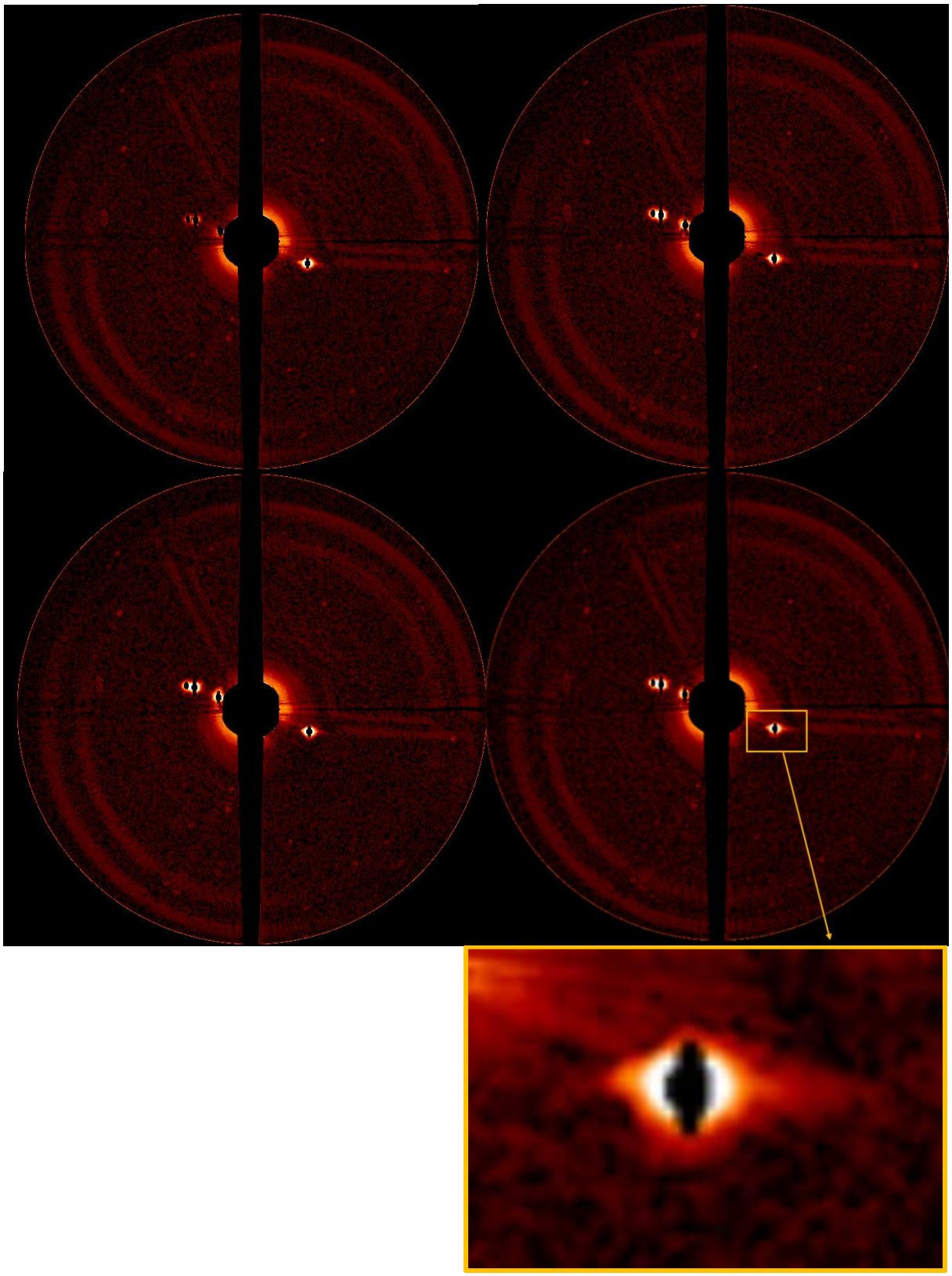

Figure 6.52: Results for four images from March 31, 2015 using the background subtraction method.

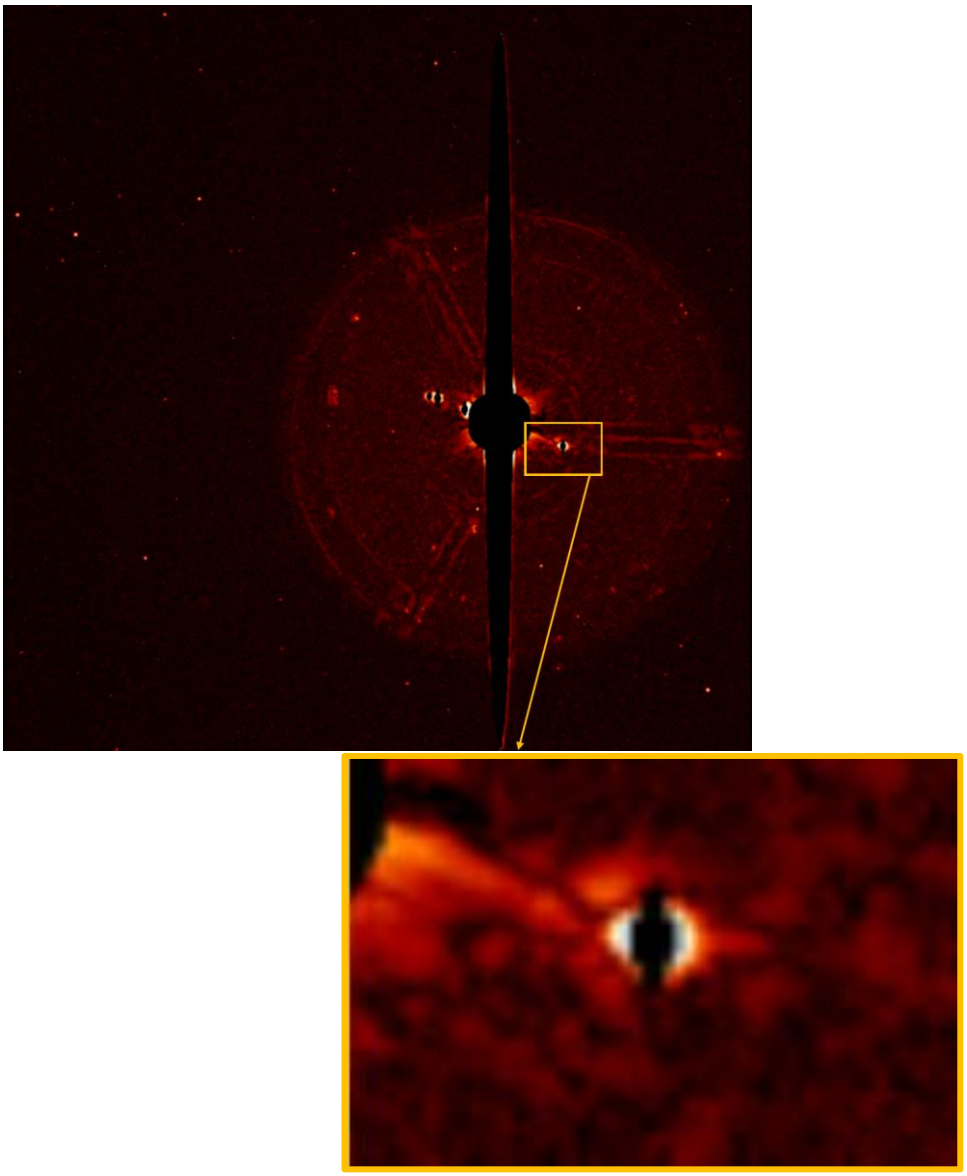

Figure 6.53: Results for images from March 31, 2015 using the stacking and unsharp masking method.

6.2 The rotational gradient method

6.2.1 The rotational gradient method centered on Jupiter

The rotational gradient method centered on Jupiter is used on our calibrated images. We used a rotational shift of 3 degrees on the images. Figure 6.54 shows the results for each observation nights using this method with IDL.

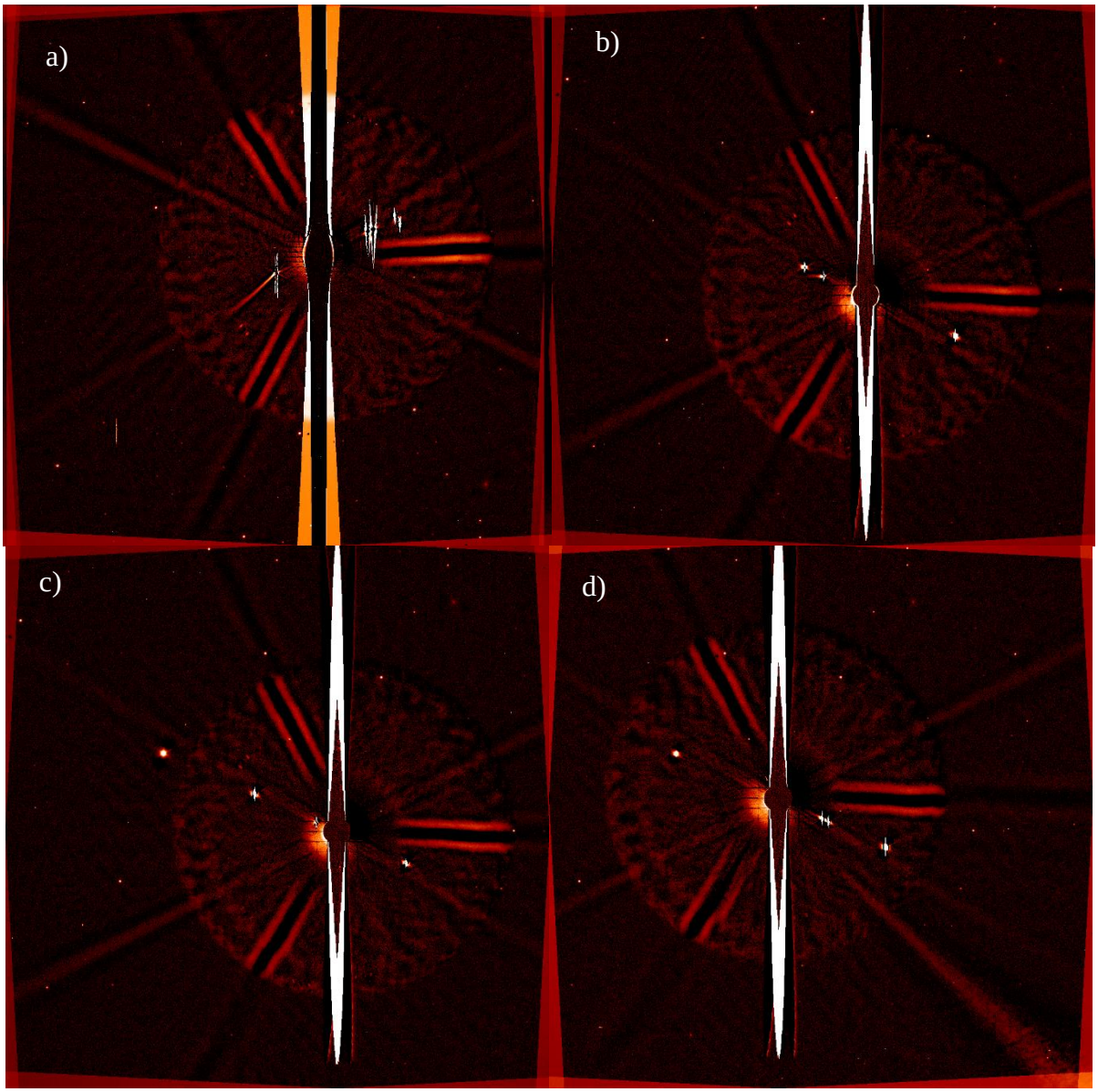

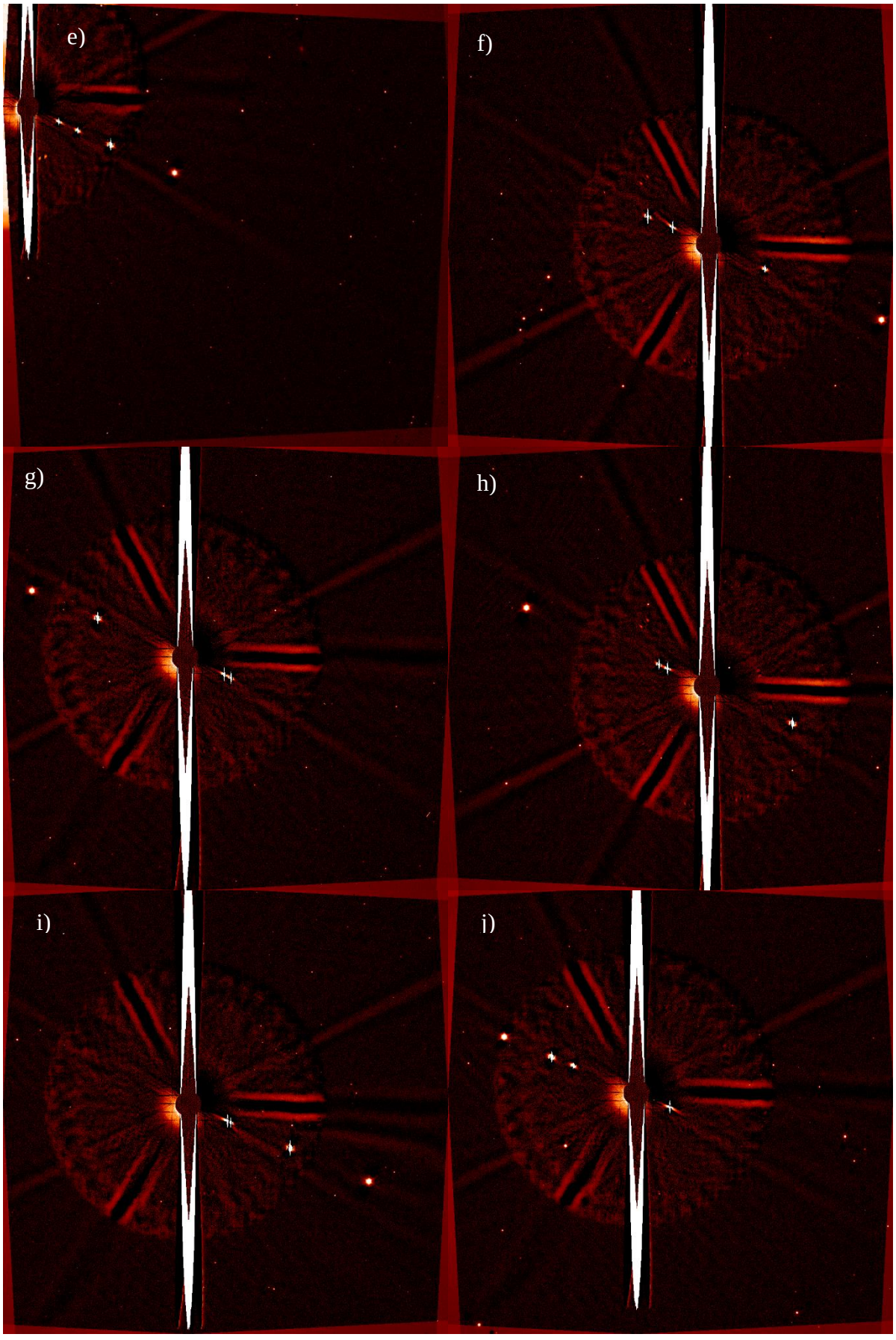
e)
f)
g)
h)
i)
j)

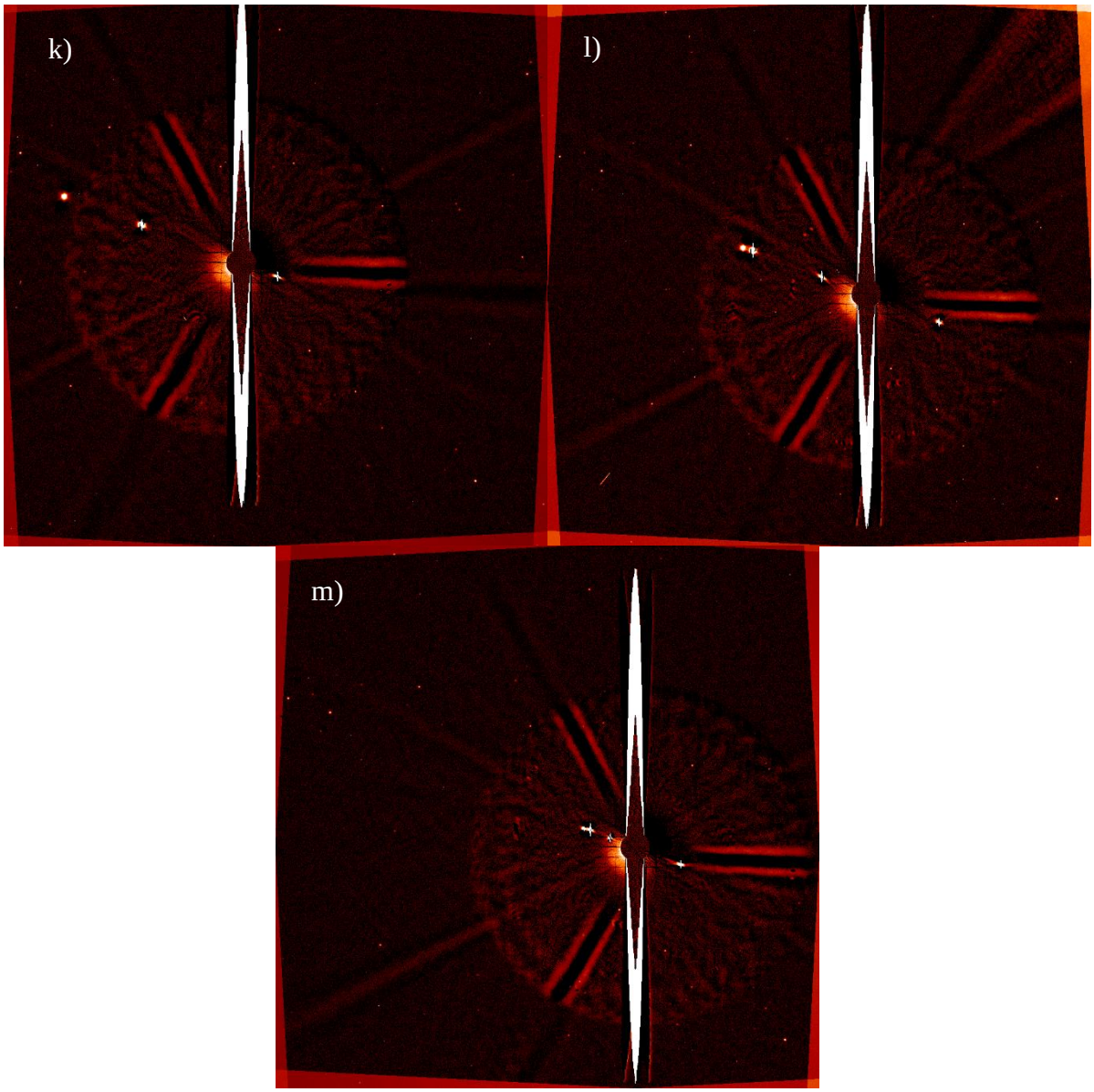

Figure 6.54 : The result of the rotational gradient method centered on Jupiter for the image from a) 2014/12/04, b) 2014/12/06, c) 2014/12/08, d) 2014/12/12, e) 2014/12/19, f) 2015/01/11, g) 2015/01/13, h) 2015/01/20, i) 2015/01/28, j) 2015/02/12, k) 2015/03/29, l) 2015/03/30, m) 2015/03/31.

6.2.2 The rotational gradient method centered on Io

The rotational gradient method is a method used to emphasize or not the presence of a sodium jet on our calibrated images when centered on Io. As explained in the section 5.4, this method is subjective: a too important value of the dα can make appear false details or restore these details with a bad morphology and a too low value of the dα cannot show the low-contrast structures. Therefore, we experiment with different values to best reveal what we want to observe. This is the reason why, for this method and for emphasizing the presence of the jets,

we used a rotational shift of 8 degrees on the images. The following Figures illustrate the results of the rotational gradient method centered on Io.

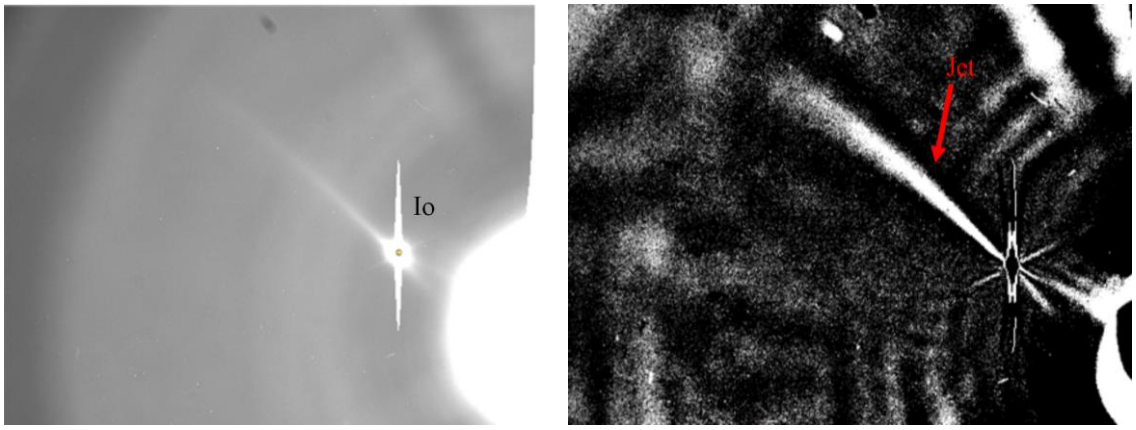

Figure 6.55: Image from December 4, 2014 (Left). The result of the rotational gradient method on the image centered on Io. The presence of a jet is emphasized (Right).

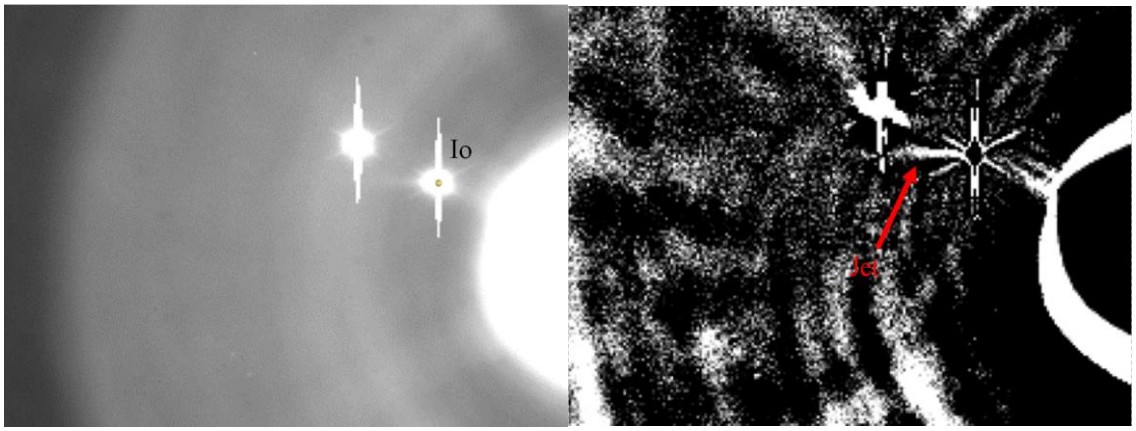

Figure 6.56: Image from December 6, 2014 (Left). The result of the rotational gradient method on the image centered on Io. The presence of a jet is emphasized (Right).

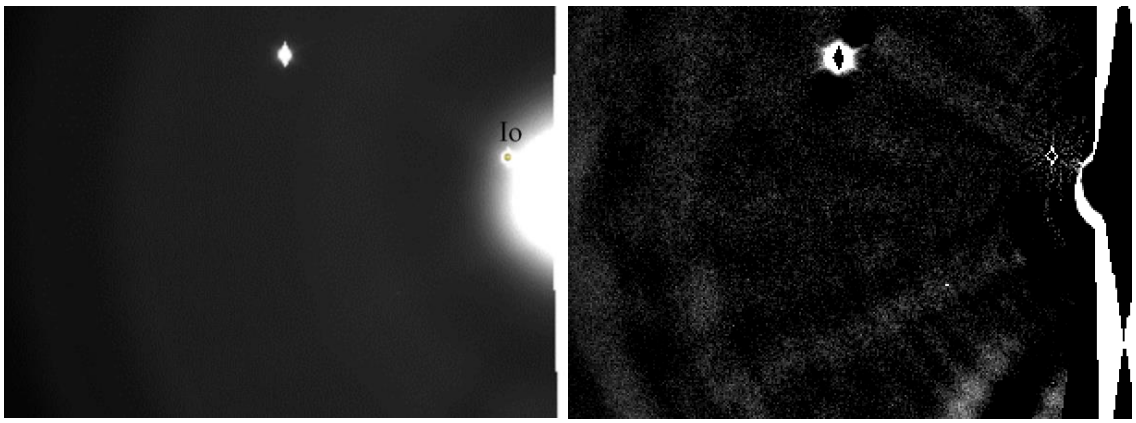

Figure 6.57: Image from December 8, 2014 (Left). The result of the rotational gradient method on the image centered on Io. The presence of a jet is not emphasized (Right).

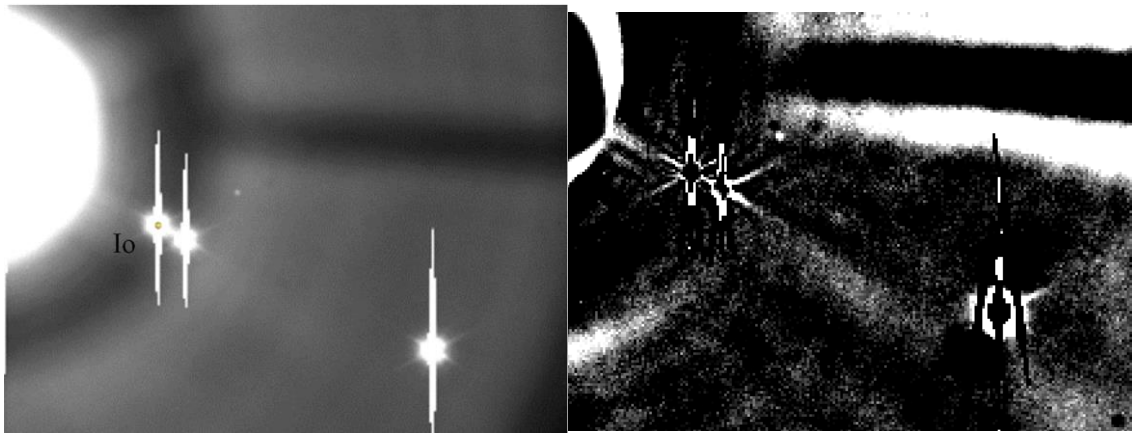

Figure 6.58: Image from December 12, 2014 (Left). The result of the rotational gradient method on the image centered on Io. The presence of a jet is not emphasized (Right).

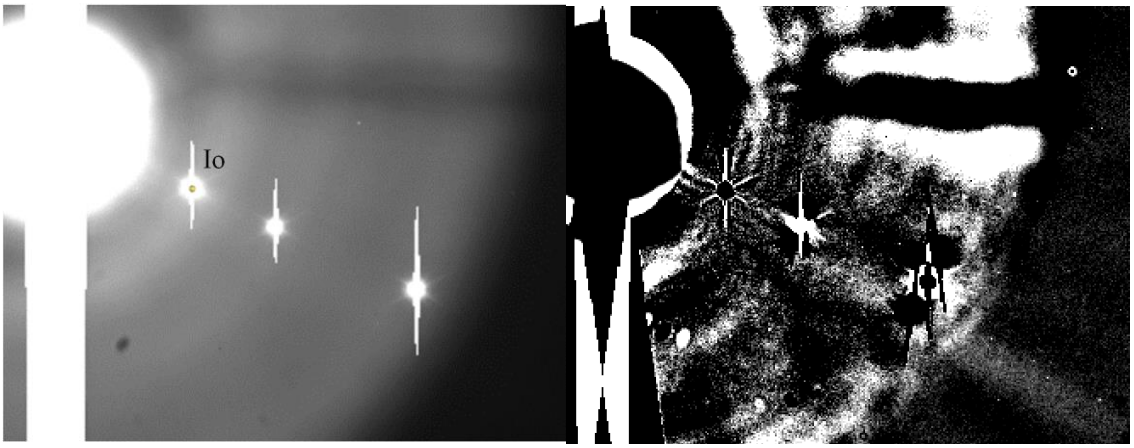

Figure 6.59: Image from December 19, 2014 (Left). The result of the rotational gradient method on the image centered on Io. The presence of a jet is not emphasized (Right).

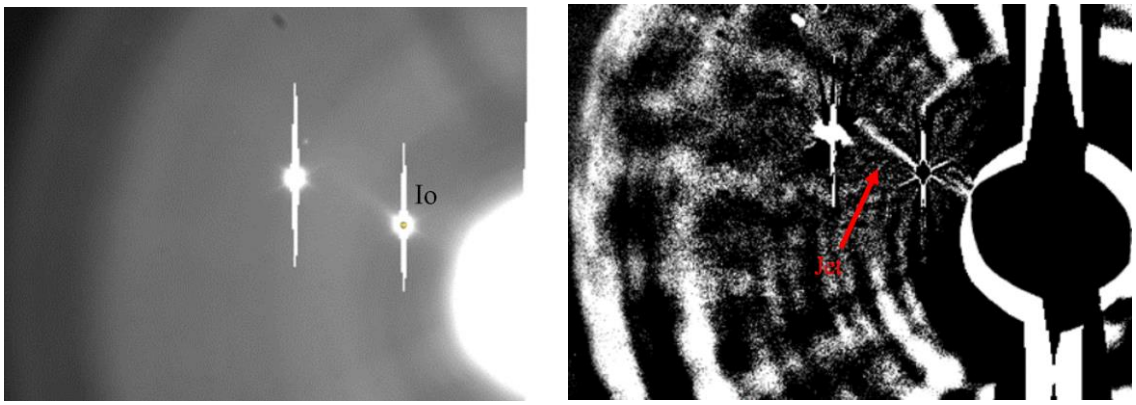

Figure 6.60: Image from January 11, 2015 (Left). The result of the rotational gradient method on the image centered on Io. The presence of a jet is emphasized (Right).

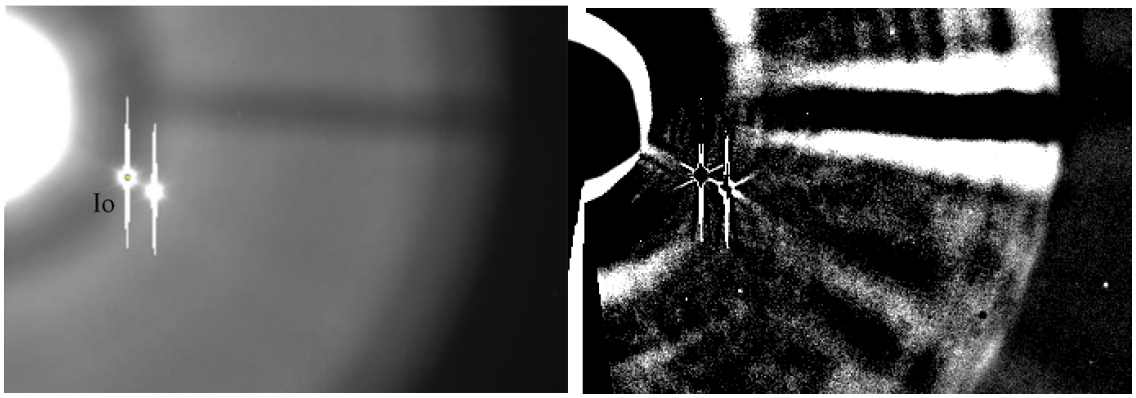

Figure 6.61: Image from January 13, 2015 (Left). The result of the rotational gradient method on the image centered on Io. The presence of a jet is not emphasized (Right).

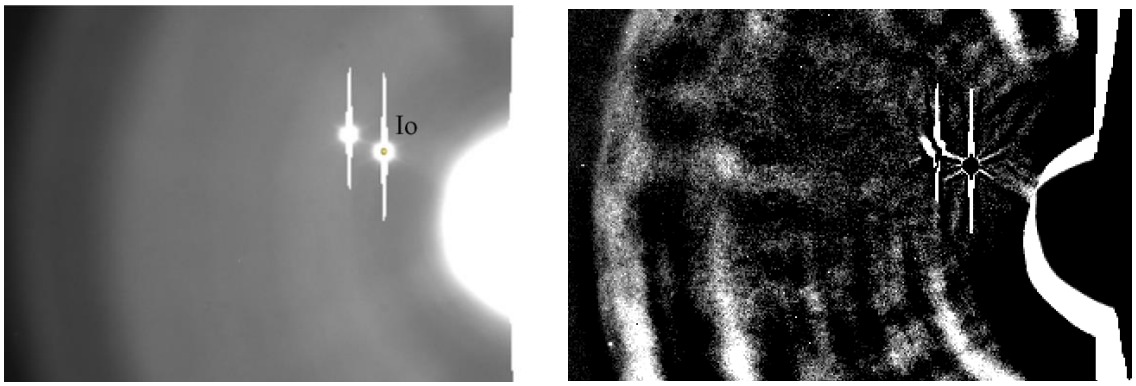

Figure 6.62: Image from January 20, 2015 (Left). The result of the rotational gradient method on the image centered on Io. The presence of a jet is not emphasized (Right).

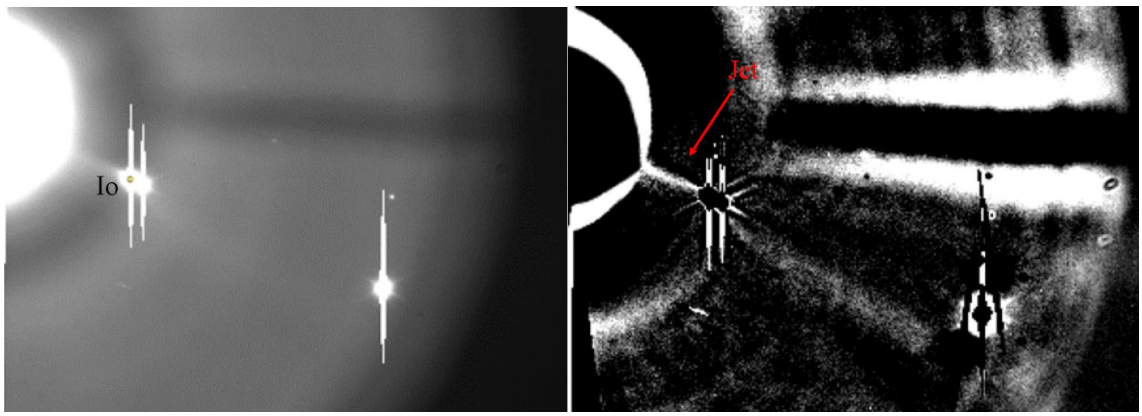

Figure 6.63: Image from January 28, 2015 (Left). The result of the rotational gradient method on the image centered on Io. The presence of a jet is emphasized (Right).

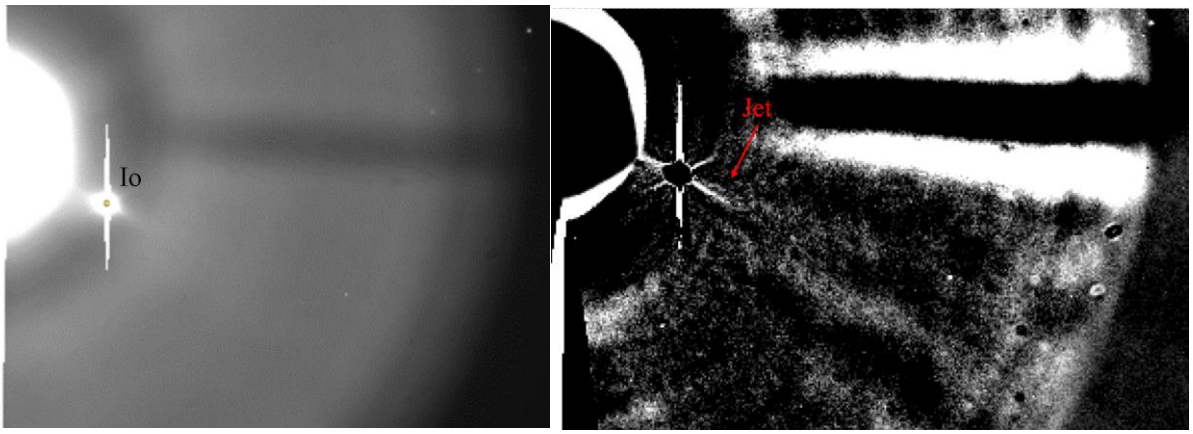

Figure 6.64: Image from February 12, 2015 (Left). The result of the rotational gradient method on the image centered on Io. The presence of a jet is not quite emphasized (Right).

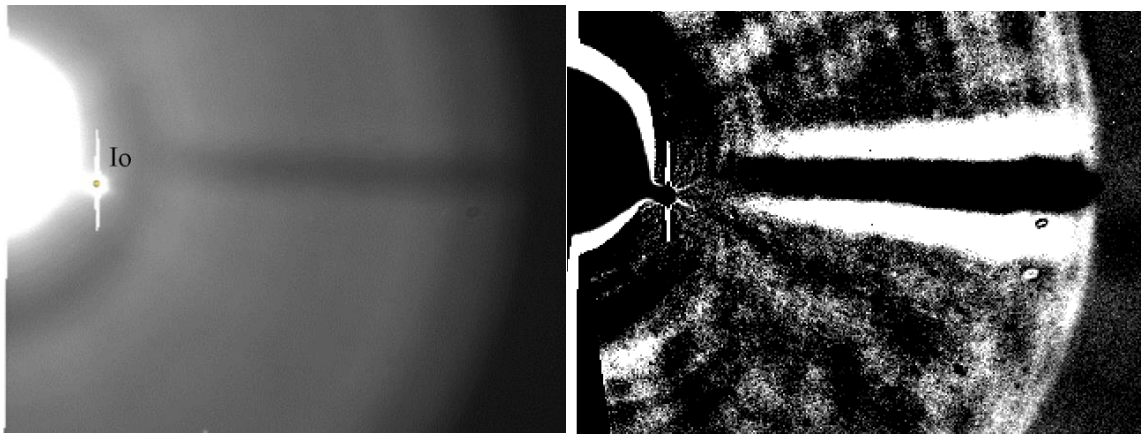

Figure 6.65: Image from March 29, 2015 (Left). The result of the rotational gradient method on the image centered on Io. The presence of a jet is not emphasized (Right).

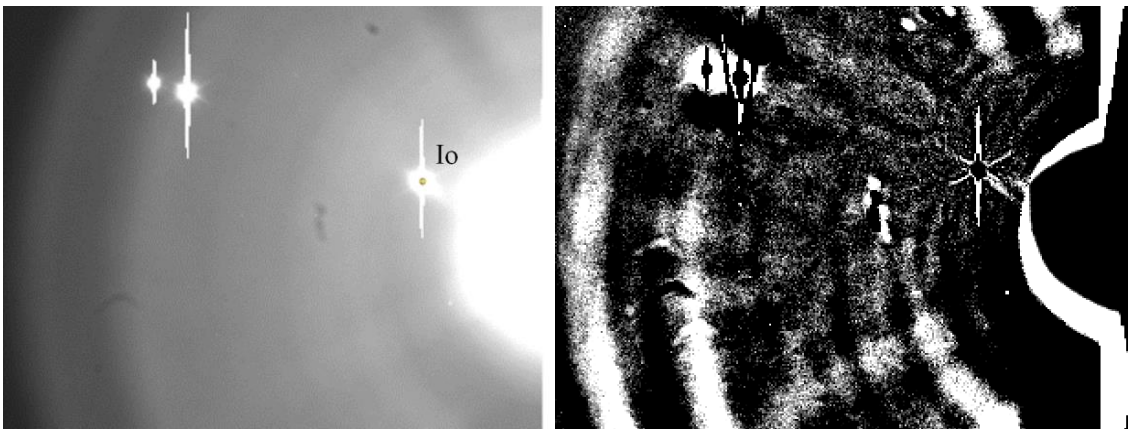

Figure 6.66: Image from March 30, 2015 (Left). The result of the rotational gradient method on the image centered on Io. The presence of a jet is not emphasized (Right).

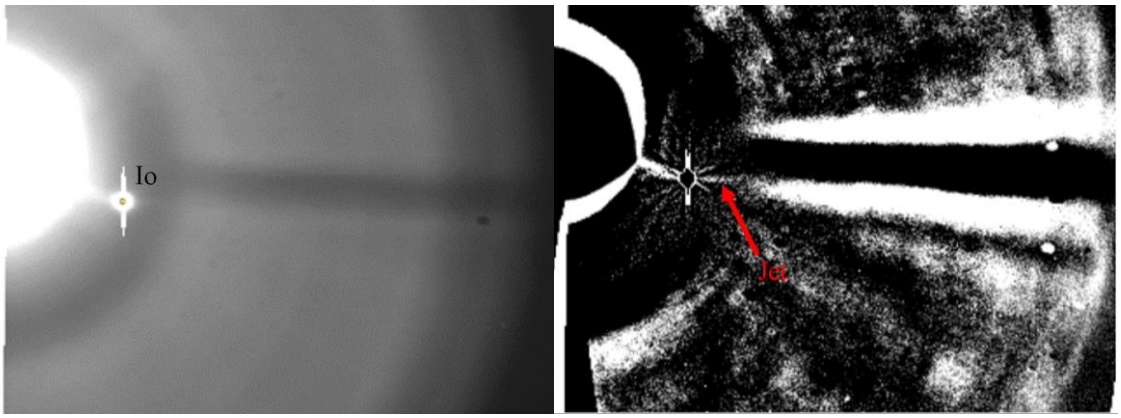

Figure 6.67: Image from March 31, 2015 (Left). The result of the rotational gradient method on the image centered on Io. The presence of a jet is emphasized (Right).

For the thirteen nights where Io is present on the images, we detect six nights with jet coming out of Io's atmosphere by the rotational gradient method. This method is very useful in the detection of jets since it makes possible to better highlight the weaker details of the image and thus to emphasize or not the presence of a jet for a particular night.

6.3 Comparison of the methods used with IDL

To verify the efficiency of the three different methods explained in the section 5.3, we compared these three methods used on an image of December 6, 2014. Of course, the stacking and unsharp masking method uses 7 images of that night, including the image used for the other methods. In order to quantify these methods, one possible way is to compare the SNR of each images. In order to correctly measure the SNR of our images, it would be necessary to be able to have an original image whose noise can be negligible to represent the signal. Then, once our image is processed, we can measure the SNR of our processed image and compare it to our original image. If the SNR has increased, it means that the method used has reduced the noise of the image and therefore the image is of better quality. If not, it means the method did not work. Unfortunately, we have no original image whose noise can be neglected compared to the signal so we cannot properly measure the SNR of our images.

Using the SNR definition mentioned in section 5.2 as the ratio of the mean signal on the standard deviation of the noise, we can measure a SNR just in order to compare the four methods used with IDL. We measure the signal mean of our original image and divide it by the standard deviation of the processed image. We can see in the Figure 6.68 that the background subtraction method differs from the other three methods, even if the stacking and unsharp masking method is slightly behind. We will perform our measurements on the jet on the results obtained with the background subtraction method.

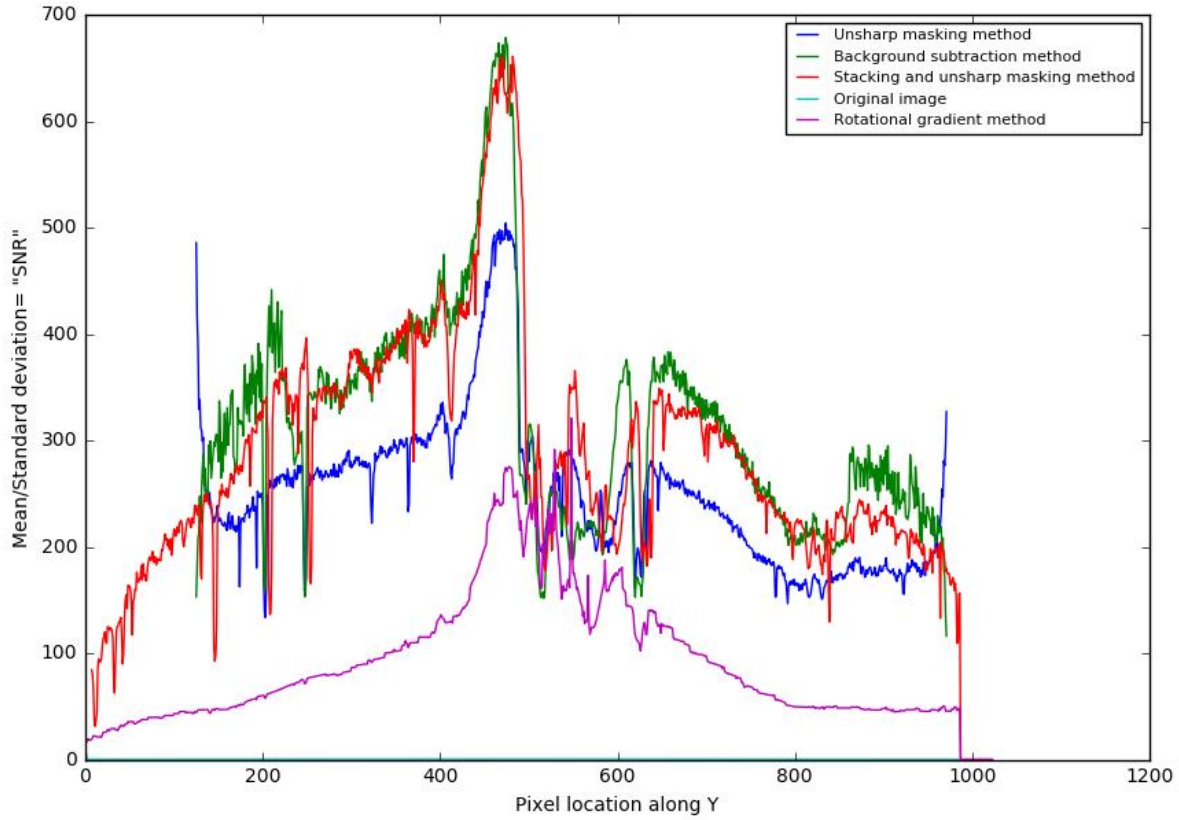

Figure 6.68: Comparison of the "SNR" of an image from December 6, 2014 processed with four different methods.

6.4 Discussion

For this work, we use several nights of observation in order to observe sodium jets from Io using the TRAPPIST-South telescope. Table 6.1 shows the detection or not of a jet for each observation night. The Figure 6.69 shows a schematic top view of the Jupiter-Io system with the positions of Io in its orbit for each night of observations and its position when we observed a jet. The ephemerids were computed using the IDL implementation of the SPICE toolkit from the NASA's Navigation and Ancillary Information Facility (NAIF[7]). Our results show that among our fifteen nights of observation, six nights have a jet coming out of Io's atmosphere. In this section, we measure the physical observable properties of the jet on our images.

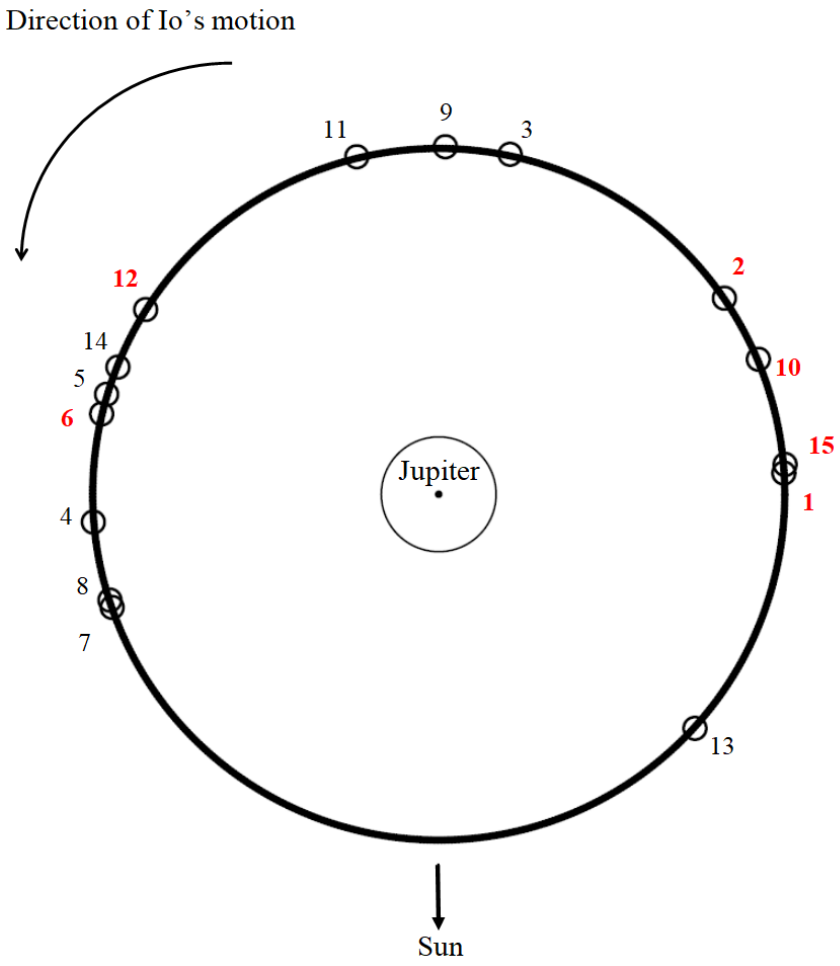

Figure 6.69: Io's orbital geometry for each of the observed events listed in Table 6.1. Io is not shown to scale. The numbers in red represent the detection of a jet for the event.

[7]https://naif.jpl.nasa.gov/naif/

Table 6.1: Jet detection for the observation nights	
Date	Jet detection
1. 2014/12/04	Yes
2. 2014/12/06	Yes
3. 2014/12/08	No
4. 2014/12/12	No
5. 2014/12/19	No
6. 2015/01/11	Yes
7. 2015/01/13	No
8. 2015/01/20	No
9. 2015/01/23	No
10. 2015/01/28	Yes
11. 2015/02/01	No
12. 2015/02/12	Yes
13. 2015/03/29	No
14. 2015/03/30	No
15. 2015/03/31	Yes

The most spectacular night is that of December 4, 2014. Indeed, the presence of the jet on the images is undeniable. The Figure 6.70 shows the profile of length of the jet for the night of December 4, 2014. We measure the jet length profile by drawing a line from the center of Io with the MaxImDL software which allows us to obtain the value of the pixels along this line corresponding to the jet. On each profile, we notice the portion corresponding to the saturation at Io and then an exponential decay of the pixel value. This is also done for the other night where we successfully detected a jet (Fig. 6.72, Fig. 6.73, Fig. 6.74, Fig. 6.75, Fig. 6.76 and Fig. 6.77). The Table 6.2 illustrates the fit coefficients of the exponential function of the jet's length profile for each night with a jet. We also measured, for the December 4th image, a second profile taken away from the jet direction shown in Figure 6.71 to illustrate that we do not get the same saturation profile for the two and therefore we have a contribution related to the presence of the jet.

For each Figure illustrating the length profile of each jet, we have, with MaxIm DL, obtained a three-dimensional (3D) view of the two-dimensional area containing this jet. The red line serves as an indicator of the location of this jet on this 3D representation. Next to this 3D representation, we show a zoom of a processed image on which we made our measurement. The line represents the line drawn in the MaxIm DL software to obtain the jet length profile. We notice on the bottom graph of Figure 6.70 that the fit is a good exponential fit and that the jet's extent is quite important (see Table 6.4).

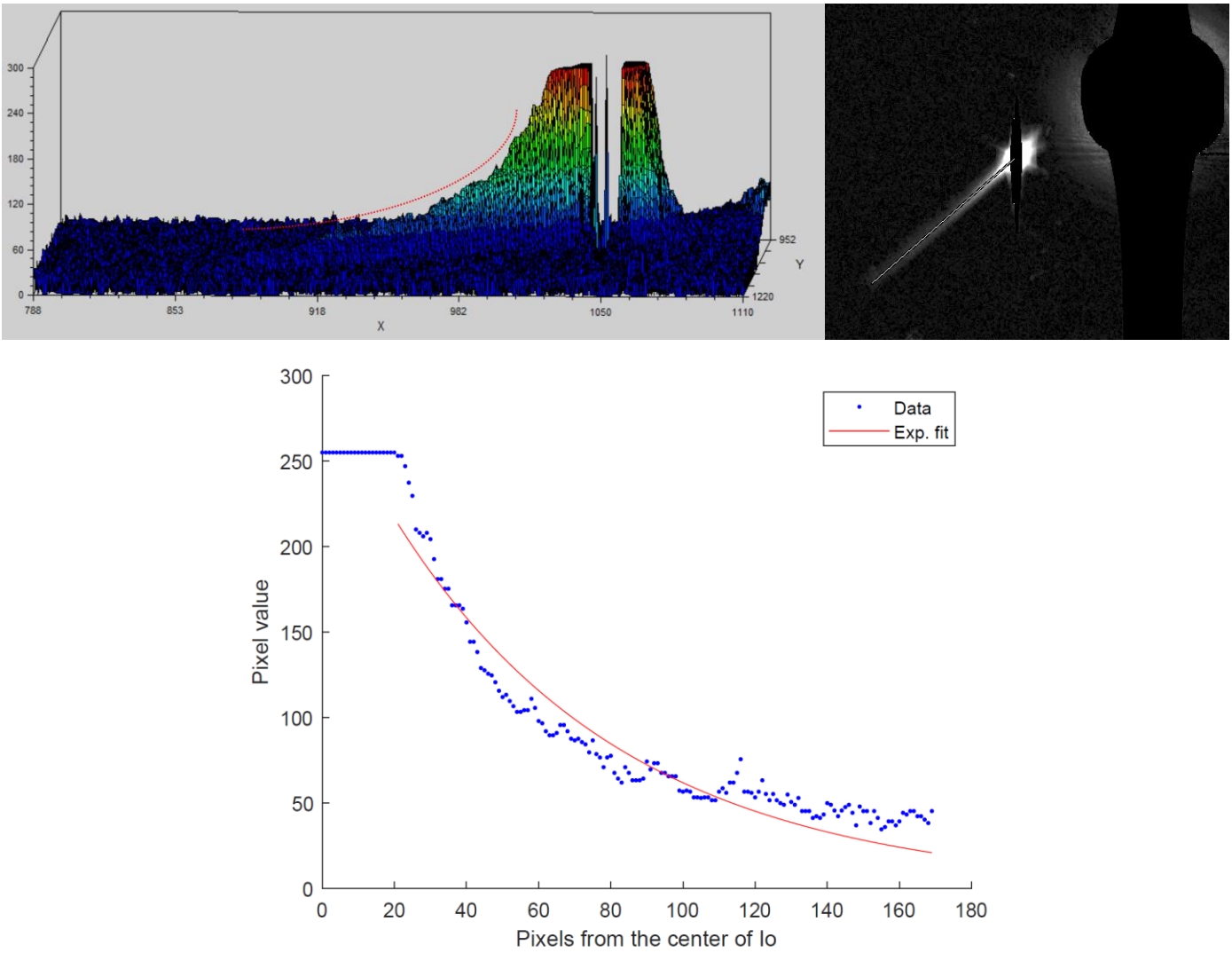

Figure 6.70: Profile of the jet's length from December 4, 2014. The top left graph was generated by MaximDL.

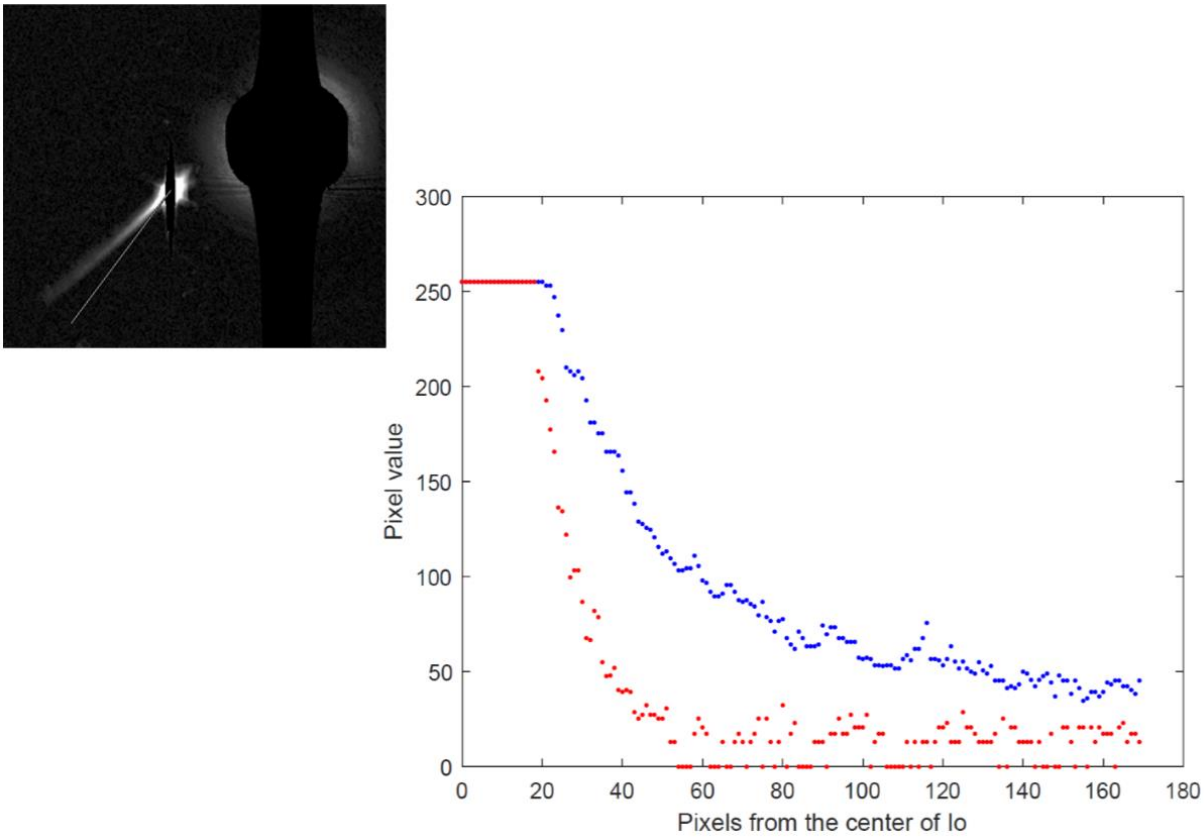

Figure 6.71: Comparison of the profile of the jet's length from December 4, 2014 in blue and a second profile taken next to the jet shown on the image (left) in red.

We notice for the December 4 night the presence of a second jet "oriented on the image" towards Jupiter. Indeed, we only see on the image a two-dimensional projection of the jet although this latter has probably a three-dimensional structure. This jet must be on Io's opposite side of observation, thus we only see a certain part of it. Figure 7.72 shows the second jet's length profile for that night, for which the exponential fit is quite good.

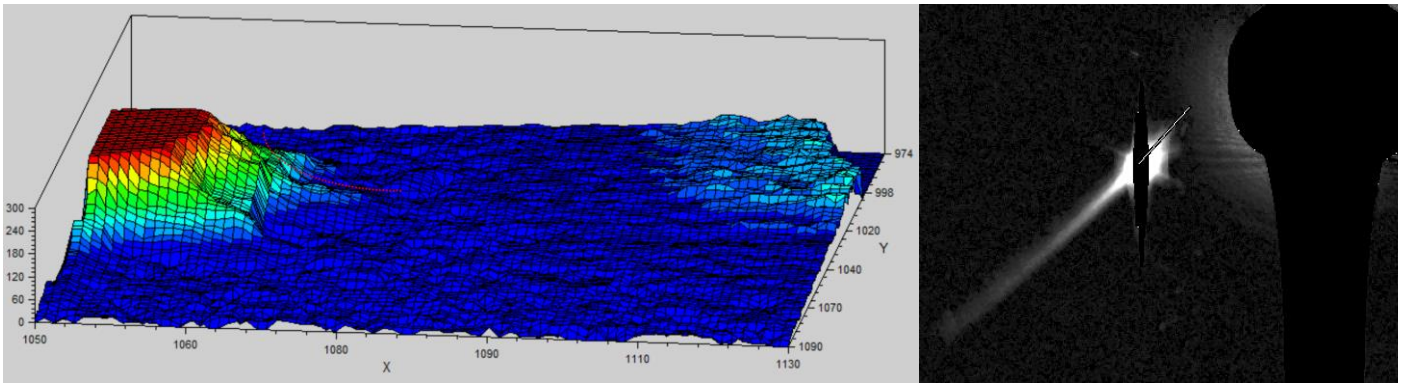

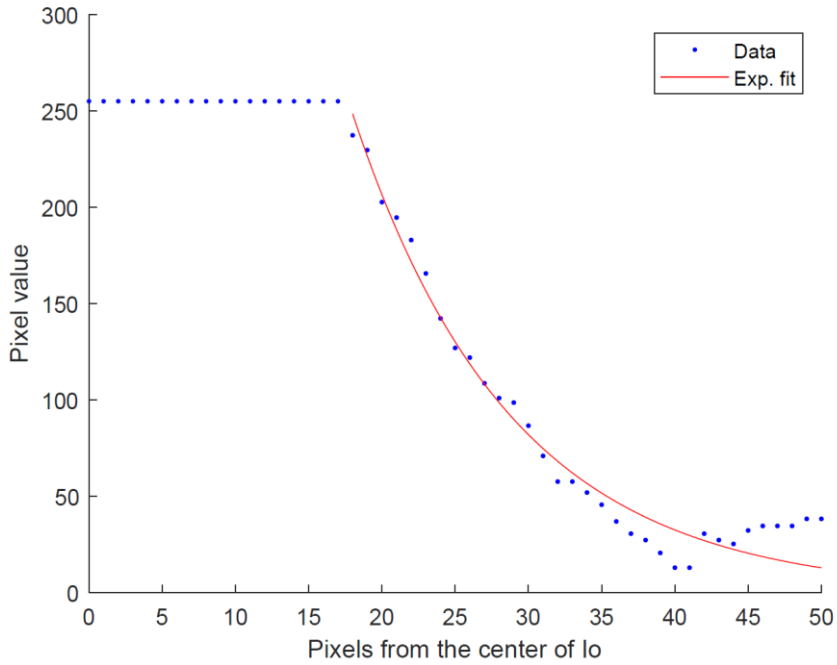

Figure 6.72: Profile of the second jet's length from December 4, 2014. The top right graph was generated by MaximDL.

For the night of December 6, 2014 since we observe Io during a little over two hours, we measure the jet's length profile on different spaced times shown on Figure 6.73. After Pilcher et al. (1984), the direction of the jet oscillates over a period of several hours depending on the magnetic longitude of Io. We can see on the different profiles (Fig. 6.73) that the extent of the jet's length varies over time. This could be explained by the oscillation of the jet due to the variation of the magnetic longitude of Io. On the Figure 6.73, we observe that the exponential fit is a quite good fit and that the jet's length is shorter than the first night of observation, but it is still relatively extended (see Table 6.4).

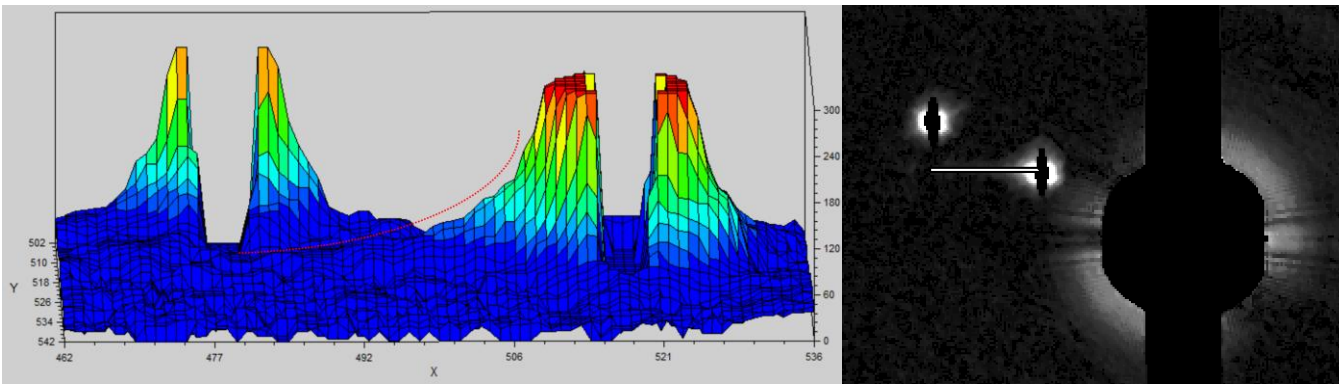

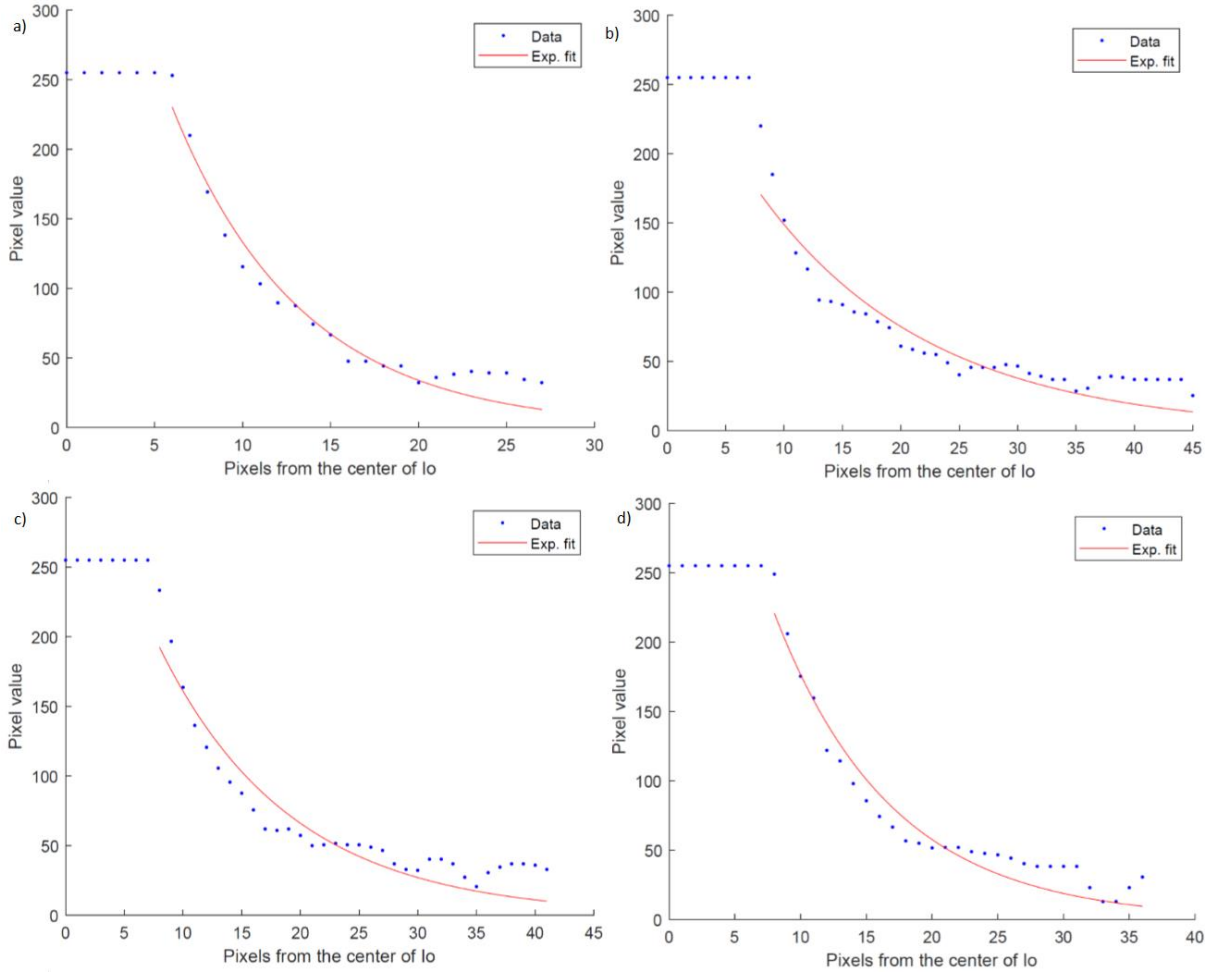

Figure 6.73: Profiles of the jet's length from December 6, 2014 from one image taken at a) 06h45, b) 07h09, c) 07h50 and d) 08h31. The top left graph was generated by MaximDL.

On Figure 6.74, we notice that the exponential fit is a relatively good fit. The total extent of the jet from January 11, 2015 is contaminated by the egrets of Ganymede as shown on the top left graph of Figure 6.74.

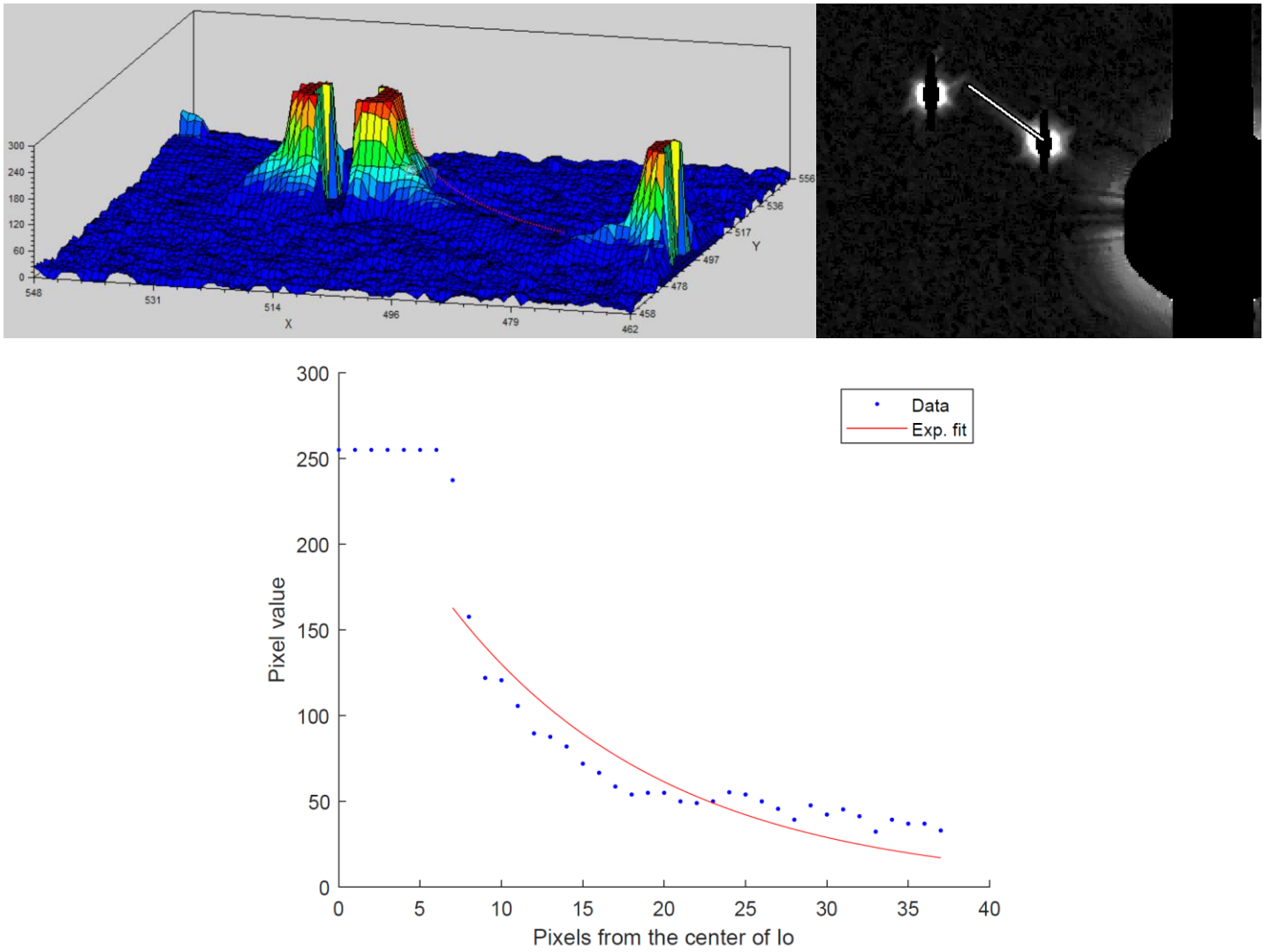

Figure 6.74: Profile of the jet's length from January 11, 2015. The top left graph was generated by MaximDL.

For the January 28, 2015 night, we detected a jet "towards" Jupiter. The Figure 6.75 illustrates the jet's extent profile of that night and its exponential fit is very good. Its extent is shorter than the others previous night (see Table 6.4).

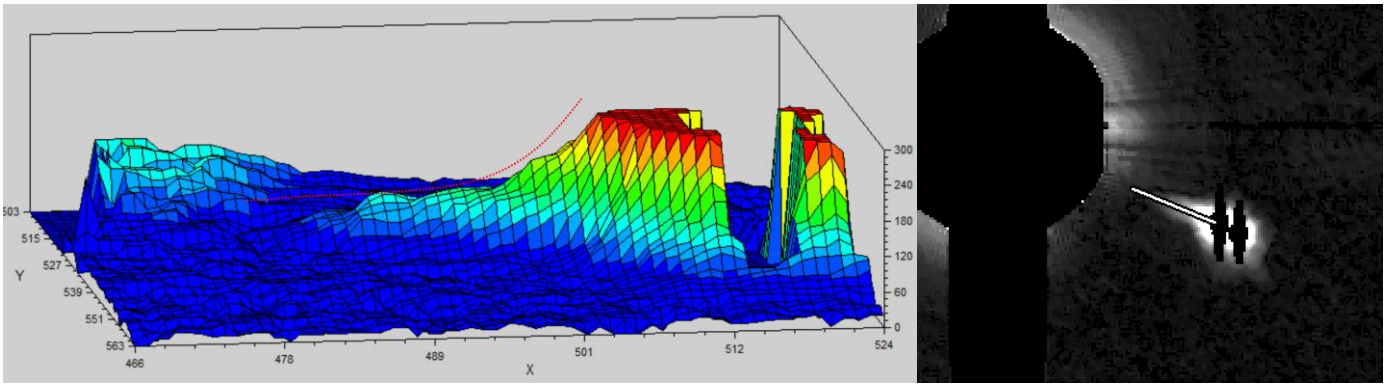

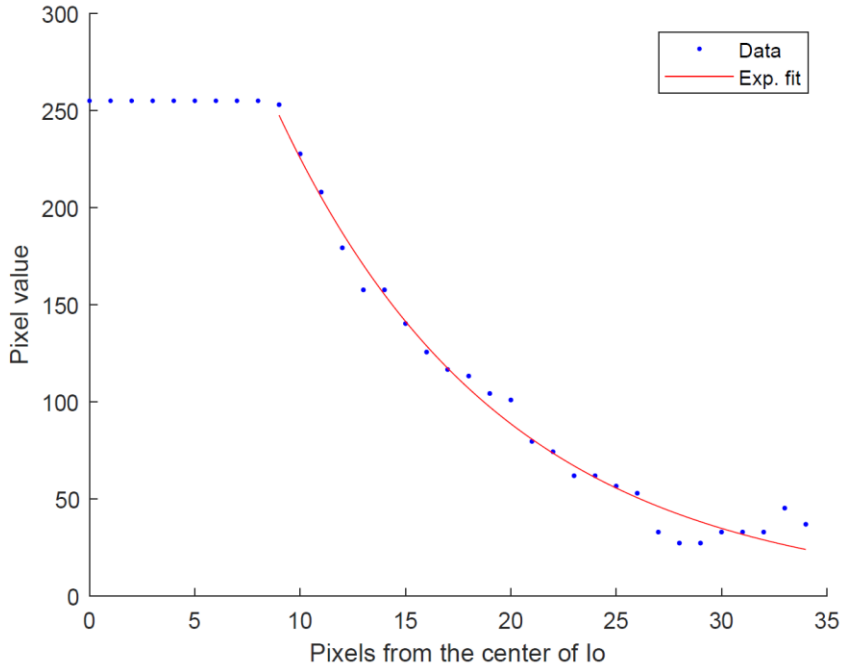

Figure 6.75: Profile of the jet's length from January 28, 2015. The top left graph was generated by MaximDL.

The jet's length profile from February 12, 2015 is shown on the Figure 6.76. We find that its exponential fit is a relatively quite good fit. On the top left graph from the Figure 6.76, we also notice that the mask used to cover Io's saturation part does not cover it entirely.

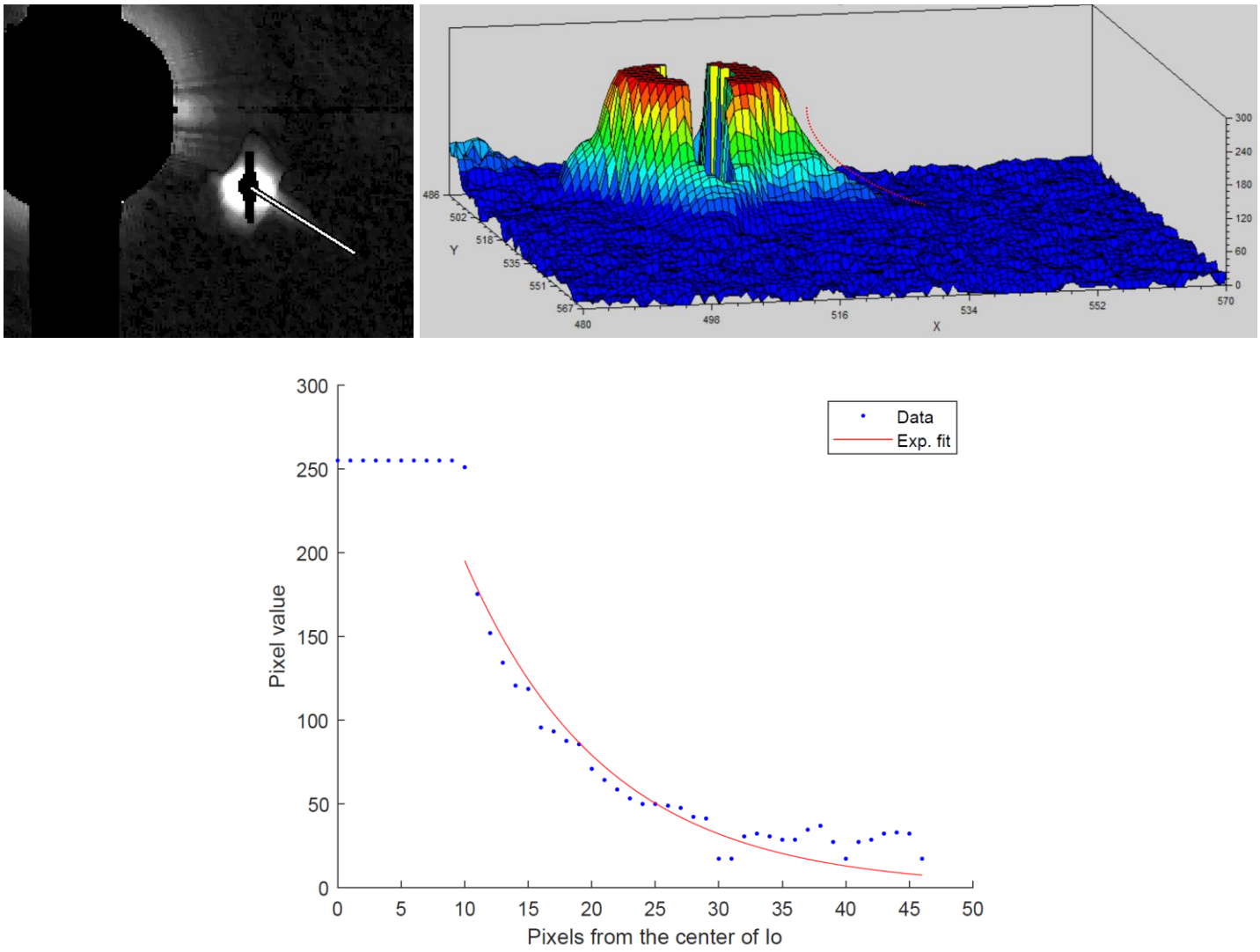

Figure 6.76: Profile of the jet's length from February 12, 2015. The top right graph was generated by MaximDL.

The jet's length profile for the March 31, 2015 night is illustrated on the Figure 6.77 and shows that the extent of this jet is quite short (see Table 6.5).

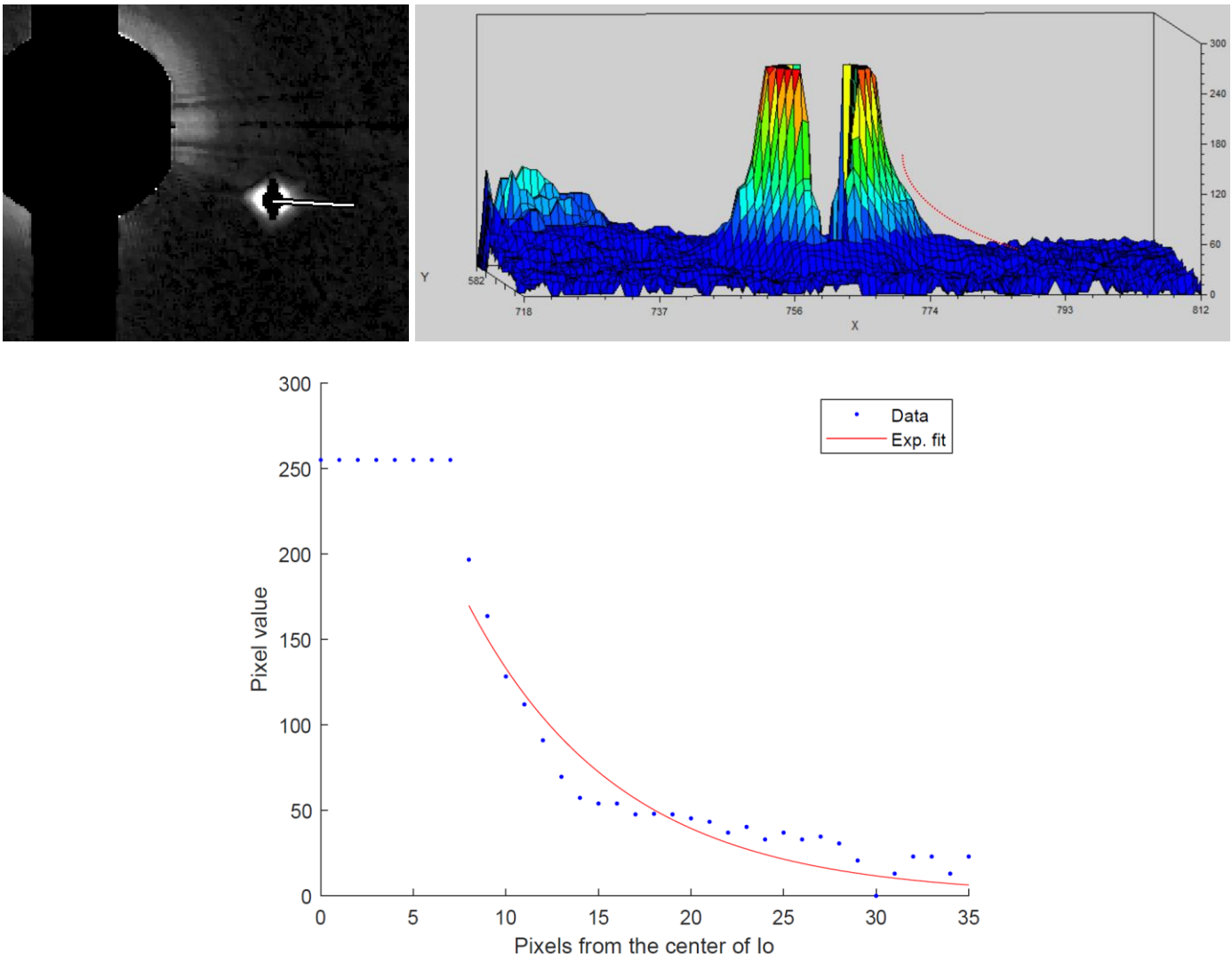

Figure 6.77: Profile of the jet's length from March 31, 2015. The top right graph was generated by MaximDL.

Table 6.2: Fit coefficients of the exponential function of the jet's length profile	
Date	Exponential function: $ae^{(bx)}$
2014/12/04	1) a = 296.3 b = - 0.01565 2) a = 1310 b = - 0.09235
2014/12/06	a) a = 522.9 b = - 0.1367

	b) a = 294.7 b = - 0.06835 c) a = 392.1 b = - 0.08901 d) a = 540.7 b = - 0.1119
2015/01/11	a = 275.5 b = - 0.07506
2015/01/28	a = 573.1 b = - 0.09022
2015/02/12	a = 481.1 b = - 0.09022
2015/03/31	a = 449.5 b = - 0.1216

For the night of December 4, we also measure the width profile of the jet at three different locations as shown in the Figure 6.78. These profiles allow us to measure the FWHM (Full Width at Half Maximum) of the normal function (see Table 6.3). Table 6.3 illustrates the coefficients and FWHM of the fitted normal law of the width jet's profile for that night.

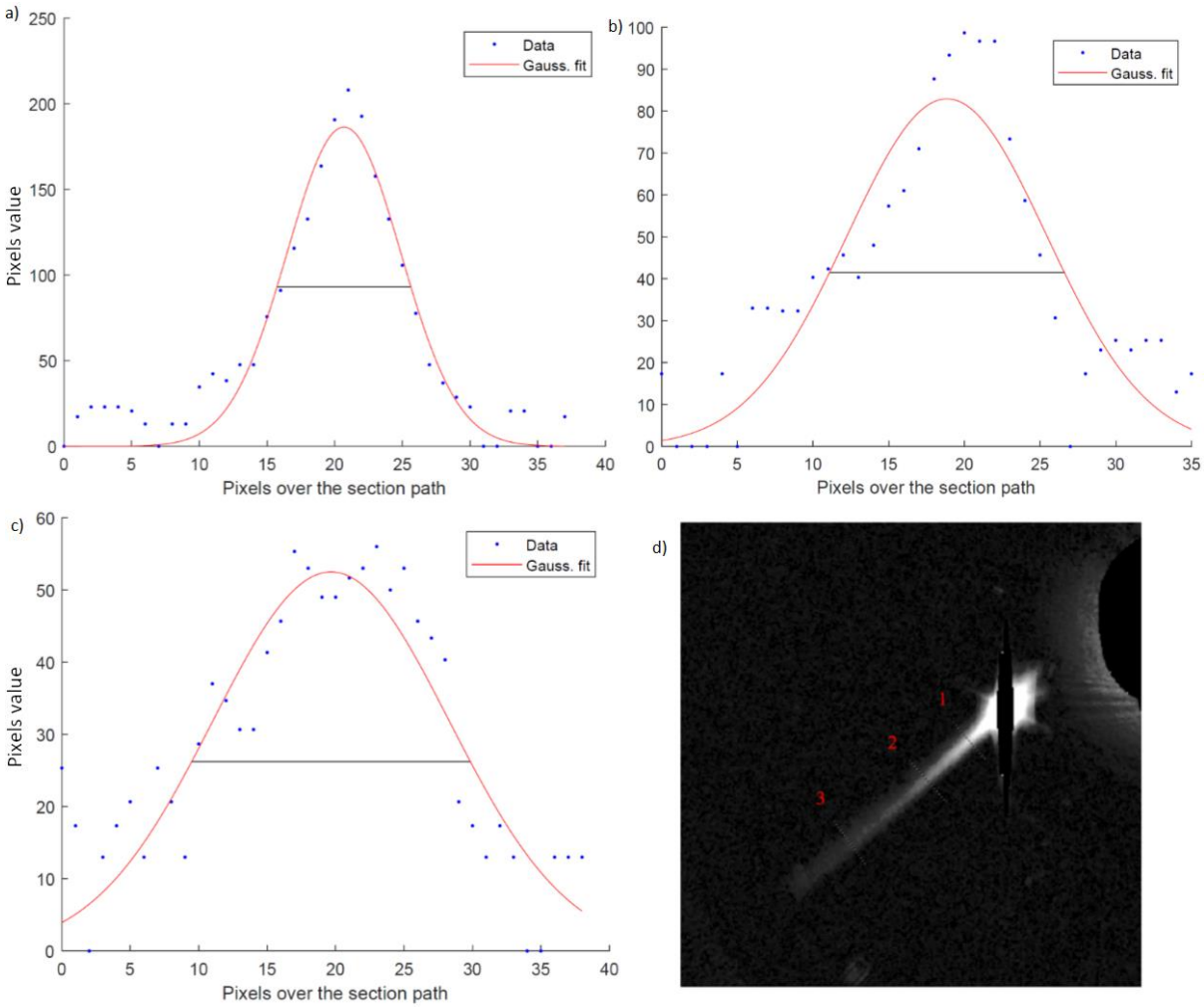

Figure 6.78: Width profile of the jet from December 4, 2014 in three different sections shown in panel d). a) Width profile of the section 1. b) Width profile of the section 2. c) Width profile of the section 3. The black line shows the FWHM of the gaussian fit.

Table 6.3: Coefficients and FWHM of the fitted normal law of the width jet's profile		
Section	Normal law: $ae^{\left[-\left(\frac{(x-b)}{c}\right)^2\right]}$	FWHM
1	a = 186.4 b = 20.68 c = 5.94	In pixel: 9.89 In km: ~ 6162.651 In R_{Io}: ~ 3.383
	a = 82.93	In pixel: 15.5281

2	b = 18.85 c =19.326	In km: ~ 9675.861 In R_{Io}: ~ 5.312
3	a = 52.5 b = 19.67 c = 12.22	In pixel: 20.345 In km: ~ 12677.490 In R_{Io}: ~ 6.959

The real extent of all the jets for each night was measured and is shown on Table 6.4 and Table 6.5. We measure the length of the jets for each night by measuring the distance between Io and Jupiter. We measure this distance by calculating the angle θ (shown in Figure 6.78) given by:

$$d\theta = \sqrt{dRa^2 + dDec^2}$$

where Ra (radian) represents the right ascension of Io with respect to Jupiter and Dec (radian), its declination. This relation allows us to establish the distance Jupiter-Io during our observations:

$$D_{J-I} = tg\ \theta\ D_{E-J}$$

where D_{J-I} represents the Jupiter-Io distance and D_{E-J}, the Earth-Jupiter one. Then, we transpose this distance on the images which gives us the D_{J-I} in pixels. This leads to the measure of the jet's extent also in pixels that we can extrapolate in kilometers and Jovian radii. In order to quantify the angle of each observed jet on our images, we measure an α angle from the line connecting Jupiter to Io as shown in Figure 6.79. Figure 6.79 is a schematic view of the method for the measurements.

Table 6.4: Measures of the observable physical properties of the jets			
Date	2014/12/04	2014/12/06	2015/01/11
dRa (“)	-107.903	-105.13	112.194
dDec (“)	41.868	40.583	-42.757
Distance Earth-Jupiter (10^6 km)	733.142711	728.915426	665.757762
Distance Jupiter-Io (km)	411387.214	398237.257	387532.687
Distance Jupiter-Io on the image (pixel)	~ 82.525	~ 73.356	~ 79.469
Jet’s length on the image (pixel)	1) ~ 110.255 2) ~ 20.802	~ 39.535	~ 35.365
Jet’s length (km)	1) ~ 549618.219 2) ~ 103701.551	~ 214576.656	~ 172457.521
Jet’s length (R_J)	1) ~ 7.861 2) ~ 1.483	~ 3.069	~ 2.466
Jet’s angle α (°)	1) ~ 340 2) ~ 160	~ 19	~ 16

Table 6.5: Measures of the observable physical properties of the jets			
Date	2015/01/28	2015/02/12	2015/03/31
dRa (“)	-120.447	102.174	-115.249
dDec (“)	44.190	-36.847	38.369
Distance Earth-Jupiter (10^6 km)	652.085059	650.974475	709.657877
Distance Jupiter-Io (km)	405599.303	342790.555	417913.473
Distance Jupiter-Io on the image (pixels)	~ 86.601	~ 72.337	~ 81.507
Jet’s length on the image (pixels)	~ 15.602	~ 35.365	~ 14.562
Jet’s length (km)	~ 73073.350	~ 167586.450	~ 74664.456
Jet’s length (R_J)	~ 1.045	~ 2.397	~ 1.0679
Jet’s angle α (°)	~ 0	~ 16	~ 13

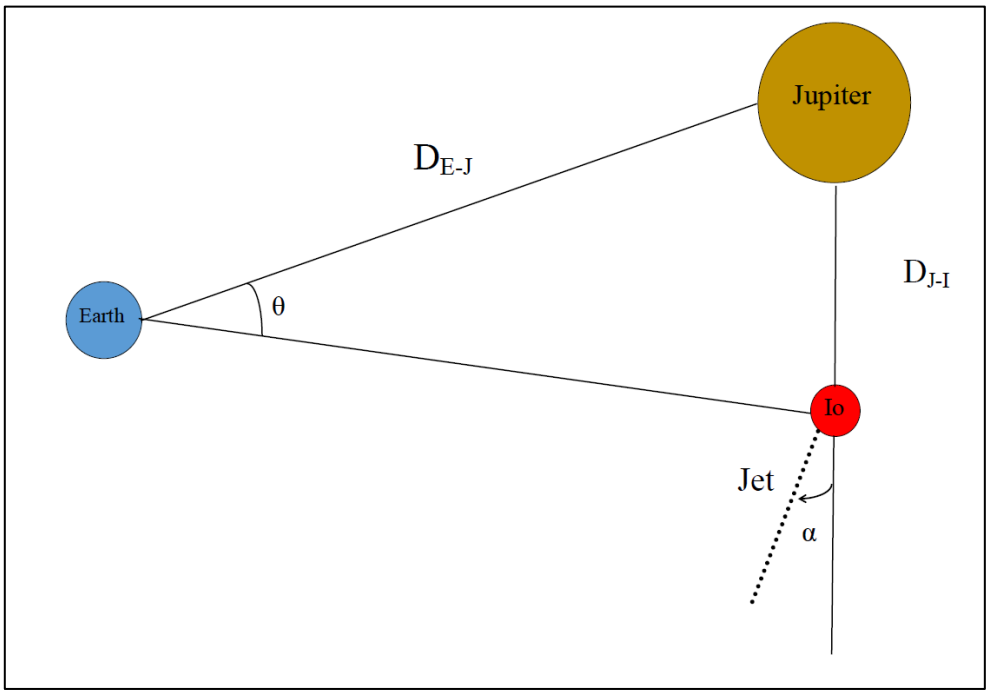

Figure 6.79: Schematic view of the measurements done for the jet's properties (not at scale).

Chapter 7

Conclusions and future works

7.1 Conclusions

We observed Io and the Jovian system with the TRAPPIST-South telescope and a narrow band NaI filter for 15 nights of observations spanning four months from December 4, 2014 to March 31, 2015. We used several image processing methods to improve the signal-to-noise ratio and clean our reduced images in order to optimize the region where a jet would be located and to optimize our measurements. We also used the rotational gradient method to confirm (or not) the presence of a sodium jet on our images. We detected six nights with jets coming out of Io's atmosphere. We thought at first that this phenomenon was quite rare and that we only detected a single jet, the one of the first observation night. In view of our results, we can say that such events appear more frequently than thought because we observe this jet during six observation nights. We then measured the length of all detected jets and the angle with the to the Jupiter-Io line. We measured several jets with a length extending over several Jovian radii (Table 6.4 and 6.5). The night of December 4, 2014 is the most impressive, the extent of the detected jet is approximately 7 R_J equivalent to about 301 R_{Io}.

Our first study of these fast sodium jets from Io allows us to improve the next observations with the ultimate aim of observing these jets and finally improve our understanding about them. We found that we observed the jets better when Io was at the maximum elongation of its orbit (Fig. 6.69) and when the other Galilean satellites were not near Io. All these parameters must be

taken into account for the next observations. Io's fast sodium jet remains a rather complex phenomenon. Further study would answer many questions.

7.2 Perspectives and future works

Our study of Io's sodium jets observation is under development. Indeed, now that this preliminary study has been done, we can improve the next observations as well as the image processing. In this way, we will be able to improve our understanding of the physics related to these jets. There are still many gray areas with regard to sodium jets. Several questions remain unanswered and observation in optimized conditions would make it possible to answer them.

By correlating the observations of Io's active volcanism with the observation of sodium jets, we could verify whether this volcanic activity influences the formation of the jets as well as their intensity. By observing more continuously and over long periods, we could detect if this phenomenon is periodic or purely random. For that, we could observe Io at the same position on its orbit at a certain specific period. If the jets are a random phenomenon, is it due to the heterogeneity of its atmosphere? What are the processes influencing the direction, the intensity of these sodium jets as well as their spatial distribution? An optimized observation would answer all these questions and TRAPPIST is very well suited for the job.

For future studies, we could measure the flux of these jets in a precise way by improving the calibration of our images by measuring the flux of a star or even another Galilean satellite with a very short exposure time (~ 3 seconds) before and after the observation of Jupiter. By observing a standard star, we could make corrections related to the instrumentation and this would make possible to calibrate the flux of the image and thus, to determine the brightness of the jets, to compare them from one image to another and to finally compare them with physical modeling. Another way to improve the observations is to avoid the very important contamination of Jupiter by blocking the photons emitted by Jupiter either through a coronagraph, or through a dark filter that acts as a mask on Jupiter. Subsequently, thanks to these optimized methods in the observation of Io sodium jets, we can also improve the image

processing as well as create a program that could reliably detect the presence or absence of a jet.

This first study opens the door to new observations and further studies to answer many questions about sodium jets and the complex interaction between Io and the Jovian magnetosphere.

Appendix 1

```
pro clean_trappist01

;Reglage de la tble de couleur
loadct, 3
gamma_ct, 0.4
;@add_lib_n1

;Ici, chaque ligne permet de charger une image

image=mrdfits('/LPAP/HST/redu/io_trappist/Jupiter_Reduced/r2014/6997_7012_B2R11_ren
amed/TRAP_2014-12-06T06_26_18.fits')
dgtv, image

;autres exemples
image=mrdfits('/LPAP/HST/redu/io_trappist/Jupiter_Reduced/r2015/7033_7113_B2R11_ren
amed/TRAP_2015-01-11T07_44_59.fits')
image=mrdfits('/LPAP/HST/redu/io_trappist/Jupiter_Reduced/r2015/7033_7113_B2R11_ren
amed/TRAP_2015-03-31T04_00_46.fits')
image=mrdfits('/LPAP/HST/redu/io_trappist/Jupiter_Reduced/r2015/7033_7113_B2R11_ren
amed/TRAP_2015-03-30T04_05_15.fits')



sz=size(image) ;taille de l'image



;Recherche du centre de Jupiter

x_arr=rebin(findgen(sz(1)),sz(1), sz(2))
y_arr=rotate(rebin(findgen(sz(2)),sz(2), sz(1)),1)


imbleed=image gt 3.e4  ;selection des pts brillants
mask_jup=erode(imbleed, fltarr(40,40)+1) ;masque pour isoler Jupiter
mask_jup2=dilate(erode(imbleed, fltarr(5,20)+1),fltarr(10,25)+1) ;masque de toute la
zone contaminée par Jupiter



x_bary=mean(x_arr*mask_jup)/mean(mask_jup)
y_bary=mean(y_arr*mask_jup)/mean(mask_jup)
print,'Le barycentre de Jupiter est: ', x_bary, y_bary
x_center=round(x_bary)
y_center=round(y_bary)


image_sat=image-image*mask_jup2 ;image sans Jupiter


ind=where(image_sat gt 3.e4) ;recherche l'indice des pts très brillants
imbleed2=image_sat gt 3.e4
mask_sat=(dilate(erode(imbleed2,fltarr(1,3)+1),fltarr(3,5)+1)+imbleed2) gt 0
```

```
;Option: masque qui cache tous les satellites
ind=where(mask_sat eq 1)
result=linfit(x_arr(ind), y_arr(ind))
mask_sat3=mask_sat*0.
mask_sat3(*,y_center-20:y_center+20)=1.
mask_sat3=rot(mask_sat3,-result(1)/!dtor,1,x_center,y_center,/pivot, missing=0)


;Exemple simple de mise en evidence des details d'une image
dgtv, ((image*(mask_sat eq 0)-median(image*(mask_sat eq 0),15))>0)<5000



;image3=image2

;Decoupe manuelle des satellites et du jet
image3=image_sat-image_sat*mask_sat

v=defroi(sz(1),sz(2))
image3(v)=0

v=defroi(sz(1),sz(2))
image3(v)=0

;Construction des scans
n_angles=3600. ; nombre de coupes
coef=n_angles/360. ;angle entre 2 coupes


profile_arr=fltarr(sz(1),n_angles)
profile_arr3=fltarr(sz(1),n_angles)

.run
for i=0,n_angles do begin

imrot=rot(image3, i/n_angles*360.,1,x_center, y_center, missing=0,/pivot)
profile_arr(0:sz(1)-x_center-1,i)=imrot(x_center:*, y_center)


imrot=rot(image, i/n_angles*360.,1,x_center, y_center, missing=0,/pivot)
profile_arr3(0:sz(1)-x_center-1,i)=imrot(x_center:*, y_center)

endfor
end

dgtv, profile_arr

;Interpolations des "trous"

profile_arr2=fltarr(sz(1),n_angles)
profile_arr2b=fltarr(sz(1),n_angles)

absc=findgen(n_angles)/coef
.run
for i=0,sz(1)-1 do begin

    ind=where(profile_arr(i,*) gt median(profile_arr(i,*)/3.))
    if ind(0) ne -1 then begin

        abscc=absc(ind)
        ordo=reform(profile_arr(i,ind))

        profile_arr2(i,*)=interpol(ordo,abscc,absc)

        profile_smo=smooth(profile_arr2(i,*),10, /EDGE_WRAP)
        profile_smo2=smooth((profile_arr(i,*) gt 0)*1.,9)
        indi=where(profile_smo2 eq 1.)
```

```
        abscc=absc(indi)
        ordo=reform(profile_smo(indi))

        profile_arr2b(i,*)=interpol(ordo,abscc,absc)


    endif

endfor
end

dgtv, profile_arr2

;Reconstruction de l'image du background

x_arr=rebin(findgen(sz(1)),sz(1), sz(2))-x_center
y_arr=rotate(rebin(findgen(sz(2)),sz(2), sz(1))-y_center,1)

scan_angle=atan((y_arr)/(x_arr))+(((x_arr) lt 0)*!pi)
ind_neg=where(scan_angle lt 0)
if ind_neg(0) ne -1 then scan_angle(ind_neg)=scan_angle(ind_neg)+2*!pi
dista=(x_arr)/cos(scan_angle)
dista(x_center,*)=abs(y_arr(x_center,*))



imback=bilinear(profile_arr2b,dista,round(scan_angle/!dtor*(n_angles/360.)))
dgtv,imback

;-----------------------
;Quelques tests d'affichage

image_clean=image-image*mask_jup2-image_sat*mask_sat


dgtv, abs(image_clean*(imback ne 0)-imback*(mask_sat eq 0)*(mask_jup2 eq 0))<2000

dgtv, abs(median(image_clean-imback,3))<2000
dgtv, abs(median(image_clean-median(image,15),3))<2000

method1=abs((image_clean-median(image,15)))
method2=abs(median(image_clean-imback,3))

ind=where(image gt 3.e4 or imback eq 0 or image_clean eq 0)
method1(ind)=0.
method2(ind)=0.

dgtv, method1<2000
dgtv, method2<2000


end
```

Bibliography

Anderson, J.D., Jacobson, R.A., Lau, E.L., Moore, W.B., Schubert, G., 2001. Io's gravity field and interior structure. J. Geophys. Res. Planets 106, 32963–32969. https://doi.org/10.1029/2000JE001367

Bagenal, F., 1997. The ionization source near Io from Galileo wake data. Geophys. Res. Lett. 2111–2114. https://doi.org/10.1029/97GL02052@10.1002/(ISSN)1944-8007.GALIJOV1

Bagenal, F., Dowling, T.E., McKinnon, W.B., 2004. Jupiter : the planet, satellites and magnetosphere.

Blöcker, A., Saur, J., Roth, L., Strobel, D.F., 2018. MHD Modeling of the Plasma Interaction With Io's Asymmetric Atmosphere. J. Geophys. Res. Space Phys. 123, 9286–9311. https://doi.org/10.1029/2018JA025747

Bonfond, B., Grodent, D., Gérard, J.-C., Stallard, T., Clarke, J.T., Yoneda, M., Radioti, A., Gustin, J., 2012. Auroral evidence of Io's control over the magnetosphere of Jupiter. Geophys. Res. Lett. 39. https://doi.org/10.1029/2011GL050253

Brown, R.A., 1983. Observed departure of the Io plasma torus from rigid corotation with Jupiter. Astrophys. J. Lett. 268, L47–L50. https://doi.org/10.1086/184027

Burger, M.H., Schneider, N.M., Wilson, J.K., 1999. Galileo's close-up view of the Io sodium jet. Geophys. Res. Lett. 26, 3333–3336. https://doi.org/10.1029/1999GL003654

Chamberlain, J.W., Hunten, D.M., 1987. Theory of planetary atmospheres. An introduction to their physics andchemistry.

Connerney, J.E.P., Kotsiaros, S., Oliversen, R.J., Espley, J.R., Joergensen, J.L., Joergensen, P.S., Merayo, J.M.G., Herceg, M., Bloxham, J., Moore, K.M., Bolton, S.J., Levin, S.M., 2018. A New Model of Jupiter's Magnetic Field From Juno's First Nine Orbits. Geophys. Res. Lett. 45, 2590–2596. https://doi.org/10.1002/2018GL077312

Davies, A.G., Davies, R.L., Veeder, G.J., Kleer, K. de, Pater, I. de, Matson, D.L., Johnson, T.V., Wilson, L., 2018. Discovery of a Powerful, Transient, Explosive Thermal Event at Marduk Fluctus, Io, in Galileo NIMS Data. Geophys. Res. Lett. 45, 2926–2933. https://doi.org/10.1002/2018GL077477

Delamere, P.A., Bagenal, F., Ergun, R., Su, Y.-J., 2003. Momentum transfer between the Io plasma wake and Jupiter's ionosphere. J. Geophys. Res. Space Phys. 108. https://doi.org/10.1029/2002JA009530

Douté, S., Schmitt, B., Lopes-Gautier, R., Carlson, R., Soderblom, L., Shirley, J., the Galileo NIMS Team, 2001. Mapping SO2 Frost on Io by the Modeling of NIMS Hyperspectral Images. Icarus 149, 107–132. https://doi.org/10.1006/icar.2000.6513

Fei, null, Bertka, null, Finger, null, 1997. High-Pressure Iron-Sulfur Compound, Fe3S2, and Melting Relations in the Fe-FeS System. Science 275, 1621–1623. https://doi.org/10.1126/science.275.5306.1621

Geissler, P.E., McMillan, M.T., 2008. Galileo observations of volcanic plumes on Io. Icarus 197, 505–518. https://doi.org/10.1016/j.icarus.2008.05.005

Gledhill, J.A., 1967. Magnetosphere of Jupiter. Nature 214, 155. https://doi.org/10.1038/214155a0

Harvey, J.E., Ftaclas, C., 1995. Diffraction effects of telescope secondary mirror spiders on various image-quality criteria. Appl. Opt. 34, 6337–6349. https://doi.org/10.1364/AO.34.006337

Herbert, F., 1996. A simple transport model for the Io plasma torus “ribbon.” Geophys. Res. Lett. 23, 2875–2878. https://doi.org/10.1029/96GL02756

Hikida, R., Yoshioka, K., Murakami, G., Kimura, T., Tsuchiya, F., Yamazaki, A., Yoshikawa, I., Iwagami, N., 2018. Identification of Extreme Ultraviolet Emission Lines of the Io Plasma Torus Observed by Hisaki/EXCEED. J. Geophys. Res. Planets 123, 1723–1731. https://doi.org/10.1029/2018JE005629

Hill, T.W., Michel, F.C., 1976. Heavy ions from the Galilean satellites and the centrifugal distortion of the Jovian magnetosphere. J. Geophys. Res. 1896-1977 81, 4561–4565. https://doi.org/10.1029/JA081i025p04561

Hinson, D.P., Kliore, A.J., Flasar, F.M., Twicken, J.D., Schinder, P.J., Herrera, R.G., 1998. Galileo radio occultation measurements of Io’s ionosphere and plasma wake. J. Geophys. Res. Space Phys. 103, 29343–29357. https://doi.org/10.1029/98JA02659

Hinton, P.C., Bagenal, F., Bonfond, B., 2019. Alfvén Wave Propagation in the Io Plasma Torus. Geophys. Res. Lett. 46, 1242–1249. https://doi.org/10.1029/2018GL081472

Howell, R.R., Spencer, J.R., Goguen, J.D., Marchis, F., Prangé, R., Fusco, T., Blaney, D.L., Veeder, G.J., Rathbun, J.A., Orton, G.S., Grocholski, A.J., Stansberry, J.A., Kanner, G.S., Hege, E.K., 2001. Ground-based observations of volcanism on Io in 1999 and early 2000. J. Geophys. Res. Planets 106, 33129–33139. https://doi.org/10.1029/2000JE001382

Jehin, E., Gillon, M., Queloz, D., Magain, P., Manfroid, J., Chantry, V., Lendl, M., Hutsemékers, D., Udry, S., 2011. TRAPPIST: TRAnsiting Planets and PlanetesImals Small Telescope. The Messenger 145, 2–6.

Jehin, E., Opitom, C., Manfroid, J., Hutsemekers, D., Gillon, M., 2014. The TRAPPIST comet survey in 2014. Bull. Am. Astron. Soc. 46.

Jessup, K.L., Spencer, J.R., Ballester, G.E., Howell, R.R., Roesler, F., Vigel, M., Yelle, R., 2004. The atmospheric signature of Io’s Prometheus plume and anti-jovian hemisphere: evidence for a sublimation atmosphere. Icarus, Special Issue: Io after Galileo 169, 197–215. https://doi.org/10.1016/j.icarus.2003.11.015

Johnson, R.E., 1994. Formation of Na-Containing Molecular Ions at Io. Icarus 111, 65–72. https://doi.org/10.1006/icar.1994.1133

Keszthelyi, L., Jaeger, W.L., Turtle, E.P., Milazzo, M., Radebaugh, J., 2004. A post-Galileo view of Io’s interior. Icarus, Special Issue: Io after Galileo 169, 271–286. https://doi.org/10.1016/j.icarus.2004.01.005

Keszthelyi, L., McEwen, A.S., Phillips, C.B., Milazzo, M., Geissler, P., Turtle, E.P., Radebaugh, J., Williams, D.A., Simonelli, D.P., Breneman, H.H., Klaasen, K.P., Levanas, G., Denk, T., Alexander, D.D.A., Capraro, K., Chang, S.H., Chen, A.C., Clark, J., Conner, D.L., Culver, A., Handley, T.H., Jensen, D.N., Knight, D.D., LaVoie, S.K., McAuley, M., Mego, V., Montoya, O., Mortensen, H.B., Noland, S.J., Patel, R.R., Pauro, T.M., Stanley, C.L., Steinwand, D.J., Thaller, T.F., Woncik, P.J., Yagi, G.M., Yoshimizu, J.R., Castillo, E.M.A.D., Belton, M.J.S., Beyer, R., Branston, D., Fishburn, M.B., Mueller, B., Ragan, R., Samarasinha, N., Anger, C.D., Cunningham, C., Little, B., Arriola, S., Carr, M.H., Asphaug, E., Moore, J., Morrison, D., Rages, K., Banfield, D., Bell, M., Burns, J.A., Carcich, B., Clark, B., Currier, N., Dauber, I., Gierasch, P.J., Helfenstein, P., Mann, M., Othman, O., Rossier, L., Solomon, N., Sullivan, R., Thomas, P.C., Veverka, J., Becker, T., Edwards, K., Gaddis, L., Kirk, R., Lee, E., Rosanova, T., Sucharski, R.M., Beebe, R.F., Simon, A., Bender, K., Chuang, F., Fagents, S., Figueredo, P., Greeley, R., Homan, K., Kadel, S., Kerr, J., Klemaszewski, J., Lo, E., Schwarz, W., Sullivan, R., Williams, K., Bierhaus, E., Brooks, S., Chapman, C.R., Merline, B., Keller, J., Schenk, P., Tamblyn, P., Bouchez, A., Dyundian, U., Ingersoll,

A.P., Showman, A., Spitale, J., Stewart, S., Vasavada, A., Cunningham, W.F., Johnson, T.V., Jones, T.J., Kaufman, J.M., Magee, K.P., Meredith, M.K., Orton, G.S., Senske, D.A., West, A., Winther, D., Collins, G., Fripp, W.J., Head, J.W., Pappalardo, R., Pratt, S., Procter, L., Spaun, N., Colvin, T., Davies, M., DeJong, E.M., Hall, J., Suzuki, S., Gorjian, Z., Giese, B., Koehler, U., Neukum, G., Oberst, J., Roatsch, T., Tost, W., Schuster, P., Wagner, R., Dieter, N., Durda, D., Greenberg, R.J., Hoppa, G., Jaeger, W., Plassman, J., Tufts, R., Fanale, F.P., Granahan, J.C., Ip, W.H., McElroy, M., Yatteau, J., Moore, W.B., Schubert, G., Pilcher, C.B., 2001. Imaging of volcanic activity on Jupiter's moon Io by Galileo during the Galileo Europa Mission and the Galileo Millennium Mission. J. Geophys. Res. Space Phys. 106, 33025–33052.

Khurana, K.K., Jia, X., Kivelson, M.G., Nimmo, F., Schubert, G., Russell, C.T., 2011. Evidence of a global magma ocean in Io's interior. Science 332, 1186–1189. https://doi.org/10.1126/science.1201425

Kieffer, S.W., Lopes-Gautier, R., McEwen, A.S., Smythe, W., Keszthelyi, L., Carlson, R., 2000. Prometheus: Io's wandering plume. Science 288, 1204–1208. https://doi.org/10.1126/science.288.5469.1204

Kivelson, M.G., Khurana, K.K., Volwerk, M., 2002. The Permanent and Inductive Magnetic Moments of Ganymede. Icarus 157, 507–522. https://doi.org/10.1006/icar.2002.6834

Koga, R., Tsuchiya, F., Kagitani, M., Sakanoi, T., Yoneda, M., Yoshioka, K., Kimura, T., Murakami, G., Yamazaki, A., Yoshikawa, I., Smith, H.T., 2018. The time variation of atomic oxygen emission around Io during a volcanic event observed with Hisaki/EXCEED. Icarus 299, 300–307. https://doi.org/10.1016/j.icarus.2017.07.024

Kumar, S., 1985. The SO2 atmosphere and ionosphere of Io: Ion chemistry, atmospheric escape, and models corresponding to the Pioneer 10 radio occultation measurements. Icarus 61, 101–123. https://doi.org/10.1016/0019-1035(85)90158-7

Küppers, M., Schneider, N.M., 2000. Discovery of chlorine in the Io torus. Geophys. Res. Lett. 27, 513–516. https://doi.org/10.1029/1999GL010718

Larson, S.M., Sekanina, Z., 1985. Coma morphology and dust-emission pattern of periodic comet Halley. III - Additional high-resolution images taken in 1910. Astron. J. 90, 823–826. https://doi.org/10.1086/113792

Lellouch, E., 2005. Io's Atmosphere and Surface-Atmosphere Interactions. Space Sci. Rev. 116, 211–224. https://doi.org/10.1007/s11214-005-1957-z

Lellouch, E., Ali-Dib, M., Jessup, K.-L., Smette, A., Käufl, H.-U., Marchis, F., 2015. Detection and characterization of Io's atmosphere from high-resolution 4-μm spectroscopy. Icarus 253, 99–114. https://doi.org/10.1016/j.icarus.2015.02.018

Lopes, R.M.C., 2014. Chapter 35 - Io: The Volcanic Moon, in: Spohn, T., Breuer, D., Johnson, T.V. (Eds.), Encyclopedia of the Solar System (Third Edition). Elsevier, Boston, pp. 779–792.

Lopes, R.M.C., Kamp, L.W., Smythe, W.D., Mouginis-Mark, P., Kargel, J., Radebaugh, J., Turtle, E.P., Perry, J., Williams, D., Carlson, R.W., Douté, S., 2004. Lava lakes on Io: Observations of Io's volcanic activity from Galileo NIMS during the 2001 fly-bys. Icarus 169, 140–174. https://doi.org/10.1016/j.icarus.2003.11.013

Miller, J., 2009. Analysis quantifies effects of tides in Jupiter and lo. Phys. Today 62, 11. https://doi.org/10.1063/1.3206081

Monnereau, M., Dubuffet, F., 2002. Is Io's Mantle Really Molten? Icarus 158, 450–459. https://doi.org/10.1006/icar.2002.6868

Na, C.Y., Trafton, L.M., Barker, E.S., Stern, S.A., 1998. A Search for New Species in Io's Extended Atmosphere. Icarus 131, 449–453. https://doi.org/10.1006/icar.1997.5879

O'Reilly, T.C., Davies, G.F., 1981. Magma transport of heat on Io: A mechanism allowing a thick lithosphere. Geophys. Res. Lett. 8, 313–316. https://doi.org/10.1029/GL008i004p00313

Peale, S.J., Cassen, P., Reynolds, R.T., 1979. Melting of Io by Tidal Dissipation. Science 203, 892–894. https://doi.org/10.1126/science.203.4383.892

Pearl, J., Hanel, R., Kunde, V., Maguire, W., Fox, K., Gupta, S., Ponnamperuma, C., Raulin, F., 1979. Identification of gaseous SO2 and new upper limits for other gases on Io. Nature 280, 755–758. https://doi.org/10.1038/280755a0

Pilcher, C.B., Fertel, J.H., Smyth, W.H., Combi, M.R., 1984. Io's sodium directional features - Evidence for a magnetospheric-wind-driven gas escape mechanism. Astrophys. J. 287, 427–444. https://doi.org/10.1086/162702

Porco, C.C., West, R.A., McEwen, A., Genio, A.D.D., Ingersoll, A.P., Thomas, P., Squyres, S., Dones, L., Murray, C.D., Johnson, T.V., Burns, J.A., Brahic, A., Neukum, G., Veverka, J., Barbara, J.M., Denk, T., Evans, M., Ferrier, J.J., Geissler, P., Helfenstein, P., Roatsch, T., Throop, H., Tiscareno, M., Vasavada, A.R., 2003. Cassini Imaging of Jupiter's Atmosphere, Satellites, and Rings. Science 299, 1541–1547. https://doi.org/10.1126/science.1079462

Rathbun, J.A., Spencer, J.R., 2010. Ground-based observations of time variability in multiple active volcanoes on Io. Icarus 209, 625–630. https://doi.org/10.1016/j.icarus.2010.05.019

Rathbun, J.A., Spencer, J.R., Davies, A.G., Howell, R.R., Wilson, L., 2002. Loki, Io: A periodic volcano. Geophys. Res. Lett. 29, 1443. https://doi.org/10.1029/2002GL014747

Saur, J., Neubauer, F.M., Connerney, J.E.P., Zarka, P., Kivelson, M.G., 2004. Plasma interaction of Io with its plasma torus, in: Jupiter. The Planet, Satellites and Magnetosphere. pp. 537–560.

Saur, J., Strobel, D.F., Neubauer, F.M., Summers, M.E., 2003. The ion mass loading rate at Io. Icarus 163, 456–468. https://doi.org/10.1016/S0019-1035(03)00085-X

Schneider, N.M., Taylor, M.H., Crary, F.J., Trauger, J.T., 1997. On the nature of the λIII brightness asymmetry in the Io torus. J. Geophys. Res. Space Phys. 102, 19823–19833. https://doi.org/10.1029/97JA00773

Schneider, N.M., Trauger, J.T., 1995. The Structure of the Io Torus. Astrophys. J. 450, 450. https://doi.org/10.1086/176155

Schneider, N.M., Trauger, J.T., Wilson, J.K., Brown, D.I., Evans, R.W., Shemansky, D.E., 1991. Molecular Origin of Io's Fast Sodium. Science 253, 1394–1397. https://doi.org/10.1126/science.253.5026.1394

Smyth, W.H., Marconi, M.L., 1998. An explanation for the east–west asymmetry of the Io plasma torus. J. Geophys. Res. Space Phys. 103, 9091–9100. https://doi.org/10.1029/97JA03597

Strom, R.G., Schneider, N.M., Terrile, R.J., Cook, A.F., Hansen, C., 1981. Volcanic eruptions on Io. J. Geophys. Res. Space Phys. 86, 8593–8620. https://doi.org/10.1029/JA086iA10p08593

Summers, M.E., Strobel, D.F., 1996. Photochemistry and Vertical Transport in Io's Atmosphere and Ionosphere. Icarus 120, 290–316. https://doi.org/10.1006/icar.1996.0051

Thomas, N., 1996. High resolution spectra of Io's neutral potassium and oxygen clouds. Astron. Astrophys. 313, 306–314.

Thomas, N., Bagenal, F., Hill, T.W., Wilson, J.K., 2004. The Io neutral clouds and plasma torus, in: Jupiter. The Planet, Satellites and Magnetosphere. pp. 561–591.

Trafton, L., 1975. Detection of a potassium cloud near Io. Nature 258, 690. https://doi.org/10.1038/258690a0

Tsuchiya, F., Arakawa, R., Misawa, H., Kagitani, M., Koga, R., Suzuki, F., Hikida, R., Yoshioka, K., Steffl, A., Bagenal, F., Delamere, P., Kimura, T., Kasaba, Y., Murakami, G., Yoshikawa, I., Yamazaki, A., Yoneda, M., 2019. Azimuthal Variation in the Io Plasma Torus Observed by the Hisaki Satellite From 2013 to 2016. J. Geophys. Res. Space Phys. 124, 3236–3254. https://doi.org/10.1029/2018JA026038

Turtle, E.P., Keszthelyi, L.P., McEwen, A.S., Radebaugh, J., Milazzo, M., Simonelli, D.P., Geissler, P., Williams, D., Perry, J., Jaeger, W.L., Klaasen, K.P., Breneman, H.H., Denk, T., Phillips, C.B., 2004. The final Galileo SSI observations of Io: Orbits G28-I33. Icarus 169, 3–28. https://doi.org/10.1016/j.icarus.2003.10.014

Vasyliunas, V.M., 1983. Plasma distribution and flow, in: Physics of the Jovian Magnetosphere. pp. 395–453.

Veeder, G.J., Matson, D.L., Johnson, T.V., Blaney, D.L., Goguen, J.D., 1994. Io's heat flow from infrared radiometry: 1983–1993. J. Geophys. Res. Planets 99, 17095–17162. https://doi.org/10.1029/94JE00637

Wilson, J.K., Mendillo, M., Baumgardner, J., Schneider, N.M., Trauger, J.T., Flynn, B., 2002. The Dual Sources of Io's Sodium Clouds. Icarus 157, 476–489. https://doi.org/10.1006/icar.2002.6821

Wilson, J.K., Schneider, N.M., 1999. Io's sodium directional feature: Evidence for ionospheric escape. J. Geophys. Res. Planets 104, 16567–16583. https://doi.org/10.1029/1999JE900017

Yoneda, M., Nozawa, H., Misawa, H., Kagitani, M., Okano, S., 2010. Jupiter's magnetospheric change by Io's volcanoes. Geophys. Res. Lett. 37. https://doi.org/10.1029/2010GL043656

Yoneda, M., Tsuchiya, F., Misawa, H., Bonfond, B., Tao, C., Kagitani, M., Okano, S., 2013. Io's volcanism controls Jupiter's radio emissions. Geophys. Res. Lett. 40, 671–675. https://doi.org/10.1002/grl.50095